Physics of Brain Folding

Inaugural-Dissertation
zur
Erlangung des Doktorgrads
der Mathematisch-Naturwissenschaftlichen Fakultät
der Universität zu Köln

vorgelegt von
Lucas de Queiroz da Costa Campos
aus Recife, Brasilien

Köln
2021

Berichterstatter: Dr. habil. Jens Elgeti
Prof. Dr. Matthias Sperl
Prof. Dr. Dr. Svenja Caspers

Tag der mündlichen Prüfung: 03. August 2021

Abstract

The human brain is characterized by its folded structure, being the most folded brain among all primates. The process by which these folds emerge, called gyrogenesis, is still not fully understood. The brain is divided into an outer region, called gray matter, which grows at a faster rate than the inner region, called white matter. It is hypothesized that this imbalance in growth – and the mechanical stress thereby generated – drives gyrogenesis, which is the focus of this thesis.

Finite element simulations are performed where the brain is modeled as a non-linear elastic and growth is introduced via a multiplicative decomposition. A small section of the brain, represented by a rectangular slab, is analyzed. This slab is divided into a thin hard upper layer mimicking the gray matter, and a soft substrate, mimicking the white matter. The top layer is then grown tangentially, while the underlying substrate does not grow. JuFold, the software developed to perform these simulations, is introduced, and its design is explained. An overview of its capabilities, and examples of simulation possibilities are shown. Additionally, one patent-leading application of JuFold in the realm of material science showcases its flexibility.

Simulations are first performed by minimizing the elastic energy, corresponding to the slow growth regime. Systems with homogeneous cortices are studied, where growth initially compresses, and then buckles the cortical region, which generates wavy patterns with wavelength proportional to cortical thickness. After buckling, the sulcal regions (i.e. the valleys of the system) are thinner than the gyral regions (i.e. the hills). Introducing thickness inhomogeneities along the cortex lead to new and localized configurations, which are strongly dependent not only on the thickness of the region, but also on its gradient. Furthermore, cortical landmarks appear sequentially, consistent with the hierarchical folding observed during gestation. A linear stability theory is developed based on thin plate theory and is compared with homogeneous and inhomogeneous systems.

Next, we turn to more physically stringent dynamic simulations. For slow growth rate and time-constant thickness, the results obtained through energy minimization are recovered, justifying previous literature. For faster growth, an overshoot of the

wavenumber and a broad wavenumber spectrum are observed immediately after buckling. After a relaxation period, where the average wavenumber decreases and the wavenumber spectrum narrows, it is observed that the system stabilizes into a finite spectrum, whose average wavelength is smaller than that expected from energy minimization arguments.

Cortical inhomogeneities are further explored in this new regime. Systems with inhomogeneous cortical thickness are revisited, with effects similar to the homogeneous cortex (i.e., results are consistent between the slow growth and the quasistatic regimes, and overshoot is observed in the fast growth regimes). Systems with inhomogeneous cortical growth are simulated, with this new type of inhomogeneity inducing fissuration and localized folding. The interplay between these two inhomogeneities is studied, and their interaction is shown to be nonlinear, with each inhomogeneity type inhibiting the folding effects of the other. That is, the folding profile of each individual region emerges as a result of the local inhomogeneity, and the system does not display an intermediate behavior. Finally, these results are compared with an extended linear stability theory.

Taken together, our simulations and analytical theory expose new phenomena predicted by an incremented buckling hypothesis for folding and show a series of new avenues which could give rise to the important cortical features in the mammalian brain, especially those related to higher-order folding.

Zusammenfassung

Das menschliche Gehirn zeichnet sich durch seine gefaltete Struktur aus und ist das am stärksten gefaltete Gehirn unter allen Primaten. Der Prozess, durch den diese Falten entstehen, genannt Gyrogenese, ist noch nicht vollständig verstanden. Das Gehirn ist in einen äußeren Bereich, die so genannte graue Substanz, und einen innenliegenden Bereich, die so genannte weiße Substanz, die langsamer wächst als der äußere Bereich, unterteilt. Der Fokus dieser Arbeit basiert auf der Hypothese, dass dieses Ungleichgewicht im Wachstum und die dadurch erzeugte mechanische Spannung die Gyrogenese antreibt.

Es werden Finite-Elemente-Simulationen durchgeführt, bei denen das Gehirn als nichtlineares elastisches Medium modelliert wird und das Wachstum über eine multiplikative Zerlegung eingeführt wird. Ein kleiner Ausschnitt des Gehirns, dargestellt durch eine rechteckige Platte, wird analysiert. Diese Platte besteht aus einer dünnen harten oberen Schicht, die die graue Substanz nachahmt, und einem weichen Substrat, das die weiße Substanz nachahmt. Die obere Schicht wächst tangential, während das Substrat nicht wächst.

JuFold, die Software, die zur Durchführung dieser Simulationen entwickelt wurde, wird vorgestellt und ihr Aufbau erläutert. Es wird ein Überblick über die Möglichkeiten der Software gegeben und es werden Beispiele für Simulationsmöglichkeiten gezeigt. Zusätzlich wird anhand einer patentierten Anwendung von JuFold im Bereich der Materialwissenschaften die Flexibilität der Software demonstriert.

Die Simulationen werden zunächst unter Minimierung der elastischen Energie durchgeführt, was dem Regime des langsamen Wachstums entspricht. Es werden Systeme mit homogenem Kortex untersucht, bei denen das Wachstum den Kortex zunächst komprimiert und danach einknickt, was wellenförmige Muster mit einer zur kortikalen Dicke proportionalen Wellenlänge erzeugt. Nach dem Einknicken sind die sulkalen Regionen (d.h. die Täler des Systems) dünner als die gyralen Regionen (d.h. die Hügel). Die Einführung von Dickeninhomogenitäten entlang des Kortexes führt zu neuen und lokalisierten Konfigurationen, die nicht nur von der Dicke der Region, sondern auch von dessen Gradienten stark abhängig sind. Zudem entstehen kortikale Landmarken sequentiell, was mit der hierarchischen Faltung während der Gestation

übereinstimmt. Es wird eine lineare Stabilitätstheorie entwickelt, die auf der Theorie der dünnen Platten basiert und mit homogenen und inhomogenen Systemen verglichen wird.

Als nächstes wenden wir uns physikalisch stringenteren dynamischen Simulationen zu. Für langsame Wachstumsraten und zeitlich konstante Dicke werden die durch Energieminimierung erhaltenen Ergebnisse reproduziert, was die bisherige Literatur rechtfertigt. Bei schnellerem Wachstum werden unmittelbar nach dem Knicken ein Überschwingen der Wellenzahl und ein breites Wellenzahlspektrum beobachtet. Nach einer Relaxationsperiode, in der die mittlere Wellenzahl abnimmt und das Wellenzahlspektrum schmaler wird, wird beobachtet, dass sich das System in einem endlichen Spektrum stabilisiert, dessen Wellenlänge kleiner ist als die man basierend auf Gründen der Energieminimierung erwartet.

Kortikale Inhomogenitäten werden in diesem neuen Regime weiter erforscht. Systeme mit inhomogener kortikaler Dicke werden erneut untersucht, mit ähnlichen Effekten wie beim homogenen Kortex (d.h. die Ergebnisse sind konsistent zwischen dem langsamen Wachstumsregime und dem quasistatischen Regime; ein Überschwingen wird im schnellen Wachstumsregime beobachtet). Es werden Systeme mit inhomogenem kortikalem Wachstum simuliert, wobei diese neue Art von Inhomogenität Risse und lokalisierte Faltung induziert. Das Zusammenspiel zwischen diesen beiden Inhomogenitäten wird untersucht und es wird gezeigt, dass ihre Interaktion nichtlinear ist, wobei jeder Inhomogenitätstyp die Falteffekte ds anderen hemmt. Das heißt, das Faltungsprofil jeder einzelnen Region entsteht als Ergebnis der lokalen Inhomogenität und das System zeigt kein Übergangsverhalten. Schließlich werden diese Ergebnisse mit einer erweiterten linearen Stabilitätstheorie verglichen.

Zusammengenommen zeigen unsere Simulationen und die analytische Theorie neue Phänomene auf, die von einer inkrementellen Knickhypothese für die Faltung vorhergesagt werden, und sie zeigen eine Reihe von neuen Wegen auf, die zu den wichtigen kortikalen Merkmalen im Säugetiergehirn führen könnten, insbesondere zu denen, die mit der Faltung höherer Ordnung zusammenhängen.

“All models are wrong, but some are useful.”

— George Box, *Robustness in the strategy of scientific model building* [1].

Contents

Acknowledgments

Erklärung der Selbständigkeit

List of Figures

Chapter 1

Introduction

1.1 History

The brain is one of the most important organs in mammals, being the control center of many of the activities necessary for continued survival. At the same time, it is among the organs we know the least about. Understanding the inner workings of the human brain is one of the main challenges of the 21st century [2, 3].

The systematic study of the morphological properties of the brain started long ago, in the Antiquity. The Edwin Smith Papyrus, written around 1600 BCE, is one of the earliest human records on surgery. In this papyrus, we find the earliest mention of the folded nature of the brain [4],

> “If thou examinest a man having a gaping wound in his head, penetrating to the bone, smashing his skull, (and) rending open the brain of his skull, thou shouldst palpate his wound. Shouldst thou find smash which is in his skull [like] those corrugations which form in molten copper, (and) something therein throbbing (and) fluttering under thy fingers, like a weak place of an infant’s crown before it becomes whole (...)”

These corrugations are one of the most striking features of the human brain, already being prominent in the works of early anatomists, such as Andreas Vesalius [6] in the sixteenth century, or Willis in the seventeenth [7] (see Fig. 1.1). They are broadly divided into two categories. The gyrus (plural, gyri) is an outward fold, whose crown

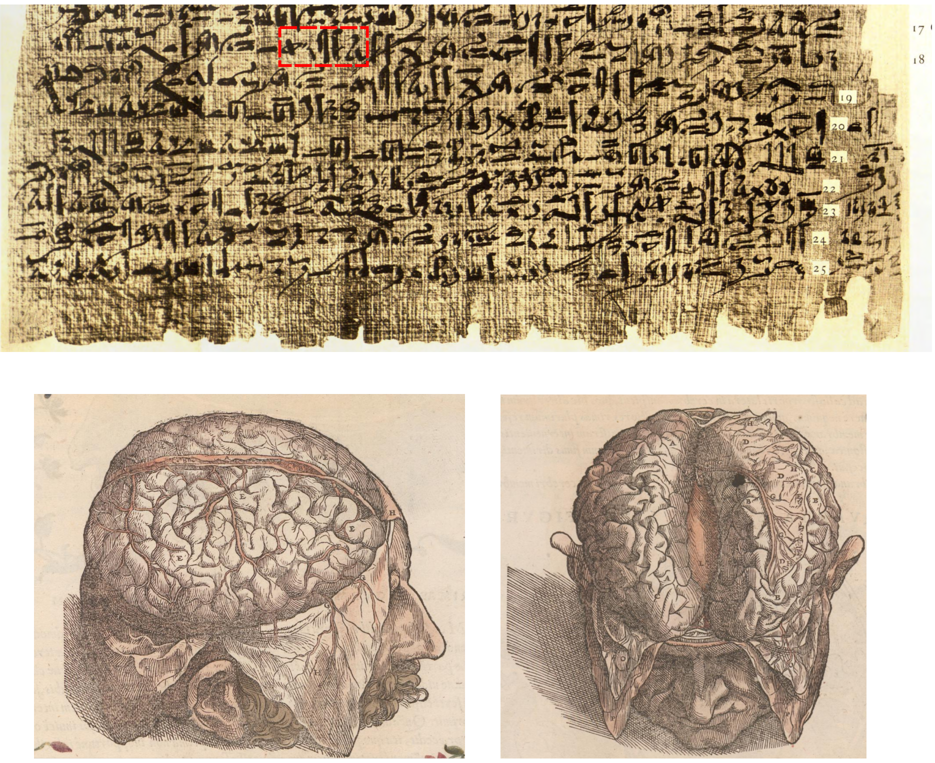

Figure 1.1: (Upper row) Section of the Edwin Smith papyrus. The first written mention of the brain is highlighted in red (Taken from [4], under license CC BY 4.0). (Lower row) Two illustrations by Vesalius, showing some of the first anatomically accurate drawings of the brain [5]. Taken from [6] under Public Domain.

is relatively circular, and the sulcus (plural, sulci) is an inward fold, dividing two adjacent gyri. *In vivo*, the sulci are often hidden by the neighboring contacting gyri.

Throughout the centuries, these folds have been mapped and classified (see Fig. 1.2) [8, 9]. In the current day, such maps are widely available, and their study is part of the fundamental education of physicians and neuroscientists around the world. In modern days, the advent of Magnetic Resonance Imaging (MRI) [10] has enabled researchers to conduct *in vivo* anatomy, allowing for much larger sample sizes when studying the anatomy of the brain, as well as the automated digital evaluation of geometrical and physiological measurements, such as curvature and blood flow. Despite the wide availability of gyral maps, the understanding of how these foldings emerge, a process called *gyrogenesis*, is still not fully understood, neither at the mechanical [11] nor at the genetic level [12].

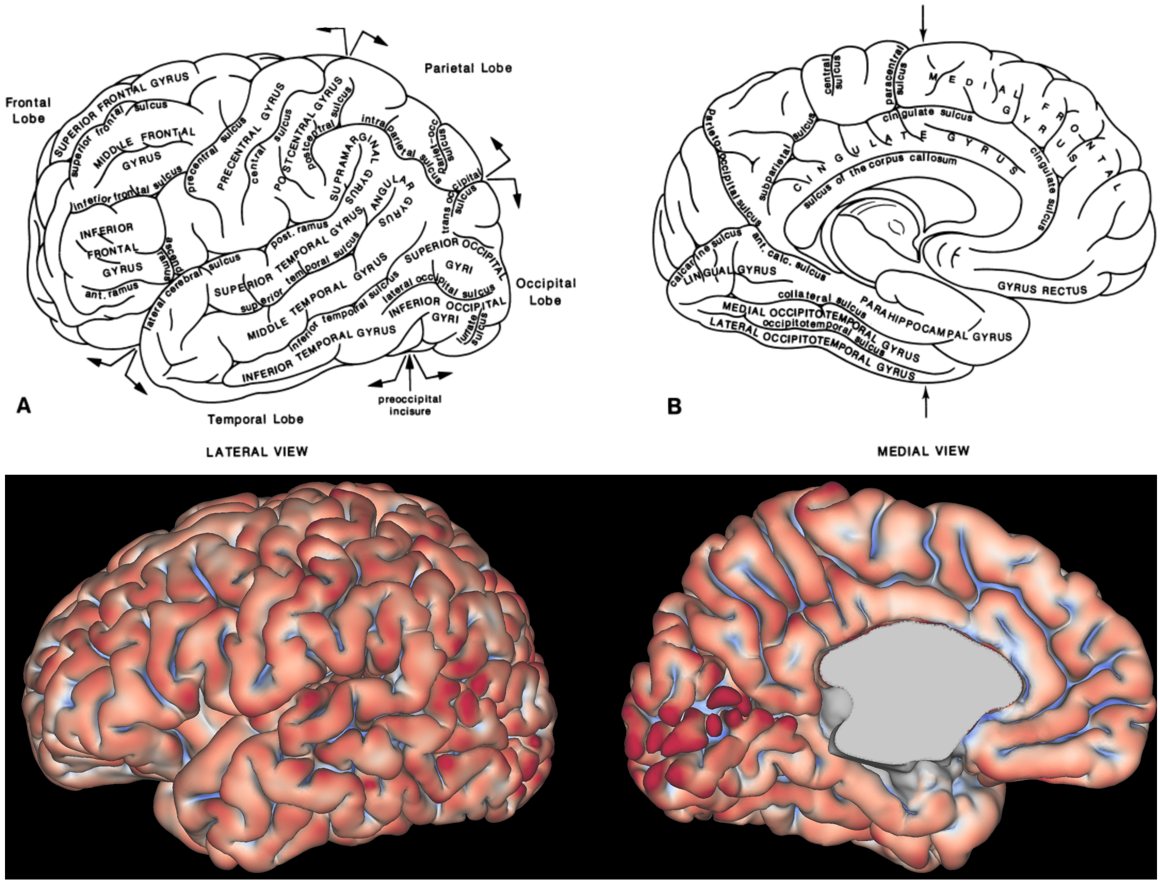

Figure 1.2: (Upper row) “Diagrams of human cerebrum from left lateral (A) and medial (B) aspects, and in transverse section”. Adapted with permission from [13]. ©1990, Springer Science Business Media New York. (Lower row) Similar diagrams, using MRI data. The cortical surface is colored according to its curvature.

1.2 Basic anatomy

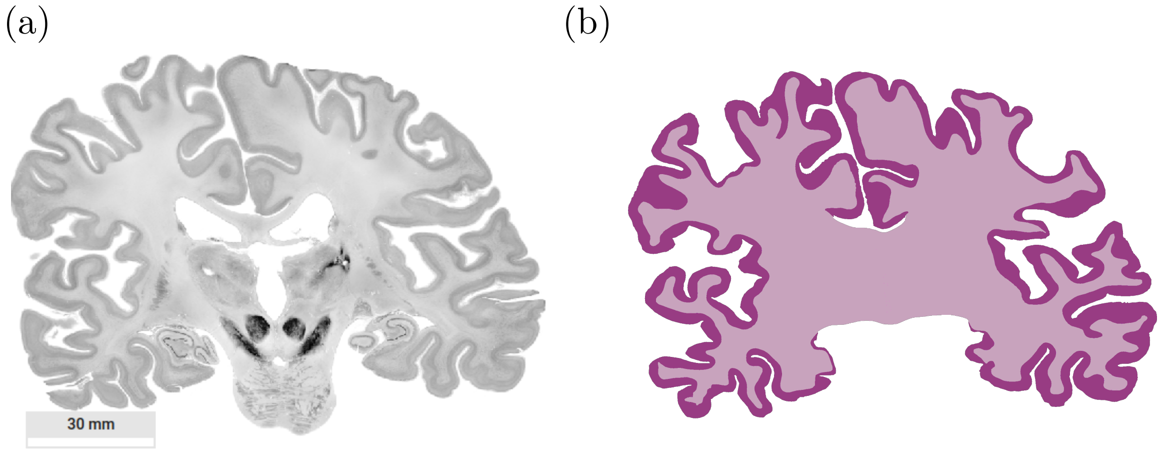

Figure 1.3: (a) Silver stained histological image of human brain, showing the cortical gray matter and white matter, as well as parts of the hypothalamus, thalamus (darker regions on the lower center), and cerebellum (adapted from Jülich BigBrain [14]). (b) Simplified view of the cerebrum, distinguishing only between gray matter (in purple), and white matter (in pink).

There are many ways to divide the brain, with varying complexity and granularity [9, 15, 16]. For the purposes of this work, only a very rough parcellation is required, where the brain can be divided into the brain stem, the cerebellum, and the cerebrum. Our work will be focused on the folding of the last of these (pictured in Fig. 1.2). The cerebrum is the largest region of the brain and houses many important substructures, like fiber tracts, many capsules, etc (see Fig. 1.3 (a)). However, the simplest – and for this work, most useful – division of the cerebrum is simply between its cortex and the bulk. The cortical region of the cerebrum is characterized by a high density of neuronal bodies, which darkens once stained, giving it the name of gray matter. The bulk of the cerebrum is mostly abscent of neuronal bodies, giving it a clearer color[1]. This region, named white matter, is composed largely of structural cells, called glia. Axons belonging to the neurons in the gray matter cross through the white matter, connecting distant parts of the brain and forming fiber tracts of aligned neurons.

The simulations in this work take a simplified view of the brain, taking into consideration only the division between cortical gray matter (from here on simply denoted as

---

[1] It is possible to find special regions with high neuronal densities, which are called deep gray matter, but due to ther distance to the cortex, their limited influence on folding is ignored.

"gray matter" or "cortex") and "white matter" or "bulk" (see Fig. 1.3 (b)). Histological sections are often stained with haematoxylin and eosin [17], which has a distinctive purple-pink color. Following this conventional color scheme, the gray matter is shown in purple and the white matter is shown in pink throughout this work.

1.3 Neuroembryology

Despite the simplified view used in the simulations, it is essential to understand the microscopic processes that occur in the gray and white matter before and during gyrogenesis in order to build a biologically-plausible physical model of folding of the cerebrum. Additionally, the knowledge of the macroscopic features provides the target which this work aims to emulate.

The discussion will now branch into two. Firstly, the microscopical processes parallel to gyrogenesis are presented. Secondly, the folding process is analysed through the lenses of macroanatomy.

1.3.1 Cellular development of the brain

At a microscopical level, the brain tissue is composed of roughly two classes of cells: neuronal and glial cells. They are responsible for markedly different functions. The first acts as the wiring of the nervous system, processing, and transmitting electrical signals. The latter performs all other functions in the brain, such as structural support, homeostasis, removal of pathogens, among others. Additionally some of the glia also aid in the control and processing of neuronal information [18]. Interestingly, the human brain contains approximately the same amount of each of these two classes of cells, both in number of cells, and in total volume [19, 20]. Thus, both cells contribute to the mechanical properties of the human brain.

In the abridged exposition below, the folding process is divided into two main steps, the migration step, and the neuronal differentiation step. Naturally, each of these is composed of a multitude of more specialized steps, which are well studied and categorized. See Refs. [21–23] for reviews on the topic.

At the seventh gestational week, the cortex is divided into several zones. The marginal zone (MZ) is the outermost region at this point, surrounding the subplate (SP), intermediate zone (IZ), the subventricular zone (SVZ), and the ventricular zone

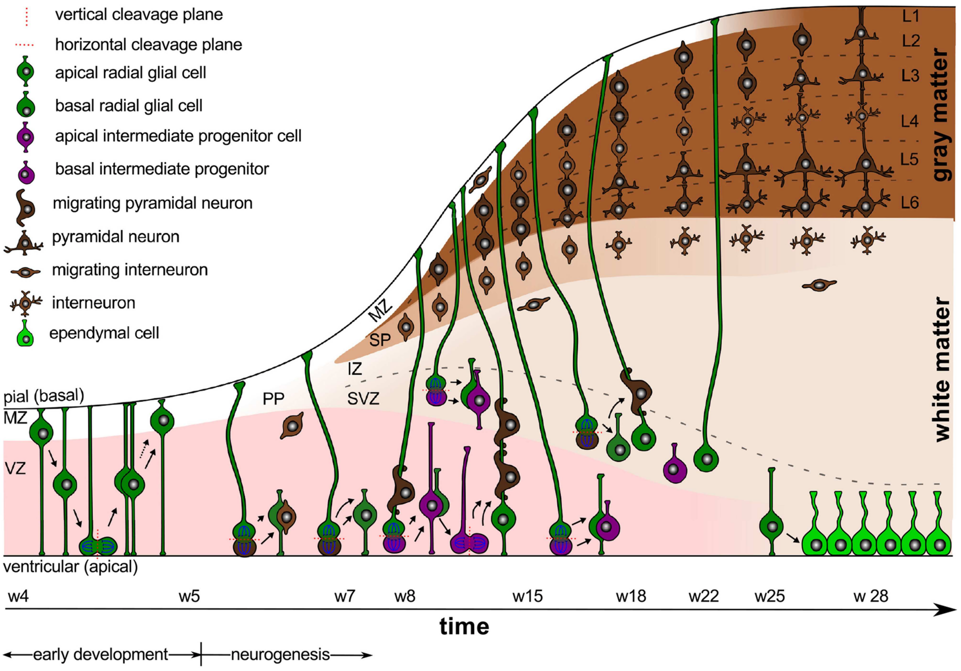

Figure 1.4: Early development and neurogenesis, from gestational week 4 to 28. During early development (before week 6), the neuroepithelial cells divide symetrically, while in neurogenesis, the division is assymetric. During neurogenesis, pyramidal neurons migrate from the ventricular region inside the brain towards the surface. As cells divide assymetrically and migrate to the cortex, the ventricular zone depletes and shrinks. Taken from [21] under License CC BY 4.0.

(VZ), the inner most region. As the brain continues to develop, the VZ, characterized by an abundance of dividing interneurons, fades as they migrate towards the outer regions of the cortex. This neuronal migration happens in waves. In each successive wave, the juvenile neurons migrate to layers VI to I, filling the deeper layers first. This process is called “inside out layering”. The neural migration is facilitated by astroglial cells, which act as scaffolds for the migrating neurons. The migrating interneurons emerge from neural stem cells in the VZ through two processes. First, the neural stem cells transition to form radial glial cells, which then divide asymmetrically generating one neuron and a new radial glial cell. Interestingly, the cells in the VZ are topographically organized in sync with their final configurations, i.e., neighboring cells in the ventricular zone will also neighbor each other once migration is done. The migration processes occur while the brain is still smooth and unfolded [21]. The migrating cells are not yet fully developed, and will specialize and connect during the 22nd week of gestation, and around gestational week 23 folding starts to be observed.

For the specialization of the neurons, a large number of processes at the cellular level are necessary, such as neuronal differentiation and dendrogenesis, neuronal orientation, and synaptogenesis, among many others [13]. Put together, these processes lead to an increase in the surface area, and thickness of the cortical plate. These two quantities do not mature at the same rate. Instead, the thickness maturates at a much earlier stage: It has been shown that the brain cortex of 2 year-old children are as thick as those of adults, while only having 2/3 of the area [13].

1.3.2 Anatomy of folding

Until about the 8th week, the brain is smooth, with the first folds start appearing around the third gestational month [24, 25]. The major folds develop first, with the Sylvian and saggital fissures emerging during the third month. During the following months of gestation, the other gyri emerge, with a well defined time course [26]. Most of the folding is already in place at time of birth, with the peak of gyrification occurring in the second gestational trimester. Folding, however, is a continuous process, continuing well into childhood [27].

Traditionally, the gyri are classified into three broad groups. The folds emerging first are denoted primary and are very similar across different individuals, being also characterized by wider gyri and deeper sulci [13]. The folds emerging later, called secondary and tertiary, are shallower, narrower, and more variable than those that precede them [28–31].

During gyrogenesis, the brain undergoes massive growth. The brain volume increases six- to sevenfold between the 28th and the 60th weeks of development, with a similar increase in cortical area (see Fig. 1.5 (b) and (c)). Both the area and volume increasing almost linearly is not what would be expected from isometric coefficient, which predicts a scaling coefficient of 2/3, i.e., $A \propto V^{2/3}$. Already in the mid-19th century, it was noted that the brain does not grow in an isometric fashion [32]. Recent experiments have further confirmed that this scaling is not observed during brain development, reporting scaling coefficients between 0.8 and 0.9 [33, 34], a noticeable increase from the 2/3 scaling predicted by isometric scaling. This scaling is made possible through folding.

One of the main quantifiers of folding is called the Gyrification Index (GI) [35, 36]. The GI of a given brain is measured as the ratio between the total surface area of the cortex and the exposed area. In that way, the GI of a lissencephalic (i.e., smooth) brain is 1.0, while gyrencephalic (i.e., folded) brains have a higher GI, with typical values in human around 2.6[2] [36].

It comes as little surprise that increases in volume and area are accompanied by a marked increase in the Gyrification Index (see Fig. 1.5 (d)). As such, the folding of the brain allows more surface to fit within a given hull.

1.3.3 Inhomogeneities in the brain

There are important spatial and temporal differences in the physical properties of the developing brain. For instance, different regions present different amounts of tangential cortical expansion [23, 40]. This expansion is caused by biomolecular processes in the outer part of the subventricular zone, which causes a proliferation of intermediate radial glial cells, which then migrate to the cortex.

While it is well known that the folded cortex has inhomogeneous cortical thickness, with the sulci being thinner than surrounding gyri, large thickness differences have been observed in the smooth brain, e.g., ferret brains at post-conceptual age P2 are

---

[2] The gyrification index is by no means the sole way to quantify gyrification, with a review and comparison between this and other quantities being available in Ref. [37].

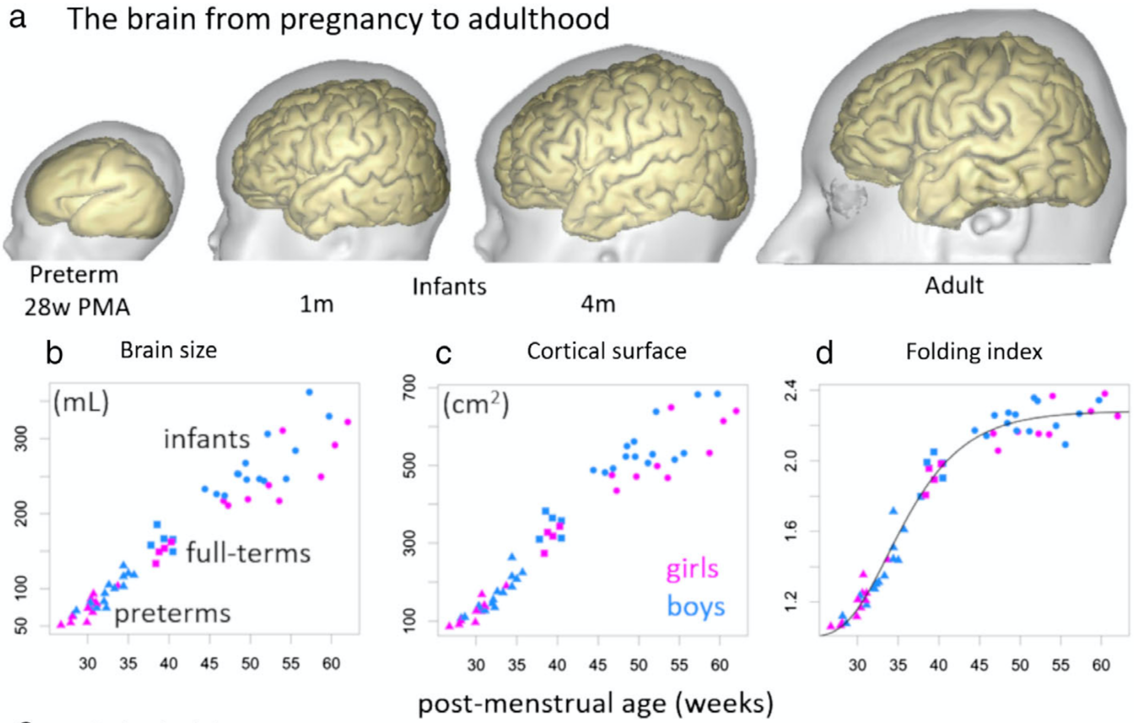

Figure 1.5: "Brain morphological changes from pregnancy to adulthood. Cortical surface reconstructions are presented for a preterm newborn at 28 weeks of postmenstrual age, term-born infants at 1 and 4 months of age, and a young adult (a). Around birth, cerebral development is characterized by important increases in brain size (b), cortical surface area (c), and folding index (d) ratio between inner cortical surface area and the area of the closed surface) as measured in preterm and full-term newborns and infants (adapted from Ref. [31]).". In this figure, the Gyrification Index is called "Folding Index". Adapted from [38], under license CC-BY.

still smooth[3] and exhibit regions with thin cortices surrounded by much thicker regions (see Fig. 1.6). Indeed measurements have shown a 2.5 fold increase in cortical thickness over a length of 2 mm [39]. Further, rheological experiments have shown that elastic properties also vary spatially during development, and undergo a notable stiffening during maturation [41, 42]. These inhomogeneities have been hypothesized to cause the stereotypical development of the mammalian brain [12].

---

[3] Ferret brains start to fold at post-conceptual day 6 [41].

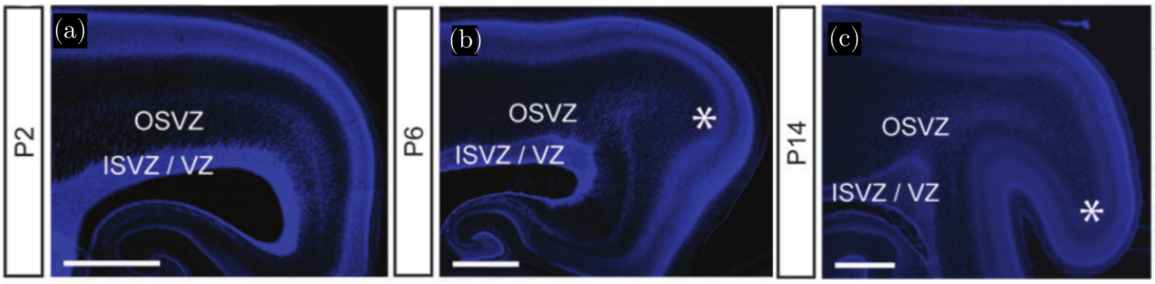

Figure 1.6: “4’,6-diamidino-2-phenylindole (DAPI) staining of the occipital cortex in the ferret brain at different post-conceptual days (P), exhibiting the cortical structure (a) before folding, (b) at the onset of folding and (c) halfway through folding. Scale bar indicate 1mm.” Asterisks indicate the prospective visual area A17. Notice the areas of thin cortex surrounded by thicker cortex in the upper right sides of (a) and (b). Adapted from Ref. [39] ©Reillo at al, 2011.

1.4 Conditions related to folding

Table 1.1: A few examples of cortical malformations that affect folding. Further details and discussions on these conditions can be obtained in Refs. [13, 43–47].

Name	**Short description**
Lissencephaly	Lack of folding
Polymicrogyria	Many small gyri, shallow sulci
Pachygiria	Overly large gyri
Ulegyria	Shrunken and flattened brain
Schizogyria	Periodically interrupted or cracked cortical surface
Hemiatrophy	Shrinking of one of the sides of the brain
Heteroptera	Misplaced nodules of gray matter
Porencephaly	Cavities in the cortex

Many misfolding conditions have been identified (see Table 1.1). Among these, polymicrogyria is one of the most common [45, 51]. Polymicrogyria is characterized by a large number of small and irregular gyri, divided by shallow sulci. There are several degrees of polymicrogyria. Sometimes, only small regions of the cortex are affected 1.7 (a)), while in other cases, the whole cortex is covered in microgyri. Two other striking misfdoling conditions are lissencephaly – the complete or partial lack of folding of the brain (Fig. 1.7 (b))–, and pachygyria – the appearance of large gyri on the brain (Fig. 1.7 (c)). These misfoldings are rare conditions. Lissencephaly, for instance, occurs in only 1 in 85,000 births [46]. Cortical misfoldings are closely

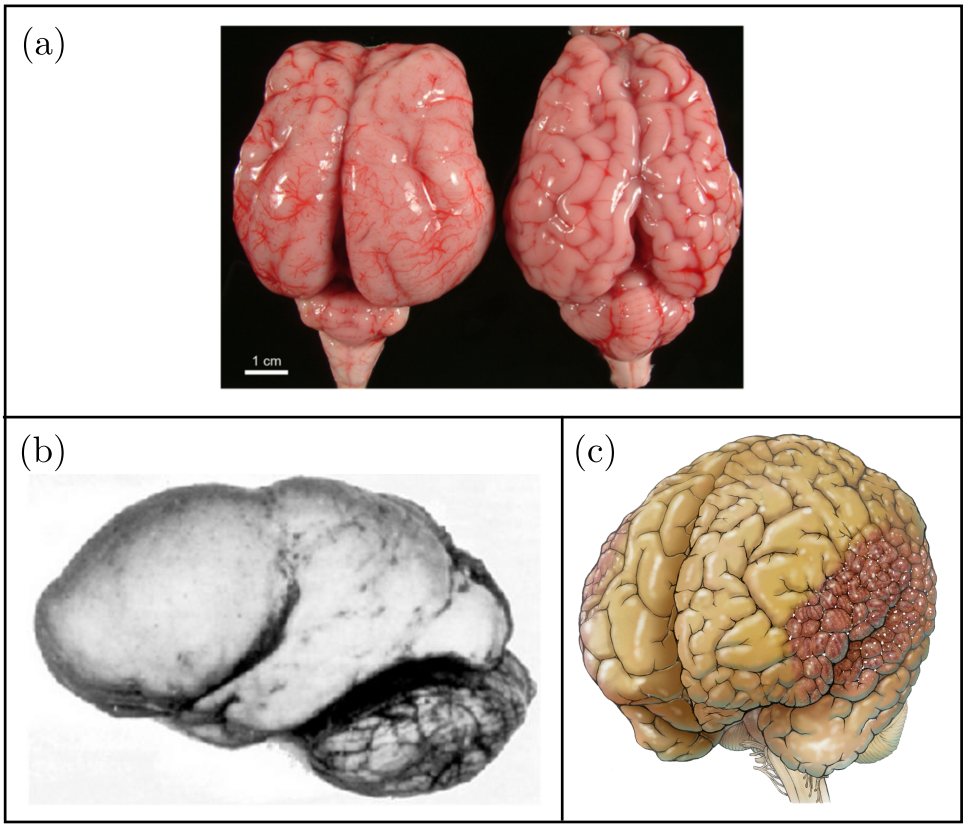

Figure 1.7: (a) Example of pachygyria (left) on a new-born Churra lamb. Compare with the control brain, on the right. Taken from [48] under CC-BY License. (b) Example of lissencephalic human brain. Adapted from [49] under CC-BY License. (c) Schematic representation of a human brain affected by polymicrogyria. Adapted from [50], with permission. ©2018 Elsevier Inc.

related to other symptoms. Epilepsy, for instance, is a common occurrence in those affected by cortical malformations. These malformations have also been associated with varying degrees of mental retardation, seizures, developmental delays, cerebral palsy, and failure to thrive [52].

The origin of these diseases have not been fully understood. Many of these conditions have been linked to genetics [45], and often manifest as over- or undermigration of neurons to the cortex. Such lack or excess of neurons may lead to mechanical changes, for instance, a change in the cortical thickness, or the softening of the brain tissue.

1.5 Hypotheses of folding

1.5.1 Skull constraints

One of the earliest, and maybe most intuitive, hypothesis regarding folding is that it is created through the constraints imposed by the skull onto the cerebrum, thus forcing it to fold in order to fit within the cranial cavity [28]. While perhaps one of the evolutionary incentives, it is not mechanically sound, as the skull does not ossify until after the brain stops growing. Indeed, evidence suggests that the pressure of the growing brain dictates the size of the skull, not vice-versa. In pathological cases, such as megaencephaly, the size of the skull is conformant to the shape of the brain [13, 44], and even in healthy individuals the gyral crowns are imprinted on the internal side of the skull [53], indicating that the skull is being shaped by the brain. In the seminal work by Barron [54], the progenitor skull tissue was removed from a sheep fetus. After the specimen's birth, brain folds were still observed, even in the abscence of the skull. Simulations suggest that the skull could be responsible for the flatness of the gyral crowns, but is not determinant for the folding of the simulated brain [55].

1.5.2 Blood vessels

Another early hypothesis for folding was that the vascularization is one of the drivers of folding. Reichert, in 1861, argued folding would lead to a better entrance of the pial blood vessels into the pial surface [56], an argument echoed by Ranke [57] and Cunningham [58]. A similar argument was made by Kükenthal and Ziehen regarding the lymphatic system [59]. One of the main arguments in favour of this hypothesis was the coincidence between the onset of vascularization with the onset of cortical expansion [60]. This idea was already rejected by the early 20th century, based on the existence of folding in internal structures as well of the cortical surface [60]. This rejection is put most strongly by Welker, who, based on findings that mechanical effects of the blood vessels on the cortex are secondary and superficial, states “No longer is it believed that major blood vessels induce fissuration during development” [13].

1.5.3 Structural connectivity

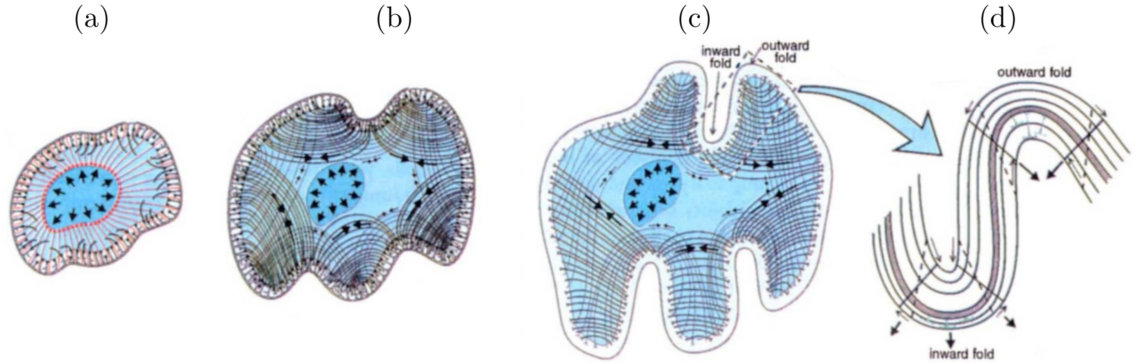

Figure 1.8: “Tension-mediated folding of cerebral cortex. **a**, Early in development, neurons (black) migrate to the cortical plate along radial glial cells (red), differentiate and emanate axons. **b**, Many axons reach specific target structures before the onset of cortical folding. Tension (arrows) would pull strongly interconnected regions together and allow weakly interconnected regions to drift apart. **c**, This leads to outward folds that separate strongly interconnected regions, and inward folds that separate weakly interconnected regions. Connections with subcortical structures (not shown) may also influence cortical folding, although to a lesser degree because the tangential force components are smaller. **d**, Cortical folding causes shearing that tends to stretch the radial axis (broken lines). Compensatory tangential forces (small arrows) would tend to thicken the deep layers along outward folds and the superficial layers of inward folds, making their constituent cells (green) taller and thinner. The converse should occur in superficial layers of outward folds and deep layers of inward folds. Additional tangential force components associated with axons in the white matter (thick arrows) should enhance these effects on deep layers and counteract them in superficial layers.” Adapted by permission from [61] Nature-Springer, Nature, ©1997.

One common hypothesis in the field is based on the tension generated by the axons crossing the white matter. Neurons, as many other biological materials, are active materials, meaning that they are in a permanent state of non-equilibrium [62]. As such, they can respond to external stimuli in complex ways. For instance, when analysed *in vitro*, neurons were observed to impart constant tension upon the substrate [63]. They behave as a complex viscoelastic material: when under intermittent stretches, neurons behave as a simple elastic, while under resting strain, the neurons increase in length, leading to a decrease in the tension observed, until equilibrium is again reached [63]. In contrast to passive materials such as rubbers and polymers which have their materials spread out, the neuronal response to tension is to grow [64], reaching a new rest length. As such, once compressed the neurons do not shrink [63].

Based on these arguments, van Essen posited that the internal wiring of the brain could be one of the main drivers of folding [61]. In this hypothesis, the tug-of-war between the cortical expansion and the tension of the neurons connecting different parts of the brain creates the gyri. Inhomogeneities in the axonal density keeps well-connected areas closer, while allowing areas with few connections to drift apart. As such, this hypothesis would explain two important factors about the morphology of the brain: its folding and its compact wiring.

While widely accepted, this hypothesis went untested for a long time [22]. One of the predictions derived from this hypothesis was that the whole gyrus would be under tension during development. Recently, Xu et al. [41] performed a series of experiments where incisions were performed in developing ferret brains, and the resulting displacements were measured. These experiments showed that while there is indeed tension on the brain, it was located too deep in the white matter. Instead, the center of the gyrus was observed to be under compression, rather than the tension predicted by the axonal traction hypothesis. The status of this hypothesis is currently disputed, with many in favor of the buckling hypothesis (see Sec. 1.5.4). However, recently improvements have been made to this theory, where the smectic organization of axonal bundles, and the cerebral cortex is then modeled as a layered liquid crystal [65], which results in stresses consistent with the experimental data.

1.5.4 Differential growth

Opposed to the tension based hypothesis, in the buckling hypothesis it is compressive stresses in the cortex that leads to folding. In this thesis, we will mainly follow this hypothesis, and consequentially explore its variants in more detail in Sec. 1.6.

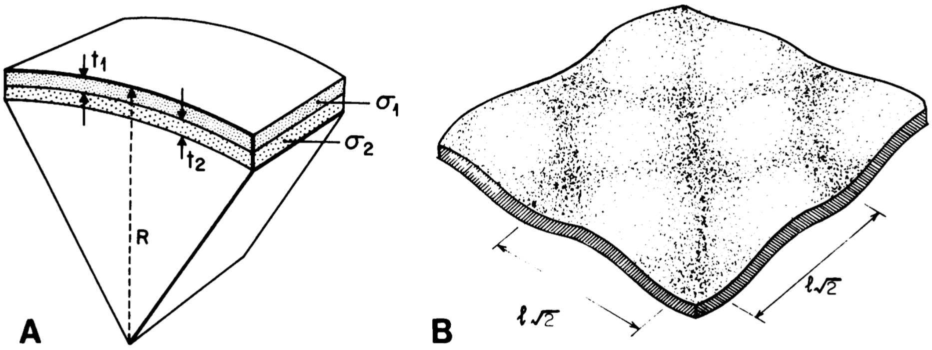

Figure 1.9: "(A) Proposed two-layered spherical model in the initial state before buckling (Symbols are defined in the text.) (B) Illustration of a segment of buckled surface predicted by the mechanical anaysis of the model in (A). The surface shown here, with the wavelength of buckling ($l\sqrt{2}$) equal in both x- and y-directions, is only one of an entire set of possible solutions." In this figure, t_1 and t_2 denote the thickness of cortical layers, and σ_1 and σ_2 denote the stress on these layers. Adapted with permission from [66]. ©1975, American Association for the Advancement of Science.

As mentioned previously, the brain is divided into two main regions: The gray matter, and the white matter. The former is subdivided into a number of layers, typically six (see Sec. 1.3.1). In 1975, Richman et al [66] argued that a mismatch between the growth of these layers could generate enough stress that the whole cerebral cortex would buckle. Richman analytically calculated the corresponding energy minimum of this mismatched system, and observed that the resulting conformation is a wavy structure, whose wavelength depends on the ratios between the stiffness of the cortical layers as well as geometrical quantities, such as the thickness of the cerebral cortex. Given the then-current estimates for the cortical thickness, the theory required a large stiffness ratio between the gray and white matter materials, in the order of 10 [11]. These ratios disagree with data from rheological experiments, which indicate a value closer to unity [11]. While more accurate estimates of the cortical thickness lead closer-to-real estimates of the wavelength [67], some issues still linger.

Firstly, this hypothesis only generates the primary folding of the cortex. Secondly, the shape of the gyri is not as those observed in the mammalian brain. Namely, the mammalian brain presents smooth gyri and cusped sulci, while the postbuckling conformations look like a smooth wave [68]. Thirdly, the folds of the brain, specially the primary gyri and sulci, are highly reproducible between different individuals [28], for which no mechanism was originally proposed. Lastly, the buckling hypothesis depends on the gray matter being at least moderately stiffer than the white matter. Currently, there is no consensus on that, with experiments indicating that the gray matter is indeed stiffer than the white matter [42, 69, 70], and vice-versa [71–73].

Another buckling-based model was put forth by Mota et al. [74], where the cortex is modeled as a thin sheet, which is then compacted, in a process similar to the production of a ball out of a sheet of paper. This model was shown to accurately predict the relation between the total cortical surface, cortical thickness and exposed area, and consequentially, GI. This model, however, exacerbates the morphological issues in the Richman model. The creases appear at random, and the shape of the folding is not at all similar to those in the brain [22].

1.6 State of the art

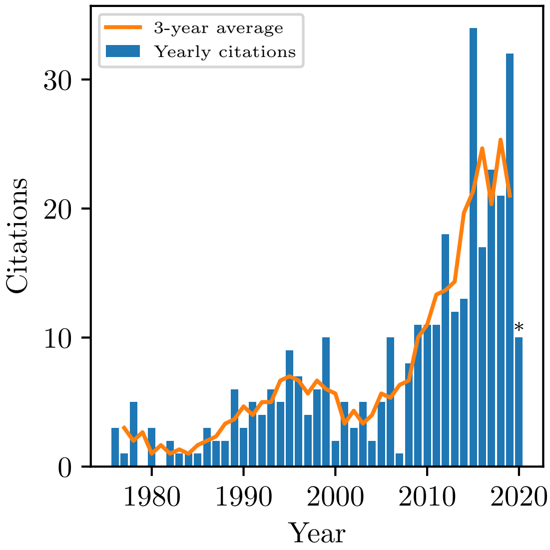

Figure 1.10: Number of citations of the original article proposing the buckling hypothesis [66], per year. Data retrieved from Web of Science on 2020-Jun-23. The asterisk indicates incomplete yearly data.

In recent years, there has been renewed interest in the buckling hypothesis (see Fig. 1.10). A slight modification to the proposal by Richman has gained wide acceptance, where no longer the difference between the growth in different cortical layers leads to buckling. Rather the difference between the cortex and the underlying white matter generates the buckling stress [68, 75, 76].

One of the earlier efforts in this new wave was that of Toro and Burnod [75]. They introduced a simple but rich model, where an elastic ring connected through a substrate to a hard core grows and folds. The ring and the substrate within are split into a moderate number of quadrilaterals, with a single layer for the ring, and another layer for the substrate. In this model, the ring is intended to mimic the growth process happening in the cortex, while the substrate mimics the white matter underneath.

The reference area of the cortical ring is grown logistically, while both the substrate and the ring are allowed to accommodate deformations plastically. In this model, folding happens in three steps. Firstly, the brain grows symmetrically, while unfolded. On the second step folding becomes energetically favorable, and the ring buckles. Lastly, there is an accommodation of the folds, where the folds migrate around the perimeter of the ring, and sometimes, merge into a larger fold (see Fig. 1.11). It was also observed that the post-buckling thickness was non-uniform, with the gyri being slightly thicker than the sulci. The effects of geometrical and mechanical differences in brain folding were studied, where it was noted that the curvature, inhomogeneities in the stiffness of the cortex, and its growth rate are important folding determinants.

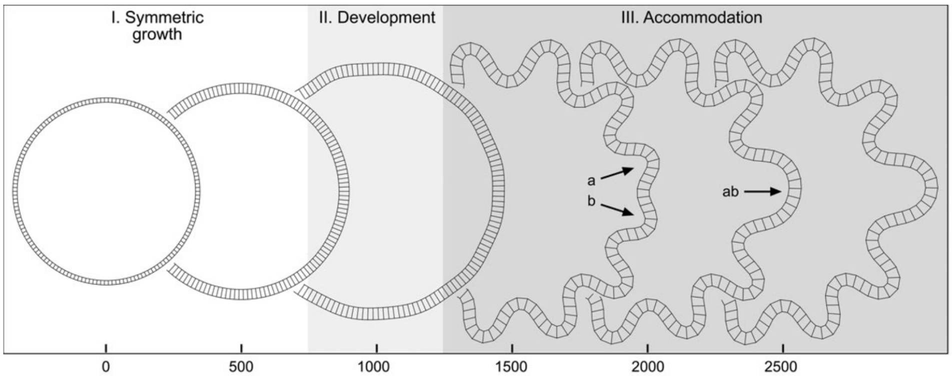

Figure 1.11: “Development of convolutions in the model. (...) Screenshots of the model at 500 iteration steps (radial elements are not drawn to avoid burden). Initially the model expands symmetrically without developing convolutions, then convolutions develop, and finally the convolutions are accommodated in the cortical layer.(...)”. Taken with permission, from [75]. ©Roberto Toro 2005.

The main shortcomings of this model come from its simplicity. While inspired by the rheology of the brain, it uses first order approximations of the viscoelastic properties of cephalic material. Furthermore, as the cortex is modeled as a monolayer of simulation cells, tangential displacements are severely restricted. As such, while it does reproduce important aspects of gyrogenesis, it does not break the sinus-like folding patterns predicted by Richman forty years prior [66].

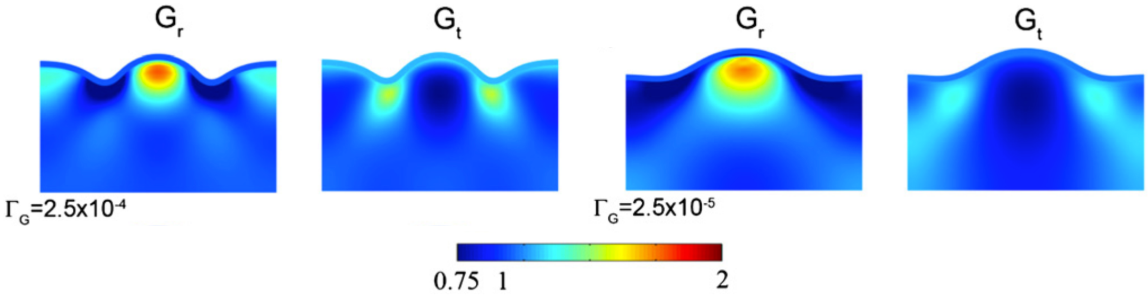

Figure 1.12: “Effects of cortical growth rate on wavelength, subcortical growth, and stress in the cortical folding model with a compressive target stress in the outer core. Columns: radial growth G_r; tangential growth G_t (...)”. Γ_G indicates the ratio between the growth rate of the cortex, and the stress response rate of the white matter. Adapted under permission from [77]. ©2013 IOP Publishing Ltd.

A few years later, Bayly et al. used a more sophisticated model, where the brain material is now modeled using the more complex framework of continuum mechanics [77]. In this framework, the material properties of the brain can be more directly connected with experimental data. The viscoelastic aspect of the white matter was introduced through a homeostatic growth law, where regions with stress smaller than a target stress shrink, while those above the target stress grow. The cortical material, however, was modeled as a purely elastic material, which grows with no regards to the current stress or strain.

It was noted that the rate by which the white matter responds to stress was important in the determination of the folding wavelength, with wavelengths consistent with those obtained experimentally (see Fig. 1.12). In contrast to the works of Richman et al., large stiffness contrasts between the white and gray matter were not necessary in the model, where as both the gray and the white matter had the same elastic properties (see Fig. 1.12). The predicted stress fields obtained computationally were consistent with those obtained experimentally in the developing ferret brain [41].

In 2014, Tallinen et al. realised fully three-dimensional simulations of the grow-

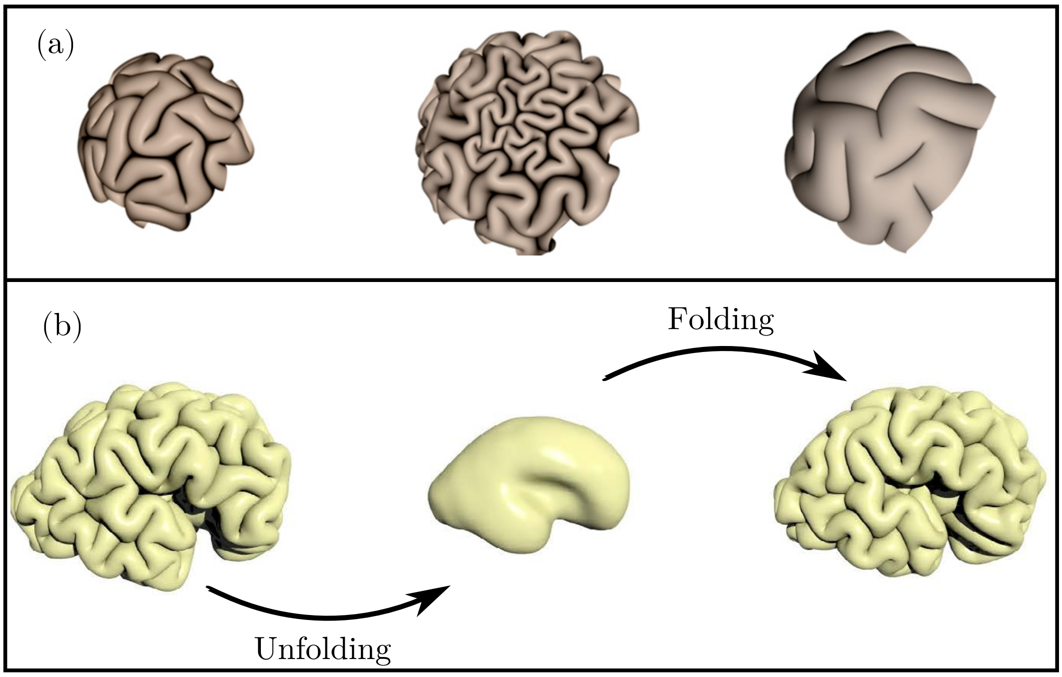

Figure 1.13: (a) Results of growth on spherical sections. In this experiment, the left configuration corresponds to a healthy brain. The middle configuration presents a thinner cortex in one patch, leading to results reminiscent of polymicrogyria. On the right, a thickned cortex leads to results similar to pachygiria. Taken under non-commercial license from [68]. ©Tallinen et al. (b) Process of unfolding and refoling a numerical brain. ©2016, Springer Nature

ing brain. In this work, they allowed the cortex of an elastic sphere to grow, and obtained fascinating folding patterns [68]. From this homogenous cortex, a realistic folding pattern emerges, with folds that are, at first sight, strikingly similar to those found in the mammalian brain. However, upon close scrutiny, it is noted that misses some important aspects of folding, such as the hierarchical folding, and reproducible directionality of the folds. The effects of the skull were also studied, and it was noted that it was not required for realistic folding characteristics of the brain (see Fig 1.13 (a)).

They built on top of the these simulations a few years later, where a virtual brain was shrunken, and then grown back to its original volume [78]. Many features of the original brain were observed in the configuration resulting from the growth of the fetal brain obtained numerically (see Fig 1.13 (b)).

Budday's group has been doing intensive research on the details of brain folding.

These works have shown a large number of interesting phenomena predicted by the buckling hypothesis. They model the gray matter similarly to Bayly [77], where the gray matter is modeled as a hyperelastic material growing autonomously, while the white matter grows only in response to stress. However, they use the simplifying assumption that the white matter always grows volumetrically. That is, even stretches in a single direction would lead to growth along all three axes.

In one of the earlier works, it was shown that successive bucklings are prime candidates for drivers of higher order folding [79]. This is in contrast to what was observed in the earlier works by Toro et al. [75], who observed the smooth emergence of higher order folds, which are not consistent with the idea of multiple buckling processes, where they performed three dimensional simulations of ellipsoids [76]. In previous works in rectangular domains, it was observed that the wavenumber of the post-buckling configuration depends on the mechanical parameters – Young Modulus and Poisson ratio – and the cortical thickness of the grown layer [80, 81]. It was shown that the curvature is also important in the determination of the folding wavelength of the folds. This helps explain the variations between the folding conformations of different species, where spherical brains have uniform folds, while elongated brains fold primarily in the longitudinal direction [28]. Another work conducted in the same lab studied the effects of stiffness and growth inhomogeneity, which indicated that in addition to secondary and tertiary buckling, structures reminiscent of the higher order folding also emerge due to growth and stiffness inhomogeneities in the brain [82].

The works highlighted so far dealt mostly with the purely mechanical aspects that might drive folding, and have not studied how growth emerges, nor the interplay between growth factors and folding. Since the seminal work by Turing [83], one of the leading frameworks in morphogenesis has been the Reaction-Diffusion paradigm, where the concentration of growth factors are explicitly modeled. One of the most common formulations of this idea is called the Gray-Scott reaction-diffusion model, modeling two reagents with concentrations u and v

$$\begin{aligned}\frac{\partial u}{\partial t} =& r_u \nabla^2 u - uv^2 + f(1-u)\\ \frac{\partial v}{\partial t} =& r_v \nabla^2 v + uv^2 - (f+k)v,\end{aligned}$$

where $r_{\{u,v\}}$ describe the diffusion rate of the reagents, k represents the conversion rate between the two reagents, and f represents the rate of the process consuming the reagents. This two-component model is known to create a plethora of different patterns, depending on the rate of reaction and feeding of each component [84] (see Fig. 1.14).

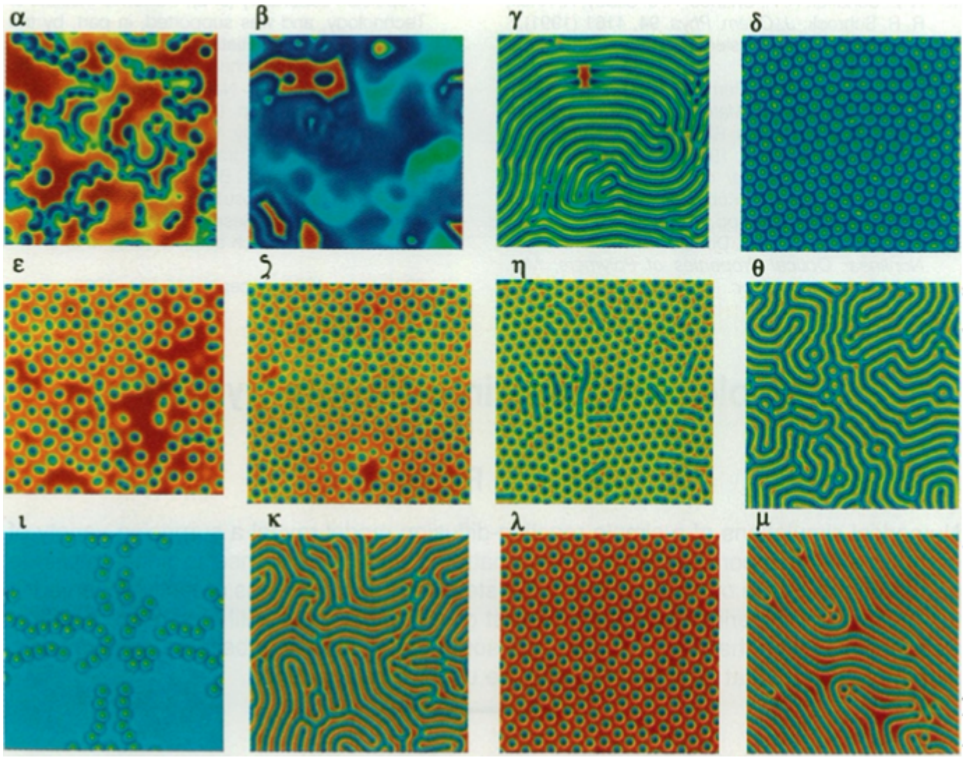

Figure 1.14: The various patterns predicted by the Gray-Scott model. Taken under permission, from [84]. ©1993 by the American Association for the Advancement of Science.

These models were applied to the brain by Lefèvre et al. where the two components are posited to be activators and inhibitors of growth [49], the former of which leads to an increase in the cortical area. These simulations were conducted on spherical manifolds, where the formation of complex labyrinths, and in some cases, isolated spots, reminiscent of polymicrogyria were observed. These results were refined by Hinz et. al., where isogeometric analyses was also employed in addition to the finite element analyses employed by Lefèvre et al. [85], leading to the ability to create smoother resolutions, indicating the possibility of even larger and detailed simulations in the future.

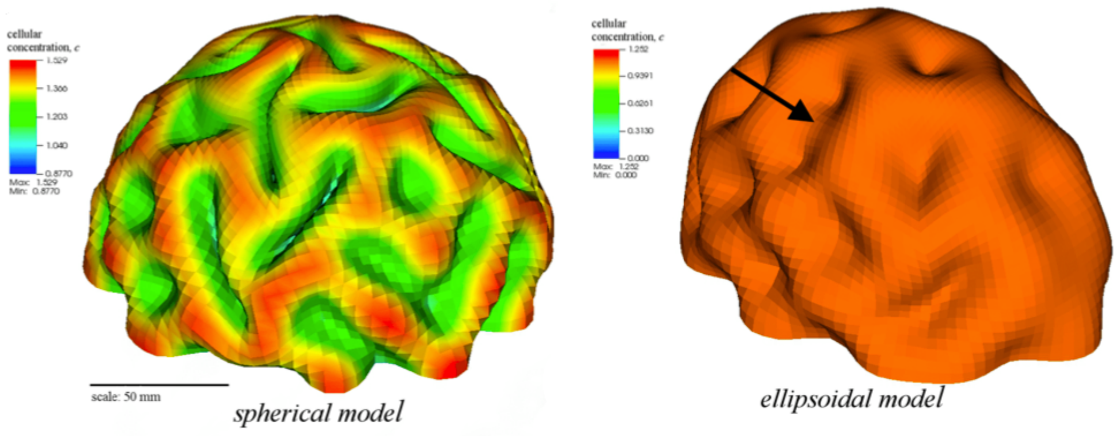

Figure 1.15: “An isometric view comparison of the hemispherical model, left, and hemi-ellipsoidal model, right”. The arrow on the left indicate a structure resembling an emergoing central sulcus. Taken with permission, from [86]. ©2017 Elsevier Ltd.

Verner and Garikipati [86] conducted a similar investigation to Lefèvre, which accounted for both mechanical distortions and diffusion of the growing factor. They modeled the cell density through a reaction-diffusion-advection equation, which is numerically more amenable. This model was employed on ellipsoidal shells and corroborated the importance of geometry, showing that structures resembling the central sulcus emerge once the eccentricity of the initial manifold is large enough. It was observed that neglecting the cell density migration inhibits the formation of the localized central sulcus (see Fig. 1.15). Such feature highlights the importance of inhomogeneity in the formation of localized structures, as the removal of cell migration from their model leads to homogeneous growth, and therefore, to non-localized structures.

1.7 Summary and Objectives

In this chapter, many of the characteristics of the mammalian brain were introduced, and the processes it undergoes were outlined. Emphasis was put on those processes that are thought to be relevant for gyrogenesis. Some of the hypotheses regarding the drivers of folding were introduced. Out of the various hypotheses proposed throughout the centuries, the buckling hypothesis has received special attention in the contemporary literature. Current models of brain development derived from the buckling hypothesis can reproduce the coarser aspects of gyrogenesis, but important features are still missing. The importance of these features is derived from their ability to distinguish between healthy and unhealthy development.

This work aims to help understand the folding process of the brain using simulation tools. The mechanistic approach, where the stresses and strains are seen as drivers of the morphogenesis will be used. Two aspect of folding will be explored in detail. Firstly, the effects of inhomogeneities in the cortex will be analysed, both in isolation and in union.

Another important aspect of folding is the interplay between the timescales of the various processes during growth. As shown in Sec. 1.3, folding is a complex process involving many steps, each with their own timescales. The importance of these timescales is probed by performing simulations with various growth rates, and performing comparisons both among themselves, and with systems obtained using the quasistatic approximation.

The source of the probed inhomogeneities will not be target of further discussion – they will be assumed to exist *a priori*. However, it is important to keep in mind the literature body showing that the inhomogeneities are possibly a natural consequence of the diffusion and reaction of growth agents throughout the brain during development and were observed in cortical and subcortical structures [39, 40] (see Subsec 1.3.3 for more details).

1.8 Structure of this thesis

The remainder of this thesis is organized as follows. In Chapter 2, the theory of continuum mechanics, with focus on nonlinear elasticity, and the finite element method are developed. They are used to obtain the equations which will be calculated numerically. The Newton-Raphson root finding algorithm and the Verlet algorithm are adapted for the case at hand. In Chapter 3, the software package developed during this thesis, JuFold, is presented. Its overall design is described, as well as a gallery of examples. Chapter 4 studies how homogeneous and inhomogeneous systems develop in the slow growth regime. We show that inhomogeneities in the thickness of cortical layer of these systems is enough to generate conformations similar to those in the mammalian brain. In Chapter 5 dynamical simulations are introduced. The relative time scales of growth and relaxation are analysed. Inhomogeneities in growth rate are introduced in isolation, and the interplay between different inhomogeneities is studied. Finally, Chapter 6 provides a summary of the results obtained, a provides an outlook for possible new research.

Chapter 2

Theory & methods

2.1 A short introduction to nonlinear elasticity

The current theory of nonlinear elasticity is the combined result of the work of many people, being an elegant, wide, and diverse field. Here we present a brief overview of the topic, covering solely the topics directly required for the critical understanding of the results in this work. Good introductions to the topic can be found in [87, 88], while more advanced accounts can be found in [89–91].

2.1.1 Configurations, coordinates, the gradient deformation tensor

The key to the undertanding of nonlinear elasticity is to keep in mind that there are two configurations, and therefore, two sets of coordinates to work with. First, there is the original configuration, denoted by $\mathcal{B}_0 \subset \mathbb{R}^3$. This is the configuration that the body would assume without external forces or contraints, being thus stress-free. Once forces and constraints act on the body, it assumes the deformed configuration, denoted by $\mathcal{B} \subset \mathbb{R}^3$[1]. As an example, a bar supported on its sides is shown in Fig. 2.1. Without external forces, the bar is flat. Once forces act on it, the bar assumes a curved configuration.

In this work, capital letters will denote entities on the original configuration, and

---

[1] In Sec. 2.2, a third, grown, configuration is introduced, which is the result of internal process that change the original configuration and produce a new stress-free configuration.

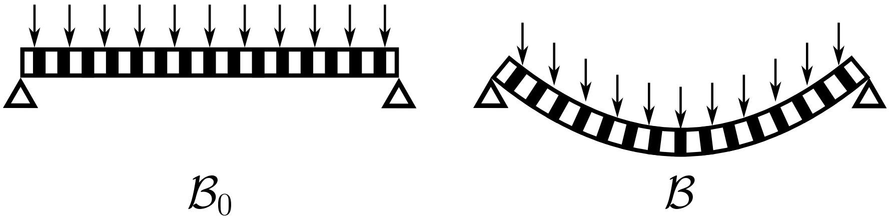

Figure 2.1: Sketch of a supported bar under a traction field (e.g., gravity), represented by arrows pointng down. The original configuration $\mathcal{B}_0$ is represented on the left. Once forces act on this body, it deforms into the configuration $\mathcal{B}$, as sketched on the right side

minuscule letters will denote entities on the deformed configuration, with minor exceptions indicated in the text. For instance, the coordinates of the original configuration are denoted by $\mathbf{X} = (X_x, X_y, X_z)$, while the deformed coordinates are denoted by $\mathbf{x} = (x_x, x_y, x_z)$. More formally, the deformed coordinates are given by a mapping $\mathbf{x} = \phi(\mathbf{X})$ from the original into the deformed coordinates, with the $\mathcal{B}_0$ being the domain of this mapping, and $\mathcal{B}$, its range. The displacement $\mathbf{u}(\mathbf{X})$ is defined as the difference between the coordinates on each configuration, $\mathbf{u}(\mathbf{X}) = \mathbf{x} - \mathbf{X}$.

It is possible to work in any of the two coordinates, with equivalent results. This work stays mostly in the original (also called *material* or *Lagrangian*) configuration. For completeness, the deformed configuration is also called *spatial* or *Eulerian*. The functional form of many quantities in the two configurations can be connected using the gradient deformation tensor

$$\mathbf{F} = \nabla_0 \mathbf{x} = \frac{\partial \mathbf{x}}{\partial \mathbf{X}}. \tag{2.1}$$

Equivalently, it is possible to write this tensor in terms of the displacement field $\mathbf{u}$ as $\mathbf{F} = \partial \mathbf{u}/\partial \mathbf{X} + \mathbf{I}$. It is worth the effort to understand the action of the gradient deformation tensor $\mathbf{F}$ on a small line in the original configuration $d\mathbf{X}$. Multipling $\mathbf{F}$ with this differential yields

$$\mathbf{F} d\mathbf{X} = \frac{\partial \mathbf{x}}{\partial \mathbf{X}} d\mathbf{X} \tag{2.2}$$

and by the application of the chain rule,

$$\mathbf{F} d\mathbf{X} = d\mathbf{x}. \tag{2.3}$$

That is, $\mathbf{F}$ takes a small line in the original configuration, and returns its corresponding line in the new configuration. Similarly, it is possible to push any quantity forward and backward between the two configurations. However, the way to perform these operations is specific to each quantity. For instance, to push the element of area, the following equation is used

$$d\mathbf{a} = J\mathbf{F}^{-1}d\mathbf{A}, \tag{2.4}$$

where $J = \det(\mathbf{F})$. Pushing quantities forwards and backwards between the two configurations is a common operation. So common, in fact, that there is a specific notation for both of these operations. $\phi_*[\mathcal{A}]$ and $\phi_*^{-1}[\mathcal{A}]$ are called the *push forward* (from $\mathcal{B}_0$ to $\mathcal{B}$) and *pull back* (vice-versa) respectively, for any given quantity $\mathcal{A}$. For instance, the pushing forward and backward of the differential line is written as $d\mathbf{x} = \phi_*[d\mathbf{X}]$ and $d\mathbf{X} = \phi_*^{-1}[d\mathbf{x}]$. This notation allows us to focus on the big picture, and hide details that, while important, might distract from the main point.

2.1.2 Strain

Comparing the displacement of two different bodies can often be misleading, as the sizes involved can be widely different. Large displacements on a large body can be created by small local deformations, while the same displacement on a much smaller body can only be created by large local deformations. In order to develop a universal theory that is independent of the dimensions of the body being studied, the strain, rather than the displacement should be used. In the small displacement regime, the strain is defined by the tensor $\epsilon_{ij} = \frac{1}{2}\left(\frac{\partial u_i}{\partial x_j} + \frac{du_j}{dx_i}\right)$, where u_i is the i-th component of the displacement. This definition carries the following advantages

1. It is independent of the length of the body;
2. It is invariant under solid-body displacement;
3. It is zero when the deformed and original configurations coincide.

While advantageous for its simplicity, the infinitesimal strain tensor $\boldsymbol{\epsilon}$ is often not appropriate, as it is not invariant under rotation and does not distinguish between the strain measured in the material and spatial coordinates. New strain tensors need to be built that bridges those gaps.

Upon deformation, the length of a small vector $d\mathbf{x}$ in deformed coordinates relates to its original length by

$$d\mathbf{x} \cdot d\mathbf{x} = \phi_*[d\mathbf{X} \cdot d\mathbf{X}] = d\mathbf{X} \cdot (\mathbf{F}^T\mathbf{F}) \cdot d\mathbf{X} = d\mathbf{X} \cdot \mathbf{C} \cdot d\mathbf{X} \tag{2.5}$$

where the tensor $\mathbf{C} = \mathbf{F}^T\mathbf{F}$ is called the *right* Cauchy-Green tensor, which has the property of pushing lengths from the original into the deformed configurations. A similar procedure can be followed by pulling the length $d\mathbf{x} \cdot d\mathbf{x}$ from the deformed to the original coordinates, obtaining in the process *left* Cauchy-Green tensor $\mathbf{b} = \mathbf{F}\mathbf{F}^T$.

Being based on the gradient deformation tensor, both of the Cauchy-Green tensors are length-independent and translationally invariant. In order to prove that they are also frame-indifferent[2], the Polar Decomposition theorem is invoked, which states that for a given matrix it is possible to obtain a decomposition such that

$$\mathbf{F} = \mathbf{U}\mathbf{R} \quad \text{or} \quad \mathbf{F} = \mathbf{R}\mathbf{V}. \tag{2.6}$$

These are called the left and right polar decompositions, respectively. Here, $\mathbf{R}$ is a rotation tensor, and $\mathbf{U}$ and $\mathbf{V}$ are symmetric tensors. As all the rotational information is in encoded into $\mathbf{R}$, it is clear that both the Cauchy-Green tensors are rotationally invariant, as the information is eliminated in the products $\mathbf{R}^T\mathbf{R}$ and $\mathbf{R}\mathbf{R}^T$. It is now possible to define the strain tensors

$$\mathbf{E} = \frac{1}{2}(\mathbf{C} - \mathbf{I}) \quad \text{and} \quad \mathbf{e} = \frac{1}{2}(\mathbf{I} - \mathbf{b}^{-1}). \tag{2.7}$$

which have the same properties as the infinitesimal strain tensor $\boldsymbol{\epsilon}$, and solve its shortcoming. These are called the *material* and the *spatial* strain tensors[3]. In the limit of small displacements, both forms of the strain tensor approach the usual linear strain tensor $\boldsymbol{\epsilon}$.

These two are some of the most commonly used strain tensors. However, other choices are possible, and useful in specific situations [93]. For instance, the Hencky strain $\mathbf{E}_0 = \log \mathbf{U}$ has several applications in hypoelasticity [94]. Even the properties

---

[2] In continuum mechanics, tensors are often defined as a linear transformation [87], in contrast to fields more closely connected differential geometry, where tensors are defined as quantities obeying certain transformation rules [92]. In continuum mechanics, quantities that do obey these transformations are called *objective tensors*.

[3] It is possible to push the material strain tensor to its spatial correspondent with $\mathbf{e} = \phi_*[\mathbf{E}] = \mathbf{F}^{-T}\mathbf{E}\mathbf{F}^{-1}$, and vice-versa.

required in the current section are somewhat opinionated, i.e., length-independence, frame-indifference, zero when configurations coincide. There are various schools of thought on how to define a strain tensor, and which properties they should obey. See Ref. [94] for a discussion on the different ways to define the strain tensor.

2.1.3 Hyperelasticity and energy density

Up to this point, no particular material has been described, and only some fundamental definitions necessary for the development of the theory have been laid down. Indeed, the equations stated so far are valid for any material, be it a steel bar or a human brain. The material properties of the studied system are finally introduced via the energy density function Ψ, which will indicate the energy cost for a given deformation in a given material.

We restrict that analyses to materials and deformations where the energy density depends only on the initial and deformed states, with no regards on the history of the deformation. Such materials are called *hyperelastic*. For an isotropic material, the same properties are required for the energy functional as were for the strain tensor. Thus, it is natural to write the energy density in terms of the strain tensors, $\mathbf{E}$ or $\mathbf{e}$, or at least of the Cauchy-Green deformation tensors $\mathbf{C}$ or $\mathbf{b}$. In the hyperelstic regime, the internal energy U is then a functional of the deformations, calculated by integrating a energy density Ψ over the whole body,

$$U[\mathbf{u}(\mathbf{X})] = \int_{\mathcal{B}_0} \Psi(\mathbf{E}(\mathbf{u}))dV. \tag{2.8}$$

The energy density then defines the type of material used. It is worth emphasizing that the energy density function is an input to the theory of nonlinear elasticity, and must either be obtained experimentally, or derived from thermodynamical arguments. The usual linear elastic material, which will be generalized shortly, is represented by the following energy density

$$\Psi_L(\boldsymbol{\epsilon}) = \frac{\lambda}{2}(\mathrm{tr}(\boldsymbol{\epsilon}))^2 + \mu\boldsymbol{\epsilon} : \boldsymbol{\epsilon}. \tag{2.9}$$

where μ and λ are called the Lamé parameters, and $\boldsymbol{\epsilon} : \boldsymbol{\epsilon} = \epsilon_{ij}\epsilon_{ij}$ denotes the double dot product. As the infinitesimal strain tensor $\boldsymbol{\epsilon}$ is not rotationally invariant, nor is Ψ_L.

This can be fixed by exchanging the infinitesimal strain tensor by the material strain tensor. This operation yields a similar, but rotationally invariant, energy density

$$\Psi_{SK}(\mathbf{E}) = \frac{1}{2}\lambda(\mathrm{tr}\mathbf{E})^2 + \mu\mathbf{E} : \mathbf{E}, \tag{2.10}$$

called the St. Venant-Kirchhoff energy density. Similarly to its infinitesimal counterpart, this energy density function fails to describe most materials when the strain is larger than a few tenths of a percent. When larger strains are involved, it is common to use the so called Neohookean models. The common feature in this family is the term

$$\Psi_{NH}(\mathbf{C}) = \frac{\mu}{2}(\mathrm{tr}\mathbf{C} - 3). \tag{2.11}$$

This model, however, presupposes that the system is completely incompressible [95]. While such restriction is often useful in analytical works, it can be detrimental in computational approaches, as it can lead to volumetric locking [96]. There are several ways to extend this equation to allow for compressibility. A common choice in the literature is

$$\Psi_{CNH}(\mathbf{C}) = \frac{\mu}{2}(\mathrm{tr}\mathbf{C} - 3 - 2\log J) + \frac{\lambda}{2}(\log J)^2. \tag{2.12}$$

This formulation has the advantage of converging to the St. Venant-Kirchhoff energy density in the low strain regime, and being well studied in the literature. We will use this density throughout this work, as it has been shown to properly model the elastic properties of the brain tisse [76, 97].

As can be noticed in Eqs. 2.10 and 2.12, the elastic properties of a homogeneous material are often parametrized by two values. So far, the Lamé parameters, μ and λ, were introduced. However, in linear elasticity, several combinations are possible, with the specific pair used depending on the context. For instance, the stiffness of the material is often given in terms of the Young Modulus E, or the bulk modulus K, while its compressibility is given by the Poisson ratio ν.

In this work, the pairs (λ, μ) and (E, ν) are used most often. For the small deformation regime, it is possible to convert the two pairs as [98]

$$\lambda = \frac{E\nu}{(1+\nu)(1-2\nu)}, \quad \mu = \frac{E}{2(1+\nu)} \tag{2.13}$$

or conversely,

$$E = \frac{\mu(3\lambda+2\mu)}{\lambda+\mu}, \quad \nu = \frac{\lambda}{2(\lambda+\mu)}. \tag{2.14}$$

These equations are not complete once compressibility is introduced. When comparing elastic tensors yielded by the compressible Neo-Hookean energy density (Eq. 2.12) with those yielded by the St. Venant-Kirchhoff energy density (Eq. 2.10), a correction term emerges, which leads to the following dependencies [87]

$$\lambda' = \frac{\lambda}{J}, \quad \mu' = \frac{\mu - \lambda\log(J)}{J}$$

and thus

$$\nu' = \frac{1}{2}\frac{\lambda}{\lambda[1-\log(J)]+\mu}, \quad E' = \frac{\mu - 3\lambda\log(J)}{J}\frac{2\mu+\lambda(3-2\log(J))}{\mu+\lambda(1-\log(J))}.$$

2.1.4 Langrangian, stress, and equations of motion

Nonlinear elasticity does not deal with forces directly, but rather with body force densities (acting on the material bulk) and traction densities (acting on the surface). In order to avoid naming conflicts, an exception to the uppercase-lowercase rule is made. The body force and traction densities are named $\mathbf{f}_0^{ext}$ and $\mathbf{t}_0^{ext}$, respectively, in material coordinates, and $\mathbf{f}^{ext}$ and $\mathbf{t}^{ext}$ in spatial coordinates. The total energy of the system system is given by two terms, the internal energy due to deformations (shown in Sec. 2.1.3) U and the kinetic energy K

$$U = \int_{\mathcal{B}_0} \Psi(\mathbf{F}(\mathbf{u}))dV, \quad K = \int_{\mathcal{B}_0} \frac{1}{2}\rho_0 \dot{\mathbf{u}} \cdot \dot{\mathbf{u}} dV. \tag{2.15}$$

For a given displacement $\mathbf{u}$, the work performed by conservative and constant external forces is given by

$$W = \int_{\mathcal{B}_0} \mathbf{f}_0^{ext} \cdot \mathbf{u} dV + \int_{\partial\mathcal{B}_0} \mathbf{t}_0^{ext} \cdot \mathbf{u} dA. \tag{2.16}$$

It is now possible to build the Lagrangian functional $\mathcal{L}$ as

$$\mathcal{L} = K - (W + U). \tag{2.17}$$

Due to the field approach taken in this work, the usual version of the Euler-Lagrange must be generalized, as the Lagrangian is now a functional over the displacement, itself a vectorial field. It is thus necessary to introduce a new derivative, known as the directional derivative [87, 89]. The definition and properties of this derivative are explained in Appendix A. In this framework, the Euler-Lagrange equation reads

$$\frac{\partial}{\partial t} D\mathcal{L}(\mathbf{u}, \dot{\mathbf{u}})[0, \delta\mathbf{v}] - D\mathcal{L}(\mathbf{u}, \dot{\mathbf{u}})[\delta\mathbf{v}, 0] = 0 \tag{2.18}$$

Applying the generalized version of the Euler-Lagrange equation is, for the most part, direct. The exception being the derivative of the internal energy,

$$\int_{\mathcal{B}_0} D\Psi(\mathbf{F}(\mathbf{u}))[\delta\mathbf{v}] dV$$

which deserves some attention. In particular, it is advantageous to rewrite this in terms of a stress tensor. This procedure is performed in Appendix. A.3, with result

$$\int_{\mathcal{B}_0} D\Psi(\mathbf{F}(\mathbf{u}))[\delta\mathbf{v}] dV = \int_{\mathcal{B}_0} \mathbf{P} : \nabla_0 \delta\mathbf{v} dV. \tag{2.19}$$

The tensor $\mathbf{P} = \frac{\partial\Psi(\mathbf{F})}{\partial\mathbf{F}}$ is called the first Piola-Kirchhoff stress tensor, and it measures the stress in the *original* coordinates. As such, it is a two-point tensor, linking a unit vector in material coordinates to a traction in spatial coordinates. Contrary to the standard Cauchy stress tensor, the first Piola-Kirchhoff stress tensor is not necessarily symmetric. This relation forms the constitutive equation for the modelled material.

The force components of the equation of motion now reads

$$D\mathcal{L}(\mathbf{u}, \dot{\mathbf{u}})[\delta\mathbf{v}, 0] = \int_{\mathcal{B}_0} \mathbf{P} : \nabla_0 \delta\mathbf{v} dV + \int_{\mathcal{B}_0} \mathbf{f}_0^{ext} \cdot \delta\mathbf{v} dV + \int_{\partial\mathcal{B}_0} \mathbf{t}_0^{ext} \cdot \delta\mathbf{v} dA, \tag{2.20}$$

Using the properties of the divergent operator $\nabla_0 \cdot$, it is possible to further decompose the forces into

$$\mathbf{P} : \nabla_0 \delta \mathbf{v} = \nabla_0 \cdot (\mathbf{P} \cdot \delta \mathbf{v}) - (\nabla_0 \cdot \mathbf{P}) \cdot \delta \mathbf{v}. \tag{2.21}$$

The weak form of the equation of motion is then found to be[4]

$$\int_{\mathcal{B}_0} \rho_0 \frac{\partial^2 \mathbf{u}}{\partial t^2} = \int_{\mathcal{B}_0} (\nabla_0 \cdot \mathbf{P}) \cdot \delta \mathbf{v} dV - \int_{\mathcal{B}_0} \mathbf{f}_0^{ext} \cdot \delta \mathbf{v} dV - \int_{\partial \mathcal{B}_0} (\mathbf{P} \cdot \mathbf{N}) \cdot \delta \mathbf{v} dA - \int_{\partial \mathcal{B}_0} \mathbf{t}_0^{ext} \cdot \delta \mathbf{v} dA \tag{2.22}$$

where the vector $\mathbf{N}$ is the normal vector to the surface $\partial \mathcal{B}_0$. It is possible to find the local (i.e., strong) version of the equations of motion using the arbitrariness of the domain and of the direction of the derivative, as

$$\begin{aligned} \rho_0 \frac{\partial^2 \mathbf{u}}{\partial t^2} &= \nabla_0 \cdot \mathbf{P} - \mathbf{f}_0^{ext} \\ \mathbf{P} \cdot \mathbf{N} &= \mathbf{t}_0^{ext}. \end{aligned} \tag{2.23}$$

This is called the Cauchy equation of motion in material coordinates. A similar procedure can be followed in the deformed coordinates to obtain

$$\begin{aligned} \rho \frac{\partial^2 \mathbf{u}}{\partial t^2} &= \nabla \cdot \sigma - \mathbf{f}^{ext} \\ \sigma \cdot \mathbf{n} &= \mathbf{t}^{ext}. \end{aligned} \tag{2.24}$$

where σ is the usual Cauchy stress tensor, $\mathbf{f}^{ext}$ are the external forces in deformed coordinates, ρ is the density in the deformed configuration, and $\mathbf{n}$ is a unitary vector. These two stress tensors are linked by the following identity

$$\sigma = \frac{\mathbf{P}\mathbf{F}^T}{J}, \tag{2.25}$$

where $J = \det(\mathbf{F})$[5]. For the brain, we also assume a dissipation in form of an external

---

[4] The advective term $\mathbf{v}\frac{d\rho}{dt}$ is small compared with the other terms in the equation, and has been ignored, in line with other works in the field [68, 78]. See Ref. [99] for a further discussion.

[5] Similarly to the strain tensors, there are many more possibilities for stress tensors than the two

force $\Gamma = -\mu \frac{\partial \mathbf{u}}{\partial t}$.

2.1.5 Quasistatic approximation

Forces applied to elastic materials induce shockwaves. The amplitudes of these shockwaves then decrease in time due to internal friction and drag. For simple elastics, these are the two important timescales of the system: the vibration period of elastic waves, and the time it takes for the energy to dissipate into heat. Growing materials in particular, have a third time scale induced by the growth process.

The interplay between the various timescales is complex, and are investigated and discussed in Ch. 5. To understand the effects of growth alone, in Ch. 4 it is supposed that the time scale of growth is much larger than the timescales of dissipation and vibration. In this regime, only the equilibrium state matters. This is to say, the only relevant deformations $\mathbf{u}$ are those that

$$0 = \nabla_0 \cdot \mathbf{P} - \mathbf{f}_0^{ext} \quad \Rightarrow \quad \nabla_0 \cdot \mathbf{P} = \mathbf{f}_0^{ext}. \tag{2.26}$$

This is called the equilibrium equation. In effect, this is equivalent to an energy minimization procedure. In order to solve this equation, it is necessary to use a nonlinar solver, as detailed in Sec. 2.4.1.

2.2 Growth

To model brain folding, it is essential to add the growth process to our theoretical roster. The growth framework first laid by Rodriguez and his collaborators will be used [100], where an additional configuration is introduced between the original and the deformed coordinates (see Fig. 2.3). This new configuration is called the grown configuration, and does not necessarily need to be consistent with boundary conditions. For instance, it can be discontinuous or have a topology distinct from the original system. If this is the case, the system will present some sort of residual stress, which is consistent with multiple experiments in grown systems [101–103].

---

mentioned in this section. Each of them have their advantages and disadvantages, but for the topics discussed in this thesis, the ones introduced here will suffice. For further discussion on other stress measures, we refer the reader to the references in the beginning of this chapter.

In mathematical terms, the gradient deformation tensor $\mathbf{F}$ is decomposed in two parts,

$$\mathbf{F} = \mathbf{F}_e\mathbf{F}_g, \tag{2.27}$$

where the deformation due to growth is completely contained in the growth tensor $\mathbf{F}_g$, while the mechanical quantities (i. e., energy, forces, etc) are derived based on the elastic tensor $\mathbf{F}_e$. The energy and forces are calculated only from the tensor $\mathbf{F}_e$. Thus, the hyperelastic energy density is redefined as

$$\Psi = \Psi(\mathbf{F}_e) \tag{2.28}$$

The extension of the first Piola-Kirchhoff tensor to the grown regime is more subtle. In order to arrive at the correct formulation of the tensor, it is important to pay attention to the configuration on which integrations are being performed, especially when these integrations were performed in the stress-free configuration. During the exposition in Sec. 2.1.3, this corresponds to the original configuration, $\mathcal{B}_0$. Once growth is introduced, this is no longer the case. Rather, the stress-free configuration is given by the *grown* configuration. That, is the total energy and the first Piola-Kirchhoff tensor are found to be

$$U = \int_{\mathcal{B}_g} \Psi(\mathbf{F}_e(\mathbf{u}))dV_g, \quad \text{and} \quad \mathbf{P}_e = \frac{\partial\Psi(\mathbf{F}_e)}{\partial\mathbf{F}_e}, \tag{2.29}$$

where $\mathcal{B}_g$ describes the grown configuration. It is, however, numerically advantageous to integrate the equations of motion in the original domain. As such, the first Piola-Kirchhoff is found to be, in the original bodies,

$$\mathbf{P} = \frac{\partial\Psi(\mathbf{F}_e)}{\partial\mathbf{F}}J_g = \frac{\partial\Psi(\mathbf{F}_e)}{\partial\mathbf{F}_e}\mathbf{F}_g^{-T}J_g, \tag{2.30}$$

where the Jacobian $J_g = \det(\mathbf{F}_g)$ emerges due to the change in the integration domain.

It is instructive to understand the effects of applying $\mathbf{F}_g$ in a few simple situations. In Fig. 2.2, for instance, the effects of applying two distinct, but spatially constant, growth tensors $\mathbf{F}_g$ to an initially square block are shown. In the absence of external forces or constraints, it is intuitive to understand what will happen. As, by construction, the energy density reaches a minimum when $\mathbf{F}_e = \mathbf{I}$, the system naturally will deform such that $\mathbf{F} = \mathbf{F}_g$, leading to the shapes seen in Fig. 2.2.

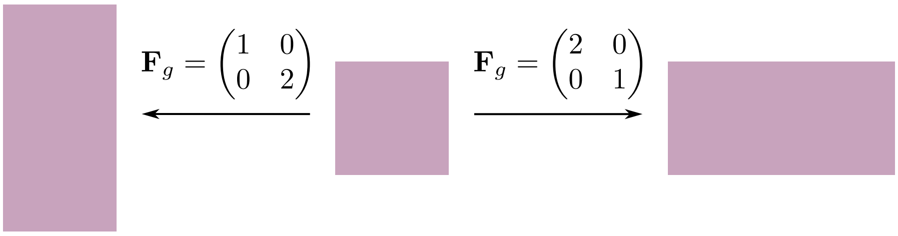

Figure 2.2: Effects of application of the constant growth tensors shown inside the figure. On left, the rectangle's height doubled, while on the left, the height is kept constant and the width is doubled.

When the growth tensor is not constant, but presents some sort of spatial dependency, it is harder to intuit the displacement of the system. One of those situations is shown in Fig. 2.3, where the top layer grows, but the underlying material stays the same size. As there can be no topological changes (i.e., no discontinuities, holes, etc), a compromise must be reached: neither the top layer can grow to its desired size, nor can the substrate avoid any deformation. Thus, a mushroom-shaped configuration is reached. As the elastic component of the deformation $\mathbf{F}_e$ cannot equal the identity at every point, residual stress is observed in the system, where the top layer is compressed by the bottom layer, and vice-versa.

Figure 2.3: Effects of application of the growth tensors shown inside the figure. From left to right, the original, grown, and final configurations are shown. On the grown configuration $\mathcal{B}_g$ the top layer grows tangentially by a factor a.

Now all the theory necessary to deal with growing elastic materials has been laid. However, Eqs. 2.23 and 4.2 can only be analytically solved in very simple configurations, under equally simple boundary and growth conditions. Rather, it is necessary to give a numerical treatment to relevant equations. The finite element method used in this work is developed in the next section.

2.3 The finite element method

Finding a solution for the equations above is, in general, non-trivial. Even in relatively simple boundary conditions, the nonlinearity of the system impedes the success of most of the standard analytical methods to solve partial differential equations. Even more so in non trivial boundary conditions, as will be the case for the systems in this thesis. Thus, computational tools are needed to solve the equilibrium equations.

For the simulations in this work, the finite element method (FEM) [104], also commonly called finite element analyses, is used. FEM is a numerical method for solving differential equations, specially those with complex boundaries. It was originally aimed at aeronautical applications [105, 106], but nowadays it is an important tool in many fields of computational physics and engineering, having been applied, for instance, in fluid dynamics [107], electrodynamics [108], and naturally, biomechanics [109], among many others.

In this section a general introduction to the method is presented, as well as the derivation of the main equation which will be used throughout the text. As a toy example, the FEM equation for the one-dimensional Poisson equation is developed in Appendix B. This example allows the reader to understand the method, and compare the solutions obtained numerically and analytically.

There are three main steps in the finite element method. First, the differential equations are replaced by an equivalent integral equation, but whose solution is less restricted. This process is called solving a problem in a *weak* sense. “Weakness” is properly defined later in this text. Second, the sought-after function is expanded in a base of well known functions, where integration might be easier. Third, these solutions are obtained on a set of simpler geometries and assembled into the required boundaries, however complex they may be. These ideas are expanded in the order proposed above.

2.3.1 Weak forms

In many physical situations it is not necessary, or even possible, to find a proper function that solves a given partial differential equation (PDE). The PDEs in these situations are too restrictive in their conditions. Instead, it is possible to search for a *distribution* that solves the equation. In general solutions u for a linear operator P given f are sought such that

$$Pu = f, \quad u \in \mathbb{K} \tag{2.31}$$

subject to some boundary conditions. Here $\mathbb{K}$ is the Banach space[6] of the functions that obey the boundary conditions prescribed. We expand on common choices and handling of different boundary conditions in Sec. 2.3.4. In the terminology of PDEs, P is a partial differential operator, and f is a function. The weak form of equation is obtained by not requiring the strong equality above, but rather equality in the internal products

$$\langle Pu, v \rangle = \langle f, v \rangle \tag{2.32}$$

where the operator $\langle \cdot, \cdot \rangle$ is the internal product of the Banach space $\mathbb{K}$. This equality must hold true for every function $v \in \mathbb{K}$. The canonical choice of internal product for functions defined in a domain Ω is

$$\langle u, v \rangle = \int_{\Omega} u^* v d\Omega, \tag{2.33}$$

where * indicates complex conjugation. Other choices of internal products are also possible, leading to different formulations of the finite element method [104]. In effect, the differential equation has been replaced by its integral form, creating the possibility of reducing the derivative order of the solution u, as partial integrations are performed to transfer those to the test function v.

This is a rather abstract treatment, and while the proof and analyses of the method depends on non-trivial mathematics, the actual effort involved in obtaining the weak form is comparatively small. An example of such a calculation is provided in Appendix B.1.

---

[6] A Banach space is a vectorial space augumented by a complete metric induced by its norm [110].

2.3.2 Function expansion

While the weak form of the differential equation tends to be easier to solve than its strong form, it still requires both the solution of a possibly difficult integral equation, and the proof that the equality in Eq. 2.32 holds for every element in $\mathbb{K}$. Both of these issues are solved by expanding the solution in a base of $\mathbb{K}$

$$u(x) = \sum_{i=0}^{\infty} u_i \psi_i(x) \tag{2.34}$$

where u_i are expansion coefficients. The appropriate base to perform the expansion will depend on the specific problem. Common choices include the Lagrange interpolating polynomials, sinusoidal functions, or various others interpolating polynomials. Introducing the expansion Eq. 2.34 into Eq. 2.32 leads to

$$\sum_{j=0}^{\infty} u_j \langle P\psi_j, v\rangle = \langle f, v\rangle . \tag{2.35}$$

By construction, Eq. 2.35 is valid for every $v(x)$. Thus, it is possible to expand the test function as well $v(x) = \sum_i v_i \psi_i(x)$

$$\sum_{i=0,j=0}^{\infty} \langle P\psi_j, \psi_i\rangle v_i u_j = \sum_{i=0}^{\infty} \langle f, \psi_i\rangle v_i . \tag{2.36}$$

As the interpolating functions ψ_i are linearly independent, the equality above holds for every term in the sum over index i, leading to

$$\sum_{j=0}^{\infty} \langle P\psi_j, \psi_i\rangle u_j = \langle f, \psi_i\rangle . \tag{2.37}$$

By enforcing this equality for every element of the base $\{\psi_i\}$, the equality is shown to be valid for every element in the space $\mathbb{K}$. Thus, instead of calculating the integral over every element of the possibly infinite space $\mathbb{K}$, integrals only need to be calculated for the elements in the base, and the results of their application to the operator P. As P might be a complicated operator, the integration must be performed numerically. However, often the basis $\{\psi_i\}$ is composed of polynomials, which often allows for exact integration (up to numerical error) using Gaussian quadrature [111]. Once the values of these integrations are calculated, they are gathered into the linear equation

$$\sum_{i=0}^{\infty} B_{ij} u_j = l_i, \tag{2.38}$$

where $B_{ij} = \langle \psi_i, P\psi_j \rangle = \langle P\psi_j, \psi_i \rangle^*$ and $l_i = \langle f, \psi_i \rangle$, which can be recast into the matrix form

$$\mathbf{Bu} = \mathbf{l} \tag{2.39}$$

where $\mathbf{B}$ is called the stiffness matrix, and $\mathbf{l}$ the force vector. Solving the linear equation is equivalent to solving Eq. 2.32 and the original problem. Naturally, in its current form, an infinite number of terms needs to be solved, which is not practical. The solution is approximated to a finite number of terms, which are then solved in finite time. See Appendix B.2 for a numerical example.

2.3.3 Discretization of space

The integration process in Eq. 2.37 is direct in one dimension, as was the case in Sec. B.2 , or in simple domains. However, it is easy to see that it can be very complex, depending on the boundaries of the problem, especially in higher dimensions. In the hypothetical experiment shown in Fig. 2.4 (a), the mathematical description of the domain necessary for the integration is difficult, let alone the integration itself.

The last insight for FEM is that space can be discretized into smaller sections where it is easy to perform the integrations required. Each of these simpler subdomains is called an *element* or *cell*, and the set of all cells is called the *mesh*. Common choices of cells shapes are triangles and quadrangles (in two dimensions), or tetrahedra and octahedra (in three dimensions), or a mixture of both. A possible meshing of the heat experiment is shown in Fig. 2.4 (b).

In each element, a family of functions to interpolate the solution is chosen. A typical choice, also used here are the Lagrange interpolating polynomials, shown in Fig. 2.5. They are defined as

$$\psi_i^{(1)}(x) = c_i^{(1)} \frac{x_{i+1} - x}{x_{i+1} - x_i} \Pi(x; x_i, x_{i+1}), \tag{2.40}$$

$$\psi_i^{(2)}(x) = c_i^{(2)} \frac{x - x_i}{x_{i+1} - x_i} \Pi(x; x_i, x_{i+1}) \tag{2.41}$$

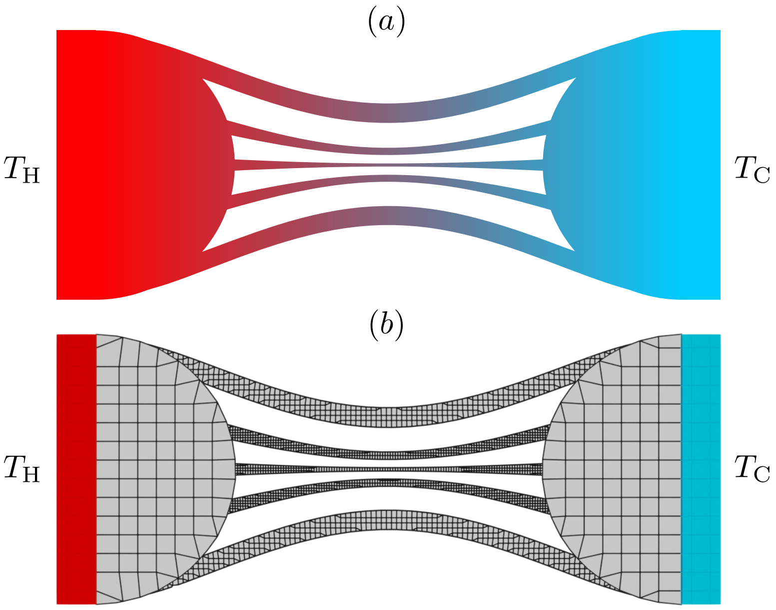

Figure 2.4: (a) Schematic of hypothetical experimental setup consisting of two heat baths connected through channels of varying sizes. The left side is kept at a hot temperature T_H, while the right is kept at a cold temperature T_C. (b) Sample meshing of the domain of the hypothetical experiment.

The expansion of the solution into thus reads

$$\phi_e(x) = \sum_{i=1}^{\infty} \sum_{l=1}^{2} c_i^{(n)} \psi_i^{(n)}(x), \tag{2.42}$$

where the x_i are the points of the discretization, c_i are coefficients to be determined, and Π_i is the signal function defined by

$$\Pi(x; x_i, x_{i+1}) = \begin{cases} 1, & \text{if } x_i \leq x < x_{i+1}, \\ 0, & \text{otherwise} \end{cases} \tag{2.43}$$

Due to the requirement that the function be continuous, the condition $c_i^{(2)} = c_{i+1}^{(1)}$ is imposed for every i and due to the signal function Π, the final matrix has a special banded structure, which greatly simplifies the solution of the final linear equation.

The generalization of the procedures in this section for higher dimensions are, for the most part, direct. Integrals are calculated over a surface (in two dimensions) or a volume (in three dimensions), derivatives are replaced by vectorial operators, such as the divergence, etc. However, one point that deserves some attention is the procedure

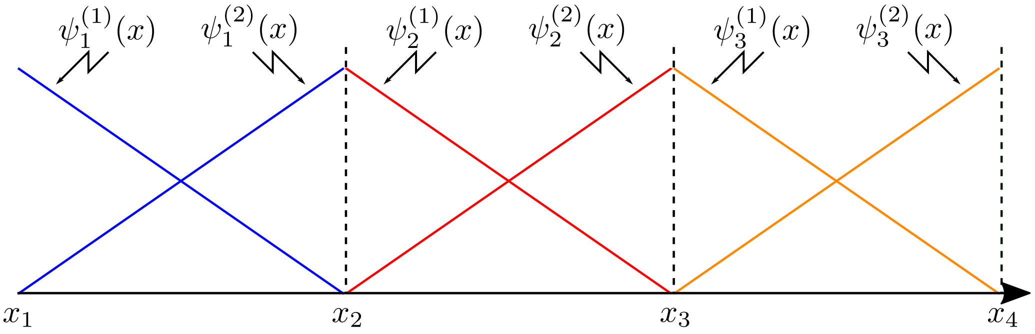

Figure 2.5: Example of first order Lagrange polynomials over three cells in the real line. The functions in each cell are denoted by a distinct color.

to build a high dimensional analogue for the base of functions, and how to build on top of the one-dimensional families. Both of these processes are easier performed when the mesh is composed of quadrangles and octahedra, as it is possible to expand the dimensionality of the domain by a direct product of functions. For instance, in two dimensions,

$$\sigma_i(x,y) = \psi_i(x)\psi_i(y). \tag{2.44}$$

This family, $\{\sigma_i\}$, is used for bidimensional scalar problems, such as the generalization of the Poisson equation used in Appendix B. In order to deal with vectorial problems, such as those in nonlinear elasticity, the range of the basis is expanded as

$$\boldsymbol{\Psi}_{2i} = \begin{pmatrix} \sigma_i(x,y) \\ 0 \end{pmatrix} \quad \boldsymbol{\Psi}_{2i+1} = \begin{pmatrix} 0 \\ \sigma_i(x,y) \end{pmatrix}. \tag{2.45}$$

The main strength of the current approach is that it is readily extensible to any number of dimensions, both in the domain as well as in the range of the problem. However, depending on the structure of the problem at hand, it is not always possible to use this simple extension. The Maxwell equations, for instance, are particularly pernicious due to its large null space. Thus, they demand a specialized set of basis functions, such as the Nedelec family [112]. This is not an issue in the simulations performed in this work, where the procedure outlined in this section is used to extend the Lagrange family of functions.

2.3.4 Boundary conditions

Often, the physical process modeled by a given differential equation must fulfill certain conditions. For instance, a metal bar might be clamped on its sizes, fixing its displacement and orientation at these points, while experiments dealing with heat might have their temperatures or heat flux specified by the experimental apparatus. Each of these conditions has a different treatment.

When the value of the solution is fixed at certain points, the boundary condition is called of Dirichlet type. Explicitly, at a boundary Ω, the solution $\mathbf{u}$ is given as

$$\mathbf{u} = \mathbf{a} \quad \text{on } \Omega \tag{2.46}$$

for some constant vector $\mathbf{a}$. In the examples above, Dirichlet conditions are imposed when the temperature is fixed in the heat experiment, or when the displacement sides of a metal bar are specified. When the solution of the differential equation is vector-valued, it is possible to have partial Dirichlet conditions, on which the boundary is allowed to vary into some directions, but not others. For instance, it is possible to set $u_x(x = 0, y) = u_x(x = L, y) = 0$, therefore fixing the x component of the displacement, while leaving the y component free to vary. This type of boundary condition is commonly called *sliding* condition.

In the Neumann boundary condition, rather than fixing the solution, its derivatives are fixed

$$\frac{d\mathbf{u}}{d\mathbf{X}} = \mathbf{b} \quad \text{on } \Omega. \tag{2.47}$$

These are often used to specify rotations in the borders of the system when dealing with mechanical problems. Another often used boundary condition is the specification of tractions, where

$$\nabla_0 \cdot \mathbf{P} = \mathbf{g} \quad \text{on } \Omega. \tag{2.48}$$

As the name implies, this boundary condition prescribes a traction on the boundaries of the body.

Once the system is cast into a weak form, these distinctions between the various types of boundary conditions change. Rather than classifying into the ones above, boundary conditions are classified as essential and natural boundary conditions. Their difference is set by whether they need to be imposed in the solution, or whether they naturally appear in the derivation of the weak form, respectively. Furthermore, once the approximations in Eq. 2.34 are introduced, the natural conditions are only approximately satisfied, while the essential conditions are satisfied exactly [104].

Often, Dirichlet conditions turn into essential conditions, while Neumann conditions often turn into natural conditions. This is not a necessary condition. It is possible to embed Dirichlet using penalty-based [113] or Nietsche's method [114], for instance.

2.3.5 Further considerations

For completeness, it is important to acknowledge that there is not a single finite element method formulation. The derivation above implicitly follows the Ritz method, where a quadratic functional

$$I(u) = \frac{1}{2}B(u,u) - l(u) \tag{2.49}$$

is minimized, leading to a linear system as presented in Eq. 2.37. There are many other possible formulations, which yield different approximations. A common approach is to define the residual

$$R = Pu - f \tag{2.50}$$

which is then minimized in a weighted-integral sense. Each set of weights will define a different linear equation, returning different – but similar – solutions. Perhaps the most common approach is using the interpolating functions $\{\phi_i\}$ as the weights, the so-called Bubnov-Galerkin method. If the equation at hand admits a bilinear weak form, the solution derived from this method will be the same as in the Ritz method. Another method derived from the weighted-integral approach is the Collocation method, on which the weight functions are the Dirac distributions centered at a given set of points. This method is beneficial in that it makes the calculations of the integrals trivial. However, it can difficult to use accurately, as the choice of the points on which to fix the solution is crucial to final accuracy of the calculated solution.

Furthermore, in the development of the FEM method, the linear nature of the operator P was used. The governing equations obtained in Sec. 2.1 are not necessarily linear, and must be treated differently.

2.4 Finite element formulation of nonlinear elasticity

In Sec. 2.3, we explored some generic aspects of the Finite Element Method. This method is now specialized to the two cases explored in this work. In Ch. 4, energy minimization is performed, which yields an nonlinear boundary value problem, while in Ch. 5 dynamical systems are studied, which are modeled as an initial value problem. Thus, the finite element method needs to be approached from slightly different angles for each of these problems.

2.4.1 Energy minimization and the linearization procedure

Static problems can be formulated as a function minimization procedure, where for every growth tensor $\mathbf{F}_g$, the potential energy of the system is minimized. The system is grown in small steps, with an increase in the entries of $\mathbf{F}_g$. Then, with the growth tensor $\mathbf{F}_g$ fixed, Eq. 2.51 is iterated until convergence is reached. The growth tensor is further increased, and the process starts anew. To find the configuration that leads to the energy minimum, the system is iterated over putative solutions using the Newton Method, as explained below. As is often the case, the minimization problem is recast as a root-finding problem, where the zeros of the objective function's derivative are sought.

There are many nonlinear root finders to choose from. Here, the Newton-Raphson solver [115] is used. An introduction to the Newton-Raphson method, as well as a comparison with the steepest descent method can be found in Appendix C. In the remainder of this subsection, the algorithm is adapted for the nonlinear elasticity equations.

We define the state vector $\mathbf{u}$ is defined as a vector encoding the displacement of every point in the discretized mesh as $\mathbf{u} = (u_x^{(1)}, u_y^{(1)}, \ldots, u_x^{(N)}, u_y^{(N)})^T$. In the notation of nonlinear elasticity, the adapted version of Eqs. C.1 and C.3 now read

$$D^2U(\mathbf{u}_k)[\delta\mathbf{v}, \delta\mathbf{u}]\mathbf{p}_k = -DU(\mathbf{u}_k)[\delta\mathbf{v}] \tag{2.51}$$

$$\mathbf{u}_{k+1} = \mathbf{u}_k + \mathbf{p}_k$$

The procedure to calculate $D^2U(\mathbf{u})[\delta\mathbf{v},\delta\mathbf{u}]$ is analogous to the calculation of Eq. 2.19, with result

$$D^2U(\mathbf{u})[\delta\mathbf{v},\delta\mathbf{u}] = \int_{\mathcal{B}_0} \nabla_0\delta\mathbf{u} : \mathcal{A} : \nabla_0\delta\mathbf{v} dV, \tag{2.52}$$

with $\mathcal{A} = \frac{\partial\mathbf{P}}{\partial\mathbf{F}}$, called the *material tangent modulus* tensor. Notice that this is a fourth order tensor, collecting $3^4 = 81$ entries. Following the same procedure as delineated in Subsections 2.3.2 and 2.3.3 – expanding $\mathbf{u}$ into a suitable basis of complete functions, discretizing space, and choosing $\delta\mathbf{v}$ and $\delta\mathbf{u}$ as members of the function base $\{\mathbf{\Psi}_i\}$ – yields

$$\mathbf{K}\mathbf{p}_k = \mathbf{r} \tag{2.53}$$

$$\mathbf{u}_{k+1} = \mathbf{u}_k + \mathbf{p}_k, \tag{2.54}$$

where the tangent matrix $\mathbf{K}$ and residual vector $\mathbf{r}$ are introduced such that

$$K_{ij} = \int_{\mathcal{B}_0} \nabla_0\mathbf{\Psi}_i : \mathcal{A} : \nabla_0\mathbf{\Psi}_j dV \quad \text{and} \quad r_i = \int_{\mathcal{B}_0} \mathbf{P} : \nabla_0\mathbf{\Psi}_i dV + \int_{\mathcal{B}_0} \mathbf{f}_0^{ext} \cdot \mathbf{\Psi}_i dV + \int_{\partial_0} \mathbf{t}_0^{ext} \cdot \mathbf{\Psi}_i dA. \tag{2.55}$$

At every step of the nonlinear solver, the linear problem in Eq. 2.53 is solved using the LU decomposition [111].

2.4.2 Dynamical simulations and equation of motion

When the timescales of growth is comparable to that of elastic response, it is necessary to consider inertial effects of the system, leading to a time-dependent problem. The procedure to solve this problem starts by recalling the Cauchy equation of motion Eq. 2.23, as

$$\rho\frac{D^2\mathbf{u}}{Dt^2} = \nabla_0 \cdot \mathbf{P} - \mathbf{f}_0^{ext} - \mu\mathbf{v}.$$

This second-order differential equation is equivalent to a pair of DEs

$$\frac{\partial\mathbf{u}}{\partial t} = \mathbf{v} \quad \text{and} \tag{2.56}$$

$$\rho \frac{\partial \mathbf{v}}{\partial t} = \nabla_0 \cdot \mathbf{P} - \mathbf{f}_0^{ext} - \mu \mathbf{v}, \tag{2.57}$$

where the vector $\mathbf{v}$ denotes the velocity of the body at this point, and the factor friction term $-\mu\mathbf{v}$ has been introduced. In order to follow the same procedure as in Sec. 2.3, the supposition that it is possible to decouple the temporal components from the spatial components is made[7]. Thus the displacement and velocity vectors are expanded in the basis $\{\mathbf{\Psi}_j\}$ as

$$\mathbf{u} = \sum_j^N U_j(t)\mathbf{\Psi}_j(\mathbf{X}) \quad \text{and} \quad \mathbf{v} = \sum_j^N V_j(t)\mathbf{\Psi}_j(\mathbf{X}) \tag{2.58}$$

which then applied to Eqs. 2.4.2 and 2.57 yields

$$\sum_j^N \mathbf{\Psi}_j \frac{\partial U_j}{\partial t} = \sum_j^N V_j \mathbf{\Psi}_j \tag{2.59}$$

$$\rho \sum_j^N \mathbf{\Psi}_j \frac{\partial V_j}{\partial t} = \nabla_0 \cdot \mathbf{P} - \mathbf{f}_0^{ext} - \mu \sum_j^N \mathbf{\Psi}_j V_j, \tag{2.60}$$

As before, it is necessary to evolve the coefficients $\{U_i\}, \{V_i\}$. As, by definition, $\{\mathbf{\Psi}_i\}$ forms a base, the terms of the sum in Eq. 2.59 are linearly independent. These terms are then written as

$$\frac{\partial U_j}{\partial t} = V_j. \tag{2.61}$$

In order to simplify the differential equation describing the evolution of the velocity coefficients $\{V_i\}$, Eq. 2.60 is replaced by its weak form

$$\rho \int_{\mathcal{B}_0} \sum_j^N \mathbf{\Psi}_i \cdot \mathbf{\Psi}_j \left(\frac{\partial}{\partial t} + \frac{\mu}{\rho} \right) V_j dV = \int_{\mathcal{B}_0} \mathbf{\Psi}_i \cdot (\nabla_0 \cdot \mathbf{P} - \mathbf{f}_0^{ext}) dV \tag{2.62}$$

or equivalently

$$\sum_j^N M_{ij} \left(\frac{\partial}{\partial t} + \frac{\mu}{\rho} \right) V_j = g_i \tag{2.63}$$

---

[7] This is a common supposition when developing dynamical finite element formulations. The complementary idea, where the basis depends on both space and time is possible, but reasonably more complex, and not as well studied [104].

where

$$M_{ij} = \rho \int_{\mathcal{B}_0} \mathbf{\Psi}_i \cdot \mathbf{\Psi}_j dV \quad \text{and} \quad g_i = \int_{\mathcal{B}_0} \mathbf{\Psi}_i \cdot (\nabla_0 \cdot \mathbf{P} - \mathbf{f}_0^{ext}) dV. \tag{2.64}$$

The $\mathbf{M}$ is called the *mass* matrix. The reason for this nomenclature becomes clear once the system of equations is assembled,

$$M_{ij} \frac{\partial V_j}{\partial t} = g_i - M_{ij} \frac{\mu}{\rho} V_j \tag{2.65}$$

$$\frac{\partial U_j}{\partial t} = V_j. \tag{2.66}$$

As it can be seen, the mass matrix $\mathbf{M}$ plays the inertial role in the equations. At every time step the linear system in Eq.2.65 needs to be solved. This will prove to not be an issue, as the mass matrix has a few properties that alleviate the computational effort. First and foremost, the mass matrix does not depend on the current configuration. Therefore, it is possible to compute its entries during the initialization of the program and reuse the results throughout the simulation. Second, it is a symmetric definite positive matrix. This permits the usage of very fast iterative solvers [116], such as Gradient Descent (GD).

The equations of motion can now be iterated with standard solvers for initial value problems. In this work, the Verlet method is used. This is a classical algorithm, first introduced in the studies of thermodynamic systems [117], but has since found widespread usage. This is for two reasons. Firstly, it has a sympletic structure, which allows for better energy conservation. Secondly, it has second-order time accuracy despite requiring a single force calculation. Thus, it provides a good balance between speed and accuracy.

Due to the friction in the system, the Verlet algorithm is not be self-consistent if used in our systems. It is possible to extend the original formulation to fix this issue, as explained in Ref. [118]. The procedure is shown in Algorithm 1, where A_i^D denotes the accelerations due to dissipative forces, A_i^C denotes acceleration due to conservative forces, and δt denotes the time step. The operations are understood to be broadcast over the index i.

Algorithm 1 Modified Verlet

```
$V_i \leftarrow V_i + (A_i^C + A_i^D)\delta t/2$
$U_i \leftarrow U_i + V_i \delta t$
Calculate $g_i$ using Eq. 2.64
Solve $\sum_j M_{ij} A_j^C = g_i$ using GD
Calculate $A_i^D = -\mu V_i$
$\bar{V}_i \leftarrow V_i + A_i^C \delta t/2$
while $V_i$ not self-consistent do
    $V_i \leftarrow \bar{V}_i + A_i^D \delta t/2$
    Calculate $A_i^D = -\mu V_i$
end while
```

Chapter 3

JuFold – A Finite Element Simulation Framework

Several works in the field of brain folding were discussed in Ch. 1. Many of them have common characteristics: they use nonlinear elasticity in order to model the large deformations that the brain undergoes during development; growth is modelled through the multiplicative decomposition proposed by Rodriguez et al. [100]; the elastic equations are solved using the Finite Element Method (FEM). JuFold is a high performance Finite Element framework for the simulation of growing materials based on the deal.II [119, 120] the library. It was developed as part of this research project, and it is one of the cornerstones of this work. All simulational results presented in the following chapters are based on JuFold. By coalescing several common tools necessary for the simulation of growing materials, it allows quick experimentation with different models. For instance, due to its modular nature, it is straightforward to change growth rules or hyperelastic density function, or even to implement new ones.

Thus, this chapter is dedicated to explaining its structure and design. Sec. 3.1 contains an overview of a common structure for software developed with JuFold. Sec. 3.2 exposes the utilities in JuFold that aid in the implementation of the simulations. Sec. 3.3 introduces the implementation decisions of JuFold in more detail, including parallelization strategy, and components. Sec. 3.4 shows a few examples of JuFold usage, some of which are further explored in Chs. 4 and 5. Finally, Sec. 3.5 exposes one specific subproject powered by JuFold.

3.1 Structure of JuFold

The current section outlines the major steps during a typical FEM simulation using JuFold. These are meant only as an overview, and they are often subdivided into many substeps. There are two main parts in this structure. Firstly there is the initialization procedure, where memory allocations one-off subprocedures are perfomed. Second, there is the solution procedure, where the system is iterated several times, until a solution or some stop condition is reached. Normally, most of the simulation runtime is spent on this step. Fig. 3.1 gives an overview of this structure, including a number of its substeps and provides a mapping between the general structure and the important entry points in JuFold.

3.1.1 Initialization stage

The first steps in the simulation are mostly setting up the stage for the main calculation including setting up boundary conditions, allocating vectors, populating these vectors, etc. These are all one-off steps, meaning that they are not a major contributor to the runtime of the simulation. However, a few of these warrant a closer look.

3.1.1.1 Mesh generation

An important step is to generate the mesh on which the simulation will be performed. For simple geometries, as the ones used in this work, it is preferable to generate the mesh programmatically. It is common that FEM libraries have a collection of often-used meshes bundled with the library. Once the mesh reaches a certain degree of complexity, it is often advantageous to use specialized software to design the mesh. For instance, a free and open source software for mesh generation is Gmsh [121]. These meshes can then be exported to a file, which is then imported into JuFold.

3.1.1.2 Boundary conditions

Complementary to the mesh generation, one must define the boundary conditions. In JuFold, this is done in two steps. First, the *boundary IDs* are set on the cells of the mesh. Second, the boundary conditions are set. The most common boundary conditions in continuum mechanics are outlined in Sec. 2.3.4.

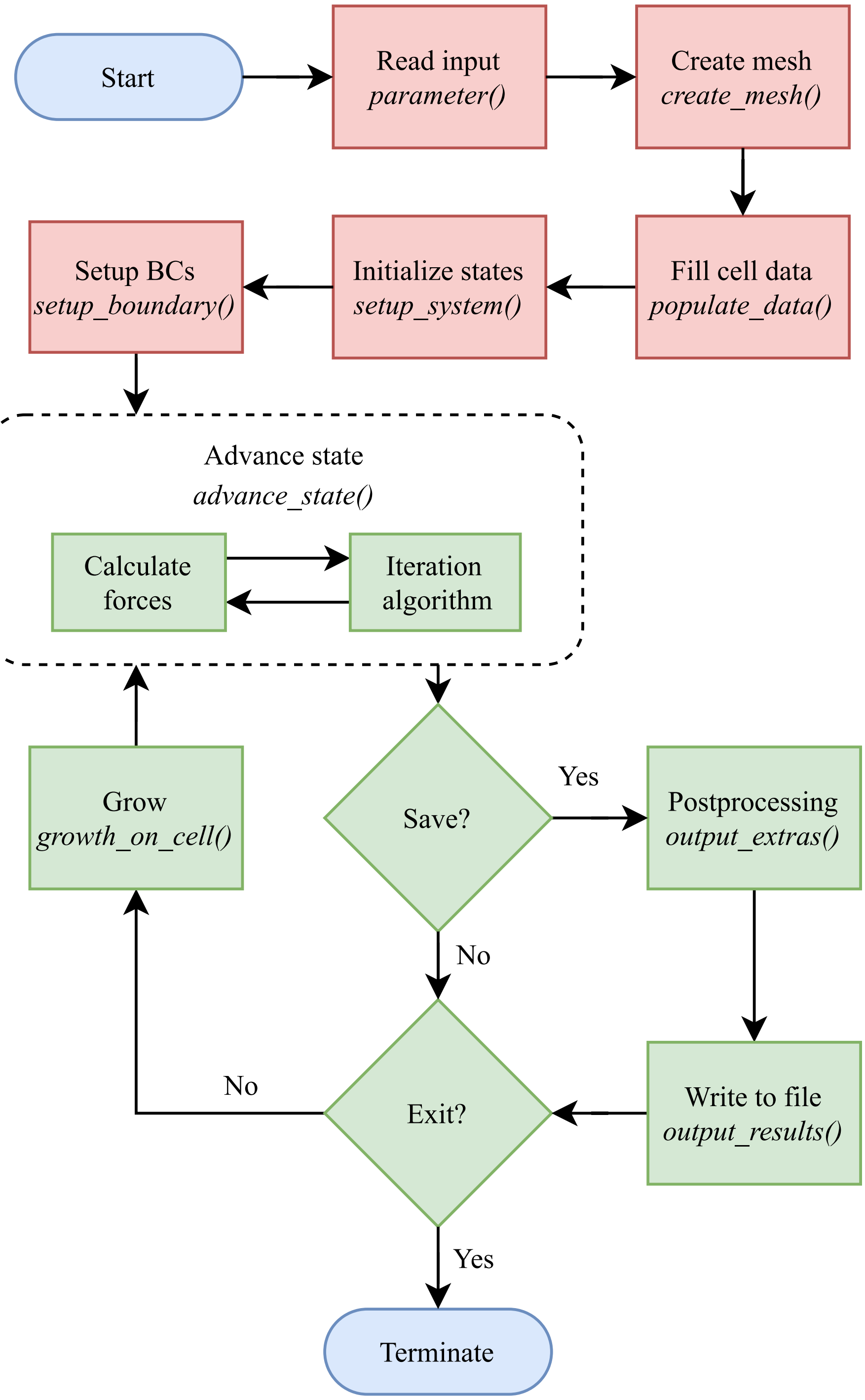

Figure 3.1: Flow of JuFold simulations with specific API function in italics. The initialization steps are shown in red, and the main loop of the simulation is shown in green. Often several steps of the iteration algorithm, as well as force and tensor calculations, are needed in order to perform a single state update. In addition to the usual steps taken by most FEM software, JuFold adds a growth step.

Essential boundary conditions are implemented in the code through constraints in the solution, by fixing degrees-of-freedom to certain values. These are encoded into a *constraint matrix*, which is created at the beginning of the simulation. Once this matrix is built, it is possible to operate on the reduced system (see App. B.3). While the most common use of the constraint matrix is to implement the simple constraints required by the essential conditions, it is possible to add all kinds of linear constraints to this matrix.

Natural boundary conditions, on the other hand, do not require any special machinery, as they are embedded into the weak form of the equation of interest (see Sec. 3.1.2.1).

3.1.2 Main loop

The following functions, in contrast with the previous subsection, perform the bulk of the computation. Thus, utmost care needs to be taken to be sure they are efficient and scalable. One of these steps in particular, the calculation of the forces, energy, elastic tensors, etc, is often the bottleneck of many applications, sometimes consuming up to 80%-90% percent of the total computing time of the application.

3.1.2.1 Computation of forces, stresses, etc

During this step, some auxiliary quantities are calculated. What these are depends on the specific algorithm used. For instance, in the dynamical simulations it would mean the forces acting upon the system, both of dissipative and conservative nature, while in energy minimization problems the residual and the elastic tensors might be calculated instead.

Normally these quantities depend on the local state of each cell and on their histories. For instance, the stress tensors are calculated at every point of the cell, using only its displacements. These local quantities are then assembled into large matrices and vectors representing their global equivalent[1]. Naturally, this step is deeply connected to the iteration step, often being called several times in succession in order to

---

[1] These global matrices, in particular, may require a lot of RAM. One technique used to alleviate this issue is called matrix-free FEM, which builds the components of the matrix on-the-fly, as required by solvers. While more economical in terms of memory, their implementation is somewhat complex. See Ref. [122] for more details.

determine how to proceed.

3.1.2.2 Iteration step

The way to advance the state of the system depends on the problem at hand, and must be implemented by the user. The idea of this function is that it takes the system from one state and propagate it to a different state. In order to aid the user in the implementation of this step, simple examples are bundled with JuFold which solve the two most common classes of problems, which the user can then tailor to their own application. The first example solves the elastostatic problem which tends to draw from numerical optimization, where the system does not abide by Newton's laws for its evolution, but simply follow cues in the potential surface. Thus, during the run of the algorithm, the evolution between two steps is perhaps non-physical, which is allowed as long as the final state represents an energy minimum. The problem is solved using the Newton-Raphson method, described in Sec. 2.4.1. The second example solves the elastodynamical problem, where the system follows the equations prescribed by Newton's 2nd law, leading to an initial value problem, which is solved by the modified Verlet algorithm introduced in Sec. 2.4.2.

3.1.2.3 Analyses

The displacements are normally the raw results of the simulation. Often they are indeed the objective of the simulation, but rarely they are the sole quantity of interest. Instead, it is common to calculate derived quantities, such as the local stress, energy, volume change, among others. Whether such calculations are performed during or after the simulation depends on the available storage and CPU time. Performing these calculations at runtime carries two main advantages. First, certain analyses demand the computation of a cohort of tensors, which have already been calculated as part of the iteration step. Caching these calculations, allows further analyses be carried out in a computer less powerful than the one used to perform the simulation itself. Second, the results are bundled in the same file. Using softwares like Paraview [123] or VisIt [124], it is possible to compare several quantities side-by-side, which is useful when trying to make sense of the results obtained. The downside of this approach is that it has the potential to grandly increase the storage requirements of simulation data.

3.2 Utilities

While the calculation of the state is unique to each problem, many of its subcomponents are common to all problems in continuum mechanics. For instance, the energy density used is dictated by the material simulated, not by the specific computational implementation. Several of these useful utilities are bundled with JuFold. We go over the most prominent of them in the section below, but minor utilities – such as the code for the calculation of the deformation gradient matrix **F**, postprocessing, interpolation of nonuniform parameters, among others – are also implemented in JuFold.

3.2.1 Energy density

One of the main components of continuum mechanics is the energy density and its associated constitutive equation, as mentioned in Sec. 2.1.3. JuFold has a few energy densities already implemented, which can be chosen at compile time (see Table 3.1). Should the user require a constitutive equation that is not already implemented in JuFold, it is possible to extend the code with minimal effort.

Table 3.1: Energy densities implemented in JuFold. The operation $||\mathbf{F}|| = \sqrt{\mathbf{F}:\mathbf{F}}$ denotes the norm of the matrix, as induced by the double internal product, and d denotes the dimension of the simulation.

Name	**Density Equation**	**Reference**
St. Venant-Kichhoff	$\psi = \mu \ \mathrm{tr}(\mathbf{E}^2) + \lambda/2 \ \mathrm{tr}(\mathbf{E})^2$	[125]
Neohookean - 1	$\psi = \mu/2 \ [||\mathbf{F}||^2 - \mathrm{d} - 2\log(J)] + \lambda\log(J)^2/2$	[87]
Neohookean - 2	$\psi = \mu/2 \ [||\mathbf{F}||^2/J^{2.0/\mathrm{d}} - \mathrm{d}] + \lambda(J-1)^2/2$	[78]
Neohookean - 3	$\psi = \mu/2 \ [||\mathbf{F}||^2 - \mathrm{d} - \log(||\mathbf{F}||+1)] + \lambda(J-\alpha)^2/2$ $\alpha = 1 + \frac{\mu}{\lambda} - \lambda\frac{\mu}{4}$	[126]

These energies are implemented in JuFold through a template interface. Their concept is composed of three main functions, each being individually responsible for the calculation of energy, PK1 tensor, and elastic tensor. This modularization helps to keep the code complexity under control, and most importantly, allows for the reuse of the code dealing with the numerical calculation of the weak form and the assembly of the relevant matrices and vectors.

3.2.2 Collision detection

The folds in the human brain tend to be closely touching in-vivo (see, for instance, Figs. 1.1 and 1.2). In order to simulate this situation, it is necessary to handle self-collisions in the mesh. Collision is traditionally divided into two steps, detection and handling [127]. In the first of these steps, as the name implies, the software detects collisions between the various cells in the mesh. Information on these collisions is then used in the second step, where the collisions are resolved.

Collision detection is further divided in two steps. In the first step, called broad phase, the easily falsifiable collisions are eliminated using a less robust – but faster – algorithm. In JuFold, the broad phase is performed by encapsulating each cell in the mesh in a circle (a sphere in 3D) containing the whole cell. Collisions between these circles are then detected, which is computationally inexpensive. If the circles collide, these cells are forwarded to the more narrow collision phase. Otherwise, these cells are discarded from the list of possible collisions. In the second phase, called the narrow phase, the remaining collision possibilities are calculated using a slower – but thorough – algorithm. The narrow phase is conducted by the calculation of the winding number [128], where for each vertex of a given cell p_i^A, we detect if it is contained in any other cell, leading to a positive winding number. If the winding number is non-zero, a collision is flagged. This division grandly speeds the collision detection, as it allows for the weeding out of many false positives at a small cost.

The collision handling step is, once again, problem-dependent, and must be implemented by the user. In the implementation used in Chs. 4 and 5, a spring-like repulsive energetic term is added to the weak form solved, as introduced in Ref. [129].

3.2.3 Internal state saving and loading

High-performance computing (HPC) systems normally have tight constraints regarding the runtime of any given instance of a program[2]. Often, the necessary runtime of simulations is longer than that. Thus, a mechanism to save the internal state of the program for later recovery is a necessary feature.

JuFold writes the system state to the disk, including all the cell data, at regular

---

[2] For instance, on the High-Performance Computing systems of the Jülich Supercomputing Center at the Research Center Jülich and at the RWTH Aachen University – JURECA and CLAIX – used in this work, programs were allowed to run for a maximum of 24 hours.

intervals set by the user. The state is saved in a number of JSON files, which has the advantage of being plain text, thus easily readable. This scheme is, *prima facie*, storage heavy, and with lots of redundant data. JuFold compresses these files in memory and saves them into a compressed format, thereby grandly reducing the size of the files written to the disk. The gunzip compression was chosen because of its availability, speed, effectiveness, and most importantly, many text editors are able to transparently decompress, edit, and recompress the gunzip file.

Besides getting around the hard requirements set by HPC systems, having such capabilities are useful in debugging, as it is easier to analyse the internal state of the program when unexpected behaviour occurs. Should the necessity arise, it is also possible to restart and run the program for a longer time than previously expected.

3.2.4 Linear multistep integrator

Due to its dependency on other quantities, integrating the growth equation can be complex. In order to get around this issue, they are integrated independently of the other components of the state, using information from previous steps via the Adams-Bashford (AB) method [130]. The user can select the order of the algorithm, with up to fourth order being available.

It is only possible to use the n-th order of the algorithm once at least $n - 1$ time steps have been iterated. JuFold automatically scales the order of the AB algorithm to handle this constraint. That is, in the first step, the first order method is used, in the following step the second order is used, and so on until the maximum order chosen by the user is reached.

3.2.5 Mesh generation

Through deal.II, JuFold includes many standard meshes and tools to modify that mesh. Additionally, the user also has the option to have the mesh as an input to the program, instead of creating it programmatically every time. This is especially useful when modeling complex systems, such as when the description of the mesh is not an assembly of simple geometrical shapes. The only limitation for JuFold is that the meshes must be composed solely of quadrilaterals and hexahedra. This is not the default mesh type for most computer-assisted design programs, which tend to output meshes composed of triangles and tetrahedra. In Gmsh specifically, it is possible to directly create meshes with the necessary conditions [131, 132]. For other software, it is possible to convert from triangular/tetrahedral meshes to quadrilateral/hexahedra meshes using the *tethex* tool [133].

3.3 Implementation details

JuFold is developed using C++ and Message Passing Interface (MPI) [134, 135], based on the deal.II library. It is optimized to run in several nodes of a supercomputer, but is also suitable for smaller-scale simulations running on a local workstation. In this section, some higher-level design decisions regarding JuFold are discussed. A brief introduction to the actual usage of JuFold is found in Appendix D,

3.3.1 Performance considerations

In C++, virtual functions and templates can both be used to provide the needed flexibility to deal with different systems. Which one to use will depend on context, compiler, and platform. The discussion of when to use each is somewhat technical. In short, the fundamental idea of both templates and virtual functions is that the programmer can define an interface which can be overloaded by the user. For the computer, the difference between the two is when to search for the overloaded function. The overload resolution of templates is performed at compile time. This allows for a greater speed of the final program, as the compiler has access to the function, and can perform further optimization. This comes at the cost that compilation takes longer, and that templates can be more difficult for understand, as only the latest version of C++ has mechanisms for the formal specification of template interfaces[3]. Also, once templates are introduced, compiler messages get more complex, with the problem being compounded for every new template added. All of these make the usage of templates difficult to beginners. We thus reserve the usage of templates for interfaces which are used in the innermost loops of our code, where performance is of essence, while keeping their complexity to a minimum.

---

[3] This version of C++, called C++20, was released not long before the writing of this thesis, and still lacks widespread adoption.

Virtual functions, on the other hand, are similar to any other method in a class, and have been part of object oriented programming for many decades now. Their overload resolution, however, happens during runtime. This can lead to lower performance[4]. It is also easier to provide a default implementation of a virtual function than of a templated function without resorting to too much boilerplate code. We use virtual functions for long-running functions, which are called comparatively few times. For instance, the main method of JuFold is a virtual function, while the functions calculating the stress are templated, as they are called in tight loops.

3.3.2 Parallelization strategy

The Message Passing Interface (MPI) is a long running standard in high-performance computation [134, 135]. This standard defines a distributed memory model, where each process is only able to access its own assigned memory, and synchronization must be performed explicitly through message passing. High-quality libraries implementing this standard are commonplace in clusters and supercomputers, with open source implementations, such as OpenMPI[5] [137], also available in consumer-grade computers.

JuFold uses MPI to parallelize simulations. It partitions the system's degrees-of-freedom between the various MPI-processes, which then performs the calculations needed for each degree-of-freedom in their domain which are then globally assembled for further usage. The partitioning ideally minimizes the "surface" between two partitions, thereby minimizing the inter-process communication. Graph partitioning algorithms, such as parallel multilevel partitioning [138] tend to lead to close-to-ideal mesh partitions, with one of the *de facto* standards being the open source library (Par)METIS [139].

As with all the rest of JuFold, the final user is in control of how the partitioning process occurs. By default, JuFold will partition the system in stripes, one for each process. This is not necessarily optimal for the general case, but tends to perform well

---

[4] In technical terms, the virtual functions are implemented as arrays of addresses to the actual implementations, called a *vtable*. Thus, once a virtual function is called, there is an indirection in the CPU cache, leading to lower performance. This is compounded by the lack of optimization at compile time, as the compiler does not have any information on the internal structure of the callee, possibly leading to missed optimization. That said, in some situations it is possible to elide the virtual function, and no performance costs are incurred.

[5] Not to be confused with OpenMP. OpenMPI is an implementation of the MPI standard, while OpenMP is a different parallelization standard, with its own set of implementations [136].

nonetheless. It is, however, often optimal for systems with enabled collision detection, as it leads to an ideal level of load balancing in the collision detection step.

MPI gives JuFold the flexibility to run concurrently in more than one node at any given time, possibly granting access to large amounts of processors and memory. The latter point is especially useful for energy minimization simulations, where the nonlinear root-finder must solve the linear problem in Eq. 2.53, which can be memory-intensive.

3.3.3 Other libraries

JuFold leverages the capabilities of other libraries. Most importantly, we used the deal.II library [119, 120] to handle the Finite Element components. Indeed, many of JuFold's capabilities are leveraged from this library. Further, the parallelization of the linear algebra components were done through the PETSc (Portable, Extensible Toolkit for Scientific Computation) library [140–142].

3.4 Gallery

To demonstrate the scope of JuFold, a few examples of usage are briefly shown in Fig. 3.2. In (a) and (b), the typical systems simulated in the following chapters are shown, where a bilayered rectangular slab has its top layer grown. Fig. 3.2 (c) shows a system similar in spirit but distinct in implementation, where the varied cortical property is no longer geometrical but mechanical, with softer regions shown in yellow, and stiffer regions in blue. Similarly to what is seen in Sec. 4.1.6.2, the softer regions deform more than the harder parts. The boundaries were left open, making the expansion of the gray matter constrained only by the underlying white matter. Fig. 3.2 (d) extends the ideas in Sec. 4.1.6.1 to the sphere. This system is thus composed of a solid sphere as the white matter, and a thin growing crown as the gray matter. The only difference between the simulations in Fig. 3.2 (a) and (d) is merely the meshing, something that can be easily changed in JuFold. Together, Fig. 3.2 (c) and (d) showcase the dimensional independence of JuFold.

Another goal of JuFold was to be modular. In Figs 3.2 two cases where growth has been disabled are shown. It is possible to adapt JuFold for such cases with ease. In (c), energy minimization is used to simulate the effects of a bacteria walking over

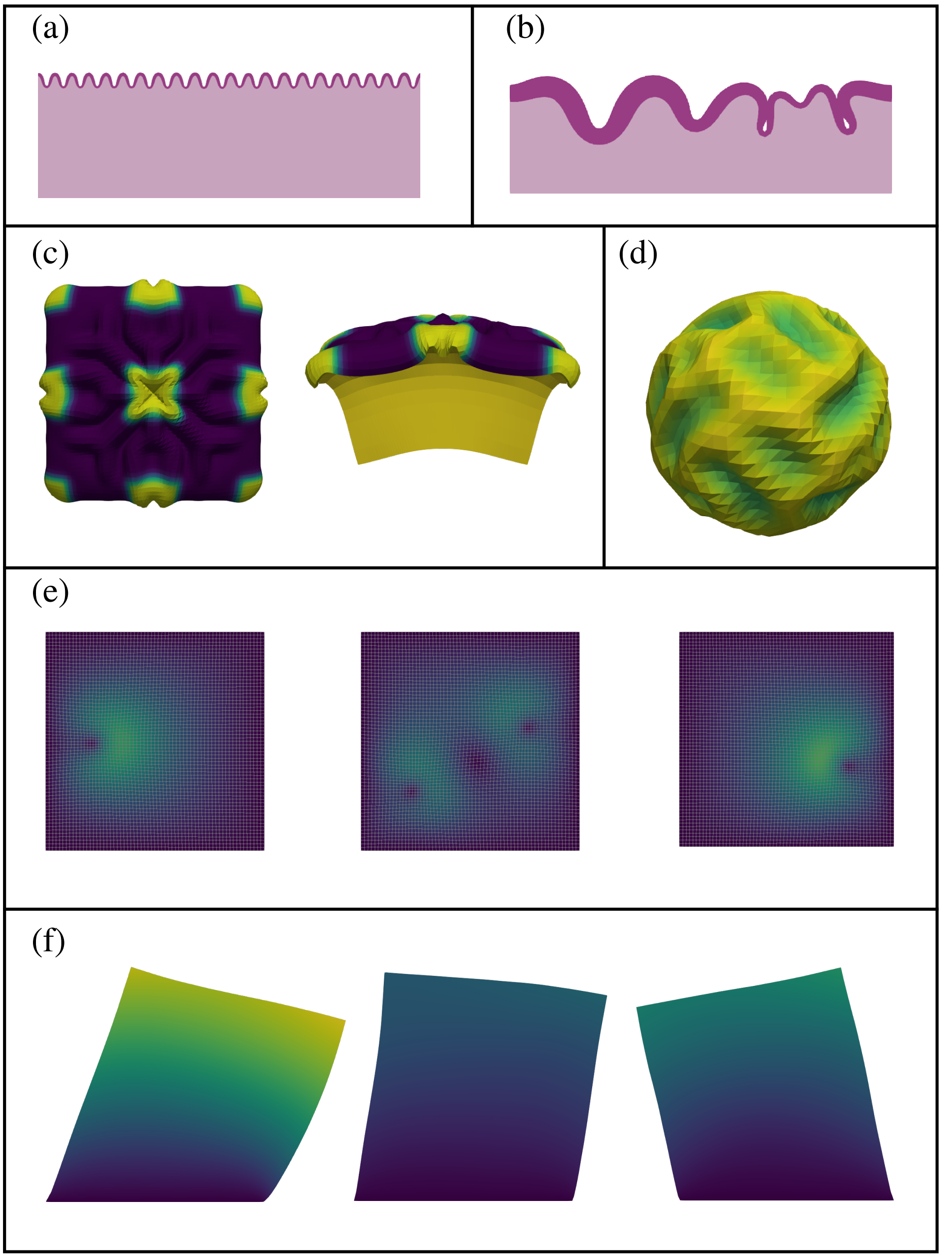

Figure 3.2: Gallery of example usages of JuFold. (a) System with homogenous top layer, as studied in Sec. 4.1.6.1 and throughout Ch. 5. (b) System with inhomogenous cortical thickness, as studied in Sec. 4.1.6.2. (c) Three dimensional system with inhomogeneities in its Young modulus. (d) Spherical simulation with a thin growing shell and an purely elastic core. (e) Example of idealized experiement, on which a bacteria crawls on top of an elastic substrate. (f) Elastodynamics example where a non-growing system is initially moving towards the left and is suddenly clamped to the bottom.

an elastic substrate, while in (d), elastodynamics is implemented through the Verlet algorithm for a soft material bouncing around after momentum is transferred in a short impulse.

3.5 Structured surfaces

JuFold has found use in other fields, in addition to brain folding. In particular, we have also applied it to the production of structured surfaces. In this project, a slab of PDMS gel is stretched and a mask in applied to the top layer of the slab. This slab is then exposed to O_2. The resulting plasma interacts with the ligant in the PDSM gel, leading to the glassification of the exposed surface [143], while keeping the surface protected by the mask intact. The glassification process changes the stress-free configuration to that with extended lengths. Once the imposed stretch is released, microscopic structures are created through buckling. This process is summarized in Fig. 3.3 (a).

Different masking procedures generate distinct folding patterns and depending on the application, it is possible to tailor the mask in order to obtain specific patterns. We believe that this approach has the potential to produce microchannel chips in a cheap and quick manner. This process has been written into a patent application, “Herstellung strukturierter Oberflächen” numbered 10 2020 118 555.3. At the time of writing of this thesis, patent approval is still pending.

As part of the writing of said patent, a few patterns have been identified. For instance, the application of a rectangular mask generates a channel once the stretch is removed (see Fig 3.3 (b)). Complementary, a cross-shaped mask leads to the formation of a channel crossing (see Fig. 3.3 (c)). Another interesting configuration emerges when the mask is composed of a single circle, which leads to a hilly configuration, which can be used as a mixing zone (see Fig. 3.3 (d)). These structures can be seen as the building blocks of, for instance, microfluidics chips, which can then be aggregated and customized to the necessities of each individual experiment.

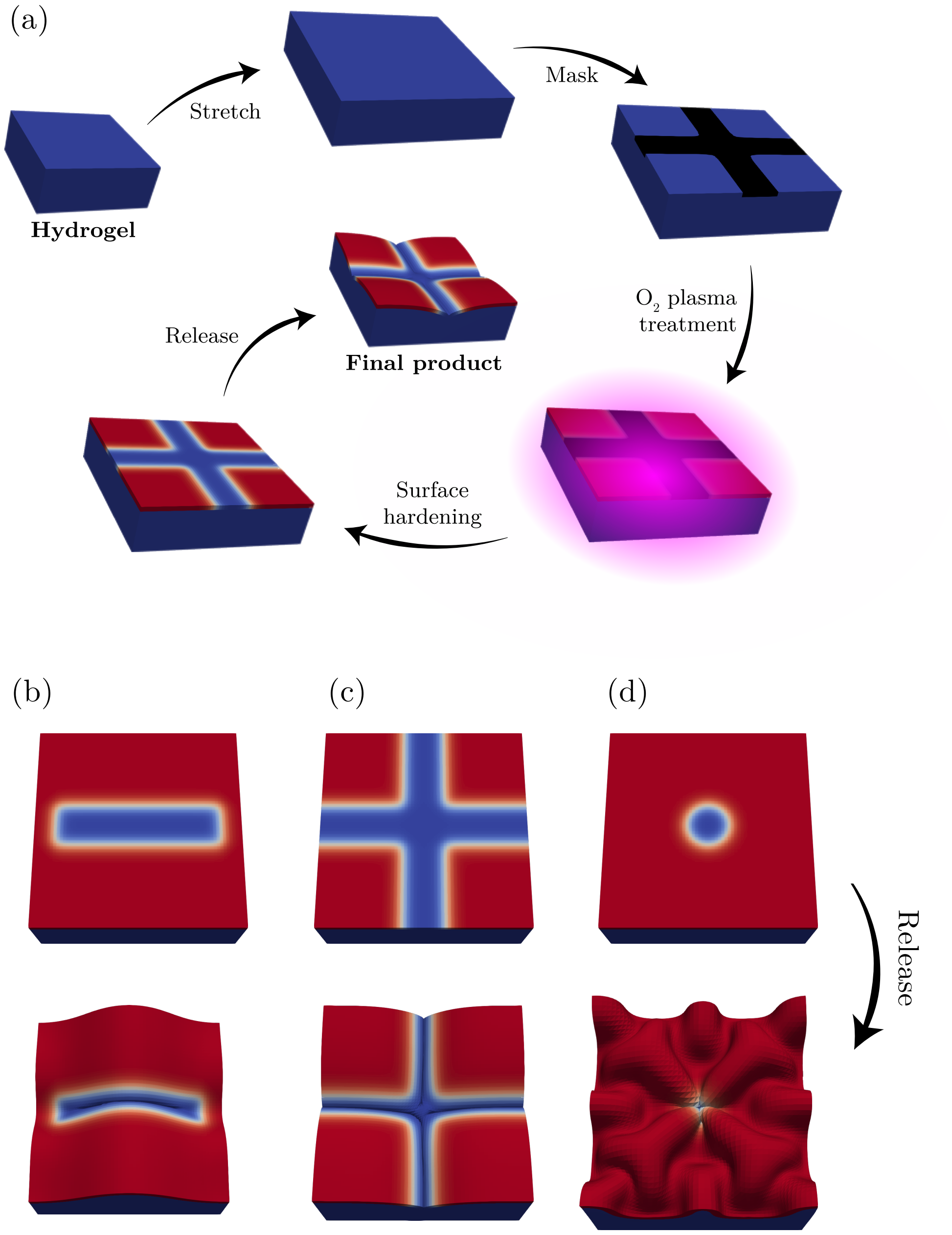

Figure 3.3: (a) Sketch of glassification process. (b-d) Simulations of unstretching following masking. In all simulations, a Young modulus ratio of $r_E = 300$ was used. Red indicates harder regions, with softer regions in blue.

Chapter 4

Energy Minimization simulations

Brain development happens over the span of weeks and months, with inertial effects becoming less pronounced. In such a long timescale, the quasi-static is often used, where for each choice of the growth tensor $\mathbf{F}_g$, the potential energy of the system is minimized. Section 4.1 comprises the bulk of this chapter, reproducing the content of our article "The role of thickness inhomogeneities in hierarchical cortical folding", published in NeuroImage [144]. In this article two distinct classes of systems are studied. First, the focus will be on the detailed study of the relatively simple, but surprisingly rich, case when the cortical thickness is initially constant in space. Secondly, how the competition between various distinct thicknesses induces new cortical conformations is discussed. Varying thickness is enough to create deep sulci, as well as structures similar to higher-order folding observed in the mammalian brain. These two systems are then analysed in light of linear stability theory. Section 4.2 presents further analyses that were not included in the paper.

4.1 The role of thickness inhomogeneities in hierarchical cortical folding

4.1.1 Abstract

The mammalian brain cortex is highly folded, with several developmental disorders affecting folding. On the extremes, lissencephaly, a lack of folds in humans, and polymicrogyria, an overly folded brain, can lead to severe mental retardation, short

life expectancy, epileptic seizures, and tetraplegia. Not only a specific degree of folding, but also stereotyped patterns are required for normal brain function. A quantitative model on how and why these folds appear during the development of the brain is the first step in understanding the cause of these conditions. In recent years, there have been various attempts to understand and model the mechanisms of brain folding. Previous works have shown that mechanical instabilities play a crucial role in the formation of brain folds, and that the geometry of the fetal brain is one of the main factors in dictating its folding characteristics. However, modeling higher-order folding, one of the main characteristics of the highly gyrencephalic brain, has not been fully tackled. The simulations presented in this work are used to study the effects of thickness inhomogeneity in the gyrogenesis of the mammalian brain *in silico*. Finite-element simulations of rectangular slabs are performed. These slabs are divided into two distinct regions, where the outer egion mimics the gray matter, and the inner region the underlying white matter. Differential growth is introduced by growing the top region tangentially, while keeping the underlying region untouched. The brain tissue is modeled as a neo-Hookean hyperelastic material. Simulations are performed with both, homogeneous and inhomogeneous cortical thickness. Our results show that the homogeneous cortex folds into a single wavelength, as is common for bilayered materials, while the inhomogeneous cortex folds into more complex conformations. In the early stages of development of the inhomogeneous cortex, structures reminiscent of the deep sulci in the brain are obtained. As the cortex continues to develop, secondary undulations, which are shallower and more variable than the structures obtained in earlier gyrification stage emerge, reproducing well-known characteristics of higher-order folding in the mammalian, and particularly the human, brain.

4.1.2 Introduction

One of the most striking features of the human brain is its highly folded structure. Indeed, neuroscientists have for a long time pondered about its importance and origin [145, 146]. The study of layered systems has been extensively conducted in the field of engineering, where it was used to model the buckling of sandwich-type panels [147], the Earth's crust [148, 149], etc. These works, however, deal mostly with stiff materials and large stiffness ratios. In recent years, there has been a surge in the number of works dealing with soft materials, with special focus in bio-compatible applications [150, 151] which provide an important tool in the understanding of the role of mechanics in the folding of the mammalian cortex.

Still, gyrogensis is not fully understood neither at the level of mechanical [152] nor molecular processes [153] One of the main hypotheses to explain the convoluted nature of the cortex, commonly called the *differential tangential growth hypothesis* [154] posits that brain folding is created by a mismatch of growth rates in the cortical plate and the white matter substrate, which leads to buckling. This hypothesis has formed the core of many new models of brain folding [155–158]. The main contention with the differential growth hypothesis, however, is its requirement of a large difference between the stiffness of the two regions [152]. In order to obtain the wavelengths compatible with the gyral width of the human brain, the initial form of the differential growth hypotheses requires the stiffness ratio between the gray and white matter to be in the order of 10 [154]. This is a major hurdle, as currently there is no consensus if the gray matter is indeed stiffer than the white matter, and if so, by how much. There is a solid body of evidence supporting the two possibilities, i.e., that the gray matter is indeed stiffer than the white matter [159–161], and vice-versa [162–164]. A second issue with the differential growth hypotheses is the shape of the sulci. This model results in smooth sinusoidal patterns, while the brain is characterized by smooth gyri and cusped sulci [68].

Much work has been done to solve the issues with differential growth, especially on the sulci formation. For instance, [68, 165] performed large simulations to understand how the geometry of the cerebrum and constraints imposed by skull affect the cortical folding, where they showed that the size and shape of the folds are dictated by the geometry of the early fetal brain. Other hypotheses have also been proposed to explain cortical gyrification. Another widely discussed hypothesis conjectured that axonal traction is the driver of folding [166]. Reaction-diffusion models, where the concentration and diffusion of growth-activator chemicals are explicitly modeled, have also been suggested as a way to explain both the gyrogenesis process, as well as the growth profile itself [167, 168].

Despite all these efforts, an aspect of brain folding that still remains elusive is the phenomenon of hierarchical folding, an important feature of the brain development, which must be included in order to understand the driving forces behind the complex folding patterns observed in the human brain.

Recent studies have analyzed the influence of growth and stiffness inhomogeneities along the cortex. [157] studied the effect of inhomogeneities of the geometry, mechanical properties and growth on gyrification. Simulating both sharp and gradual inhomogeneities, their model produced higher-order folding. Budday et al. [82, 159] performed similar inhomogeneity studies on rectangular geometries. Their simulations also produced structures with resemblance to higher-order folding. However, these previous works did not show the complex spectrum of folding present in the human brain, presenting either simple wavy patterns, or a combination of very few wavemodes.

Histological experiments have shown that the cortical thickness is no longer homogenous, even at a young age. In the experiments of [169] it can be observed that the cortical thickness is inhomogenous in the ferret brain as early as the second post-conceptual day (P2), long before folding, which occurs between P6-P21 [158]. Indeed, in the beginning of the folding process, it is possible to find regions with cortical thickness as thin as 0.34 mm surrounded by regions regions with cortices as thick as 0.86 mm, representing a 2.5-fold increase over a distance of approximately 2 mm [169].

Many works have shown that thickness of cortex of the brain strongly impacts the width and structure of brain folds [154, 156, 157, 170–172], but evidence on how competition between the different thicknesses in the cortex affect folding has been lacking. In this paper, the differential tangential growth hypothesis is augmented with an inhomogeneous cortical thickness field, yielding realistic folded structures, which could help explain formation of the deep sulci in the mammalian brain, hierarchical folding, as well as its consistent localization, in line with the works highlighted in the previous paragraphs. Additionally, the configurations obtained in this work have a wider gamut of shapes for the sulci and gyri than those obtained previously, which more closely reproduce those shaped found in the human brain.

4.1.3 Material and methods

We analyze two-dimension systems composed of two regions: A purely elastic, non-growing, softer substrate in the lower region, mimicking white matter, and a growing stiffer region on the top, emulating the cortical gray matter (see Fig. 4.1). The simulations are performed using a custom written finite element method code to solve the

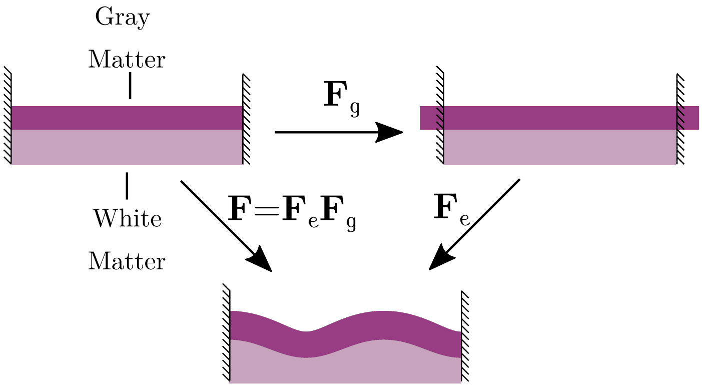

Figure 4.1: (Color online) Schematic representation of the model. The purple region atop mimics the gray matter and is grown tangentially, while the pink substrate underneath mimics the white matter and does not grow. Growth is mathematically represented by the growth tensor $\mathbf{F}_g$, which can be discontinuous. In order to keep the compatibility with the attachment constraints between the gray and white matter, the system is subject to residual stress, described in this framework by the $\mathbf{F}_e$ tensor.

continuum mechanics equations[1].

4.1.4 Theoretical background

Due to the large-strain, nonlinear nature of the human brain, the framework of continuum mechanics [177] is used. In order to distinguish between the original and deformed configurations, the following notation is introduced: The vector $\mathbf{X}$ denotes the coordinates of the original configuration, $\mathbf{x}$ the coordinates of the deformed configuration, and $\mathbf{u} = \mathbf{x} - \mathbf{X}$ denotes the displacement field. The deformation gradient tensor is written as

$$\mathbf{F} = \frac{\partial \mathbf{u}}{\partial \mathbf{X}} + \mathbf{I},$$

where $\mathbf{I}$ is the identity matrix. Growth is introduced using Rodriguez theoretical framework [178], where the deformation gradient tensor $\mathbf{F}$ is decomposed into $\mathbf{F} = \mathbf{F}_e\mathbf{F}_g$ (see Fig. 4.1), where $\mathbf{F}_e$ describes the elastic part of the deformation and $\mathbf{F}_g$ the growth contribution. The energy and stress are calculated from the elastic part of

---

[1] The simulations were written using the deal.II library [173, 174], and parallelized using MPI via PETSc [175, 176].

the deformation gradient tensor alone. Thus, in this framework, the energy-density is defined in terms of $\mathbf{F}_e$.

The brain tissue is modeled by the compressible Neo-Hookean energy-density function [177]

$$\psi(\mathbf{F}_e) = \frac{\mu}{2}\left(\mathrm{tr}(\mathbf{F}_e^T\mathbf{F}_e) - 2\log(J_e) - 2\right) + \frac{\lambda}{2}\log^2(J_e) \tag{4.1}$$

where $J_e = \det(\mathbf{F}_e)$, and μ and λ are the Lamé parameters. This energy-density family has been shown to appropriately model the brain tissue [179, 180].

Due to the relatively long time scale of cortical development when compared to the elastic response of brain tissue, the quasi-static approximation is used. At every value of $\mathbf{F}_g$ the displacement field $\mathbf{u}$ is calculated, obeying the equilibrium equation

$$\nabla \cdot \mathbf{P} = \mathbf{0}, \tag{4.2}$$

where $\mathbf{P}$ is the first Piola-Kichhoff (PK1) stress tensor. The functional form of this tensor depends slightly on which configuration the weak form of Eq. 4.2 is integrated. In the stress-free configuration – i.e., the grown configuration – the PK1 tensor is obtained as

$$\mathbf{P}_e = \frac{\partial \psi}{\partial \mathbf{F}_e}.$$

It is, however, numerically advantageous to perform the integration in the original, undeformed configuration. In such case, the total deformation tensor $\mathbf{F}$ is thermodynamic conjugate to the stress, yielding the following PK1 tensor

$$\mathbf{P} = \frac{\partial \Psi}{\partial \mathbf{F}} J_g = \frac{\partial \Psi}{\partial \mathbf{F}_e}\mathbf{F}_g^{-T} J_g, \tag{4.3}$$

where the Jacobian $J_g = \det(\mathbf{F}_g)$ is introduced due to the change in integration domain.

Both, Eq. 4.2 and Eq. 4.3 retrieve the functional form of their classical continuum mechanics counterparts in the limits of no growth, i.e., $\mathbf{F}_g = \mathbf{I}$. The values of λ and μ are chosen such that in the linear (i.e., small strain) regime, the Young moduli ratio between the gray matter (GM) and the white matter (WM) is $r_E = E_{GM}/E_{WM} = 3$, consistent with previous models [179] and the Poisson ratio $\nu = 0.35$ on both regions. Due to the nonlinear nature of Eq. 4.1, the value of the Poisson ratio ν and Young modulus are dependent on the current displacement in the system. Specifically, they depend on the determinant J_e [177] as

$$\nu = \frac{1}{2}\frac{\lambda}{\lambda[1 - \log(J_e)] + \mu},$$

and

$$E = \frac{\mu - 3\lambda\log(J_e)}{J_e}\frac{2\mu + \lambda(3 - 2\log(J_e))}{2\mu + \lambda(1 - \log(J_e))}.$$

Notably, the energy-density in Eq. 4.1 has no inherent length scale. Thus, only the ratios between the elastic moduli are important for the phenomena presented in this paper.

4.1.5 Simulation details

The cortical ribbon grows linearly, i.e., the growth tensor is described by

$$\mathbf{F}_g(\theta_g) = \theta_g\mathbf{I} + (1 - \theta_g)\hat{\mathbf{X}}_y \otimes \hat{\mathbf{X}}_y,$$

where $\hat{\mathbf{X}}_y$ indicates the unit vector pointing the in the y-axis and the growth parameter θ_g measures the degree of elongation in the cortex. For instance, at $\theta_g = 2$ the gray matter would have expanded to twice its lateral size if it were not constrained. To mimic differential growth, θ_g is varied in the interval $[1.0, 2.5]$ in the gray matter region, while it is kept at unity in the white matter region. The growth parameter θ_g is increased in small steps of 0.01.

At every growth step, Eq. 4.2 is solved using the finite element method, with boundary conditions of zero displacement on the bottom surface $X_y = 0$ and zero stress on the top surface $X_y = L_b$. In order to minimize boundary effects, periodic boundary conditions are imposed on the sides of the surface, $X_x = 0$ and $X_x = L_b$. The box lengths L_b will be specified in each section. The system being two dimensional, corresponds to an infinite system in the z-axis, with the constraint of no displacements in the z-axis.

Due to the nonlinear nature of the energy described in Eq. 4.1, the divergence of the first Piola-Kichhoff stress tensor will also be nonlinear. To find the roots of this function, the Newton method augmented by a backtracking algorithm [177, 181] is used. In order to avoid overlaps, collisions are detected and resolved using the approach introduced by [129]. As any collisions will be initiated in the cortical region, calculations are optimized by only detecting collisions in the gray area elements. This generates no artifacts, as due to the structure of the mesh, collisions are resolved before any white matter elements are involved.

In order to allow the system to overcome metastable states, a small force field pointing in the y-direction is introduced. The forces are drawn from a uniform random distribution between $[-7 \times 10^{-2}, 7 \times 10^{-2}) \times E_{GM}$. Each simulation has been repeated three times with different seeds. No significant difference is observed between runs with different seeds, or when the forces are doubled or halved.

4.1.6 Results

4.1.6.1 Homogeneous thickness of cortical ribbon

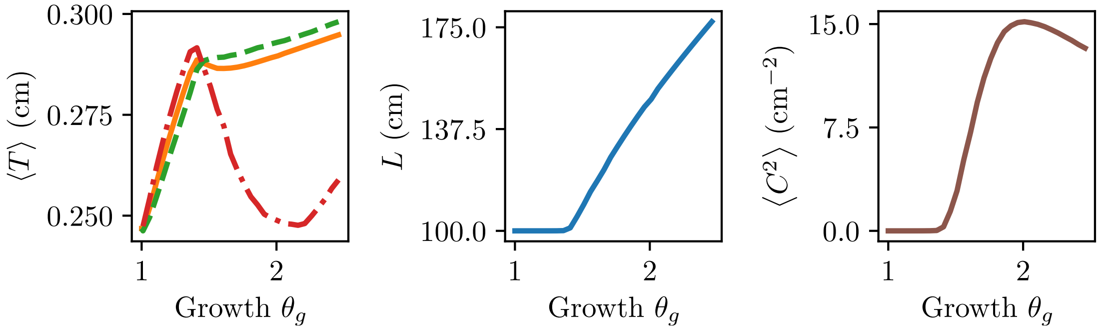

Figure 4.2: (Color online) Spatial averages of several observables in the system with initial thickness $T = 0.250$ cm, as a function of the growth parameter θ_g. (Top) Dependence of the average thickness with growth are shown, as well as the average cortical thickness of the sulci and the gyri, as defined in the text. (Center) Contour length of the top region of the system. (Bottom) Squared curvature of the system are shown, respectively. This last quantity is specially useful to characterize the onset of folding, as shown in Sec. 4.1.6.2.

We analyze the folding of a slab with constant cortical thickness T throughout, in the range $[0.1, 0.5]$cm. In this case, it is expected that the system will fold into well defined wavelengths, with no localization [182]. In order to avoid finite-size effects, the simulation box is set to $L_b = 100\text{cm} \gg \lambda_F$, where λ_F is the folding wavelength.

4.1.6.1.1 Evolution of folding

Initially (i.e., for little growth) even though the growth happens tangentially, the cortex does not increase in length, but rather in thickness due to the confinement and resulting stress (see Fig. 4.2). Eventually, at a critical growth θ_g^C, the stress exceeds the critical buckling threshold, and the system buckles in a well defined, almost sinusoidal wave pattern (see Fig. 4.3). As growth continues, the wavelength and the average thickness of the folds remain almost unchanged, while the amplitude increases. Our study confirms previous results showing that the thickness of the cortex is no longer homogeneous after buckling. Sulci (regions of positive curvature) are significantly thinner than gyri (regions of negative curvature), as indicated by the relative drop δ, which is calculated as the percentual difference between a local minimum and its surrouding maxima. As growth continues post buckling, the difference in thickness continues to increase.

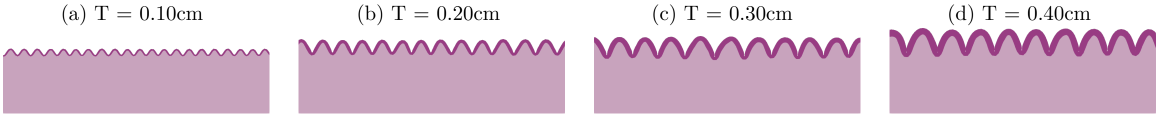
(a) T = 0.10cm (b) T = 0.20cm (c) T = 0.30cm (d) T = 0.40cm

Figure 4.3: (Color online) Folded system for the thickness indicated within the figure. In order to improve visualization, only the region $y > 95$cm is shown here. The relative drops are (a) $\delta = 0.17$ (b) $\delta = 0.28$ (c) $\delta = 0.29$ (d) $\delta = 0.37$.

4.1.6.1.2 Folding wavelength

In each simulation the Fourier transform of the function $u_y(X_x)$ (i.e., the displacement in the y direction as a function of the material coordinates) is calculated along the top region of the system. The folding wavenumber and wavelength are then obtained as

$$k_F = \underset{k}{\operatorname{argmax}}\, h_k \quad \lambda_F = \frac{2\pi}{k_F}, \tag{4.4}$$

where h_k is the coefficient of Fourier expansion for the mode with wavenumber k. That is, the folding wavenumber and wavelength are those associated with the largest amplitude. Consistently with analytical predictions and with previous works in the literature, the folding wavelength increases linearly with initial thickness T (see Fig. 4.4). The linear dependency can be obtained from simple dimensional analysis: As the elastic equations have no inherent length scale, the cortical thickness is the only relevant length scale, as long as system size is not limiting. Thus, changing the homogeneous cortical thickness can be seen as a change of measurement units, or progressive zooming in on the same base system (see Fig. 4.5). It is possible to estimate the slope for a linear elastic substrate through analytical calculations as [182]

$$\lambda_F(T) = \pi \left(\frac{2}{3} \frac{(3-4\nu) r_E}{(\nu-1)^2} \right)^{1/3} T \approx 6.17T. \tag{4.5}$$

Such slope presents a weak dependence on the stiffness ratios between the gray and white matter, obeying a cubic root power law. Thus, the specific value of the ratio r_E plays only a minor role in the determination of the folding wavelength.

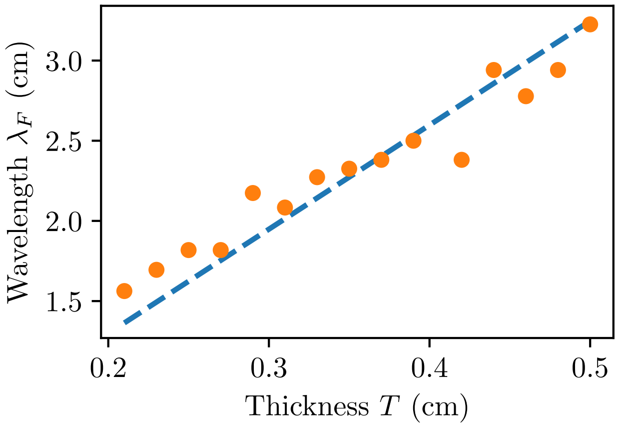

Figure 4.4: (Colors Online) Weighted wavelength of the system as function of the cortical thickness T. The orange circles indicate extrapolation results, while the broken blue lines represent the linear fit $\lambda_F = 6.49T$ cm with $R^2 = 0.94$.

4.1.6.2 Inhomogeneous thickness of cortical ribbon

The cortical thickness of the brain is spatially inhomogeneous. In order to emulate this inhomogeneity, a variable cortical thickness $T(X_x)$ is introduced. Specifically, as a generic form of thickness variation, a sinusoidal thickness variation of the form

$$T(X_x) = A \sin(2\pi X_x / L_t) + T_0$$

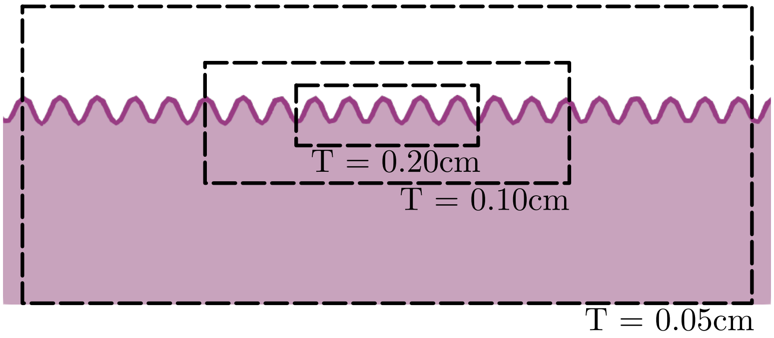

Figure 4.5: (Color online) Schematic representation of scaling of the system. Due to the lack of inherent length scale in the elastic equations, systems with thicker cortices can be seen as subregions of systems with thinner cortices. Here, each broken rectangle highlights a region which is equivalent to a system with the cortical thickness T indicated within the figure.

is chosen. This inhomogeneity introduces two new length scales beyond the base thickness T_0: the inhomogeneity amplitude A and the period of the inhomogeneity L_t. Thus, in contrast to the previous results, it is possible to choose any one of the three as the fixed length scale, and vary the remaining two independently. In this study, the thickness period $L_t = 10$ cm is chosen as the fixed scale. The folding pattern for a different periodicity L_t' can be obtained by rescaling the spatial quantities by L_t'/L_t, or a suitable power thereof.

Note that any form of thickness variation can be written as a sum of sinusoidal variations. When deformations are small, even the resulting folding patterns can be obtained by simple superposition. In the brain, however, deformations are large and nonlinear, and each thickness field must be studied independently.

Simulations are performed for base thickness in the same range as before, [0.1, 0.5] cm, and for each T_0, the amplitude A was varied in the range $[0, 0.9] \times T_0$. The inhomogeneity creates a much more localized deformation, thereby reducing possible artifacts created by finite-size effects. Thus, in order to maximize computational efficiency, the simulation box is chosen as $L_b = L_t$.

4.1.6.2.1 Shape of folding

If the natural folding wavelength λ_F of the local thickness is much smaller than the periodicity length, the system behaves essentially like the homogeneous systems studied in Section 4.1.6.1, i.e., the folding wavelength obeys Eq. 4.5, with $T = T(X_x)$. Here, the system folds into well defined waves, but with the spatially dependent wavelength commensurate with the cortical thickness of the underlying region (see Fig. 4.6 (a), (c)). Accordingly, these systems also present the constant length - constant thickness stress-relief mechanism.

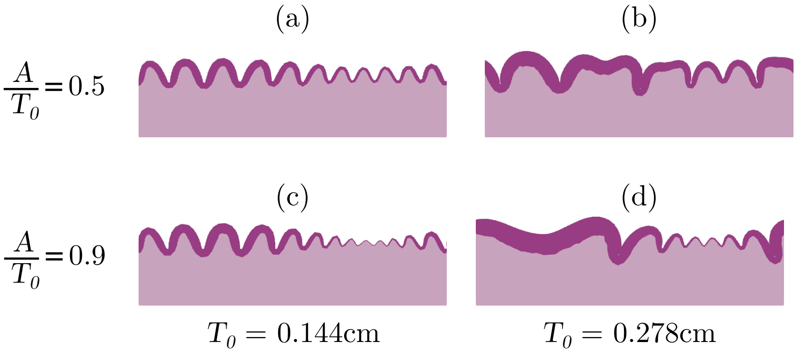

Figure 4.6: (Color online) Simulations with varying inhomogeneity amplitudes A. The simulations have a base thickness T_0 as indicated within the figure. The relative drops are (a) $\delta = 0.29$ (b) $\delta = 0.40$ (c) $\delta = 0.48$ (d) $\delta = 0.68$.

However, when the folding wavelength becomes comparable with the periodicity length, a second form of folding arises, characterized by complex folding patterns. In these conformations, several wavemodes are simultaneously obtained (see Fig. 4.6 (b), (d)), presenting similarities with the further regions of the gyrencephalic brain. See Supplementary Fig. E.1 for growth evolution over all simulated parameters, and Supplementary Fig. E.2 for their thicknesses and thickness gradients.

This new shape has distinct developmental steps, which differ from those described in Sec. 4.1.6.1. For small growth, an initially flat system (see Fig. 4.7 (a)) forms a single, deep, sulcus in an otherwise planar cortex, in the region surrounding the thickness minimum (see Fig. 4.7 (b)). The depth of this sulcus soon saturates, and due to the underlying white matter, it is energetically favorable to form additional sulci rather than to increase the depth of the existing sulcus as growth continues (see Fig. 4.7 (c)). The maturation of the new sulci occur concurrently with the formation of shallow sulci in the regions of highest thickness (see Fig. 4.7 (d)).

It is expected that the folding starts on the region of thinnest cortex. In the limit

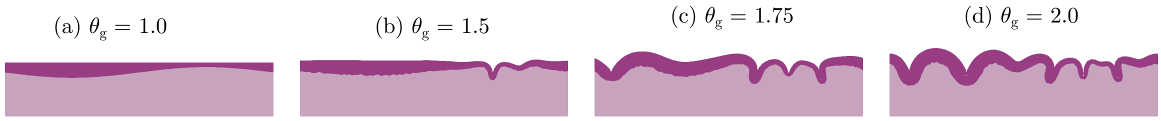

(a) $\theta_g = 1.0$ (b) $\theta_g = 1.5$ (c) $\theta_g = 1.75$ (d) $\theta_g = 2.0$

Figure 4.7: (Color online) Growth evolution of system with $T_0 = 0.322$cm and $A = 0.174$ cm. The growth parameters are indicated within the figure. The relative drops are (a) $\delta = 0.23$ (b) $\delta = 0.40$ (c) $\delta = 0.54$ (d) $\delta = 0.55$.

of small deformations, the system can be analysed by the theory of thin plates. In this domain, the bending rigidity depends on the cube power of the thickness of the plate [183]. Thus, the large differences in thickness create a stress imbalance in the region, leading to the buckling of the region with small thickness. This is specially noticeable in the formation of the deep sulci observed in Fig. 4.7. Here, the thick parts of the cortex compress laterally, which leads to stress condensation in the thin parts of the cortex. The thin region has then to absorb the compression of the whole system.

4.1.6.2.2 Dependency on stiffness ratio

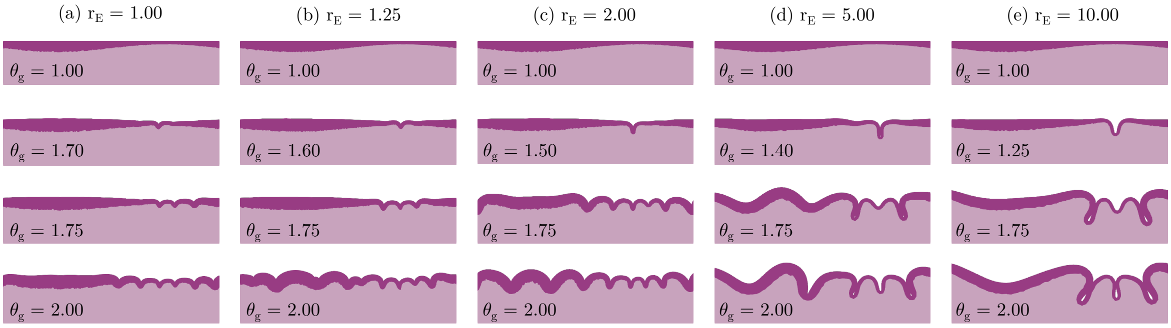

(a) $r_E = 1.00$ (b) $r_E = 1.25$ (c) $r_E = 2.00$ (d) $r_E = 5.00$ (e) $r_E = 10.00$

Figure 4.8: Growth evolution of systems with $T_0 = 0.322$ cm and $A = 0.174$ cm for various choices of stiffness ratio r_E, as indicated within the figure.

As noted in Sec. 4.1.2, the relative stiffness between the white and gray matter regions is not settled. In order to gauge the influences of the Young modulus ratios between the gray and white matter r_E, a series of simulations were performed using the same geometry as used in Fig. 4.7. Namely, they had base thickness $T_0 = 0.322$cm, and inhomogeneity amplitude $A = 0.174$cm. The stiffness ratio was chosen in the range $r_E \in [1, 10]$, with results show in Fig. 4.8. Across all analysed stiffness ratios r_E the system behaves similarly to the system show in Fig. 4.7, with a leading sulcus forming during early during the simulation, followed by several surrounding sulci at later steps.

The influences of the Young modulus ratio on the shape of the simulated cortices are two-folded. First, higher cortical stiffness works as an stabilizer to the the deep sulci forming around the region of least thickness, with stiffer cortices showing deeper sulci. Second, by stiffer cortices, fold at an earlier stage.

4.1.6.2.3 Linear stability analyses

The simulations are in qualitative agreement with the results from linear stability analysis. The details how this theory is applied to our model are outlined in 4.1.9. In short, the lowest-energy mode of a bilayer system is calculated, where we introduce a thin plate as the top region and an elastic substrate underneath. The upper plate has a sinusoidally varying bending rigidity

$$\kappa(x) = \kappa_0 + \kappa_1 \sin\left(\frac{2\pi}{L}x\right),$$

where L is the periodicity length. The system is then subject to a spatially constant compressive surface tension γ. The bending rigidity plays a similar role in this model as the thickness plays in the simulations, and the surface tension plays a similar role to growth.

According to the analytical model, homogeneous systems (i.e., $\kappa_1 = 0$) will fold into a single, well-defined wavenumber, as expected (see Fig. 4.9 (a)) [184]. However, as the bending rigidity ratio κ_1/κ_0 is increased, the folding gets more localized around the bending rigidity minimum. This phenomenon is qualitatively consistent with what was observed in the simulations. For the case with $\kappa_1/\kappa_0 = 0.9$, for instance, the linear stability analysis predicts the formation of a deep sulcus surrounding the bending rigidity minimum, similarly to the finite-element simulations (see Fig. 4.7 (b)). The analytical model predicts that as the cortical plate gets more compressed, the system develops secondary sulci, as can be noticed in region $x/L \approx 0.25$ in the system with $\gamma = -1000\kappa_0/L$ (see Fig. 4.9 (b))

4.1.6.2.4 Comparison with histological sections

It is possible to compare the structures obtained to histological sections of the human brain, as shown in Fig. 4.10. The results from our simulations present a striking similarity to some regions of the human cortex, showing a wide range of sulcal

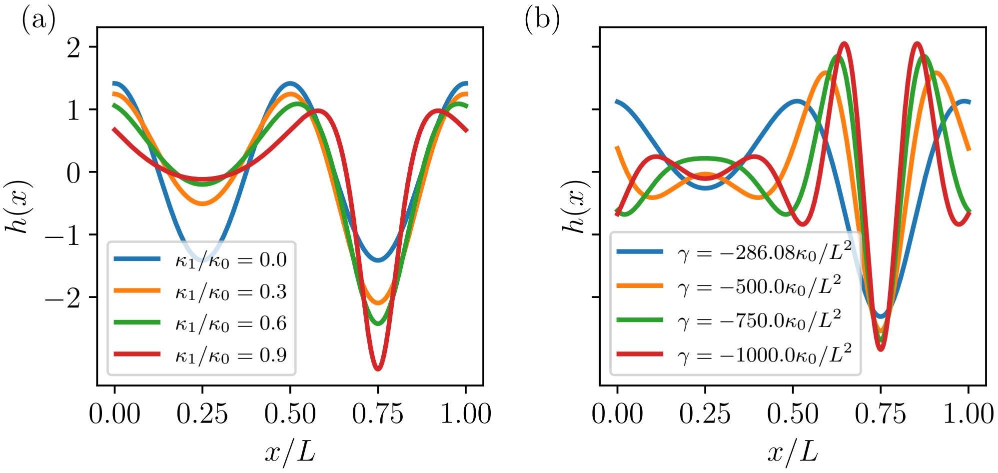

Figure 4.9: (Color online) Analytical prediction of vertical displacements η. (a) Varying bending rigidity ratios at buckling point. (b) Varying values of surface tension γ, while the bending rigidity ratio is kept constant as $\kappa_1/\kappa_0 = 0.5$. For $\gamma > -286.08\kappa_0/L$, no buckling is predicted. Note the appearance of higher order folding for $\gamma < -1000\kappa/L^2$. In both cases, the effective Young Modulus used was $\hat{E} = 2000\kappa_0/L^3$. As the curves are normalized, the predicted displacements can only be compared within the same curve, but not between curves calculated with distinct parameters.

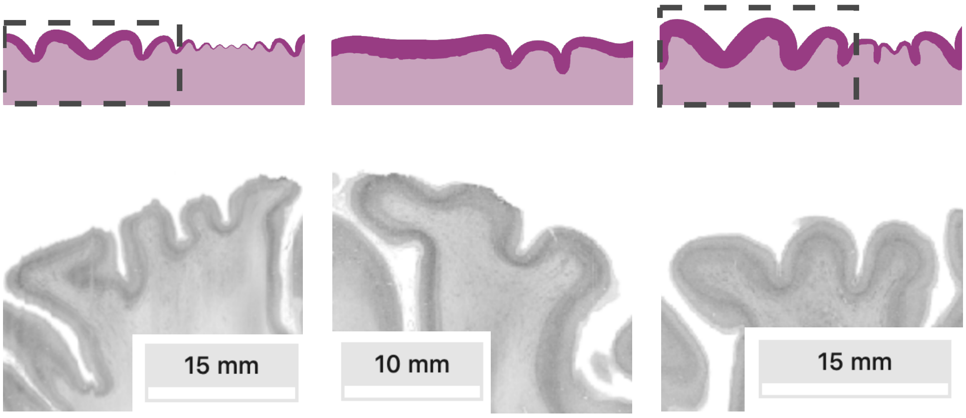

Figure 4.10: Illustrative comparison between simulation results (top) and sections of the cortex (bottom; adapted from HBP BigBrain [185]). Dashed boxes indicate regions of interest. From left to right, the simulations are performed with $T_0 = 0.189$ cm , $A = 0.102$ cm ($\delta = 0.45$); $T_0 = 0.500$ cm, $A = 0.180$ cm ($\delta = 0.40$); $T_0 = 0.367$ cm, $A = 0.198$ cm ($\delta = 0.66$). In the same order, extracts of the left superior parietal lobule (sagittal plane, $\delta = 0.36$), the right postcentral gyrus (coronal, $\delta = 0.54$), and the right posterior middle temporal gyrus (coronal, $\delta = 0.61$) are shown. Due to the arbitrary choice in the value of L_t, the thicknesses between the simulation and the histological section are not quantitatively comparable.

depths and widths, in qualitative agreement with the ones observed in regions with higher-order folding. For instance, the superior parietal lobe presents a plethora of small, shallow folds, similar to those observed in the simulations with thin cortices. Regions presenting a more complex folding pattern, such as the postcentral gyrus, or the posterior middle temporal gyrus are reproduced by simulations with thicker cortices. Furthermore, the gyral height-to-width ratio resulting from the simulations are similar to those observed in the histological sections. Obviously, these similarities in structure can also stem from very different causes, and only more detailed modeling accompanied with experimental data will be able to identify true causality.

4.1.6.2.5 Onset of buckling

Next, we turn our attention to the onset of buckling, i.e. the critical amount of growth θ_g^C above which the system starts to fold, broadly indicating when the constant-length regime ceases, and the constant-thickness starts. The critical growth θ_g^C is defined somewhat arbitrarily as the growth where the averaged squared curvature

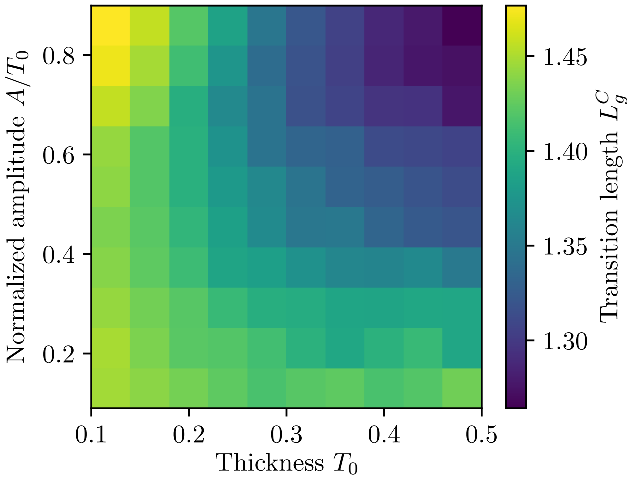

Figure 4.11: (Color online) Critical growth θ_g^C for the emergence of folding for various combinations of cortical thickness and inhomogeneity amplitudes.

of the system reaches 2cm^{-2}. The results do not change considerably for choices of critical curvature square $\langle C^2 \rangle$ in the range [1, 3]cm^{-2}. The transition points are shown in Fig. 4.11, where it is possible to observe that the critical growth θ_g^C is strongly affected by interplay between the inhomogeneity amplitude and the base thickness of the cortical plate, with a noted decrease in the value of θ_g^C as the inhomogeneity amplitude A increases. In light of these results and of the differences between the folding of thin and thick systems (see Fig. 4.6), we conjecture that the relevant parameter to cortical convolution is not solely the ratio between the maximal and minimal thickness, but that the local gradient of the cortical thickness also plays a fundamental role.

4.1.7 Conclusion

We have analyzed the effects of the cortical inhomogeneity in the formation of brain folds. To this end, two closely related systems were studied. First, analyses was carried out by simulating a rectangular bilayer slab where the neocortex grows tangentially. It was observed that the folding pattern follows well-defined wavelengths, which depended on the thickness of neocortex, consistent with previous work [156, 157, 182, 186]. According to Bok's principle, the thickness differences between the sulci and gyri are created as a consequence of the curvature of the brain. During gyrogenesis, the high curvature in the sulci spreads the cortical mantle, decreasing its thickness. The gyral crowns are not affected as strongly due to their relatively small curvature [187]. Our simulations are consistent with this principle, showing that an initially homogeneous cortex can develop cortical inhomogeneities through buckling, coherent with prior observations on homogeneous systems [157, 188–190].

Second, the effects of wavelength competition were studied through the introduction of inhomogeneities in the cortical thickness. In these systems, phenomena closely related to the mammalian gyrogenesis, such as the emergence of hierarchical folding in systems with thick cortices, were observed. Indeed, the results shown here indicate that inhomogeneities in the cortical thickness might play an important role in the localization and formation of hierarchical folding patterns of the brain. Specifically, it was shown that these inhomogeneities are sufficient to break the simple wave-like patterns observed in the homogeneous system. Further, our observations indicate that thickness inhomogeneity leads to earlier folding compared to systems with homogeneous cortical thickness. When comparing simulations with similar minimal-to-maximal thickness ratios, those with small (when compared with the inhomogeneity wavelength) base thickness folded in simple wavy patterns, similar to those in the homogenous cortex, while those with large base thickness folded into more realistic patterns. Taken together, these results indicate that large gradients in cortical thickness are necessary to create the complex structures found in the mammalian brain. Lastly, the results obtained *in silico* are consistent with those obtained from analytical models derived from thin plate theory.

Similar approaches have been taken in other studies, where other cortical inhomogeneities such as stiffness and growth, were studied both in circular [157] and rectangular [82] geometries. These studies found effects similar to those outlined above. Namely, these other kinds of inhomogeneity also led to the departure from wave-like conformations, and to the earlier onset of folding. However, inhomogeneities in cortical thickness lead to more complex configurations, a wider variety in the gyral shapes, and many more sulci per inhomogeneity period, despite the equally large inhomogeneity gradients in these works. The reason for this difference can be readily understood in energetical terms, as the potential energy in Eq. 4.6 depends linearly on the Young modulus, and arguably on the growth, while presenting a cubic dependency on the thickness. Therefore, cortical thickness gradients are amplified when compared to other types of inhomogeneity.

Besides inhomogeneities along the cortex, other mechanisms have been proposed as a driver for higher order folding. For instance, [79] has proposed a sequence of bucklings as a candidate to explain such phenomenon. These other mechanisms are not incompatible with the one presented here. Indeed, it seems likely that several are at play in the real cortex.

The computational model used to explain the hierarchical folding patterns of the mammalian brain is very general, utilizing only the fundamental elastic nature of brain tissue. The absolute values of the elastic moduli play no role, with only their ratios being important. This model is agnostic to all sorts of structural properties of the brain, such as its volume, eccentricity, functional connectivity, etc. The results derived here are applicable to the brains of other mammalians, after a suitable scaling of the thickness, growth, and periodicity lengths.

While the comparisons presented here focus mostly on smaller regions of the human brain, larger simulations are required to gauge the influence of thickness inhomogeneity on the full brain. We conjecture that the application of a biologically derived thickness field can lead to the formation of the deep sulci obtained in the mature human brain.

Based on our current results, the mutual influence of the different kinds of inhomogeneity (e.g., thickness and growth) can also be studied. The simulations in this work were performed in a flat domain. However, the curvature intrinsic to the mammalian brain has been shown to affect folding [157, 179]. Thus, models on which the effects of curvature and each type of inhomogeneity are studied together are necessary to provide predictions which can be tested against histological sections of developing mammalian brains.

We have shown the consequences of cortical thickness inhomogeneities to brain folding. What drives the development of these inhomogeneities is still a matter of ongoing research. Features of a given brain area, such as its cortical thickness are related to its function [191].

Evidence suggests that the generation of the cortical thickness in these regions are dictated by a genetic map, which induce a large abundance of progenitor cells in some regions, and a depletion in others [192]. Such differences in growth have been shown to create thicknesses inhomogeneities in the cortex [157]. Biomolecular and mechanical factors contribute to this stereotypy [153, 193], and, based on our current approach, could additionally be included in future models of brain folding.

Experimental results have shown that axons grown in response to stress [194–196]. In contrast with the growth model utilized in the current work, a model taking into account stress-dependent growth would effectively induce viscoelastic characteristics onto the white matter [197]. Indeed, it has been shown that viscoelastic properties can affect the buckling wavelength of bilayered systems [148, 155]. Thus, it would be interesting to further refine the current model with the viscoelastic characteristics of growing tissues in general [197], and of the brain in particular [198].

Finally, structural connectivity, i.e., axons within the white-matter fiber tracts, have been conjectured to be one of the drivers of folding [166]. How they would influence the conformations found in this work could be investigated further to understand the mutual influence of differential growth and axonal tension in gyrogenesis.

This paper's focus was the developing brain, but in virtue of generality of the model used, its results are extensible to other fields. For instance, it has been shown that microscopic corrugated surfaces give rise to hyperhydrophobic surfaces, in the so called Lotus effect [199, 200]. Our results can provide further insight into the self assembly of these corrugations, and in the control of their properties.

Soft layered systems can be realized experimentally by gel slabs coated with gels with different properties [150, 201]. These systems have been used as simulacra for brain folding [165, 188], where they were able to mimic the folding of a 3D-printed human brain. Thus, the production of samples with sinusoidal variation of the top-layer thickness would allow for the experimental testing of our predictions. Further, we hypothesise that it would be possible to use these systems to distinguish between the various types of inhomogeneity. For instance, by controlling the cross-linker density in different regions of the sample, it is possible to control the stiffness of gel, making stiffness inhomogeneities experimentally accessible. Similarly, it would be possible to control the hydration of the regions, mimicking inhomogeneous in growth. Brain organoids have been used as biological toy models for several aspects of brain development [202, 203], with folding having been recently achieved in such small systems [204]. These systems can thus be used in controlled studies to provide strong evidence of the drivers of brain folding.

4.1.8 Acknowledgments

The authors gratefully acknowledge the computing time granted by the JARA-HPC Vergabegremium on the supercomputer JURECA [205] at Forschungszentrum Jülich. Simulations were additionally performed with computing resources granted by RWTH Aachen University under project rwth0399. We would like to thank Dr. Claude J. Bajada for helpful discussions and feedback. This work was further supported by a grant from the Initiative and Networking Fund of the Helmholtz Association (SC) as well as the European Unions's Horizon 2020 Research and Innovation Program under Grant Agreement 785907 (Human Brain Project SGA2; SC). LCC also acknowledges the support by the International Helmholtz Research School of Biophysics and Soft Matter (IHRS BioSoft).

4.1.9 Appendix: Simplified analytical model

In order to understand the buckling of the system, we use a simplified model which can be solved analytically. Here, a thin plate with a spatially varying bending rigidity is studied. This plate is attached to a linear elastic substrate, filling the whole of the half-space $y < 0$. In the limit of small deflections and disregarding shearing, it is possible to write the displacement of the system in the Monge representation as

$$\mathbf{u}(x,0) = (0, h(x)).$$

Here, $h(x)$ indicates the local height of the plate along the x axis. The free energy of this system is composed of three terms:

$$F = F_{bend} + F_{stretch} + F_{subs}, \tag{4.6}$$

where F_{bend} is the free energy of bending the thin plate, $F_{stretch}$ is the energy required in order to stretch the plate and F_{subs} is the energy of the deformed underlying substrate. Explicitly,

$$F_{bend} = \int_0^L \kappa(x) \left(\nabla^2 h(x)\right)^2 dx$$

$$F_{stretch} = \int_0^L |\nabla h(x)|^2 \gamma dx$$

$$F_{subs} = \frac{1}{2} \int_0^\infty \int_0^L \sum_{ij} \sigma_{ij} u_{ij} dx dy$$

where $\kappa(x)$ describes the space-dependent bending rigidity, γ is the surface tension on the superficial plate, σ_{ij} are the components of the Cauchy stress tensor, and u_{ij} are the components of the strain tensor $u_{ij} = \frac{1}{2}\left(\frac{\partial u_i}{\partial x_j} + \frac{\partial u_j}{\partial x_i}\right)$. In order to keep the simplicity of the model the bending rigidity of the plate, rather than its thickness, varies sinusoidally. That is,

$$\kappa(x) = \kappa_0 + \kappa_1 \sin\left(\frac{2\pi}{L}x\right) = \kappa_0 + \kappa_1 \sin(k^* x),$$

where k^* is the characteristic wavenumber of the inhomogeneity. Due to the periodic nature of our system, the stability analysis is easier to carry out in Fourier space. Thus, the height function $h(x)$ is expanded into

$$h(x) = \frac{1}{L} \sum_k h_k \exp(ixk), k \in \frac{2\pi}{L}\mathbb{Z}$$

$$h_k = r_k \exp(i\phi_k)$$

with $\phi_k = \phi_{-k}$. In this decomposition, whole-plate dislocation(i.e., $h_0 = 0$) were disregarded.

To obtain the energy of the elastic substrate in the Fourier space, one has to solve the problem of a linear elastic substrate with given surface deformation in Fourier space, as derived in Ref. [182]. With this solution, the free energy described in Eq. 4.6 is written as

$$F = \sum_k \frac{1}{2}(\hat{E}|k| + \gamma k^2 + \kappa_0 k^4) r_k^2 + \frac{\kappa_1}{2} k^2 (k + k^*)^2 r_k r_{k+k^*} \sin(\phi_k - \phi_{k+k^*}) \tag{4.7}$$

with

$$\hat{E} = E\frac{2(\nu - 1)}{(\nu + 1)(4\nu - 3)}. \tag{4.8}$$

We search for the buckling modes that are most unstable. That is, those with wavenumber k which minimize the energy in Eq. 4.7. Due to the bound properties of the sinus, it is clear that the condition $\phi_k - \phi_{k+k^*} = 3/2\pi + 2\pi n$ is necessary to obtain this minimum. Thus, the energy is written as

$$F = \sum_k \frac{1}{2}(\hat{E}|k| + \gamma k^2 + \kappa_0 k^4) r_k^2 - \frac{\kappa_1}{2} k^2 (k + k^*)^2 r_k r_{k+k^*} \tag{4.9}$$

Unstable modes can then be obtained by standard stability analyses. Eq. 4.9 is recast into its matricial form

$$F = \frac{1}{2}\mathbf{r}^T \mathbf{H}\mathbf{r},$$

where $\mathbf{r}$ is a vector with components $\mathbf{r} = r_k$, and $\mathbf{H}$ is the Hessian matrix. Explicitly,

$$H_{ij} = 4g(k_i)\delta_{k_i,k_j} - 2f(k_i)\delta_{k_j,k_i+k^*} - 2f(-k_i)(\delta_{k_j,k^*-k_i} - \delta_{k_j,k_i-k^*}) \tag{4.10}$$

with

$$\begin{aligned} g(k) &= \frac{1}{2}(\hat{E}|k| + \gamma k^2 + \kappa_0 k^4), \\ f(k) &= \frac{\kappa_1}{2} k^2 (k + k^*)^2. \end{aligned}$$

In this form, the unstable modes are obtained as those states with negative eigenvalues for the Hessian matrix, corresponding to modes with negative energy. For homogeneous systems (i.e., $\kappa_1 = 0$), the energy contribution of each mode is independent (i.e., the Hessian matrix is diagonal), and modes that minimize the energy can be obtained analytically [184, 206], with same resulting prefactor as in Eq. 4.5. In the inhomogeneous case, the various wavemodes are coupled, and it is necessary to solve the eigenproblem numerically. Fig. 4.9 shows the results of these calculations. Each curve corresponds to the eigenfunctions with lowest eigenvalues for different elastic parameters, as indicated therein.

This analytical theory gives results which are qualitatively similar to those obtained in our simulations. In order to obtain quantitative comparisons, a more complex theory is necessary, which takes into account the lateral displacements during gyrification.

4.1.10 Supplementary material

Supplementary figures are available in Appendix E as Figs. E.1 and E.2.

4.2 Further remarks

In this section we show some further results obtained in this system that are not presented in the paper as published in NeuroImage.

4.2.1 Pressure of folding

After buckling, the cortical thickness of the slab is no longer uniform. This folding imparts a residual stress in the system. The homogeneous pressure $p = \mathrm{tr}(\sigma)$ of the system shows that while the whole of the cortical plate is under compression, it is clear that the sulcal regions are under a higher compression than the gyri (see Fig. 4.12).

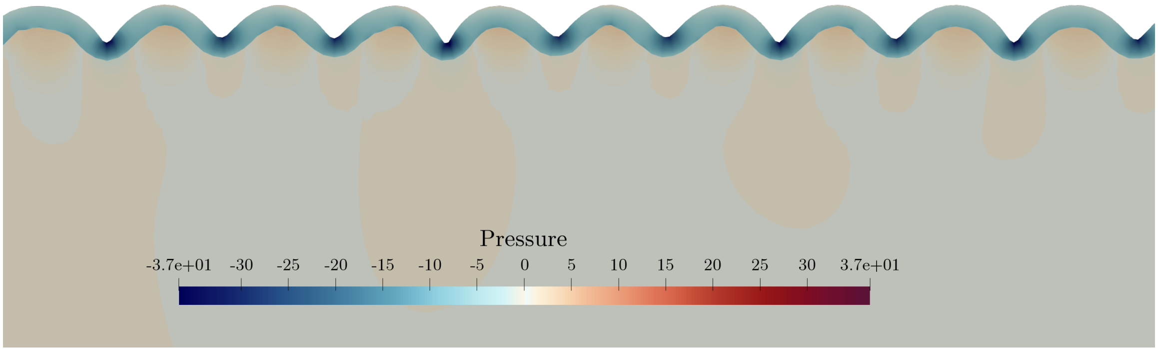

Figure 4.12: Snapshot of the simulation indicating the local pressure (see colorbar) during folding. Note the strong compressile stress in center of the sulci. Simulation with $T = 0.50$ and $\theta = 1.55$.

4.2.2 Onset of folding

In systems with short wavelength (i.e., those with thin cortices), the local folding style does not change considerably inhomogeneities are introduced (see Fig. 4.13 (a)). They are distinguished, however, in that each part of the initially flat system starts to fold at a distinct growth parameter θ_g, with the regions of thinner cortex folding at a earlier step than those with thicker cortices (see kymographs in Fig. 4.13 (b)). This effects becomes more noticeable as the thickness and inhomogeneity amplitude increases, (compare Fig. 4.13 (a, b) with (c, d)).

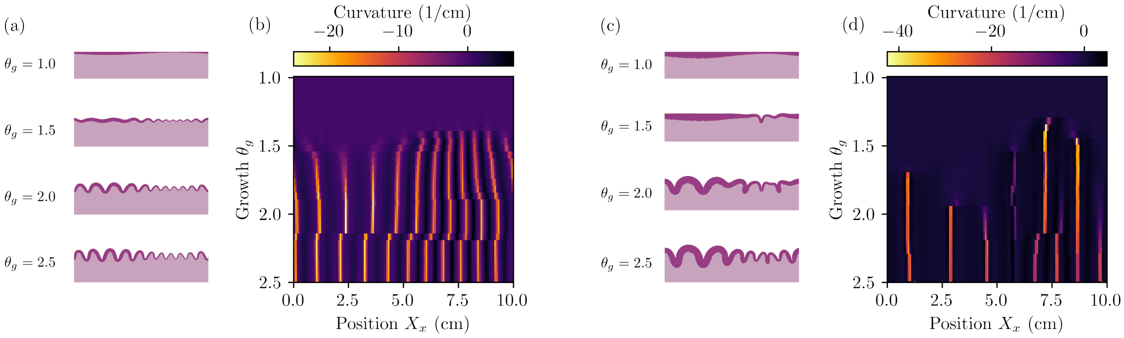

Figure 4.13: Evolution and curvature kymograph of inhomogeneous systems with (a, b) base thickness $T_0 = 0.144$ cm and inhomogeneity amplitude $A = 0.091$ cm, and (c, d) $T_0 = 0.50$ cm, $A = 0.315$ cm.

4.2.3 Reproducibility of folding

Different realizations of the simulations with the same parameters have the same behaviors during the first steps of buckling, but soon diverges once secondary folding starts (see Fig. 4.14). This is consistent with the biology of folding, where the first order folding is robust when compared between different individuals, but the higher order folding is highly individual-specific, and indicate that the energy landscape of the system is complex and highly degenerate.

Figure 4.14: Snapshots of three different realizations of systems with the same parameters, $T_0 = 0.278\text{cm}$, $A = 0.200\text{cm}$, and $\theta_g = 2.5$, and distinct random number generator seeds.

Chapter 5

Dynamical simulations

In this chapter, dynamical effects are studied. The chapter is divided in three parts. First, the consistency between the energy minimization and the slow growth regimes is demonstrated, and further effects of growth rates on the folding of the homogeneous cortex are studied. Second, inhomogeneities are analysed in this new regime. Thickness inhomogeneities are revisited, and inhomogeneities in growth rates are introduced. These are studied first in isolation, and then the effects of their interplay is analysed. Thirdly, the thin plate theory used in Sec. 4.1.9 is extended to handle multiple types of concurrent inhomogeneities, and the results obtained in the previous part are discussed in light of this theory.

5.1 Dynamical effects

In order to use the available computer time efficiently, simulations are initially performed for a single initial thickness, while the growth rate is varied carefully. Later, both the thickness and the growth rate are varied, exploring a wide, even if coarse, phase space.

The studies in Ch. 4 were done using energy minimization simulations, an approach which is often found in the literature [41, 77, 79, 188] and presupposes that the energy minimization approximation retrieves the same configurations as a system with infinitely slow growth. While relatively intuitive, there are possibly important sources of differences between the dynamical and energy minimization approaches. Most notably, minimization algorithms pay little respect to the physics of the underlying problem. They may skip energy barriers, and could lead into the global energy minimum even if it cannot be reached by the real dynamic system (see Appendix C)[1]. Another important factor is that the growth speed itself impacts folding [184].

We use the forced growth approach introduced in Eq. 4.1.5, but, in contrast with the last chapter, the value of the growth constant g is consequential, introducing the timescale of growth $\tau_g = 1/g$. The concepts of "fast" and "slow" growth are, of course, relative. In order to anchor these concepts, we compare the timescale of growth τ_g to the timescale of amplification, i.e., the time it takes for a wavemode amplitude to increase by a factor of $e \approx 2.71$. We report the results as a function of the ratio between the time scales as τ_g/τ_a, with higher values of this ratio indicating slower growth. Following Ref. [184], we obtain the timescale of amplification as

$$\tau_a = \frac{4\kappa\mu T}{\gamma^2}, \tag{5.1}$$

where κ is the bending rigidity, μ is the friction coefficient, T is the cortical thickness, and γ is the surface tension. In the linear regime, the surface tension at buckling is given by

$$\gamma_C = -3\left(\frac{\kappa\hat{E}^2}{4}\right)^{1/3}, \tag{5.2}$$

with $\hat{E}$ being the effective Young modulus, as defined in Eq. 4.8. Both the amplification timescale τ_a and the surface tension γ_C depend on the Young modulus E of the simulated material. For the brain, determining the correct value of this quantity is difficult. Rheological experiments are typically in the order of second or minutes, while brain development happens in the span of weeks and months. However, as the long-term the Young modulus is not well characterized we use the short-time Young modulus instead, which while not perfect, will be sufficient to provide a comparison timescale. Introducing the relevant physical constants in Eqs. 5.1 and 5.2 results in the following ratio for the simulations

$$\frac{\tau_g}{\tau_a} = \frac{23.31}{gT}. \tag{5.3}$$

---

[1] In the brain such a situation might arise if the cortical thickness changes after folding as it happens, for instance, during aging. The dynamical system would not necessarily change its characteristic wavelength, while a energy minimization system could present large jumps in wavelength.

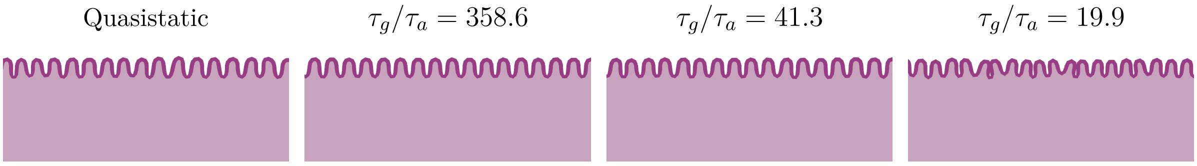

Figure 5.1: Snapshots of systems with different growth rates at normalized time $gt = 5$, with growth parameter $\theta = 2.5$.

We initially fix the thickness of the system at $T_0 = 0.5$ cm, and carefully vary the growth rate g between simulations in the range $g \in [10^{-3}, 0.336]$, introducing growth time scales in the range $\tau_g \in [2.98, 10^3]$. The system is grown until the growth parameter θ_g equals 2.5. As it is possible that the system is not fully relaxed once this point is reached, the system is then allowed to relax for an equivalent amount of time.

The resulting snapshots of few representative simulations after relaxation are shown in Fig. 5.1, where it can be seen that the folding profile of the dynamical systems are qualitatively similar to those obtained in Sec. 4.1.6.1, with a simple wave throughout the cortex. The evolution of these systems happens in three steps. Similarly to the results obtained in Chapter. 4, the system is initially compressed, keeping its mostly flat configuration. Once the surface tension is large enough, the system buckles and folds. Finally, the system undergoes a relaxation step.

This evolution can be seen in detail in Fig. 5.2. During the first step, the cortical length is mostly constant (see Fig. 5.2 (a)) while the thickness goes through a large overshoot until right before folding (Figs. 5.2 (b), (c), and (d)). Until buckling, the folding wavenumber k_F (as defined in Eq. 4.4) is stationary at zero, indicating no significant folding occurs until a certain growth threshold is reached. Once the system buckles, a particularly precipitous drop in thickness is observed, which, after some oscillation, reaches a stable growth pattern. Complementarity to the drop in cortical thickness, there is steep increase in the cortical length. It is also worth of notice that folding happens at later normalized times for increasing values of growth rate g.

The second part of this process in particular is very consequential to the folding landscape predicted. As such, the folding wavenumber during this step is shown in further detail in Fig. 5.2 (f), where it is worth to notice that on one hand slowly growing systems (including the energy minimization system) fold into the analytically predicted wavenumber before higher order effects become relevant and force an increase in wavenumber, leading to a departure from the analytically predicted value. On the

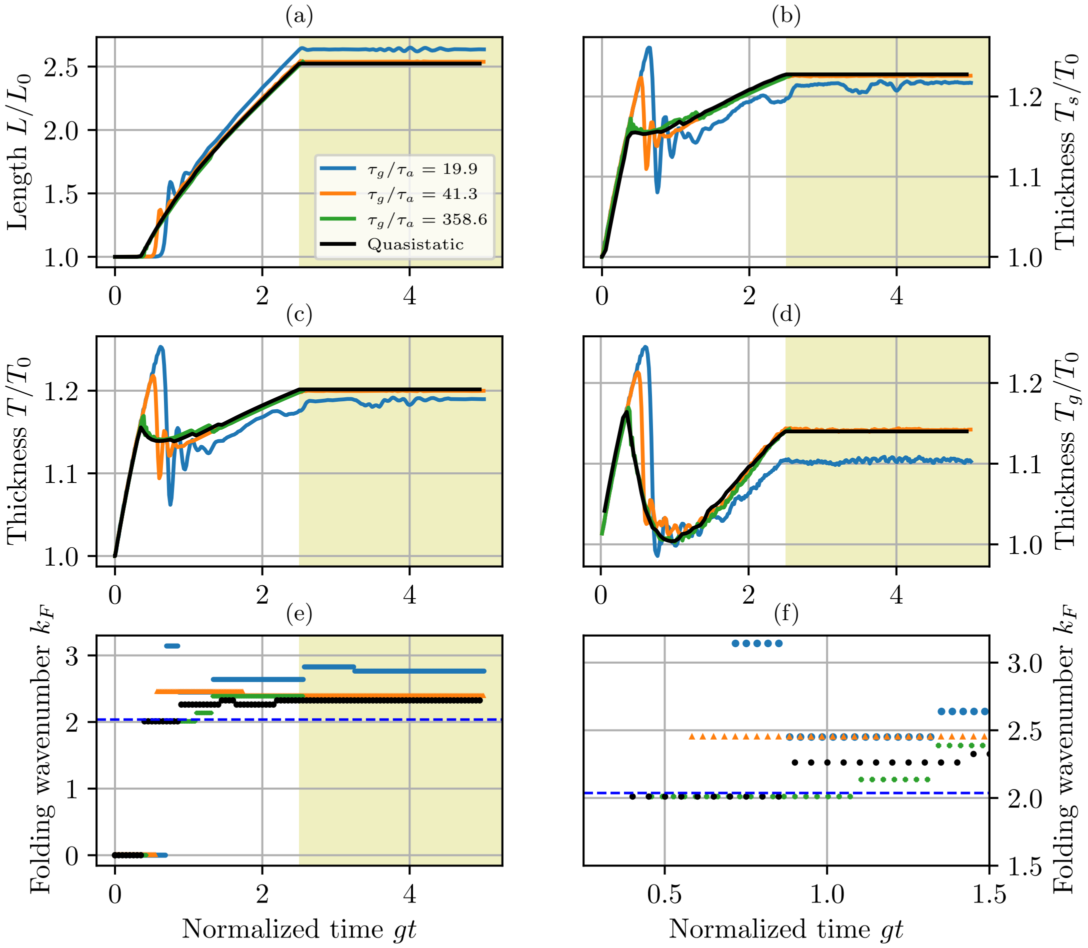

Figure 5.2: Evolution of geometrical quantities for a system with cortical thickness $T = 0.5$ cm, and growth rates g as color coded. Black lines indicate the results from energy minimization simulations. Growth was halted at $gt = 2.5$, and the system was then allowed to relax for the same time, as indicated by the shaded area. (a) Normalized cortical length L, (b) normalized sulcal thickness T_s, (c) normalized average thickness T, (d) normalized gyral thickness T_g, (e) folding wavelength k_F over the whole simulation period, (f) folding wavelength k_F around the folding step. L_0 and T indicate the initial length and average cortical thickness. The blue broken line in (e) and (f) indicates the analytically predicted value for the folding wavenumber.

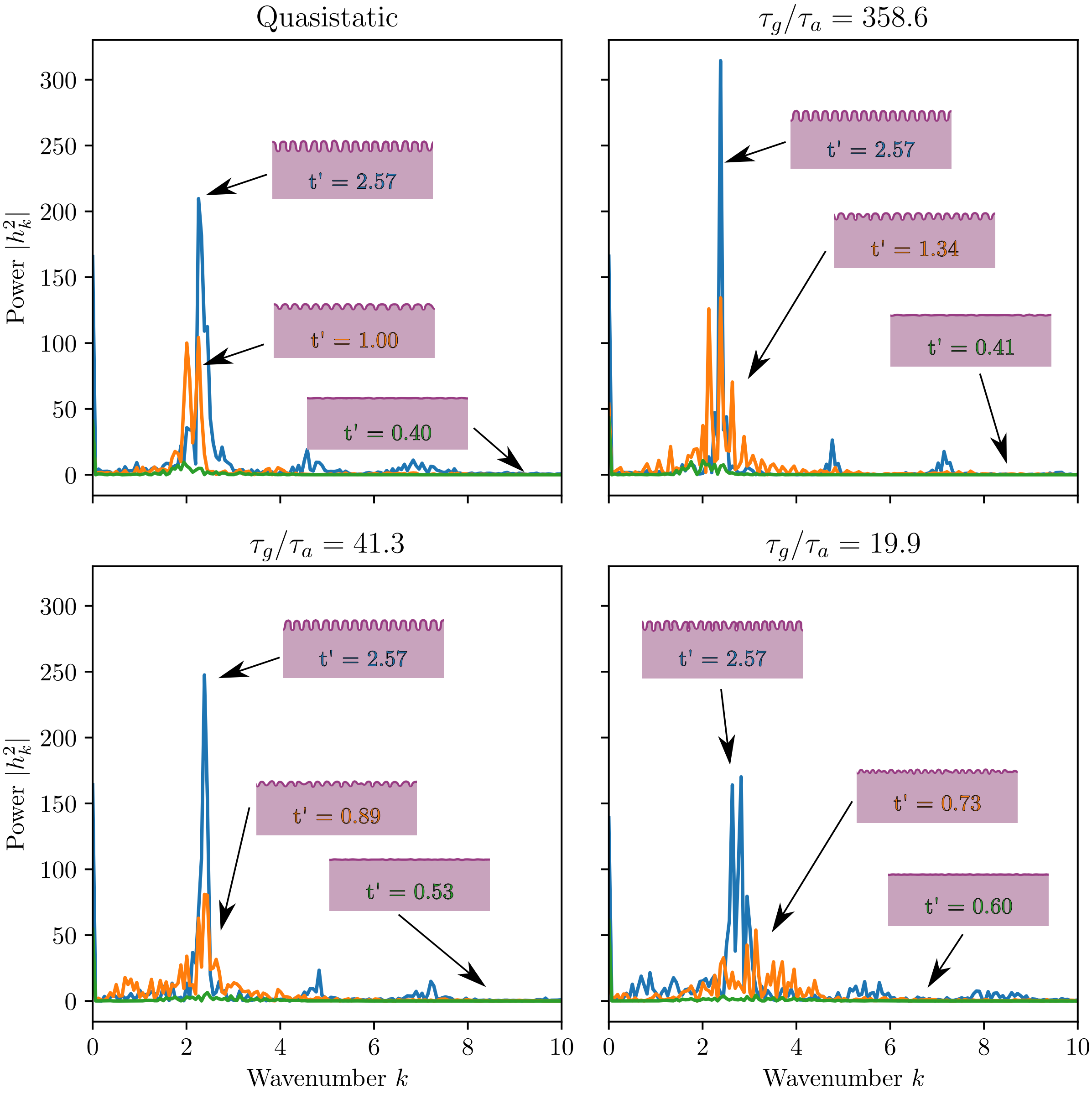

Figure 5.3: Power spectrum of system at various steps during growth. Green, orange, and blue lines indicate the spectra at the onset of folding, at the point of highest average wavenumber, and before the relaxation period, respectively. Snapshots of systems associated with the spectra are also shown.

other hand, fast growing systems fold into a higher wavenumber than predicted, which decreases towards the predicted value during relaxation. However, while the folding wavenumber decreases slightly, it is often the case that the system is locked into a metastable state corresponding to a high wavenumber.

Besides the noted differences in the folding wavenumbers, we also observe that faster growing systems present a broader (but shallower) folding spectrum than slower growing systems (see Fig. 5.3). At the onset of folding, it is possible to observe a broad power distribution around a non-zero wavenumber. However, most of the power is concentrated near zero, indicating a whole-plate dislocation as it is compressed by growth. When the system reaches its highest average wavenumber, a large number of wavenumbers are activated, with fast growing systems presenting more spread out spectra. This phenomenon is clearly seen when comparing the results for growth rate $\tau_g/\tau_a = 358.6$, which fold largely in a single wavenumber, with localized exceptions where period doubling is present, and those with growth rate $\tau_g/\tau_a = 19.9$, which exhibits several contemporaneous waves, leading to its broad power spectrum. As the system relaxes, the amplitude of most wavenumbers decays, and is absorbed into the amplitude of a few other waves. By the end of the simulation, the power is mostly concentrated in a narrow band around a single wavenumber, with much smaller peaks surrounding other wavenumbers corresponding to the higher harmonics of the main peak.

So far, the analyses were restricted to those systems with a relatively large thickness, $T_0 = 0.5$ cm. When the phase space is extended to also probe variations in cortical thickness in the range $T_0 \in [0.1, 0.5]$ cm, we observe that the simulations behaved largely the same, independently of the cortical thickness studied. Changes in thickness generate two interconnected effects. Firstly, the overestimation in the folding wavenumber k_F increases for systems with thicker cortex. Secondly, due to the overestimation, the time necessary so that the system relaxes also increases (see Fig. 5.4).

Taken together, the results in the current section show that the system studied in Chapter 4 took a physically sound path through configuration space. Further, they showed that the effect of growth rate becomes more noticeable as both the thickness and the growth rate increase. This can be understood in light of the linear stability theory developed in Ref. [144] and reproduced in as Sec. 4.1.9, where surface ten-

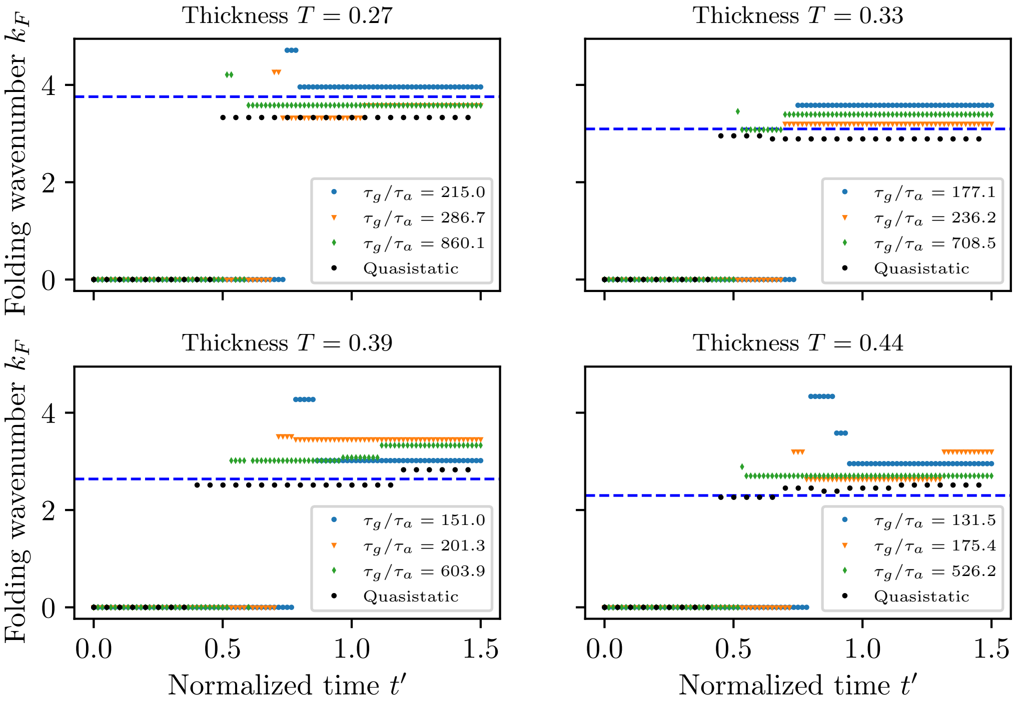

Figure 5.4: Evolution of folding wavenumber k_F as the systems grows, organized by base thickness T. Broken lines indicate the analytically predicited wavenumber.

sion plays an important role in the determination of which wavelengths are generally favorable. When the timescale of growth τ_g is comparable with the time scale of amplification τ_{ampl}, the surface tension is not able to relax fast enough, and tends to accumulate. This leads to an increase in the stretch energy, making several wavemodes energetically permissible at the same time, yielding the broad spectra seen in Fig. 5.1, and corresponding overshoot in wavenumber. As the surface tension is calculated over the whole cortex, it is natural that thicker system also have larger surface tension, magnifying the growth rate effects.

5.2 Inhomogeneities in the dynamical regime

As shown in Sec. 1.3.3, neither the cortical thickness, nor its growth rate are homogeneous throughout the mammalian cortex [193]. In the current section we revisit the growing cortex with inhomogeneous thickness, investigate the effects of inhomogeneous growth in an otherwise homogeneous cortex, and finally study the interplay between the two types of inhomogeneity on folding.

The results in the last section revealed that dynamical effects are impactful in the formation of folds, and that the magnitude of these effects increase with both growth rate and cortical thickness.

Keeping in mind that inhomogeneities in the brain may be one of the mechanisms by which some stereotypical folding patterns such as higher-order folding, emerge, it is necessary to investigate the influence of the dynamical effects on the inhomogeneous cortex.

5.2.1 Inhomogeneous thickness revisited

Systems with varying thickness were first introduced in the energy minimization regime in Sec. 4.1.6.2, and are now revisited in the dynamical regime. The cortical thickness of this system is given by

$$T(x) = T_0 + A_t \sin(2\pi X_x / L_x),$$

where the notation A_t is introduced to distinguish between inhomogeneity in thickness and in inhomogeneity in growth, which is introduced in Sec. 5.2.2. Fig. 5.5 shows the development of inhomogeneous systems with various growth rates. The folding trajectory of the cortex is largely similar to that obtained in the energy minimization regime, with folding being initiated in the thin regions of the cortex, and concentrated therein. While the energy minimization and slow growth simulations present a similar phenomenology, some differences are noticeable between the two, most notably, the region around the thickest cortex presents a flatter profile in the energy minimization regime than in the slow growth one. As the growth rate g increases, the thicker regions stabilize in a higher wavenumber (compare Fig. 5.5 (b) and (e)), indicating that the spectrum-spreading effects shown in Sec. 5.1 are compounded with those created by the inhomogeneity.

As mentioned in Sec. 4.2.3, after buckling the energy landscape of inhomogeneous systems becomes highly degenerate [2], presenting several similar but distinct accept-

---

[2] The flat case can be argued to be even more degenerate, as any change in the phase of the solution yields a new valid solution. However it represents a simpler degeneracy – affecting a single wavemode – while the one in the current case depend on the nonlinear interaction between various modes.

able configurations. This can be a challenge simulations using the energy minimization approximation, as small changes might lead to very distinct configurations, often with simulations jumping back and forth betweend various configurations. Dynamical simulations do not have this issue, as they are required to follow a continuous trajectory through phase space.

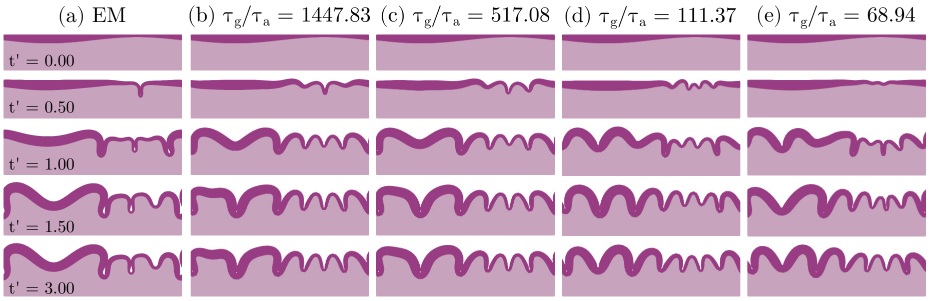

Figure 5.5: Snapshots with evolution of systems with inhomogeneous thickness. All systems have the same geometrical parameters, with base thickness $T_0 = 0.322$ cm, and $A_t = 0.174$ cm.

5.2.2 Inhomogeneous growth

So far, it was supposed that the whole cortex grows at the same rate. This is not the case in the mammalian brain, which follows a protomap of growth [193, 207]. We briefly study the effects of the distinct growth rates along the cortex. In a similar way as was done in Sec. 4.1.6.2, the inhomogeneity profile is sinusoidal, as

$$g(x) = g_0 + A_g \sin(2\pi X_x/L). \tag{5.4}$$

The notation for the normalized amplitudes $A'_g = A_g/g_0$ and $A'_t = A_t/T_0$ are adopted for easier comparison. The evolution of a system with cortical thickness $T = 0.4$ cm is shown in Fig. 5.6. In these thicker systems, the cortical development is similar to that of systems with inhomogeneous thickness. In the slow growth regime, a leading sulcus forms early during development, which is soon followed by further sulci (see Fig. 5.6 (a), (d)). Once the base growth increases, pairs of sulci appear simultaneously, generating a single gyrus instead, opposite to what was observed in system with inhomogeneous thickness.

During the whole simulation, most of the folding is concentrated in the region of high growth, with the region surrounding the slow-growth zone remaining mostly flat (see Fig. 5.6 (c)). In the case of fast growth, this region is slightly bent due to the compression from surrouding regions, but no proper folding occurs (see Fig. 5.6 (d)).

These results show that inhomogeneous growth rates also lead to inhomogeneous folding. However, the folding landscape is less complex than the one generated by inhomogeneous cortical thickness.

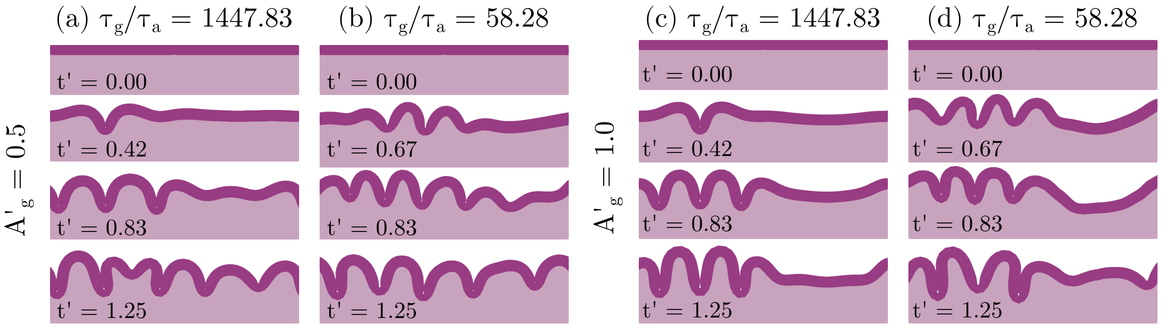

Figure 5.6: Dynamics of systems undergoing inhomogeneous growth with initial cortical thickness $T = 0.4$ cm, and growth parameters as shown within the figure.

5.2.3 Inhomogeneity interplay

In the past two sections, the dynamical effects of cortical thickness and growth inhomogeneities have been shown in isolation. In Sec. 5.2.1 it was shown that folding is concentrated in the thinner regions of the cortex, while in Sec. 5.2.2 folding was concentrated in the regions with more growth, with higher wavenumbers in these regions. We now investigate the case when the two effects compete What happens with the developing cortical plate when the thicker regions of the cortex grows faster than the thinner regions. Growth inhomogeneity is introduced to the system in Sec. 5.2.1, as shown in Fig. 5.7. As shown before, in the absence of growth inhomogeneities, this system has the tendency to initiate folding in its thinnest part. Such an effect is observed even in the presence of moderately strong growth inhomogeneities ($A_g = 0.5$, Fig. 5.7 (b)), where its effects are limited to a small decrease in wavelength on the thicker regions on the left, and a corresponding increase in wavelength on the thinner regions. Indeed, trajectories similar to the inhomogenous growth (see Sec. 5.2.2), with fissuration initiating on the faster growing regions, are only seen in very large growth inhomogeneities ($A_g \approx 1.0$). The folding pattern, however, is noticeably different to those obtained before, due to its open structure.

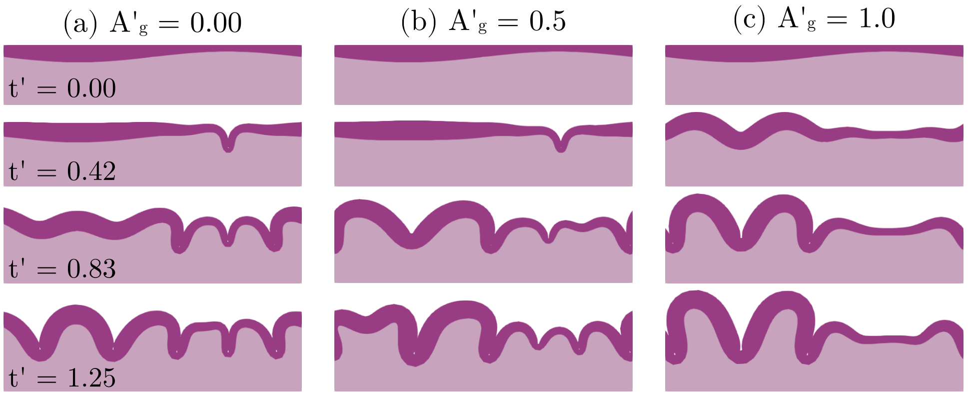

Figure 5.7: Dynamics of systems with base cortical thickness $T_0 = 0.4$ cm, thickness inhomogeneity $A'_t = 0.45$, growth rate $\tau_g/\tau_a = 11.65$, and inhomogeneity parameters as indicated within the figure.

These results indicate that inhomogeneities of cortical thickness have a strong influence on the emerging landscape of folding when compared with growth inhomogeneity, with small differences in cortical thickness leading to large differences in folding landscape. In contrast, differences in cortical growth lead to relatively tame changes in cortical landscape, mostly inhibiting local folding.

The physical reason for this, as hinted in Sec. 4.1.7, is that the thickness has an amplified role on the energy of the system. Firstly, the thickness itself has a cubic-power influence on the energy polynomial $g(k)$ (see Eq. 5.8), through the bending rigidity κ, which, in turn, serves as the prefactor of fourth power component in the energy, leading to further amplification of the role of the cortical thickness. In comparison, the growth rate arguably influences the energy only through the surface tension γ, itself a prefactor of a quadratic term. This idea is further explored in the following section.

5.3 Linear stability theory

5.3.1 Surface tension inhomogeneity

This section offers a similar treatment to growth inhomogeneity as was done to thickness inhomogeneity in Sec. 5.3. We map the problem to an analytically treatable one, in the realm of linear plate theory. We suppose a spatially-dependent surface tension in the form

$$\gamma(x) = \gamma_0 + \gamma_1 \sin(k^* x), \tag{5.5}$$

whose net effect is similar to that in bending rigidity, yielding the following energy

$$F = \sum_{k=1}^{\infty} \frac{1}{2}(\hat{E}|k| + \gamma k^2 + \kappa k^4) r_k^2 - \frac{\gamma_1}{2} k(k+k^*) r_k r_{k+k^*}, \tag{5.6}$$

where the condition $\phi_k - \phi_{k+k^*} = 2(n+1)\pi$ has been applied. The associated Hessian matrix has a similar structure to that in Eq. 4.10, with terms

$$\begin{aligned} H_{ij} = {} & 4g(|k_i|)\delta_{k_i,k_j} - 2f_2(k_i)\delta_{k_j,k_i+k^*} \\ & - 2f_2(-k_i)(\delta_{k_j,k^*-k_i} - \delta_{k_j,k_i-k^*}), \end{aligned} \tag{5.7}$$

with

$$\begin{aligned} g(k) &= \frac{1}{2}(\hat{E}|k| + \gamma k^2 + \kappa_0 k^4), \\ f_2(k) &= \frac{\gamma_1}{2} k(k+k^*). \end{aligned}$$

Now the off-diagonal terms depend on the surface tension. The eigenfunctions associated with the most negative eigenvalues are shown in Fig. 5.8, where it is seen that the folding is localized in the regions of largest surface tension.

5.3.2 Inhomogeneity interplay

In the linear regime, the effects of inhomogeneities in rigidity and surface tension are energetically decoupled. The net contribution of both types of inhomogeneity is concentrated in the off-diagonal components of the Hessian matrix as

$$\begin{aligned} H_{ij} = {} & 4g(|k_i|)\delta_{k_i,k_j} - 2f_3(k_i)\delta_{k_j,k_i+k^*} \\ & - 2f_3(-k_i)(\delta_{k_j,k^*-k_i} - \delta_{k_j,k_i-k^*}), \end{aligned} \tag{5.8}$$

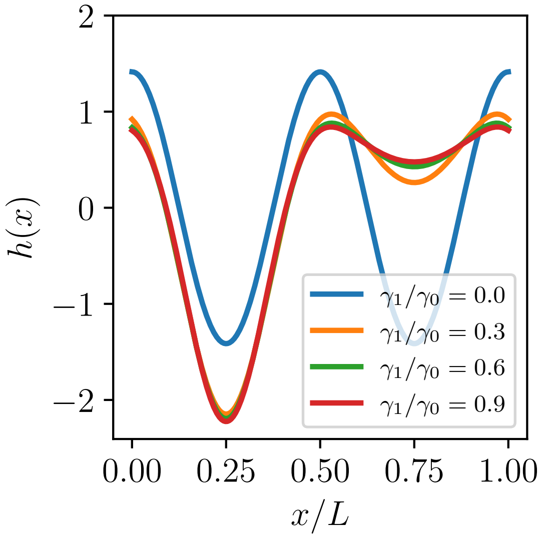

Figure 5.8: Analytical prediction of most unstable modes of a system with inhomogeneous surface tension γ, and effective Young modulus $\hat{E} = 2000\kappa_0/L^3$. For each curve, the value of γ_0 was chosen as the least negative value that leads to a stable mode.

with off-diagonal terms, $f_3(k) = \frac{\kappa_1}{2}k^2(k+k^*)^2 + \frac{\gamma_1}{2}k(k+k^*)$ obtained as the individual off-diagonal terms in Eq. 4.9 and Eq. 5.6.

Due to their opposite signs, it is expected that these two sources of inhomogeneity would have opposite effects. Large values of surface tension lead to higher wavenumbers, and therefore more folding, while higher values of bending rigidity lowers the wavenumber, as a harder cortex is more difficult to bend. Fig. 5.9 shows the most negative solutions of the eigenproblem induced by the expanded Hessian matrix. The region where folding is observed depends on the inhomogeneity used. Inhomogeneities in bending rigidity leads to folding on the right side of the system, where the cortex is softest (see left column of Fig. 5.9), while surface tension inhomogeneities leads to folding on the left side, where the system is most under tension (Fig. 5.9, upper row). In both of the previous cases, the effects seen were mostly due to a single type of inhomogeneity. The interplay between the two is shown in the middle column Fig. 5.9. These show that the energy competition makes the folding pattern flip between the two sides of the system, depending on the relative amplitude between the two inhomogeneities.

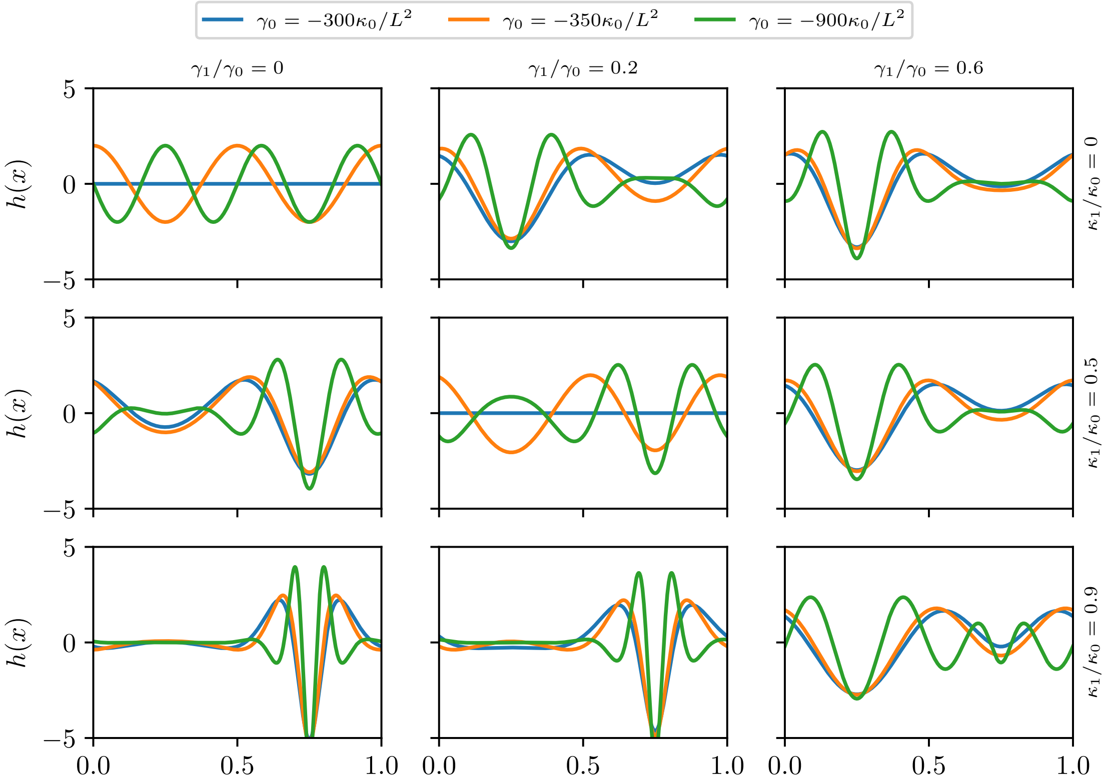

Figure 5.9: Analytical prediction of most unstable modes, with effective Young modulus $\hat{E} = 2000\kappa_0/L^3$. Different from Figs. 4.9 (a) and 5.8, here the value of γ_0 is imposed, being roughly mapped to growth.

5.4 Conclusions

The model used in this chapter departed from the energy minimization regime, and the systems studied before were reanalysed taking into consideration dynamical effects. It was shown that dynamical systems behave roughly in the same manner as those obtained in the energy minimization regime. The timescale of growth, when compared with the timescale of the relaxation, is vital in the determination of the wavelength on which the system will fold. In many cases we observe that there would be an overshoot in the folding wavenumber, which becomes more pronounced for thicker systems, or those with a high growth rate. These overshoots were followed by a relaxation period, where the wavenumber of the system would approach the wavelength predicted by energy minimization approaches, but not necessarily reach it. This fact makes it possible that the wavelengths obtained in the real cortex would be smaller than those predicted without taking dynamical effects into account. These results also serve as a consistency check of the results in Ch. 4, showing that the trajectory the system performed in phase space was physically sound despite the quasi-static approximation.

Inhomogeneities in the growth rate were also introduced, in addition to the cortical thickness inhomogeneity studied in Ch. 4. It was observed that growth inhomogeneity has a similar effect to that of cortical thickness, creating a leading sulcus around the region of fastest growth, while inhibiting folding in regions of little growth. The interplay between the two kinds of inhomogeneity was studied, where the thickest regions grow faster than the thinner regions, leading to an effective competition between the two kinds of inhomogeneity. The observed configurations are not simply additive, as one could expect *a priori*. Instead, it was observed that they interfere with each other, with early folding being located either at the thinnest or at the thickest point, but not in both at the same time, nor in a in-between location.

We further developed the linear stability theory developed in Sec. 4.1.9, in order to aid in the understanding of the configurations obtained in the simulations. This theory was then extended to deal with two types of inhomogeneity, bending rigidity and surface tension, with qualitative matching between the simulation and theory results. In energetical terms, the effects of either type of inhomogeneity is to couple distinct wavemodes, producing non-sinusoidal waves. In the first case the theory produces configurations that are highly localized around the regions of less stiff cortex, while in the latter case produced folding on the area of maximal absolute surface tension. These can be roughly mapped onto cortical thickness and growth rate inhomogeneities, respectively. This theory was also used to explain the relative predominance of the effects of cortical thickness when compared to growth rate inhomogeneities.

Chapter 6

Conclusions and further remarks

This thesis aimed to contribute to the understanding of the mechanics involved in gyrogenesis, the process by which the mammalian brain acquires its characteristic folding. We performed simulations using a nonlinear elasticity framework, where the brain was modelled as a perfect elastic undergoing large deformations. JuFold, the simulation software used in this thesis implementing the finite element method to solve the differential equations derived from nonlinear elasticity, is made available as an open source library. Based on the differential growth hypothesis [154], the simulated systems were composed of two layers, where the upper layer grows tangentially, mimicking the gray matter found in the brain cortex, while the lower layer, mimicking the white matter, does not grow. In order to probe different timescales, simulations were performed using both energy minimization and full dynamics.

It was shown that, in the energy minimization regime, systems with homogeneous thickness fold into well-defined waves, whose wavelengths depend linearly on the cortical thickness. These findings are consistent with previous literature [156, 157, 182, 186]. In these simulations, the thicknesses of the sulci and gyri diverge after folding, with the sulci being much thinner than the corresponding gyri, in agreement with what has been observed in histological sections [187]. Similarly, we found that the sulci are under higher compressive stress than the gyri. In systems with spatial variation of the cortical thickness, formations similar to the higher-order folding – one of the hallmarks of highly-folded brains – were observed. In these conditions, the thinner regions fold first, followed by regions of successive cortical thickness. In extreme cases, an isolated fold forms in an otherwise flat cortex, reminiscent of the central sulcus of the squirrel monkey brain [13]. These leading folds are soon followed by secondary folding. We observed that while the initial folding is highly reproducible, the final folding pattern is susceptible to any small noise and is unique, explaining the “reproducible uniqueness” seen in the brain [31]. In order to explain the simulation results, a linear stability theory based on the Föppl-von Kármán elastic plate theory was developed, where inhomogeneities in thickness are mapped to a spatially dependent bending rigidity. The results obtained from the simulations and the theory are in qualitative agreement, yielding configurations whose folding is most localised in the thinnest (i.e., low bending rigidity) region.

When analyzed in the dynamical regime, systems with homogeneous thickness presented a weak dependency between their growth rates and folding wavenumbers. Most importantly, we found that the wavemodes predicted by the energy minimization approach are recovered in the limit of slow growth, thus justifying much work in the literature – including our own – that assumed that energy minimization is equivalent to slow growth or the quasistatic approximation *a posteriori*. It was also observed that the opposite condition, of fast growth rate, creates two effects on the homogeneous cortex. Firstly, it leads to folding in a higher wavenumber than the energetical minimum. Secondly, it allows for a larger number of wavemodes to be excited, creating an initially more complex folding than systems in the slow growth regime. Still, after a short period even these systems relax to an extremely narrow wavenumber spectrum, which is not necessarily the same as observed in the energy minimization regime. These indicate that, while the folding of the brain can be influenced by the growth rate, faster growth does not lead to complex growth on its own. By how much these two wavelengths differ depends on the cortical thickness of the system, as well as on the rate by which the cortical plate grows.

Thickness inhomogeneities in the dynamical regime generate qualitatively similar results to those in the slow growth regime, with its effects being compounded by faster growth rates. Complementarily, inhomogeneities in cortical growth – with cortical thickness initially constant – showed that growth differences also lead to localised folding. However, these systems do not exhibit the same folding complexity as simulations with inhomogeneous thickness. This difference can be understood based on a further specialised stability theory. The interplay between both kinds of inhomogeneity were studied, showing a complex interaction where the effects of each type of inhomogeneity are somewhat mutually exclusive, with the repercussions of thickness inhomogeneity being much more pronounced. Most notably, relatively large inhomogeneities needed to be imposed on the growth rate before patterns characteristic of thickness inhomogeneity were inhibited. Finally, these results were analysed in light of the linear stability theory, where, in addition to the spatially varying bending rigidity introduced earlier, the surface tension was also considered inhomogeneous. This improved theory qualitatively reproduces the results obtained in the simulations, and explains the relative prominence of the bending rigidity (which corresponds to the cortical thickness in our simulations) in relation to the surface tension (corresponding to the growth rate).

While the results in this work give important insight into the mechanics of folding, there are many important issues left before gyrogenesis is fully understood. Theoretical arguments indicate that cell division and apoptosis lead to tissue fluidisation [208] – and to an effective Maxwell-like rheology – due to cell division and death relaxing the stress in the system. Such a theory has been successfully applied to several epithelial tissues in the mammalian body [209–211]. It is necessary to observe, however, that the development of the brain is markedly distinct from those tissues, with cell division and apoptosis being much less frequent, and cellular differentiation being more prominent. In experiments on short time scales (i.e., in the range of minutes) where small cubes of brain tissue undergo a prescribed shear, it has been observed that the brain behaves as a Kelvin-Voigt viscoelastic, presenting a finite steady-state stress [212]. As current experiments have not been able to probe the long-term behavior of brain tissue, it remains to be seen whether the microscopic processes connected to gyrogenesis can also lead to fluidisation, and if so, what influence it will have in folding.

The elastic model used in this work, while validated *ex-vivo*, can be improved with further experimental data. The elastic properties of the brain tissue were supposed to be constant throughout the cortex. While a valid approximation for smaller sections of the brain, previous rheological works have shown that different parts of the brain have different stiffness [42]. Additionally, the differential growth hypothesis – and consequentially this work – supposes that the gray matter is stiffer than the white matter. This fact is far from settled, with works in the literature supporting both claims that the gray matter is indeed stiffer than the white matter [69, 70, 213] and vice-versa [71–73].

On that note, it is important to point out that there are several other proposals to explain brain folding. Structural connectivity (i.e., neuronal axons connecting different parts of the brain), for instance, has been proposed as a driver of folding, with wide adoption. How it would influence the conformations used in this work can be further investigated to understand the mutual influences of differential growth and axonal tension in gyrogenesis. Indeed, it is possible to incorporate the mechanical effects of the structural connectivity by expanding the model to include inhomogeneous external tractions. For example, revised models of axonal traction have emerged where the white matter is supposed softer than the gray matter, yielding folded configurations not through compressive stress but through as "brain-as-smetic" (i.e., a liquid crystal) approach [65].

With competing hypotheses, it becomes necessary to design experiments which are able to test these hypotheses against each other. In recent years, layered soft gels have been used as models for brain folding [78]. Using 3D-printed templates, it is possible to mimic the embryonic brain, and upon hydration and consequential swelling, folding patterns reminiscent of those in the human brain are obtained. In this vein, PDMS can be manipulated using oxygen plasma to have a stiff surface and a soft bulk [143, 214], creating simulacra of the results from this work. This correspondence can be extended by careful masking the surface of the PDMS, making it possible to control the pattern of these stiff configurations. Performing such a process in an initially stretched slab of PDMS allows the system to create an effectively grown state which coincides with the protocol used in the simulations of this thesis. Conclusions drawn from these simulacra, however, are of limited scope, and they carry the supposition that the brain is a perfect (or at most, highly visco-) elastic and completely disregard the biology behind the folding process.

In order to perform biologically meaningful comparisons, gel simulacra are thus not fully adequate, and experiments on the developing brain are necessary. These are difficult, for a plethora of reasons. Not only are they long and expensive, but most importantly, they are riddled with ethical issues. In recent years, a new possibility for biological experiments in the field of brain development has emerged, through the usage of *in vitro* brain organoids [202, 203], three-dimensional self-assembled cell agregates similar to the developing brain. These organoids allow great control over the experiment, both at the genetical and mechanical levels, being possible to create mutant genes, or to use laser microdissections to kill specific cells. Only recently folding has been achieved in such small systems [204], but they already show promise as an important tool in the experimental study of gyrogenesis.

Finally, it is important to further emphasise the duality between gyrogenesis models and the modelling of elastic materials. As mentioned above, elastic gels have been used – even if in a limited fashion – as simulacra of developing brains. However, this mapping goes both ways, and the knowledge obtained from the study of brain folding can be applied to material science. Most notably, not only are our results useful to explain gyrogenesis, but they are also directly applicable to the study of microscopic surfaces where surface swelling leads to corrugations [199], where they can aid the understanding of these corrugations, and to help control their emergence. This application has been submitted as a patent application, whose approval is still pending.

In summary, while the contributions in this work will hopefully prove helpful in the understanding of gyrogenesis, there is still a long road before every one of its aspects are fully understood. As with many other fields, the knowledge on the causes behind gyrogenesis can be further improved by novel theoretical works and more complex modeling. However, new experiments, especially those probing the long term behavior of brain tissue, are necessary in order to validate the assumptions of current theories, and to inform new works.

Bibliography

[1] G.E.P. Box. “Robustness in the Strategy of Scientific Model Building”. In: *Robustness in Statistics*. Elsevier, 1979, pp. 201–236. ISBN: 978-0-12-438150-6. DOI: `10.1016/B978-0-12-438150-6.50018-2`. URL: `https://linkinghub.elsevier.com/retrieve/pii/B9780124381506500182` (page i).

[2] A. Paul Alivisatos et al. “The Brain Activity Map Project and the Challenge of Functional Connectomics”. In: *Neuron* 74.6 (June 2012), pp. 970–974. ISSN: 08966273. DOI: `10.1016/j.neuron.2012.06.006`. URL: `https://linkinghub.elsevier.com/retrieve/pii/S0896627312005181` (page 3).

[3] Henry Markram. “The Human Brain Project”. In: *Scientific American* 306.6 (2012), pp. 50–55. ISSN: 00368733, 19467087. JSTOR: `26014516` (page 3).

[4] James Henry Breasted, ed. *Facsimile Plates and Line for Line Hieroglyphic Transliteration*. Reissued. The Edwin Smith Surgical Papyrus published in facsimile and hieroglyphic transliteration with translation and commentary in two volumes ; Vol. 2. Chicago, Ill: The Univ. of Chicago Press, 1991. ISBN: 978-0-918986-73-3 (pages 3, 4).

[5] J.H. Scatliff and S. Johnston. “Andreas Vesalius and Thomas Willis: Their Anatomic Brain Illustrations and Illustrators”. In: *American Journal of Neuroradiology* 35.1 (Jan. 2014), pp. 19–22. ISSN: 0195-6108, 1936-959X. DOI: `10.3174/ajnr.A3766`. URL: `http://www.ajnr.org/lookup/doi/10.3174/ajnr.A3766` (page 4).

[6] Andreae Vesalii. *Andreae Vesalii Bruxellensis, Scholae Medicorum Patauinae Professoris, de Humani Corporis Fabrica Libri Septem*. 7 vols. Padua: School of medicine, Padua, 1543 (pages 3, 4).

[7] Thomas Willis and William Feindel. *Anatomy of the Brain and Nerves.* 1965. ISBN: 978-0-7735-9440-1 (page 3).

[8] Magnus Gustaf Retzius. *Das Menschenhirn. Studien in der makroskopischen Morphologie.* P.A. Norstedt, 1896 (page 4).

[9] K. Brodmann. *Vergleichende Lokalisationslehre der Grosshirnrinde in ihren Prinzipien dargestellt auf Grund des Zellenbaues von Dr. K. Brodmann, ...* J.A. Barth, 1909 (pages 4, 6).

[10] Dominik Weishaupt, Victor D. Koechli, and Borut Marincek. *How Does MRI Work? An Introduction to the Physics and Function of Magnetic Resonance Imaging.* 2nd ed. Berlin ; New York: Springer, 2006. 169 pp. ISBN: 978-3-540-30067-0 (page 4).

[11] P. V. Bayly, L. A. Taber, and C. D. Kroenke. "Mechanical Forces in Cerebral Cortical Folding: A Review of Measurements and Models". In: *Journal of the Mechanical Behavior of Biomedical Materials* 29 (2014), pp. 568–581. ISSN: 1751-6161. DOI: `10.1016/j.jmbbm.2013.02.018`. URL: `http://www.sciencedirect.com/science/article/pii/S175161611300074X` (pages 4, 17).

[12] Tao Sun and Robert F. Hevner. "Growth and Folding of the Mammalian Cerebral Cortex: From Molecules to Malformations". In: *Nature Reviews Neuroscience* 15.4 (Mar. 2014), pp. 217–232. DOI: `10.1038/nrn3707`. URL: `https://doi.org/10.1038/nrn3707` (pages 4, 11).

[13] Wally Welker. "Why Does Cerebral Cortex Fissure and Fold?" In: *Cerebral Cortex: Comparative Structure and Evolution of Cerebral Cortex, Part II.* Ed. by Edward G. Jones and Alan Peters. Cerebral Cortex. Boston, MA: Springer US, 1990, pp. 3–136. ISBN: 978-1-4615-3824-0. DOI: `10.1007/978-1-4615-3824-0_1`. URL: `https://doi.org/10.1007/978-1-4615-3824-0_1` (pages 5, 9, 12, 14, 15, 110).

[14] Katrin Amunts et al. "BigBrain: An Ultrahigh-Resolution 3D Human Brain Model". In: *Science* 340.6139 (2013), pp. 1472–1475. ISSN: 0036-8075. DOI: `10.1126/science.1235381`. URL: `https://science.sciencemag.org/content/340/6139/1472` (page 6).

[15] Simon B. Eickhoff, B. T. Thomas Yeo, and Sarah Genon. “Imaging-Based Parcellations of the Human Brain”. In: *Nature Reviews Neuroscience* 19.11 (Nov. 2018), pp. 672–686. ISSN: 1471-003X, 1471-0048. DOI: `10.1038/s41583-018-0071-7`. URL: `http://www.nature.com/articles/s41583-018-0071-7` (page 6).

[16] Marty G. Woldorff et al. “Functional Parcellation of Attentional Control Regions of the Brain”. In: *Journal of Cognitive Neuroscience* 16.1 (Jan. 2004), pp. 149–165. ISSN: 0898-929X, 1530-8898. DOI: `10.1162/089892904322755638`. URL: `https://direct.mit.edu/jocn/article/16/1/149-165/83066` (page 6).

[17] M Titford. “The Long History of Hematoxylin”. In: *Biotechnic & Histochemistry* 80.2 (Jan. 2005), pp. 73–78. ISSN: 1052-0295, 1473-7760. DOI: `10.1080/10520290500138372`. URL: `http://www.tandfonline.com/doi/full/10.1080/10520290500138372` (page 7).

[18] Gertrudis Perea, Marta Navarrete, and Alfonso Araque. “Tripartite Synapses: Astrocytes Process and Control Synaptic Information”. eng. In: *Trends in Neurosciences* 32.8 (Aug. 2009), pp. 421–431. ISSN: 1878-108X. DOI: `10.1016/j.tins.2009.05.001` (page 7).

[19] Suzana Herculano-Houzel. “The Remarkable, yet Not Extraordinary, Human Brain as a Scaled-up Primate Brain and Its Associated Cost”. In: *Proceedings of the National Academy of Sciences* 109 (Supplement 1 June 26, 2012), pp. 10661–10668. ISSN: 0027-8424, 1091-6490. DOI: `10.1073/pnas.1201895109`. pmid: 22723358. URL: `https://www.pnas.org/content/109/Supplement_1/10661` (page 7).

[20] Christopher S. von Bartheld, Jami Bahney, and Suzana Herculano-Houzel. “The Search for True Numbers of Neurons and Glial Cells in the Human Brain: A Review of 150 Years of Cell Counting: Quantifying Neurons and Glia in Human Brain”. In: *Journal of Comparative Neurology* 524.18 (Dec. 15, 2016), pp. 3865–3895. ISSN: 00219967. DOI: `10.1002/cne.24040`. URL: `http://doi.wiley.com/10.1002/cne.24040` (page 7).

[21] Silvia Budday, Paul Steinmann, and Ellen Kuhl. "Physical Biology of Human Brain Development". In: *Frontiers in Cellular Neuroscience* 9 (July 8, 2015). ISSN: 1662-5102. DOI: `10.3389/fncel.2015.00257`. URL: `http://journal.frontiersin.org/Article/10.3389/fncel.2015.00257/abstract` (pages 7–9).

[22] Virginia Fernández, Cristina Llinares-Benadero, and Víctor Borrell. "Cerebral Cortex Expansion and Folding: What Have We Learned?" In: *The EMBO Journal* 35.10 (May 17, 2016), pp. 1021–1044. ISSN: 0261-4189, 1460-2075. DOI: `10.15252/embj.201593701`. URL: `https://onlinelibrary.wiley.com/doi/abs/10.15252/embj.201593701` (pages 7, 16, 18).

[23] Arnold Kriegstein, Stephen Noctor, and Verónica Martínez-Cerdeño. "Patterns of Neural Stem and Progenitor Cell Division May Underlie Evolutionary Cortical Expansion". In: *Nature Reviews Neuroscience* 7.11 (Nov. 2006), pp. 883–890. ISSN: 1471-003X, 1471-0048. DOI: `10.1038/nrn2008`. URL: `http://www.nature.com/articles/nrn2008` (pages 7, 10).

[24] Scott F. Gilbert. *Developmental biology*. 9th ed. OCLC: ocn551199641. Sunderland, Mass: Sinauer Associates, 2010. ISBN: 978-0-87893-384-6 978-0-87893-564-2 (page 9).

[25] R. O'Rahilly and F. Müller. "Minireview: summary of the initial development of the human nervous system". eng. In: *Teratology* 60.1 (July 1999), pp. 39–41. ISSN: 0040-3709. DOI: `10.1002/(SICI)1096-9926(199907)60:1<39::AID-TERA11>3.0.CO;2-I` (page 9).

[26] Je G Chi, Elizabeth C Dooling, and Floyd H. Gilles. "Gyral development of the human brain". en. In: *Annals of Neurology* 1.1 (Jan. 1977), pp. 86–93. ISSN: 0364-5134, 1531-8249. DOI: `10.1002/ana.410010109`. URL: `http://doi.wiley.com/10.1002/ana.410010109` (page 9).

[27] Gang Li et al. "Computational neuroanatomy of baby brains: A review". en. In: *NeuroImage* 185 (Jan. 2019), pp. 906–925. ISSN: 10538119. DOI: `10.1016/j.neuroimage.2018.03.042`. URL: `https://linkinghub.elsevier.com/retrieve/pii/S1053811918302556` (page 9).

[28] Wilfrid E. Le Gros Clark and P. B. Medawar. *Essays on Growth and Form Presented to D'Arcy Wentworth Thompson.* Oxford: Clarendon Press, 1945 (pages 10, 14, 17, 22).

[29] K. E. Garcia, C. D. Kroenke, and P. V. Bayly. "Mechanics of cortical folding: stress, growth and stability". en. In: *Philosophical Transactions of the Royal Society B: Biological Sciences* 373.1759 (Nov. 2018), p. 20170321. ISSN: 0962-8436, 1471-2970. DOI: `10.1098/rstb.2017.0321`. URL: `https://royalsocietypublishing.org/doi/10.1098/rstb.2017.0321` (page 10).

[30] David Germanaud et al. "Larger Is Twistier: Spectral Analysis of Gyrification (SPANGY) Applied to Adult Brain Size Polymorphism". In: *NeuroImage* 63.3 (Nov. 2012), pp. 1257–1272. ISSN: 10538119. DOI: `10.1016/j.neuroimage.2012.07.053`. URL: `https://linkinghub.elsevier.com/retrieve/pii/S1053811912007835` (page 10).

[31] Jessica Dubois et al. "The Dynamics of Cortical Folding Waves and Prematurity-Related Deviations Revealed by Spatial and Spectral Analysis of Gyrification". In: *NeuroImage* 185 (Jan. 2019), pp. 934–946. ISSN: 10538119. DOI: `10.1016/j.neuroimage.2018.03.005`. URL: `https://linkinghub.elsevier.com/retrieve/pii/S1053811918301903` (pages 10, 11, 110).

[32] JGF Baillarger. "De l'étendue de La Surface Du Cerveau et de Ses Rapports Avec Le Developpement de l'intelligence". In: *Ann Med Psychol* 5 (1853), pp. 1–9 (page 10).

[33] K. Im et al. "Brain Size and Cortical Structure in the Adult Human Brain". In: *Cerebral Cortex* 18.9 (Sept. 1, 2008), pp. 2181–2191. ISSN: 1047-3211, 1460-2199. DOI: `10.1093/cercor/bhm244`. URL: `https://academic.oup.com/cercor/article-lookup/doi/10.1093/cercor/bhm244` (page 10).

[34] R. Toro et al. "Brain Size and Folding of the Human Cerebral Cortex". In: *Cerebral Cortex* 18.10 (Oct. 1, 2008), pp. 2352–2357. ISSN: 1047-3211, 1460-2199. DOI: `10.1093/cercor/bhm261`. URL: `https://academic.oup.com/cercor/article-lookup/doi/10.1093/cercor/bhm261` (page 10).

[35] Karl Zilles et al. "The human pattern of gyrification in the cerebral cortex". In: *Anatomy and Embryology* 179.2 (Nov. 1988), pp. 173–179. ISSN: 1432-0568.

DOI: 10.1007/BF00304699. URL: https://doi.org/10.1007/BF00304699 (page 10).

[36] Karl Zilles et al. "Gyrification in the Cerebral Cortex of Primates". en. In: *Brain, Behavior and Evolution* 34.3 (1989), pp. 143–150. ISSN: 0006-8977, 1421-9743. DOI: 10.1159/000116500. URL: https://www.karger.com/Article/FullText/116500 (page 10).

[37] Joshua S. Shimony et al. "Comparison of cortical folding measures for evaluation of developing human brain". en. In: *NeuroImage* 125 (Jan. 2016), pp. 780–790. ISSN: 10538119. DOI: 10.1016/j.neuroimage.2015.11.001. URL: https://linkinghub.elsevier.com/retrieve/pii/S105381191501023X (page 10).

[38] Jessica Dubois et al. "MRI of the Neonatal Brain: A Review of Methodological Challenges and Neuroscientific Advances". In: *Journal of Magnetic Resonance Imaging* (May 18, 2020), jmri.27192. ISSN: 1053-1807, 1522-2586. DOI: 10.1002/jmri.27192. URL: https://onlinelibrary.wiley.com/doi/abs/10.1002/jmri.27192 (page 11).

[39] Isabel Reillo et al. "A Role for Intermediate Radial Glia in the Tangential Expansion of the Mammalian Cerebral Cortex". In: *Cerebral Cortex* 21.7 (July 2011), pp. 1674–1694. ISSN: 1460-2199, 1047-3211. DOI: 10.1093/cercor/bhq238. URL: https://academic.oup.com/cercor/article-lookup/doi/10.1093/cercor/bhq238 (pages 11, 12, 25).

[40] Camino de Juan Romero and Víctor Borrell. "Genetic Maps and Patterns of Cerebral Cortex Folding". In: *Current Opinion in Cell Biology* 49 (Dec. 2017), pp. 31–37. ISSN: 09550674. DOI: 10.1016/j.ceb.2017.11.009. URL: https://linkinghub.elsevier.com/retrieve/pii/S0955067417300716 (pages 10, 25).

[41] Gang Xu et al. "Axons Pull on the Brain, But Tension Does Not Drive Cortical Folding". In: *Journal of Biomechanical Engineering* 132.7 (June 2010), pp. 071013-071013–8. ISSN: 0148-0731. DOI: 10.1115/1.4001683. URL: http://dx.doi.org/10.1115/1.4001683 (pages 11, 16, 20, 93).

[42] Silvia Budday et al. "Mechanical Properties of Gray and White Matter Brain Tissue by Indentation". In: *Journal of the Mechanical Behavior of Biomedical Materials* 46 (June 2015), pp. 318–330. ISSN: 17516161. DOI: 10.1016/j.jmbbm.

2015.02.024. URL: `https://linkinghub.elsevier.com/retrieve/pii/S1751616115000673` (pages 11, 18, 111).

[43] Edwin Clarke and Charles Donald O'Malley. *The Human Brain and Spinal Cord: A Historical Study Illustrated by Writings from Antiquity to the Twentieth Century*. 2nd ed., rev. and enl. Norman Neurosciences Series no. 2. San Francisco: Norman Pub, 1996. 951 pp. ISBN: 978-0-930405-25-0 (page 12).

[44] A. James Barkovich et al. "A Developmental and Genetic Classification for Malformations of Cortical Development: Update 2012". In: *Brain* 135.5 (May 2012), pp. 1348–1369. ISSN: 1460-2156, 0006-8950. DOI: `10.1093/brain/aws019`. URL: `https://academic.oup.com/brain/article-lookup/doi/10.1093/brain/aws019` (pages 12, 14).

[45] Waney Squier and Anna Jansen. "Polymicrogyria: Pathology, Fetal Origins and Mechanisms". In: *Acta Neuropathologica Communications* 2.1 (Dec. 2014), p. 80. ISSN: 2051-5960. DOI: `10.1186/s40478-014-0080-3`. URL: `https://actaneurocomms.biomedcentral.com/articles/10.1186/s40478-014-0080-3` (pages 12, 14).

[46] Renzo Guerrini. "Genetic Malformations of the Cerebral Cortex and Epilepsy". In: *Epilepsia* 46.s1 (Mar. 2005), pp. 32–37. ISSN: 0013-9580, 1528-1167. DOI: `10.1111/j.0013-9580.2005.461010.x`. URL: `http://doi.wiley.com/10.1111/j.0013-9580.2005.461010.x` (page 12).

[47] Rahul S. Desikan and A. James Barkovich. "Malformations of Cortical Development". In: *Annals of Neurology* 80.6 (Dec. 2016), pp. 797–810. ISSN: 03645134. DOI: `10.1002/ana.24793`. URL: `http://doi.wiley.com/10.1002/ana.24793` (page 12).

[48] Valentín Pérez et al. "Hereditary Lissencephaly and Cerebellar Hypoplasia in Churra Lambs". In: *BMC Veterinary Research* 9.1 (2013), p. 156. ISSN: 1746-6148. DOI: `10.1186/1746-6148-9-156`. URL: `http://bmcvetres.biomedcentral.com/articles/10.1186/1746-6148-9-156` (page 13).

[49] Julien Lefèvre and Jean-François Mangin. "A Reaction-Diffusion Model of Human Brain Development". In: *PLoS Computational Biology* 6.4 (Apr. 22, 2010). Ed. by Karl J. Friston, e1000749. ISSN: 1553-7358. DOI: `10.1371/journal.`

pcbi.1000749. URL: https://dx.plos.org/10.1371/journal.pcbi.1000749 (pages 13, 23).

[50] Richard S. Smith et al. "Sodium Channel SCN3A (NaV1.3) Regulation of Human Cerebral Cortical Folding and Oral Motor Development". In: *Neuron* 99.5 (Sept. 2018), 905–913.e7. ISSN: 08966273. DOI: 10.1016/j.neuron.2018.07.052. URL: https://linkinghub.elsevier.com/retrieve/pii/S0896627318306500 (page 13).

[51] A. James Barkovich. "Current Concepts of Polymicrogyria". In: *Neuroradiology* 52.6 (June 2010), pp. 479–487. ISSN: 0028-3940, 1432-1920. DOI: 10.1007/s00234-009-0644-2. URL: http://link.springer.com/10.1007/s00234-009-0644-2 (page 12).

[52] Russell L. Cecil, Lee Goldman, and Andrew I. Schafer, eds. *Goldman's Cecil Medicine*. 24th ed. Philadelphia: Elsevier/Saunders, 2012. 2569 pp. ISBN: 978-1-4377-1604-7 978-1-4377-2788-3 978-0-8089-2437-1 978-1-4377-3665-6 (page 14).

[53] Leonard Radinsky. "Cerebral Clues". In: *Natural History* May.85 (1976), pp. 54–59. ISSN: 0028-0712 (page 14).

[54] Donald H. Barron. "An Experimental Analysis of Some Factors Involved in the Development of the Fissure Pattern of the Cerebral Cortex". In: *Journal of Experimental Zoology* 113.3 (Apr. 1950), pp. 553–581. ISSN: 0022-104X, 1097-010X. DOI: 10.1002/jez.1401130304. URL: http://doi.wiley.com/10.1002/jez.1401130304 (page 14).

[55] Tuomas Tallinen et al. "Gyrification from Constrained Cortical Expansion". In: *Proceedings of the National Academy of Sciences* 111.35 (2014), pp. 12667–12672. DOI: 10.1073/pnas.1406015111. URL: http://www.pnas.org/content/111/35/12667.abstract (page 14).

[56] Karl Bogislavs Reichert. *Der Bau Des Menschlichen Gehirns: Durch Abbildungen Mit Erläuterndem Texte*. Vol. 2. Wilhelm Engelmann, 1859 (page 14).

[57] O Ranke. "Beiträge Zur Kenntnis Der Normalen Und Pathologischen Hirnrindenbildung". In: *Beitr Pathol Anat* 47 (1910), pp. 51–125 (page 14).

[58] Daniel John Cunningham. *Textbook of Anatomy*. W. Wood, 1906 (page 14).

[59] W Kükenthal and Th Ziehen. “Das Centralnervensystem Der Cetaceen”. In: (1889) (page 14).

[60] Cornelius Ubbo Ariëns Kappers and International Congress of Medicine. *Anatomy and Embryology: Cerebral Localization and the Significance of Sulci.* p. [273]-392. London: H. Frowde : Hodder & Stoughton, 1913. p. [273]-392. URL: `https://babel.hathitrust.org/cgi/pt?id=iau.31858023671914&view=1up&seq=18` (page 15).

[61] David C. van Essen. “A Tension-Based Theory of Morphogenesis and Compact Wiring in the Central Nervous System”. In: *Nature* 385.6614 (Jan. 1997), pp. 313–318. DOI: `10.1038/385313a0`. URL: `http://dx.doi.org/10.1038/385313a0` (pages 15, 16).

[62] Sriram Ramaswamy. “The Mechanics and Statistics of Active Matter”. In: *Annual Review of Condensed Matter Physics* 1.1 (Aug. 10, 2010), pp. 323–345. ISSN: 1947-5454, 1947-5462. DOI: `10.1146/annurev-conmatphys-070909-104101`. URL: `http://www.annualreviews.org/doi/10.1146/annurev-conmatphys-070909-104101` (page 16).

[63] T. J. Dennerll et al. “The Cytomechanics of Axonal Elongation and Retraction.” In: *Journal of Cell Biology* 109.6 (Dec. 1, 1989), pp. 3073–3083. ISSN: 0021-9525. DOI: `10.1083/jcb.109.6.3073`. URL: `https://rupress.org/jcb/article/109/6/3073/28999/The-cytomechanics-of-axonal-elongation-and` (page 16).

[64] D. Bray. “Axonal Growth in Response to Experimentally Applied Mechanical Tension”. In: *Developmental Biology* 102.2 (Apr. 1984), pp. 379–389. ISSN: 00121606. DOI: `10.1016/0012-1606(84)90202-1`. URL: `https://linkinghub.elsevier.com/retrieve/pii/0012160684902021` (page 16).

[65] O. V. Manyuhina, David Mayett, and J. M. Schwarz. “Elastic Instabilities in a Layered Cerebral Cortex: A Revised Axonal Tension Model for Cortex Folding”. In: *New Journal of Physics* 16.12 (Dec. 2014), p. 123058. DOI: `10.1088/1367-2630/16/12/123058`. URL: `https://doi.org/10.1088/1367-2630/16/12/123058` (pages 16, 112).

[66] D.P. Richman et al. “Mechanical Model of Brain Convolutional Development”. In: *Science* 189.4196 (1975), pp. 18–21. ISSN: 0036-8075. DOI: `10.1126/science.1135626`. URL: `http://science.sciencemag.org/content/189/4196/18` (pages 17, 18, 20).

[67] Katja Heuer and Roberto Toro. “Role of Mechanical Morphogenesis in the Development and Evolution of the Neocortex”. In: *Physics of Life Reviews* (Jan. 2019), S157106451930020X. ISSN: 15710645. DOI: `10.1016/j.plrev.2019.01.012`. URL: `https://linkinghub.elsevier.com/retrieve/pii/S157106451930020X` (page 17).

[68] Tuomas Tallinen et al. “Gyrification from constrained cortical expansion”. In: *Proceedings of the National Academy of Sciences* 111.35 (2014), pp. 12667–12672. DOI: `10.1073/pnas.1406015111`. URL: `http://www.pnas.org/content/111/35/12667.abstract` (pages 17, 19, 21, 35, 69).

[69] Michael A. Green, Lynne E. Bilston, and Ralph Sinkus. “In Vivobrain Viscoelastic Properties Measured by Magnetic Resonance Elastography”. In: *NMR in Biomedicine* 21.7 (Aug. 2008), pp. 755–764. DOI: `10.1002/nbm.1254`. URL: `https://doi.org/10.1002/nbm.1254` (pages 18, 111).

[70] Curtis L. Johnson et al. “Local Mechanical Properties of White Matter Structures in the Human Brain”. In: *NeuroImage* 79 (Oct. 2013), pp. 145–152. DOI: `10.1016/j.neuroimage.2013.04.089`. URL: `https://doi.org/10.1016/j.neuroimage.2013.04.089` (pages 18, 111).

[71] A. Manduca et al. “Magnetic Resonance Elastography: Non-Invasive Mapping of Tissue Elasticity”. In: *Medical Image Analysis* 5.4 (Dec. 2001), pp. 237–254. DOI: `10.1016/s1361-8415(00)00039-6`. URL: `https://doi.org/10.1016/s1361-8415(00)00039-6` (pages 18, 111).

[72] Paul J. McCracken et al. “Mechanical Transient-Based Magnetic Resonance Elastography”. In: *Magnetic Resonance in Medicine* 53.3 (2005), pp. 628–639. DOI: `10.1002/mrm.20388`. URL: `https://doi.org/10.1002/mrm.20388` (pages 18, 111).

[73] J. A. W. van Dommelen et al. “Mechanical Properties of Brain Tissue by Indentation: Interregional Variation”. In: *Journal of the Mechanical Behavior of Biomedical Materials* 3.2 (Feb. 2010), pp. 158–166. DOI: `10.1016/j.jmbbm.`

2009.09.001. URL: `https://doi.org/10.1016/j.jmbbm.2009.09.001` (pages 18, 111).

[74] Bruno Mota and Suzana Herculano-Houzel. “Cortical Folding Scales Universally with Surface Area and Thickness, Not Number of Neurons”. In: *Science* 349.6243 (2015), pp. 74–77. ISSN: 0036-8075. DOI: `10.1126/science.aaa9101`. URL: `http://science.sciencemag.org/content/349/6243/74` (page 18).

[75] Roberto Toro and Yves Burnod. “A Morphogenetic Model for the Development of Cortical Convolutions”. In: *Cerebral Cortex* 15.12 (Mar. 2005), pp. 1900–1913. DOI: `10.1093/cercor/bhi068`. URL: `https://doi.org/10.1093/cercor/bhi068` (pages 19, 22).

[76] Silvia Budday et al. “Size and curvature regulate pattern selection in the mammalian brain”. In: *Extreme Mechanics Letters* 4 (2015), pp. 193–198. ISSN: 2352-4316. DOI: `https://doi.org/10.1016/j.eml.2015.07.004`. URL: `http://www.sciencedirect.com/science/article/pii/S2352431615000863` (pages 19, 22, 32).

[77] P. V. Bayly et al. “A Cortical Folding Model Incorporating Stress-Dependent Growth Explains Gyral Wavelengths and Stress Patterns in the Developing Brain”. In: *Physical Biology* 10.1 (Jan. 2013), p. 016005. DOI: `10.1088/1478-3975/10/1/016005`. URL: `https://doi.org/10.1088/1478-3975/10/1/016005` (pages 20, 22, 93).

[78] Tuomas Tallinen et al. “On the growth and form of cortical convolutions”. In: *Nat Phys* 12.6 (June 2016), pp. 588–593. ISSN: 1745-2473. URL: `http://dx.doi.org/10.1038/nphys3632` (pages 21, 35, 58, 112).

[79] Silvia Budday, Paul Steinmann, and Ellen Kuhl. “Secondary Instabilities Modulate Cortical Complexity in the Mammalian Brain”. In: *Philosophical Magazine* 95.28-30 (2015), pp. 3244–3256. DOI: `10.1080/14786435.2015.1024184`. URL: `http://dx.doi.org/10.1080/14786435.2015.1024184` (pages 22, 85, 93).

[80] Jan Groenewold. “Wrinkling of Plates Coupled with Soft Elastic Media”. In: *Physica A: Statistical Mechanics and its Applications*. Statistical Thermodynamics and Colloid Science 298.1 (Sept. 1, 2001), pp. 32–45. ISSN: 0378-4371. DOI: `10.1016/S0378-4371(01)00209-6`. URL: `http://www.sciencedirect.com/science/article/pii/S0378437101002096` (page 22).

[81] Alexandra Schweikart and Andreas Fery. “Controlled Wrinkling as a Novel Method for the Fabrication of Patterned Surfaces”. In: *Microchimica Acta* 165.3 (June 1, 2009), pp. 249–263. ISSN: 1436-5073. DOI: 10.1007/s00604-009-0153-3. URL: https://doi.org/10.1007/s00604-009-0153-3 (page 22).

[82] Silvia Budday and Paul Steinmann. “On the influence of inhomogeneous stiffness and growth on mechanical instabilities in the developing brain”. In: *International Journal of Solids and Structures* 132-133 (Feb. 2018), pp. 31–41. DOI: 10.1016/j.ijsolstr.2017.08.010. URL: https://doi.org/10.1016/j.ijsolstr.2017.08.010 (pages 22, 70, 84).

[83] Alan Turing. “The Chemical Basis of Morphogenesis”. In: *Philosophical Transactions of the Royal Society of London. Series B, Biological Sciences* 237.641 (Aug. 14, 1952), pp. 37–72. ISSN: 2054-0280. DOI: 10.1098/rstb.1952.0012. URL: https://royalsocietypublishing.org/doi/10.1098/rstb.1952.0012 (page 22).

[84] J. E. Pearson. “Complex Patterns in a Simple System”. In: *Science* 261.5118 (July 9, 1993), pp. 189–192. ISSN: 0036-8075, 1095-9203. DOI: 10.1126/science.261.5118.189. URL: https://www.sciencemag.org/lookup/doi/10.1126/science.261.5118.189 (page 23).

[85] Jochen Hinz et al. “Isogeometric Analysis of the Gray-Scott Reaction-Diffusion Equations for Pattern Formation on Evolving Surfaces and Applications to Human Gyrification”. In: (Oct. 28, 2019). arXiv: 1910.12588 [cs, math]. URL: http://arxiv.org/abs/1910.12588 (page 23).

[86] S. N. Verner and K. Garikipati. “A Computational Study of the Mechanisms of Growth-Driven Folding Patterns on Shells, with Application to the Developing Brain”. In: *Extreme Mechanics Letters* 18 (2018), pp. 58–69. ISSN: 2352-4316. DOI: 10.1016/j.eml.2017.11.003. URL: http://www.sciencedirect.com/science/article/pii/S235243161730144X (page 24).

[87] Javier Bonet, Antonio J. Gil, and Richard D. Wood. *Nonlinear Solid Mechanics for Finite Element Analysis: Statics*. Cambridge University Press, 2016. ISBN: 978-1-107-11579-8. URL: https://www.amazon.com/Nonlinear-Mechanics-Finite-Element-Analysis-ebook/dp/B01HTT8XCG?SubscriptionId=0JYN1NVW651KCA56C102

tag=techkie-20&linkCode=xm2&camp=2025&creative=165953&creativeASIN=B01HTT8XCG (pages 27, 30, 33, 34, 58).

[88] A.J.M. Spencer. *Continuum Mechanics*. Dover Books on Physics. Dover Publications, 2012. ISBN: 978-0-486-13947-0 (page 27).

[89] Jerrold E. Marsden and Thomas J. R. Hughes. *Mathematical Foundations of Elasticity*. New York: Dover, 1994. 556 pp. ISBN: 978-0-486-67865-8 (pages 27, 34).

[90] Gerhard Holzapfel. *NONLINEAR SOLID MECHANICS. A Continuum Approach for Engineering*. second print. John Wiley & Sons, 2001 (page 27).

[91] P Haupt. "Continuum Mechanics and Theory of Materials". In: *Applied Mechanics Reviews* 55.2 (Apr. 3, 2002), B23–B23. ISSN: 0003-6900. DOI: 10.1115/1.1451084. URL: https://doi.org/10.1115/1.1451084 (page 27).

[92] George B. Arfken, Hans-Jurgen Weber, and Frank E. Harris. *Mathematical Methods for Physicists: A Comprehensive Guide*. 7th ed. Amsterdam ; Boston: Elsevier, 2013. 1205 pp. ISBN: 978-0-12-384654-9 (page 30).

[93] R. L. Fosdick and A. S. Wineman. "On general measures of deformation". en. In: *Acta Mechanica* 6.4 (Dec. 1968), pp. 275–295. ISSN: 0001-5970, 1619-6937. DOI: 10.1007/BF01172146. URL: http://link.springer.com/10.1007/BF01172146 (page 30).

[94] Patrizio Neff, Bernhard Eidel, and Robert J. Martin. "Geometry of Logarithmic Strain Measures in Solid Mechanics". en. In: *Archive for Rational Mechanics and Analysis* 222.2 (Nov. 2016), pp. 507–572. ISSN: 0003-9527, 1432-0673. DOI: 10.1007/s00205-016-1007-x. URL: http://link.springer.com/10.1007/s00205-016-1007-x (pages 30, 31).

[95] Thomas J Pence and Kun Gou. "On compressible versions of the incompressible neo-Hookean material". en. In: *Mathematics and Mechanics of Solids* 20.2 (Feb. 2015), pp. 157–182. ISSN: 1081-2865, 1741-3028. DOI: 10.1177/1081286514544258. URL: http://journals.sagepub.com/doi/10.1177/1081286514544258 (page 32).

[96] Allan F. Bower. *Applied mechanics of solids*. OCLC: ocn277196164. Boca Raton: CRC Press, 2010. ISBN: 978-1-4398-0247-2 (page 32).

[97] Silvia Budday and Paul Steinmann. “On the influence of inhomogeneous stiffness and growth on mechanical instabilities in the developing brain”. In: *International Journal of Solids and Structures* 132-133 (Feb. 2018), pp. 31–41. DOI: `10.1016/j.ijsolstr.2017.08.010`. URL: `https://doi.org/10.1016/j.ijsolstr.2017.08.010` (page 32).

[98] M.H. Sadd. *Elasticity: Theory, Applications, and Numerics*. Elsevier Science, 2014. ISBN: 978-0-12-410432-7 (page 32).

[99] Kip S Thorne and Roger D Blandford. *Modern classical physics: optics, fluids, plasmas, elasticity, relativity, and statistical physics*. English. ISBN: 9781400874484 OCLC: 1145892621. 2017 (page 35).

[100] Edward K. Rodriguez, Anne Hoger, and Andrew D. McCulloch. “Stress-dependent finite growth in soft elastic tissues”. In: *Journal of Biomechanics* 27.4 (1994), pp. 455–467. ISSN: 0021-9290. DOI: `http://dx.doi.org/10.1016/0021-9290(94)90021-3`. URL: `http://www.sciencedirect.com/science/article/pii/0021929094900213` (pages 36, 53).

[101] S. Q. Liu and Y. C. Fung. “Zero-Stress States of Arteries”. In: *Journal of Biomechanical Engineering* 110.1 (Feb. 1, 1988), pp. 82–84. ISSN: 0148-0731. DOI: `10.1115/1.3108410`. URL: `https://asmedigitalcollection.asme.org/biomechanical/article/110/1/82/395434/Zero-Stress-States-of-Arteries` (page 36).

[102] H. C. Han and Y. C. Fung. “Residual strains in porcine and canine trachea”. In: *Journal of Biomechanics* 24.5 (Jan. 1, 1991), pp. 307–315. ISSN: 0021-9290. DOI: `10.1016/0021-9290(91)90349-R`. URL: `http://www.sciencedirect.com/science/article/pii/002192909190349R` (page 36).

[103] J. P. Xie et al. “The Zero-Stress State of Rat Veins and Vena Cava”. In: *Journal of Biomechanical Engineering* 113.1 (Feb. 1, 1991), pp. 36–41. ISSN: 0148-0731. DOI: `10.1115/1.2894083`. URL: `https://asmedigitalcollection.asme.org/biomechanical/article/113/1/36/399244/The-Zero-Stress-State-of-Rat-Veins-and-Vena-Cava` (page 36).

[104] J. N. Reddy. *An Introduction to the Finite Element Method*. McGraw-Hill Education, 2005. ISBN: 978-0-07-246685-0 (pages 39, 40, 46, 49).

[105] M. J. TURNER et al. “Stiffness and Deflection Analysis of Complex Structures”. In: *Journal of the Aeronautical Sciences* 23.9 (1956), pp. 805–823. DOI: `10.2514/8.3664`. URL: `https://doi.org/10.2514/8.3664` (page 39).

[106] R. W. CLOUGH. “The Finite Element Method in Plane Stress Analysis”. In: *Proceedings of 2nd ASCE Conference on Electronic Computation, Pittsburgh Pa., Sept. 8 and 9, 1960* (1960). URL: `https://ci.nii.ac.jp/naid/10027962709/` (page 39).

[107] Vivette Girault and Pierre-Arnaud Raviart. *Finite Element Methods for Navier-Stokes Equations: Theory and Algorithms*. Springer Series in Computational Mathematics. Berlin Heidelberg: Springer-Verlag, 1986. ISBN: 978-3-642-64888-5. DOI: `10.1007/978-3-642-61623-5`. URL: `https://www.springer.com/gp/book/9783642648885` (page 39).

[108] Jian-Ming Jin. *The Finite Element Method in Electromagnetics*. 3 edition. Hoboken. New Jersey: Wiley-IEEE Press, Mar. 31, 2014. 876 pp. ISBN: 978-1-118-57136-1 (page 39).

[109] Ophélie Foubet, Miguel Trejo, and Roberto Toro. “Mechanical morphogenesis and the development of neocortical organisation”. In: *Cortex* (Mar. 2018). DOI: `10.1016/j.cortex.2018.03.005`. URL: `https://doi.org/10.1016/j.cortex.2018.03.005` (page 39).

[110] John DePree and Charles Swartz. *Introduction to Real Analysis*. 1 edition. New York: Wiley, June 14, 1988. 355 pp. ISBN: 978-0-471-85391-6 (page 40).

[111] William H. Press et al. *Numerical Recipes 3rd Edition: The Art of Scientific Computing*. 3 edition. Cambridge, UK; New York: Cambridge University Press, Sept. 6, 2007. 1256 pp. ISBN: 978-0-521-88068-8 (pages 41, 48, C 11).

[112] J. C. Nedelec. “Mixed finite elements in $\mathbb R^3$”. In: *Numerische Mathematik* 35.3 (Sept. 1, 1980), pp. 315–341. ISSN: 0945-3245. DOI: `10.1007/BF01396415`. URL: `https://doi.org/10.1007/BF01396415` (page 44).

[113] Ivo Babuska. “The finite element method with penalty”. en. In: *Mathematics of Computation* 27.122 (May 1973), pp. 221–221. ISSN: 0025-5718. DOI: `10.1090/S0025-5718-1973-0351118-5`. URL: `http://www.ams.org/jourcgi/jour-getitem?pii=S0025-5718-1973-0351118-5` (page 46).

[114] Mika Juntunen and Rolf Stenberg. “Nitsche’s method for general boundary conditions”. en. In: *Mathematics of Computation* 78.267 (Sept. 2009), pp. 1353–1374. ISSN: 0025-5718, 1088-6842. DOI: `10.1090/S0025-5718-08-02183-2`. URL: `http://www.ams.org/jourcgi/jour-getitem?pii=S0025-5718-08-02183-2` (page 46).

[115] Jorge Nocedal and Stephen J. Wright. *Numerical optimization.* 2. ed. Springer series in operations research and financial engineering. New York, NY: Springer, 2006. XXII, 664. ISBN: 978-0-387-30303-1. URL: `http://gso.gbv.de/DB=2.1/CMD?ACT=SRCHA&SRT=YOP&IKT=1016&TRM=ppn+502988711&sourceid=fbw_bibsonomy` (pages 47, C 9, C 13).

[116] Daniele Bertaccini and Fabio Durastante. *Iterative Methods and Preconditioning for Large and Sparse Linear Systems with Applications.* Boca Raton: Taylor & Francis Inc, Feb. 22, 2018. 354 pp. ISBN: 978-1-4987-6416-2 (page 50).

[117] Loup Verlet. “Computer "Experiments" on Classical Fluids. I. Thermodynamical Properties of Lennard-Jones Molecules”. en. In: *Physical Review* 159.1 (July 1967), pp. 98–103. ISSN: 0031-899X. DOI: `10.1103/PhysRev.159.98`. URL: `https://link.aps.org/doi/10.1103/PhysRev.159.98` (page 50).

[118] Gerhard Besold et al. “Towards better integrators for dissipative particle dynamics simulations”. en. In: *Physical Review E* 62.6 (Dec. 2000), R7611–R7614. ISSN: 1063-651X, 1095-3787. DOI: `10.1103/PhysRevE.62.R7611`. URL: `https://link.aps.org/doi/10.1103/PhysRevE.62.R7611` (page 50).

[119] G. Alzetta et al. “The deal.II Library, Version 9.0”. In: *Journal of Numerical Mathematics* 26.4 (2018), pp. 173–183. DOI: `10.1515/jnma-2018-0054` (pages 53, 63).

[120] W. Bangerth, R. Hartmann, and G. Kanschat. “deal.II – a General Purpose Object Oriented Finite Element Library”. In: *ACM Trans. Math. Softw.* 33.4 (2007), pp. 24/1–24/27 (pages 53, 63).

[121] Christophe Geuzaine and Jean-François Remacle. “Gmsh: A 3-D finite element mesh generator with built-in pre- and post-processing facilities”. en. In: *International Journal for Numerical Methods in Engineering* 79.11 (Sept. 2009), pp. 1309–1331. ISSN: 00295981, 10970207. DOI: `10.1002/nme.2579`. URL: `http://doi.wiley.com/10.1002/nme.2579` (page 54).

[122] Martin Kronbichler and Katharina Kormann. “A Generic Interface for Parallel Cell-Based Finite Element Operator Application”. In: *Computers & Fluids* 63 (June 2012), pp. 135–147. ISSN: 00457930. DOI: `10.1016/j.compfluid.2012.04.012`. URL: `https://linkinghub.elsevier.com/retrieve/pii/S0045793012001429` (page 56).

[123] Utkarsh Ayachit. *The ParaView Guide: Updated for ParaView Version 4.3.* Ed. by Lisa Avila. In collab. with Berk Geveci. Full color version. Los Alamos: Kitware, 2015. 261 pp. ISBN: 978-1-930934-30-6 (page 57).

[124] Hank Childs et al. “VisIt: An End-User Tool for Visualizing and Analyzing Very Large Data”. In: *High Performance Visualization Enabling Extreme-Scale Scientific Insight.* Oct. 2012, pp. 357–372 (page 57).

[125] Jerrold E. Marsden and Thomas J. R. Hughes. *Mathematical foundations of elasticity.* New York: Dover, 1994. ISBN: 978-0-486-67865-8 (page 58).

[126] Breannan Smith, Fernando De Goes, and Theodore Kim. “Stable Neo-Hookean Flesh Simulation”. In: *ACM Trans. Graph.* 37.2 (Mar. 2018), 12:1–12:15. ISSN: 0730-0301. DOI: `10.1145/3180491`. URL: `http://doi.acm.org/10.1145/3180491` (page 58).

[127] David H. Eberly. *Game physics.* 2nd ed. Interactive 3D technology series. OCLC: ocn482580968. Burlington, MA: Morgan Kaufmann/Elsevier, 2010. ISBN: 978-0-12-374903-1 (page 59).

[128] Steven G. Krantz. *Handbook of complex variables.* Boston, Mass: Birkhuser, 1999. ISBN: 978-0-8176-4011-8 (page 59).

[129] Aleka McAdams et al. “Efficient elasticity for character skinning with contact and collisions”. en. In: *ACM Transactions on Graphics* 30.4 (July 2011), p. 1. ISSN: 07300301. DOI: `10.1145/2010324.1964932`. URL: `http://portal.acm.org/citation.cfm?doid=2010324.1964932` (pages 59, 73).

[130] J. C Butcher. *Numerical Methods for Ordinary Differential Equations.* 2016. ISBN: 978-1-119-12153-4 978-1-119-12151-0. URL: `http://site.ebrary.com/id/11235763` (page 60).

[131] J.-F. Remacle et al. "Blossom-Quad: A non-uniform quadrilateral mesh generator using a minimum-cost perfect-matching algorithm". en. In: *International Journal for Numerical Methods in Engineering* 89.9 (Mar. 2012), pp. 1102–1119. ISSN: 00295981. DOI: `10.1002/nme.3279`. URL: `http://doi.wiley.com/10.1002/nme.3279` (page 61).

[132] J.-F. Remacle et al. "A frontal Delaunay quad mesh generator using the L^∞ norm". en. In: *International Journal for Numerical Methods in Engineering* 94.5 (May 2013), pp. 494–512. ISSN: 00295981. DOI: `10.1002/nme.4458`. URL: `http://doi.wiley.com/10.1002/nme.4458` (page 61).

[133] Mikhail Artemyev. *martemyev/tethex*. original-date: 2015-03-13T15:57:41Z. May 2020. URL: `https://github.com/martemyev/tethex` (page 61).

[134] Lyndon Clarke, Ian Glendinning, and Rolf Hempel. "The MPI Message Passing Interface Standard". en. In: *Programming Environments for Massively Parallel Distributed Systems*. Ed. by Karsten M. Decker and René M. Rehmann. Monte Verità. Basel: Birkhäuser, 1994, pp. 213–218. ISBN: 978-3-0348-8534-8. DOI: `10.1007/978-3-0348-8534-8_21` (pages 61, 62).

[135] Message Passing Interface Forum. *MPI: A Message-Passing Interface Standard, Version 3.1*. High Performance Computing Center Stuttgart (HLRS), June 2015 (pages 61, 62).

[136] Timothy G. Mattson, Yun He, and Alice Evelyn Koniges. *The OpenMP Common Core: Making OpenMP Simple Again*. Scientific and Engineering Computation. Cambridge, Massachusetts: The MIT Press, 2019. ISBN: 978-0-262-53886-2 (page 62).

[137] Richard L. Graham, Timothy S. Woodall, and Jeffrey M. Squyres. "Open MPI: A Flexible High Performance MPI". en. In: *Parallel Processing and Applied Mathematics*. Ed. by Roman Wyrzykowski et al. Lecture Notes in Computer Science. Berlin, Heidelberg: Springer, 2006, pp. 228–239. ISBN: 978-3-540-34142-0. DOI: `10.1007/11752578_29` (page 62).

[138] George Karypis and Vipin Kumar. "Multilevelk-way Partitioning Scheme for Irregular Graphs". en. In: *Journal of Parallel and Distributed Computing* 48.1 (Jan. 1998), pp. 96–129. ISSN: 0743-7315. DOI: `10.1006/jpdc.1997.1404`. URL:

`http://www.sciencedirect.com/science/article/pii/S0743731597914040` (page 62).

[139] Dominique Lasalle and George Karypis. “Multi-threaded Graph Partitioning”. In: *2013 IEEE 27th International Symposium on Parallel and Distributed Processing*. Cambridge, MA, USA: IEEE, May 2013, pp. 225–236. ISBN: 978-1-4673-6066-1 978-0-7695-4971-2. DOI: `10.1109/IPDPS.2013.50`. URL: `http://ieeexplore.ieee.org/document/6569814/` (page 62).

[140] Satish Balay et al. *PETSc Web page*. 2019. URL: `http://www.mcs.anl.gov/petsc` (page 63).

[141] Satish Balay et al. *PETSc Users Manual*. Tech. rep. ANL-95/11 - Revision 3.11. Argonne National Laboratory, 2019. URL: `http://www.mcs.anl.gov/petsc` (page 63).

[142] Satish Balay et al. “Efficient Management of Parallelism in Object Oriented Numerical Software Libraries”. In: *Modern Software Tools in Scientific Computing*. Ed. by E. Arge, A. M. Bruaset, and H. P. Langtangen. Birkhäuser Press, 1997, pp. 163–202 (page 63).

[143] Senjiang Yu et al. “Harnessing Fold-to-Wrinkle Transition and Hierarchical Wrinkling on Soft Material Surfaces by Regulating Substrate Stiffness and Sputtering Flux”. In: *Soft Matter* 14.32 (2018), pp. 6745–6755. ISSN: 1744-683X, 1744-6848. DOI: `10.1039/C8SM01287C`. URL: `http://xlink.rsc.org/?DOI=C8SM01287C` (pages 65, 112).

[144] Lucas da Costa Campos et al. “The Role of Thickness Inhomogeneities in Hierarchical Cortical Folding”. In: *NeuroImage* 231 (May 2021), p. 117779. ISSN: 10538119. DOI: `10.1016/j.neuroimage.2021.117779`. URL: `https://linkinghub.elsevier.com/retrieve/pii/S1053811921000562` (pages 67, 98).

[145] Th. Ludw. Wilh. Bischoff. *Die Grosshirnwindungen des Menschen mit Berücksichtigung ihrer Entwicklung bei dem Fötus und ihrer Anordnung bei den Affen.* Mänchen: Verlag der Akademie, 1868 (page 68).

[146] D. J. Cunningham. “The Complete Fissures of the Human Cerebrum, and their Significance in Connection with the Growth of the Hemisphere and the Appearance of the Occipital Lobe”. In: *Journal of Anatomy and Physiology* 24.Pt 3 (Apr. 1890), pp. 309–345. URL: `https://www.ncbi.nlm.nih.gov/pmc/articles/PMC1328054/` (page 68).

[147] N. J. Hoff and S. E. Mautner. “The Buckling of Sandwich-Type Panels”. en. In: *Journal of the Aeronautical Sciences* 12.3 (July 1945), pp. 285–297. ISSN: 1936-9956. DOI: `10.2514/8.11246`. URL: `https://arc.aiaa.org/doi/10.2514/8.11246` (page 68).

[148] M. A Biot. “Folding instability of a layered viscoelastic medium under compression”. In: *Proceedings of the Royal Society of London. Series A. Mathematical and Physical Sciences* 242.1231 (1957), pp. 444–454. ISSN: 2053-9169. DOI: `10.1098/rspa.1957.0187`. URL: `http://www.royalsocietypublishing.org/doi/10.1098/rspa.1957.0187` (pages 68, 86).

[149] Hans Ramberg. “Folding of laterally compressed multilayers in the field of gravity, I”. en. In: *Physics of the Earth and Planetary Interiors* 2.4 (June 1970), pp. 203–232. ISSN: 00319201. DOI: `10.1016/0031-9201(70)90010-5`. URL: `https://linkinghub.elsevier.com/retrieve/pii/0031920170900105` (page 68).

[150] Silvia Budday et al. “Wrinkling instabilities in soft bilayered systems”. en. In: *Philosophical Transactions of the Royal Society A: Mathematical, Physical and Engineering Sciences* 375.2093 (May 2017), p. 20160163. ISSN: 1364-503X, 1471-2962. DOI: `10.1098/rsta.2016.0163`. URL: `https://royalsocietypublishing.org/doi/10.1098/rsta.2016.0163` (pages 69, 86).

[151] Hugues Vandeparre et al. “Hierarchical wrinkling patterns”. en. In: *Soft Matter* 6.22 (2010), p. 5751. ISSN: 1744-683X, 1744-6848. DOI: `10.1039/c0sm00394h`. URL: `http://xlink.rsc.org/?DOI=c0sm00394h` (page 69).

[152] P.V. Bayly, L.A. Taber, and C.D. Kroenke. “Mechanical forces in cerebral cortical folding: A review of measurements and models”. In: *Journal of the Mechanical Behavior of Biomedical Materials* 29 (2014), pp. 568–581. ISSN: 1751-6161. DOI: `http://doi.org/10.1016/j.jmbbm.2013.02.018`. URL: `http://www.sciencedirect.com/science/article/pii/S175161611300074X` (page 69).

[153] Tao Sun and Robert F. Hevner. “Growth and folding of the mammalian cerebral cortex: from molecules to malformations”. In: *Nature Reviews Neuroscience* 15.4 (Mar. 2014), pp. 217–232. DOI: `10.1038/nrn3707`. URL: `https://doi.org/10.1038/nrn3707` (pages 69, 85).

[154] D.P. Richman et al. “Mechanical model of brain convolutional development”. In: *Science* 189.4196 (1975), pp. 18–21. ISSN: 0036-8075. DOI: `10.1126/science.1135626`. URL: `http://science.sciencemag.org/content/189/4196/18` (pages 69, 70, 109).

[155] P. V. Bayly et al. “A Cortical Folding Model Incorporating Stress-Dependent Growth Explains Gyral Wavelengths and Stress Patterns in the Developing Brain”. In: *Physical Biology* 10.1 (2013), p. 016005. DOI: `10.1088/1478-3975/10/1/016005`. URL: `https://doi.org/10.1088/1478-3975/10/1/016005` (pages 69, 86).

[156] Silvia Budday, Paul Steinmann, and Ellen Kuhl. “The role of mechanics during brain development”. In: *Journal of the Mechanics and Physics of Solids* 72 (2014), pp. 75–92. ISSN: 0022-5096. DOI: `http://doi.org/10.1016/j.jmps.2014.07.010`. URL: `http://www.sciencedirect.com/science/article/pii/S0022509614001483` (pages 69, 70, 83, 109).

[157] Roberto Toro and Yves Burnod. “A Morphogenetic Model for the Development of Cortical Convolutions”. In: *Cerebral Cortex* 15.12 (Mar. 2005), pp. 1900–1913. DOI: `10.1093/cercor/bhi068`. URL: `https://doi.org/10.1093/cercor/bhi068` (pages 69, 70, 83–85, 109).

[158] Gang Xu et al. “Axons Pull on the Brain, But Tension Does Not Drive Cortical Folding”. In: *Journal of Biomechanical Engineering* 132.7 (June 2010), pp. 071013-071013–8. ISSN: 0148-0731. DOI: `10.1115/1.4001683`. URL: `http://dx.doi.org/10.1115/1.4001683` (pages 69, 70).

[159] Silvia Budday et al. “Mechanical properties of gray and white matter brain tissue by indentation”. In: *Journal of the Mechanical Behavior of Biomedical Materials* 46 (June 2015), pp. 318–330. DOI: `10.1016/j.jmbbm.2015.02.024`. URL: `https://doi.org/10.1016/j.jmbbm.2015.02.024` (pages 69, 70).

[160] Michael A. Green, Lynne E. Bilston, and Ralph Sinkus. “In vivobrain viscoelastic properties measured by magnetic resonance elastography”. In: *NMR in Biomedicine* 21.7 (Aug. 2008), pp. 755–764. DOI: `10.1002/nbm.1254`. URL: `https://doi.org/10.1002/nbm.1254` (page 69).

[161] Curtis L. Johnson et al. “Local mechanical properties of white matter structures in the human brain”. In: *NeuroImage* 79 (Oct. 2013), pp. 145–152. DOI: `10.1016/j.neuroimage.2013.04.089`. URL: `https://doi.org/10.1016/j.neuroimage.2013.04.089` (page 69).

[162] A. Manduca et al. “Magnetic resonance elastography: Non-invasive mapping of tissue elasticity”. In: *Medical Image Analysis* 5.4 (Dec. 2001), pp. 237–254. DOI: `10.1016/s1361-8415(00)00039-6`. URL: `https://doi.org/10.1016/s1361-8415(00)00039-6` (page 69).

[163] Paul J. McCracken et al. “Mechanical transient-based magnetic resonance elastography”. In: *Magnetic Resonance in Medicine* 53.3 (2005), pp. 628–639. DOI: `10.1002/mrm.20388`. URL: `https://doi.org/10.1002/mrm.20388` (page 69).

[164] J.A.W. van Dommelen et al. “Mechanical properties of brain tissue by indentation: Interregional variation”. In: *Journal of the Mechanical Behavior of Biomedical Materials* 3.2 (Feb. 2010), pp. 158–166. DOI: `10.1016/j.jmbbm.2009.09.001`. URL: `https://doi.org/10.1016/j.jmbbm.2009.09.001` (page 69).

[165] Tuomas Tallinen et al. “On the growth and form of cortical convolutions”. In: *Nat Phys* 12.6 (June 2016). Letter, pp. 588–593. ISSN: 1745-2473. URL: `http://dx.doi.org/10.1038/nphys3632` (pages 69, 86).

[166] David C. van Essen. “A tension-based theory of morphogenesis and compact wiring in the central nervous system”. In: *Nature* 385.6614 (Jan. 1997), pp. 313–318. DOI: `10.1038/385313a0`. URL: `http://dx.doi.org/10.1038/385313a0` (pages 69, 86).

[167] Jochen Hinz et al. “Isogeometric Analysis of the Gray-Scott Reaction-Diffusion Equations for Pattern Formation on Evolving Surfaces and Applications to Human Gyrification”. In: *arXiv:1910.12588 [cs, math]* (Oct. 2019). arXiv: 1910.12588. URL: `http://arxiv.org/abs/1910.12588` (page 69).

[168] S.N. Verner and K. Garikipati. “A computational study of the mechanisms of growth-driven folding patterns on shells, with application to the developing brain”. In: *Extreme Mechanics Letters* 18 (2018), pp. 58–69. ISSN: 2352-4316. DOI: `https://doi.org/10.1016/j.eml.2017.11.003`. URL: `http://www.sciencedirect.com/science/article/pii/S235243161730144X` (page 69).

[169] Isabel Reillo et al. “A Role for Intermediate Radial Glia in the Tangential Expansion of the Mammalian Cerebral Cortex”. In: *Cerebral Cortex* 21.7 (2011), pp. 1674–1694. ISSN: 1460-2199, 1047-3211. DOI: `10.1093/cercor/bhq238`. URL: `https://academic.oup.com/cercor/article-lookup/doi/10.1093/cercor/bhq238` (page 70).

[170] Este Armstrong et al. “The Ontogeny of Human Gyrification”. In: *Cerebral Cortex* 5.1 (Jan. 1995), pp. 56–63. ISSN: 1047-3211. DOI: `10.1093/cercor/5.1.56`. URL: `https://doi.org/10.1093/cercor/5.1.56` (page 70).

[171] Katja Heuer and Roberto Toro. “Role of mechanical morphogenesis in the development and evolution of the neocortex”. en. In: *Physics of Life Reviews* (Jan. 2019), S157106451930020X. ISSN: 15710645. DOI: `10.1016/j.plrev.2019.01.012`. URL: `https://linkinghub.elsevier.com/retrieve/pii/S157106451930020X` (page 70).

[172] Bruno Mota and Suzana Herculano-Houzel. “Cortical folding scales universally with surface area and thickness, not number of neurons”. In: *Science* 349.6243 (2015), pp. 74–77. ISSN: 0036-8075. DOI: `10.1126/science.aaa9101`. URL: `http://science.sciencemag.org/content/349/6243/74` (page 70).

[173] G. Alzetta et al. “The `deal.II` Library, Version 9.0”. In: *Journal of Numerical Mathematics* 26.4 (2018), pp. 173–183. DOI: `10.1515/jnma-2018-0054` (page 71).

[174] W. Bangerth, R. Hartmann, and G. Kanschat. “deal.II – a General Purpose Object Oriented Finite Element Library”. In: *ACM Trans. Math. Softw.* 33.4 (2007), pp. 24/1–24/27 (page 71).

[175] Satish Balay et al. *PETSc Web page*. `http://www.mcs.anl.gov/petsc`. 2019. URL: `http://www.mcs.anl.gov/petsc` (page 71).

[176] Satish Balay et al. *PETSc Users Manual.* Tech. rep. ANL-95/11 - Revision 3.11. Argonne National Laboratory, 2019. URL: `http://www.mcs.anl.gov/petsc` (page 71).

[177] Javier Bonet, Antonio J. Gil, and Richard D. Wood. *Nonlinear Solid Mechanics for Finite Element Analysis: Statics.* Cambridge University Press, 2016. ISBN: 978-1107115798 (pages 71–73).

[178] Edward K. Rodriguez, Anne Hoger, and Andrew D. McCulloch. "Stress-dependent finite growth in soft elastic tissues". In: *Journal of Biomechanics* 27.4 (1994), pp. 455–467. ISSN: 0021-9290. DOI: `http://dx.doi.org/10.1016/0021-9290(94)90021-3`. URL: `http://www.sciencedirect.com/science/article/pii/0021929094900213` (page 71).

[179] Silvia Budday et al. "Size and curvature regulate pattern selection in the mammalian brain". In: *Extreme Mechanics Letters* 4 (2015), pp. 193–198. ISSN: 2352-4316. DOI: `https://doi.org/10.1016/j.eml.2015.07.004`. URL: `http://www.sciencedirect.com/science/article/pii/S2352431615000863` (pages 72, 85).

[180] S. Budday et al. "Mechanical characterization of human brain tissue". In: *Acta Biomaterialia* 48 (Jan. 2017), pp. 319–340. DOI: `10.1016/j.actbio.2016.10.036`. URL: `https://doi.org/10.1016/j.actbio.2016.10.036` (page 72).

[181] Jorge Nocedal and Stephen J. Wright. *Numerical optimization.* 2. ed. Springer series in operations research and financial engineering. New York, NY: Springer, 2006. XXII, 664. ISBN: 978-0-387-30303-1 (page 73).

[182] Jan Groenewold. "Wrinkling of plates coupled with soft elastic media". en. In: *Physica A: Statistical Mechanics and its Applications.* Statistical Thermodynamics and Colloid Science 298.1 (Sept. 2001), pp. 32–45. ISSN: 0378-4371. DOI: `10.1016/S0378-4371(01)00209-6`. URL: `http://www.sciencedirect.com/science/article/pii/S0378437101002096` (pages 74, 76, 83, 88, 109).

[183] E. Ventsel and T. Krauthammer. *Thin Plates and Shells: Theory: Analysis, and Applications.* Taylor & Francis, 2001. ISBN: 9780824705756 (page 79).

[184] Raphael Hornung. "Simulation of Growing Cell Sheets". PhD Thesis. Universität zu Köln, 2019. URL: `https://kups.ub.uni-koeln.de/10340/` (pages 80, 89, 94).

[185] Katrin Amunts et al. “BigBrain: An Ultrahigh-Resolution 3D Human Brain Model”. In: *Science* 340.6139 (2013), pp. 1472–1475. ISSN: 0036-8075. DOI: `10.1126/science.1235381`. URL: `https://science.sciencemag.org/content/340/6139/1472` (page 82).

[186] M. A Biot. “Bending of an Infinite Beam on an Elastic Foundation”. In: *Journal of Applied Mechanics* 59 (1937), A1–A7 (pages 83, 109).

[187] S. T. Bok. “Der Einfluß der in den Furchen und Windungen auftretenden Krümmungen der Großhirnrinde auf die Rindenarchitektur”. de. In: *Zeitschrift für die gesamte Neurologie und Psychiatrie* 121.1 (Dec. 1929), pp. 682–750. ISSN: 0303-4194. DOI: `10.1007/BF02864437`. URL: `http://link.springer.com/10.1007/BF02864437` (pages 84, 109).

[188] Maria Holland et al. “Symmetry Breaking in Wrinkling Patterns: Gyri Are Universally Thicker than Sulci”. In: *Physical Review Letters* 121.22 (Nov. 2018), p. 228002. DOI: `10.1103/PhysRevLett.121.228002`. URL: `https://link.aps.org/doi/10.1103/PhysRevLett.121.228002` (pages 84, 86, 93).

[189] Davide Riccobelli and Giulia Bevilacqua. “Surface tension controls the onset of gyrification in brain organoids”. en. In: *Journal of the Mechanics and Physics of Solids* 134 (Jan. 2020), p. 103745. ISSN: 0022-5096. DOI: `10.1016/j.jmps.2019.103745`. URL: `http://www.sciencedirect.com/science/article/pii/S0022509619304065` (page 84).

[190] Wally Welker. “Why Does Cerebral Cortex Fissure and Fold?” en. In: *Cerebral Cortex: Comparative Structure and Evolution of Cerebral Cortex, Part II*. Ed. by Edward G. Jones and Alan Peters. Cerebral Cortex. Boston, MA: Springer US, 1990, pp. 3–136. ISBN: 978-1-4615-3824-0. DOI: `10.1007/978-1-4615-3824-0_1`. URL: `https://doi.org/10.1007/978-1-4615-3824-0_1` (page 84).

[191] S. Geyer and R. Turner, eds. *Microstructural parcellation of the human cerebral cortex: from Brodman’s post-mortem map to in vivo mapping with high-field magnetic resonance imaging*. OCLC: ocn858958295. Heidelberg ; New York: Springer, 2013. ISBN: 978-3-642-37823-2 (page 85).

[192] Camino de Juan Romero and Víctor Borrell. “Genetic Maps and Patterns of Cerebral Cortex Folding”. In: *Current Opinion in Cell Biology* 49 (2017), pp. 31–37. ISSN: 09550674. DOI: `10.1016/j.ceb.2017.11.009`. URL: `https://linkinghub.elsevier.com/retrieve/pii/S0955067417300716` (page 85).

[193] Arnold Kriegstein, Stephen Noctor, and Verónica Martínez-Cerdeño. “Patterns of neural stem and progenitor cell division may underlie evolutionary cortical expansion”. en. In: *Nature Reviews Neuroscience* 7.11 (2006), pp. 883–890. ISSN: 1471-003X, 1471-0048. DOI: `10.1038/nrn2008`. URL: `http://www.nature.com/articles/nrn2008` (pages 85, 99, 101).

[194] D. Bray. “Axonal Growth in Response to Experimentally Applied Mechanical Tension”. In: *Developmental Biology* 102.2 (Apr. 1984), pp. 379–389. ISSN: 0012-1606. DOI: `10.1016/0012-1606(84)90202-1`. pmid: `6706005` (page 86).

[195] S. R. Heidemann and R. E. Buxbaum. “Mechanical Tension as a Regulator of Axonal Development”. In: *Neurotoxicology* 15.1 (1994), pp. 95–107. ISSN: 0161-813X. pmid: `8090366` (page 86).

[196] S. Chada et al. “Cytomechanics of Neurite Outgrowth from Chick Brain Neurons”. In: *Journal of Cell Science* 110 (Pt 10) (May 1997), pp. 1179–1186. ISSN: 0021-9533. pmid: `9191042` (page 86).

[197] Jonas Ranft et al. “Fluidization of tissues by cell division and apoptosis”. In: *Proceedings of the National Academy of Sciences* 107.49 (2010), pp. 20863–20868. ISSN: 0027-8424. DOI: `10.1073/pnas.1011086107`. URL: `http://www.pnas.org/content/107/49/20863` (page 86).

[198] S Budday et al. “Rheological characterization of human brain tissue.” In: *Acta biomaterialia* 60 (2017), pp. 315–329. ISSN: 1878-7568. DOI: `10.1016/j.actbio.2017.06.024` (page 86).

[199] Lichao Gao and Thomas J. McCarthy. “The "Lotus Effect" Explained: Two Reasons Why Two Length Scales of Topography Are Important”. en. In: *Langmuir* 22.7 (Mar. 2006), pp. 2966–2967. ISSN: 0743-7463, 1520-5827. DOI: `10.1021/la0532149`. URL: `https://pubs.acs.org/doi/10.1021/la0532149` (pages 86, 113).

[200] Abraham Marmur. “The Lotus Effect: Superhydrophobicity and Metastability”. en. In: *Langmuir* 20.9 (Apr. 2004), pp. 3517–3519. ISSN: 0743-7463, 1520-5827. DOI: `10.1021/la036369u`. URL: `https://pubs.acs.org/doi/10.1021/la036369u` (page 86).

[201] Anesia Auguste et al. “The role of substrate pre-stretch in post-wrinkling bifurcations”. en. In: *Soft Matter* 10.34 (July 2014), p. 6520. ISSN: 1744-683X, 1744-6848. DOI: `10.1039/C4SM01038H`. URL: `http://xlink.rsc.org/?DOI=C4SM01038H` (page 86).

[202] Jaydeep Sidhaye and Järgen A. Knoblich. “Brain Organoids: An Ensemble of Bioassays to Investigate Human Neurodevelopment and Disease”. In: *Cell Death & Differentiation* (June 1, 2020), pp. 1–16. ISSN: 1476-5403. DOI: `10.1038/s41418-020-0566-4`. URL: `https://www.nature.com/articles/s41418-020-0566-4` (pages 86, 112).

[203] Xuyu Qian, Hongjun Song, and Guo-li Ming. “Brain Organoids: Advances, Applications and Challenges”. In: *Development* 146.8 (Apr. 15, 2019). ISSN: 0950-1991, 1477-9129. DOI: `10.1242/dev.166074`. pmid: `30992274`. URL: `https://dev.biologists.org/content/146/8/dev166074` (pages 86, 112).

[204] Eyal Karzbrun et al. “Human Brain Organoids on a Chip Reveal the Physics of Folding”. In: *Nature Physics* 14.5 (5 May 2018), pp. 515–522. ISSN: 1745-2481. DOI: `10.1038/s41567-018-0046-7`. URL: `https://www.nature.com/articles/s41567-018-0046-7` (pages 86, 113).

[205] Jülich Supercomputing Centre. “JURECA: Modular supercomputer at Jülich Supercomputing Centre”. In: *Journal of large-scale research facilities* 4.A132 (2018). DOI: `10.17815/jlsrf-4-121-1`. URL: `http://dx.doi.org/10.17815/jlsrf-4-121-1` (page 87).

[206] E. Hannezo, J. Prost, and J.-F. Joanny. “Instabilities of Monolayered Epithelia: Shape and Structure of Villi and Crypts”. en. In: *Physical Review Letters* 107.7 (Aug. 2011), p. 078104. ISSN: 0031-9007, 1079-7114. DOI: `10.1103/PhysRevLett.107.078104`. URL: `https://link.aps.org/doi/10.1103/PhysRevLett.107.078104` (page 89).

[207] P. A. Habas et al. “Early Folding Patterns and Asymmetries of the Normal Human Brain Detected from in Utero MRI”. In: *Cerebral Cortex* 22.1 (Jan. 1, 2012), pp. 13–25. ISSN: 1047-3211, 1460-2199. DOI: `10.1093/cercor/bhr053`. URL: `https://academic.oup.com/cercor/article-lookup/doi/10.1093/cercor/bhr053` (page 101).

[208] Jonas Ranft et al. “Fluidization of Tissues by Cell Division and Apoptosis”. In: *Proceedings of the National Academy of Sciences* 107.49 (2010), pp. 20863–20868. ISSN: 0027-8424. DOI: `10.1073/pnas.1011086107`. URL: `http://www.pnas.org/content/107/49/20863` (page 111).

[209] Tobias Büscher et al. “Tissue Evolution: Mechanical Interplay of Adhesion, Pressure, and Heterogeneity”. In: *New Journal of Physics* 22.3 (Mar. 25, 2020), p. 033048. ISSN: 1367-2630. DOI: `10.1088/1367-2630/ab74a5`. URL: `https://iopscience.iop.org/article/10.1088/1367-2630/ab74a5` (page 111).

[210] Benot Perthame and Nicolas Vauchelet. “Incompressible Limit of a Mechanical Model of Tumour Growth with Viscosity”. In: *Philosophical Transactions of the Royal Society A: Mathematical, Physical and Engineering Sciences* 373.2050 (Sept. 13, 2015), p. 20140283. ISSN: 1364-503X, 1471-2962. DOI: `10.1098/rsta.2014.0283`. URL: `https://royalsocietypublishing.org/doi/10.1098/rsta.2014.0283` (page 111).

[211] S. Tlili et al. “Migrating Epithelial Monolayer Flows Like a Maxwell Viscoelastic Liquid”. In: *Physical Review Letters* 125.8 (Aug. 18, 2020), p. 088102. ISSN: 0031-9007, 1079-7114. DOI: `10.1103/PhysRevLett.125.088102`. URL: `https://link.aps.org/doi/10.1103/PhysRevLett.125.088102` (page 111).

[212] S. Budday et al. “Viscoelastic Parameter Identification of Human Brain Tissue”. In: *Journal of the Mechanical Behavior of Biomedical Materials* 74 (Oct. 2017), pp. 463–476. DOI: `10.1016/j.jmbbm.2017.07.014`. URL: `https://doi.org/10.1016/j.jmbbm.2017.07.014` (page 111).

[213] Silvia Budday et al. “Mechanical Properties of Gray and White Matter Brain Tissue by Indentation”. In: *Journal of the Mechanical Behavior of Biomedical Materials* 46 (June 2015), pp. 318–330. DOI: `10.1016/j.jmbbm.2015.02.024`. URL: `https://doi.org/10.1016/j.jmbbm.2015.02.024` (page 111).

[214] Chuanyong Zong et al. “Photocontrollable Wrinkle Morphology Evolution on Azo-Based Multilayers for Hierarchical Surface Micropatterns Fabrication”. In: *Langmuir* 35.7 (Feb. 19, 2019), pp. 2601–2609. ISSN: 0743-7463, 1520-5827. DOI: `10.1021/acs.langmuir.8b04237`. URL: `https://pubs.acs.org/doi/10.1021/acs.langmuir.8b04237` (page 112).

[215] Andreu Mas-Colell. *Microeconomic Theory.* Oxford University Press, June 1995. ISBN: 0195073401. URL: `https://www.xarg.org/ref/a/0195073401/` (page C 9).

[216] Ian Goodfellow, Yoshua Bengio, and Aaron Courville. *Deep Learning.* MIT Press, 2016. URL: `http://www.deeplearningbook.org` (page C 9).

[217] Tjalling J. Ypma. “Historical Development of the Newton–Raphson Method”. In: *SIAM Review* 37.4 (Dec. 1995), pp. 531–551. DOI: `10.1137/1037125`. URL: `https://doi.org/10.1137/1037125` (page C 11).

Appendix A

The directional derivative

A.1 Definition

This derivative expands the idea of the usual derivative, from the Euclidean fields to general items. The item can be mostly anything: matrices, determinants, functions, etc., and it can depend on any other, equally general, item. It then exposes how the item changes for a small perturbation in their dependencies. We use the following notation to denote the direction derivative of a given item $\mathcal{F}$

$$D\mathcal{F}(\mathbf{x})[\delta\mathbf{x}] \triangleq \left.\frac{d\mathcal{F}(\mathbf{x}+\varepsilon\delta\mathbf{x})}{d\varepsilon}\right|_{\varepsilon=0}, \varepsilon \in \mathbb{R} \tag{A.1}$$

This equation can be read as the change in the item $\mathcal{F}$ starting in the position $\mathbf{x}$ in the direction $\delta\mathbf{x}$.

A.2 Properties

- Linearity in the direction:

  $D\mathcal{F}(\mathbf{x})[\delta\mathbf{x}_1 + \delta\mathbf{x}_2] = D\mathcal{F}(\mathbf{x})[\delta\mathbf{x}_1] + D\mathcal{F}(\mathbf{x})[\delta\mathbf{x}_2]$

- Lineary in the argument:

  $D(\mathcal{F}_1(\mathbf{x}) + \mathcal{F}_2(\mathbf{x}))[\delta\mathbf{x}] = D\mathcal{F}_1(\mathbf{x})[\delta\mathbf{x}] + D\mathcal{F}_2(\mathbf{x})[\delta\mathbf{x}]$

- Leibniz rule for products:

$$D(\mathcal{F}_1(\mathbf{x}) \cdot \mathcal{F}_2(\mathbf{x}))[\delta \mathbf{x}] = D\mathcal{F}_1(\mathbf{x})[\delta \mathbf{x}] \cdot \mathcal{F}_2(\mathbf{x}) + \mathcal{F}_1(\mathbf{x}) \cdot D\mathcal{F}_2(\mathbf{x})[\delta \mathbf{x}]$$

- Chain rule:

$$D\mathcal{F}_1(\mathcal{F}_2(\mathbf{x}))[\delta \mathbf{x}] = \mathcal{F}_1(\mathcal{F}_2(\mathbf{x}))[D\mathcal{F}_2(\mathbf{x})[\delta \mathbf{x}]]$$

A.3 Useful linearizations

In order to calculate the linearization of the stress, it is advantageous to first perform the linearization of the gradient deformation tensor **F** as

$$\begin{aligned} D\mathbf{F}(\mathbf{u})[\delta \mathbf{v}] =& \left.\frac{d\mathbf{F}(\mathbf{u} + \varepsilon \delta \mathbf{v})}{d\varepsilon}\right|_{\varepsilon=0} \\ =& \left.\frac{d}{d\varepsilon} \frac{\partial(\mathbf{u} + \varepsilon \delta \mathbf{v})}{\partial \mathbf{X}}\right|_{\varepsilon=0} \\ =& \left.\frac{d}{d\varepsilon}\left(\frac{\partial \mathbf{u}}{\partial \mathbf{X}} + \varepsilon \frac{\partial(\delta \mathbf{v})}{\partial \mathbf{X}}\right)\right|_{\varepsilon=0} \\ =& \frac{\partial(\delta \mathbf{v})}{\partial \mathbf{X}} \\ =& \nabla_0(\delta \mathbf{v}). \end{aligned}$$

Using the chain rule as defined in Sec. A.2, it is possible to write

$$D\Psi(\mathbf{F}(\mathbf{u}))[\delta \mathbf{v}] = D\Psi(\mathbf{F})[D\mathbf{F}(\mathbf{u})[\delta \mathbf{v}]], \tag{A.2}$$

where the linearization of the gradient deformation tensor is then applied to find

$$\begin{aligned} D\Psi(\mathbf{F}(\mathbf{u}))[\delta \mathbf{v}] =& D\Psi(\mathbf{F})[\nabla_0 \delta \mathbf{v}] \\ =& \left.\frac{d\Psi(\mathbf{F} + \varepsilon \nabla_0 \delta \mathbf{v})}{d\varepsilon}\right|_{\varepsilon=0} \\ =& \left.\frac{\partial \Psi(\mathbf{F})}{\partial \mathbf{F}} : \frac{d(\mathbf{F} + \varepsilon \nabla_0 \delta \mathbf{v})}{d\varepsilon}\right|_{\varepsilon=0} \\ =& \mathbf{P} : \nabla_0 \delta \mathbf{v}. \end{aligned} \tag{A.3}$$

This is the linearization used in Sec. 2.1.4.

Appendix B

Example of FEM – the Poisson equation

B.1 Weak form

As a toy example, the Poisson equation, which describes the electric potential field $\phi_e(x)$ generated by a charge density $\rho_e(x)$, will be used. In order to simplify the treatment below, a simple boundary condition is used, in which the potential is set in the borders of the system to zero. This problem can be stated as

$$\frac{d^2\phi_e(x)}{dx^2} = \rho_e(x), \text{ with } \phi_e(0) = \phi_e(1) = 0. \tag{B.1}$$

The differential problem stated in Eq. B.1 can be replaced by its weak form

$$\int_0^1 v(x)\frac{d^2\phi_e(x)}{dx^2}dx = \int_0^1 v(x)\rho_e(x)dx. \tag{B.2}$$

Using the partial integration theorem, the derivatives are distributed from the potential $\phi_e(x)$ to the weight function $v(x)$:

$$-\int_0^1 \frac{dv(x)}{dx}\frac{d\phi_e(x)}{dx}dx = \int_0^1 v(x)\rho_e(x)dx \tag{B.3}$$

Now not only was the weak form of Eq. B.1 obtained but also, and most importantly, while in Eq. B.1 the potential $\phi_e(x)$ must be a member of $\mathcal{C}^2$, in Eq. B.3 it must only belong to $\mathcal{C}^1$.

B.2 Function expansion

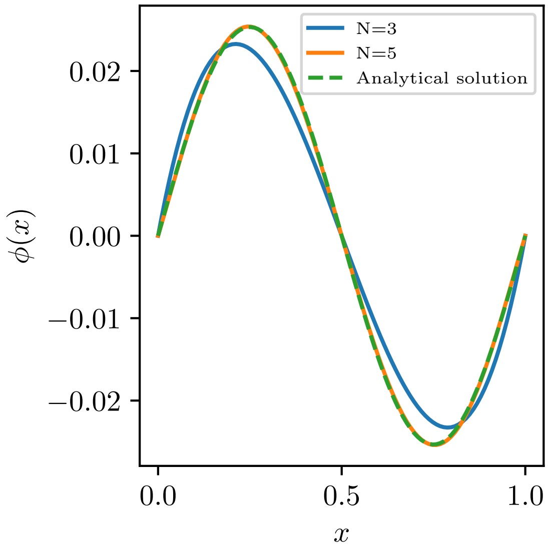

Figure B.1: Approximations using the weak form to solve the Poisson equation, where N indicated the number of terms in the approximating polynomial. .

Eq. B.1 is solved for $\rho_e(x) = -\sin(2\pi x)$ using terms up to third order, i.e, the polynomial base is composed of three terms, $\psi_0(x) = 1$, $\psi_1(x) = (1-x)x$, and $\psi_2(x) = (1-x)x^2$, with a generic element of the space being written as $\phi(x) = \phi_0 + \phi_1\psi_1(x) + \phi_2\psi_2(x)$. Using any of the two boundary conditions it is possible to see that ϕ_0 is necessarily equal to zero. Thus, it is removed, and the calculations are performed in a reduced system. This application of the necessary boundary conditions and consequential reduction in the number of degrees-of-freedeom is one of the first steps to be carried out in the application of the FEM method, as it spares the effort of spurious calculations[1]. The stiffness matrix $\mathbf{B}$ and force vector $\mathbf{l}$ of this problem are

$$B_{ij} = \int_0^1 \frac{d\psi_i}{dx}\frac{d\psi_j}{dx} \quad \text{and} \quad l_i = \int_0^1 \psi_i \rho_e(x)$$

---

[1] Had the constant term ϕ_0 been carried out to the next steps, the stiffness matrix would have an extra row a column filled with zeroes, leading to an ill-posed problem.

with values

$$\mathbf{B} = \begin{pmatrix} 1/3 & 1/6 \\ 1/6 & 2/15 \end{pmatrix} \quad \text{and} \quad \mathbf{l} = \begin{pmatrix} 0 \\ -3/4\pi^3 \end{pmatrix}.$$

The coefficients of the electric potential ϕ are then calculated by the inversion of the stiffness matrix $\mathbf{B}$,

$$\phi = \mathbf{B}^{-1}\mathbf{l} = \begin{pmatrix} -1 \\ 2 \end{pmatrix} \frac{30}{4\pi^3}$$

In Fig. B.1, the results of this approximation are shown with $N = 2$, as calculated here, and with $N = 4$.

B.3 Space discretization

The previous example is now expanded for the discretized system. In this example, the domain is discretized in five points, with spacing $\Delta x = 0.25$, using the Lagrange functions introduced in Eq. 2.42. Each element yields the reduced matrix

$$B^e_{ij} = (-1)^{\delta_{ij}+1} \frac{0.25}{\Delta x^2} = \begin{pmatrix} -4 & 4 \\ 4 & -4 \end{pmatrix} \tag{B.4}$$

The full-sized matrices for elements 1 and 2, are, for instance

$$B^{(1)}_{ij} = \begin{pmatrix} -4 & 4 & 0 & 0 & 0 \\ 4 & -4 & 0 & 0 & 0 \\ 0 & 0 & 0 & 0 & 0 \\ 0 & 0 & 0 & 0 & 0 \\ 0 & 0 & 0 & 0 & 0 \end{pmatrix} ; \; B^{(2)}_{ij} = \begin{pmatrix} 0 & 0 & 0 & 0 & 0 \\ 0 & -4 & 4 & 0 & 0 \\ 0 & 4 & -4 & 0 & 0 \\ 0 & 0 & 0 & 0 & 0 \\ 0 & 0 & 0 & 0 & 0 \end{pmatrix} \tag{B.5}$$

leading to total matrices $\mathbf{B}$ and $\mathbf{l}$

$$\mathbf{B} = \begin{pmatrix} -4 & 4 & 0 & 0 & 0 \\ 4 & -8 & 4 & 0 & 0 \\ 0 & 4 & -8 & 4 & 0 \\ 0 & 0 & 4 & -8 & 4 \\ 0 & 0 & 0 & 4 & -4 \end{pmatrix} ; \; \mathbf{l} = \begin{pmatrix} -0.058 \\ -0.203 \\ 0.000 \\ 0.203 \\ 0.058 \end{pmatrix} \tag{B.6}$$

One final step is required before the system is solved. The boundary conditions of the problem are imposed at this point. The weights $c_1 = c_5 = 0$ are set such that $u(0) = u(1) = 0$. Therefore, there is only the need to solve the *reduced* system

$$\mathbf{B}_{res}\mathbf{c}_{res} = \mathbf{l_{les}} \Rightarrow \begin{pmatrix} -8 & 4 & 0 \\ 4 & -8 & 4 \\ 0 & 4 & -8 \end{pmatrix} \begin{pmatrix} c_2 \\ c_3 \\ c_4 \end{pmatrix} = \begin{pmatrix} -0.203 \\ 0.000 \\ 0.203 \end{pmatrix} \tag{B.7}$$

to obtain

$$\mathbf{c} = \begin{pmatrix} 0.000 & 0.025 & 0.000 & -0.025 & 0.000 \end{pmatrix}^T \tag{B.8}$$

This numerical solution is seen in Fig. B.2, where the solution in a finer discretization is also shown.

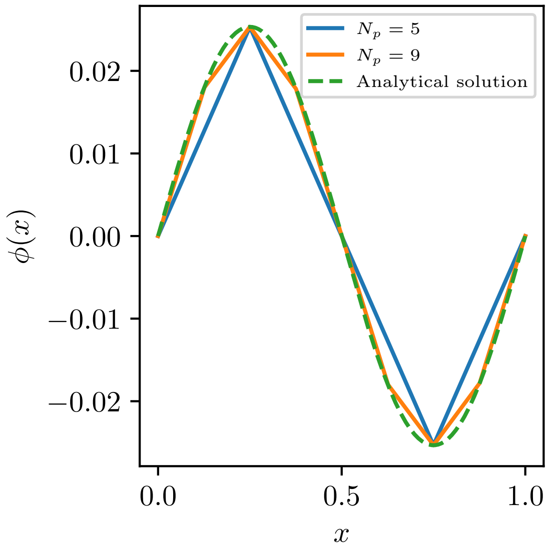

Figure B.2: Approximate solution of Eq. B.1 using $N_p = 5$ and $N_p = 9$ mesh points and linear interpolators. Each straight line is imersed in its own element

Appendix C

Nonlinear solvers

In this work, it is necessary to minimize energy functions which depends on the current displacement $\mathbf{u}$. This fundamental idea – finding a condition $\mathbf{x}^*$ that minimizes a given function $f(\mathbf{x})$ – is common to many fields of science. From the field of Economy, the minimum expenditure problem (and its complement, the utility maximization problem) computes the minimal amount of wealth required to reach some certain level of happiness [215]. Another important example comes from Machine Learning, where weights between the connections of a neural network are sought such that the resulting predictions are close to some data obtained a priori [216]. This is represented by a problem-dependent error function, that must be minimized [216]. These are only two examples of numerical minimization. These two examples, in addition to the energy minimization problem, illustrate the wide variety of fields that have founded use in numerical optimization.

C.1 Line search methods

The branch of mathematics that deals with these problems is called *Mathematical optimization*. The subfield of nonlinear optimization is specially interesting for this work, as it specializes in nonlinear functions and/or constraints. In the interest of space, a full survey of the field cannot be presented (the interested reader can find an introduction to the topic in Ref. [115], and the references therein). Instead, two algorithms are presented, the steepest descent and the Newton method, both in the *line search* family, and a small modification that grandly improves their properties is shown.

Only real functions on Euclidean space are used, i.e., $\mathbf{x} \in \mathbb{R}^n$, and $f(\mathbf{x}) : \mathbb{R}^n \to \mathbb{R}$, where the dimension n is dictated by the problem at hand. In JuFold, this dimension is roughly the number of spatial dimensions (2 or 3), times the number of points in the mesh.

In general, given a multi-variable function $f(\mathbf{x})$ (henceforth called the *objective function*), standard calculus tells us the necessary conditions for some point $\mathbf{x}^*$ to be a *minimum* are

- the gradient must vanish at this point. That is, $\nabla f(\mathbf{x}^*) = \mathbf{0}$;
- the Hessian matrix must be positive definite. That is, $\mathbf{v}^T \nabla^2 f(\mathbf{x}^*) \mathbf{v} > 0$ for every $\mathbf{v} \in \mathbb{R}^n$.

When the gradient $\nabla f(\mathbf{x})$ is nonlinear, finding the solution may involve finding the roots of a set of complicated equations, for which no general solution exists. In these situations, numerical solutions are necessary, and the algorithms mentioned before come to the rescue.

The commonality tying together the members of the line search family is that a minimum of a function $f(\mathbf{x})$ is sought by iterating over the following equation

$$\mathbf{x}_{k+1} = \mathbf{x}_k + \mathbf{p}_k \tag{C.1}$$

where $\mathbf{x}_k$ is the current guess for the minimal point and $\mathbf{x}_{k+1}$ is the new estimate. The vector $\mathbf{p}_k$ is called the *descent direction*. Ideally, the descent direction and the object function gradient are such that $\mathbf{p}_k \cdot \nabla f(\mathbf{x}_k) < 0$. This condition will guarantee that the function is smaller at the new estimate than at the current one. The algorithms in this family are distinguished from one another in the way they build the descent direction $\mathbf{p}_k$. The simplest method in this family, called steepest descent, assigns $\mathbf{p}_k$ as the negative of the gradient of the objective function. That is,

$$\mathbf{p}_k = -\nabla f(\mathbf{x}_k), \tag{C.2}$$

guaranteeing a decrease in the objective function. Another important member of this family is the Newton method, where the information regarding the curvature of the function at the point is also used. In this method, the descent direction is calculated by

$$\nabla^2 f(\mathbf{x}_k)\mathbf{p}_k = -\nabla f(\mathbf{x}_k). \tag{C.3}$$

There is a clear trade-off between these two algorithms: at every step of the Newton method the linear equation therein is solved, which can be computationally intensive. Comparatively, the calculation of the descent direction in the steepest descent is very direct. However, in general the Newton method is able to find the minimum of the objective function in a much smaller number of steps. Indeed, it can be proven that the Newton method converges quadratically once in the neighborhood of the solution. Furthermore, the radius of convergence of the Newton method is much larger than that of the steepest descent [111][1].

C.1.1 Numerical experiments

We are now going to compare the two algorithms exposed above. As a working example, the Rosenbrock function

$$R(x, y) = 100(y - x^2)^2 + (1 - x)^2, \tag{C.4}$$

is used. This function is often used to stress-test optimization algorithms because of its shape, with its long and narrow valley, but single global minimum at (1, 1) (cf Fig. C.1), making it challenging to find the exact global minimum.

Both algorithms are run with starting position $\mathbf{x}_k = (-1.5, -1)$, with results as summarized in Table C.1. While the Newton method converged in only six steps, the steepest descent algorithm diverged altogether.

Table C.1: Results of minimization of the Rosenbrock function.

Algorithm	Root	Steps
Steepest descent	Diverged	∞
Newton method	(1.0, 1.0)	6

---

[1] For a review on the history of this algorithm see [217]

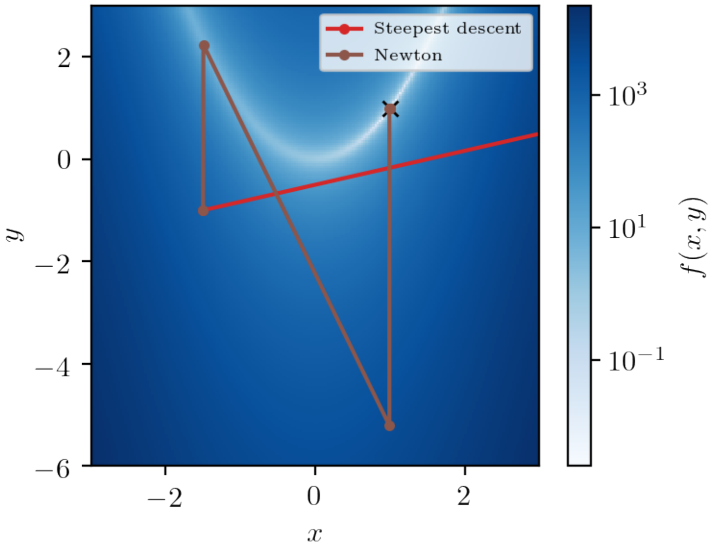

Figure C.1: Plot of the Rosenbrock function as defined in Eq. C.4 and trajectory of nonlinear solvers. The black × indicates the location of the global minimum. Both solvers were initiated at $\mathbf{x}_0 = (-1.5, -1)$.

C.2 Adaptive step

The last example shows one of the main issues with the steepest gradient: it often diverges. However, another, subtle issue is hinted in Fig. C.1. Even the Newton algorithm takes some large steps, going over a wide area of the function domain. In the example above, this poses no issue, as the function is defined at every point of $\mathbb{R}^2$. This is not the case for many hyperelastic energy density functions. For instance, in the function defined in Eq. 2.12, any configuration that leads to a negative J has an undefined energy[2]. As the derivatives of the energy are not defined in this point, the algorithm cannot proceed any further and the system is left at an unphysical state.

The two issues above, lack of convergence and wide search space, have the same solution. The step described in Eq. C.1 is modified to include an adaptive step length α_k,

---

[2] Note that while systems with negative J have no realistic meaning, the trajectory of the nonlinear solver is not constrained by the physics of the problem at hand. It is perfectly valid, for instance, for an algorithm to jump over energy barriers that would otherwise impede the evolution of the system in that direction.

$$\mathbf{x}_{k+i} = \mathbf{x}_k + \alpha_k \mathbf{p}_k. \tag{C.5}$$

such that $0 < \alpha_k \leq 1$.

We now contend with the natural question of how to choose the value of α_k. Such value should not be too small, so as to not slow the algorithm down too much, but it should also be small enough to avoid the issues exposed above. The ideal value would be one that minimizes the function $\phi(\alpha) = f(\mathbf{x}_k + \alpha\mathbf{p}_k)$ for fixed $\mathbf{x}_k$ and $\mathbf{p}_k$. This is often unfeasible, as it would just put us back into the original problem.

One practical approach to break this deadlock is to find an inexact (but still good enough) value of α_k in not too many evaluations of f. There are many possible algorithms (and trade-offs) for the computation of α_k, some of them of incredible complexity. One of the simpler algorithms, called *backtracking* is used. In such method, the scaling is initially chosen as $\alpha_k = 1.0$. If this choice would sufficiently decrease the value of the objective function $f(\mathbf{x})$, it is accepted. Otherwise, a new value is assigned to α_k, $\alpha_k \leftarrow \alpha_k \rho$, where ρ is called the *backtracking factor* with condition $0 < \rho < 1$. Such process is repeated until an appropriate value of scaling is obtained, or until its value is too small, which is then accepted unconditionally.

The concept of sufficient decrease is given concrete meaning by the *Armijo condition*,

$$f(\mathbf{x}_k + \alpha_k\mathbf{p}_k) \leq f(\mathbf{x}_k) + c\alpha_k \nabla f(\mathbf{x}_k) \cdot \mathbf{p}_k, \tag{C.6}$$

for some constant c, such that $0 < c < 1$. According to Ref. [115], the value of c is normally chosen to be very small. Specifically, they recommend choosing $c = 10^{-4}$. The main advantage of using the Armijo condition, rather than, say, a constant, is that it also takes into account the local configuration (via the gradient $\nabla f(\mathbf{x}_k)$) to decide whether the reduction is indeed sufficient.

C.2.1 Numerical experiments

The steepest descent algorithm and the Newton-Raphson algorithm are both augmented by an adaptive step size, with results as seen in Table C.2. This change fixes the issue with steepest descent, as it is now a converging, even if slow, algorithm. This slow convergence is characteristic to the steepest descent algorithm, hindering its usage in most applications. Specifically, this algorithm has a zigzagging nature in any

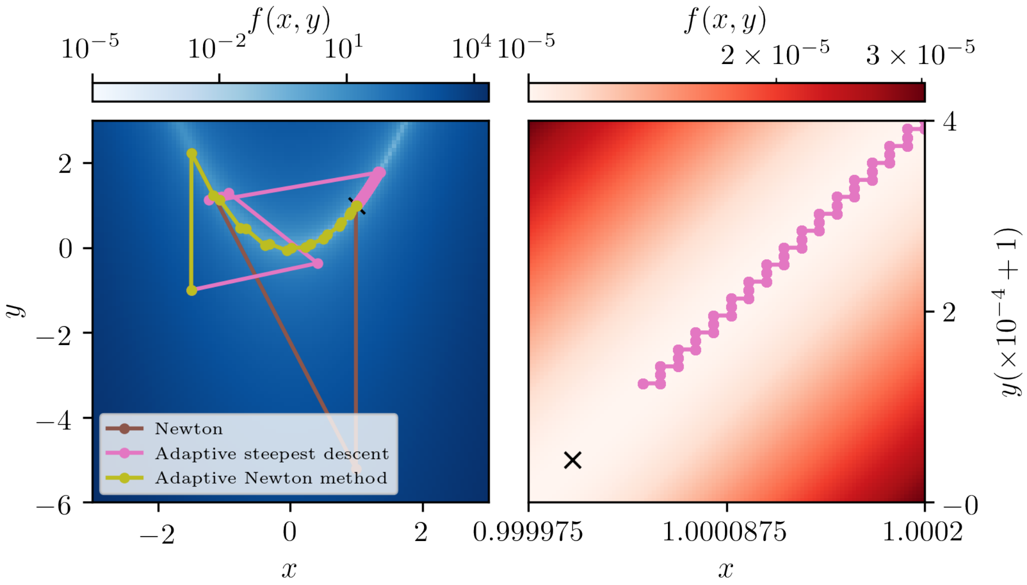

Figure C.2: (a) Trajectory of algorithms in the function domain. In both cases, the algorithms start at $\mathbf{x} = (-1.5, -1.0)$. Compare specially the area explored by the direct Newton method versus its augmented version. (b) Zigzagging behaviour of the adaptive steepest descent algorithm when close to the solution.

convex configuration. This behavior is observed in Fig. C.2 (b), where at each step, the solution barely moves in the direction of the solution.

Table C.2: Results of minimization of the Rosenbrock function with adaptive step size. The adaptive steepest descent was stopped after 10,000 steps.

Algorithm	Root	Steps
Adaptive steepest descent	(1.00004, 1.00009)	10000
Adaptive Newton method	(1.0, 1.0)	23

On the other hand, the augmented Newton method converges slower than its simple counterpart, with 23 steps being necessary in this specific example to find the minimum, compared with the 6 steps necessary before. This is a worth trade-off in some situations where the energy landscape is complex, as this way regions where the energy diverges are avoided.

Appendix D

JuFold Usage

The main component of the JuFold framework is the JuFold class. The user is expected to create a derived class to JuFold, and overload a number of pure virtual functions. In that way, the user is able to insert their model into the framework, which can then be compiled and executed. The location of these functions in the flow of the system are shown in italics in Fig. 3.1. The functions that *must* be overloaded in a minimal program, and their brief description are the following:

- `JuFold::reinit_vectors()`: The place to allocate the memory for the data in the simulations. Called during `setup_system()`.
- `JuFold::populate_cell_data()`: Writes supplementary data to be used in each simulation cell, e.g., spatially varying elastic parameters.
- `JuFold::advance_state()`: Advances the state of the system using the appropriate algorithm.
- `JuFold::growth_on_cell()`: Changes the growth tensor $\mathbf{F}_g$, thereby growing the system.

For performance reasons, there is another type of overloading to be done. The user must also provide a few classes for template specialization. These are few in number. In short, `Hyperelastic` is a class containing the hyperelastic model of the simulation. `Parameters` is a class containing the parameter data required for the simulation, and `PerCellData` is a class containing the data for each cell. More details on each, including their formal concept definition, are available in JuFold's soon to be released online documentation.

Appendix E

Extra plots

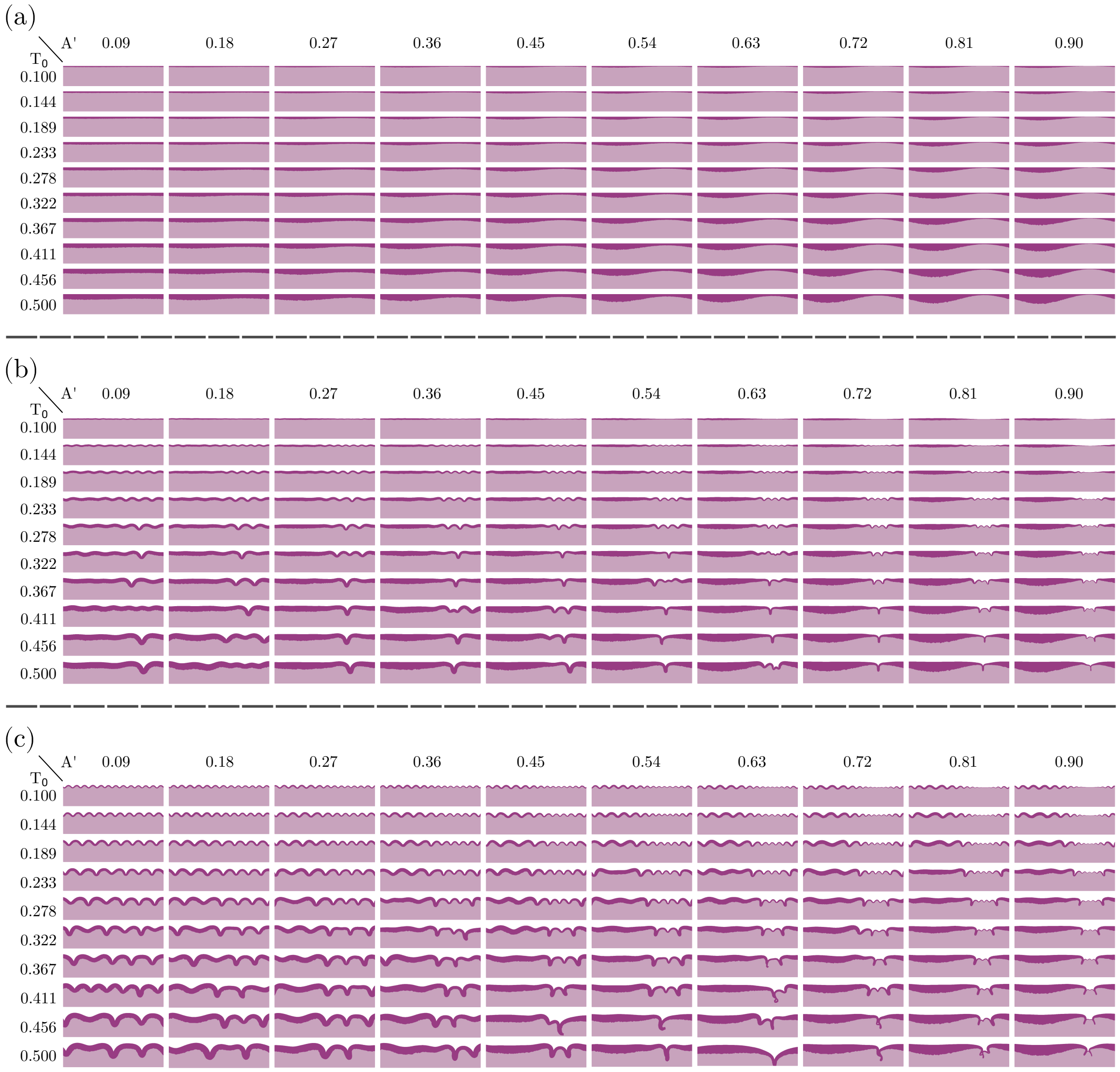

Figure E.1: (Supplementary Material) Visual phase space of inhomogenous simulations at several evolution steps. The values in the x-axis indicate the normalized inhomogeneity amplitude $A' = A/T_0$, while the values in the y-axis indicate the base thickness T_0. The growth parameter θ_g of each subfigure is (a) $\theta_g = 1.00$, (b) $\theta_g = 1.45$, (c) $\theta_g = 1.70$.

Figure E.2: (Supplementary Material) Measured thickness field T and thickness gradient T', from the simulations shown in Fig. E.1. The gradient is calculated as $T' = dT/dl$, where l is the arclength of the system. Both quantities are projected back into the original coordinates. The growth parameter θ_g of each subfigure is (a) $\theta_g = 1.00$, (b) $\theta_g = 1.45$, (c) $\theta_g = 1.70$.

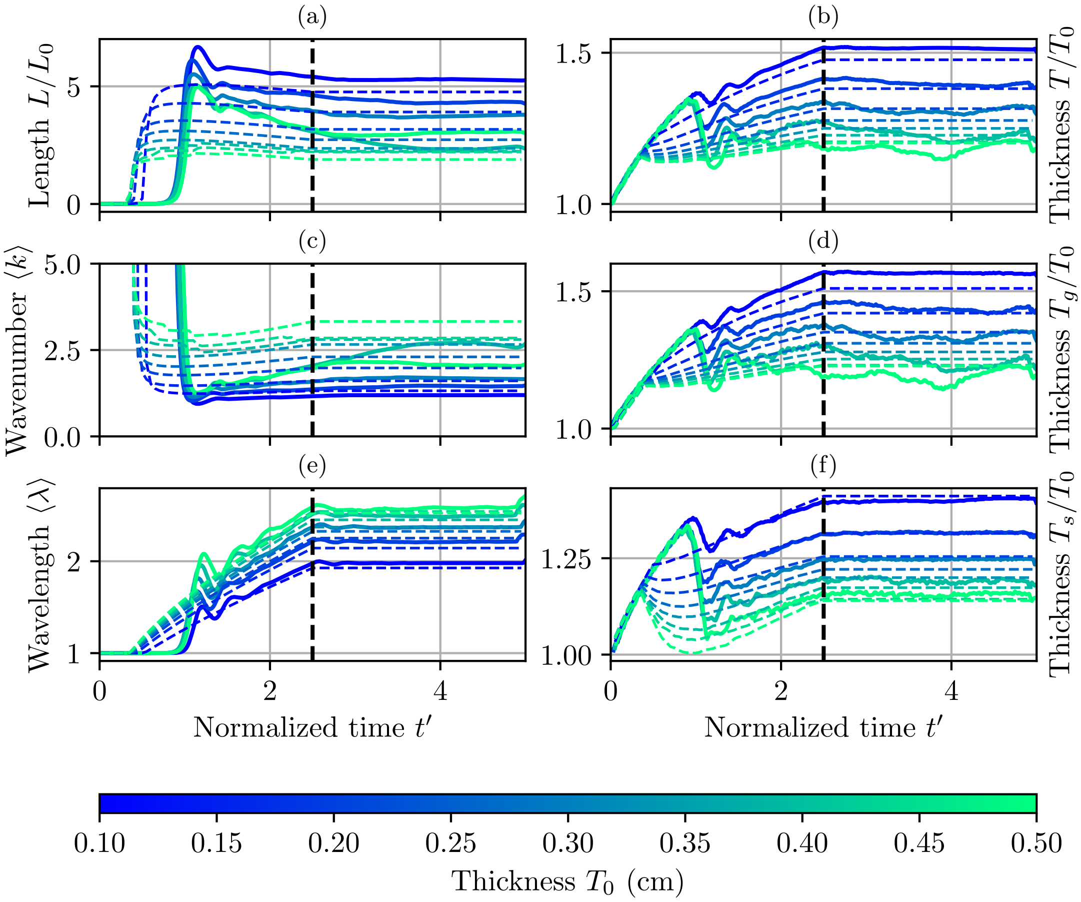

Figure E.3: Evolution of various quantities for system with growth rate $g = 1.000$. Solid lines indicate results obtained in the dynamical regime, and dashed lines indicate thos obtained in the quasistatic regime.

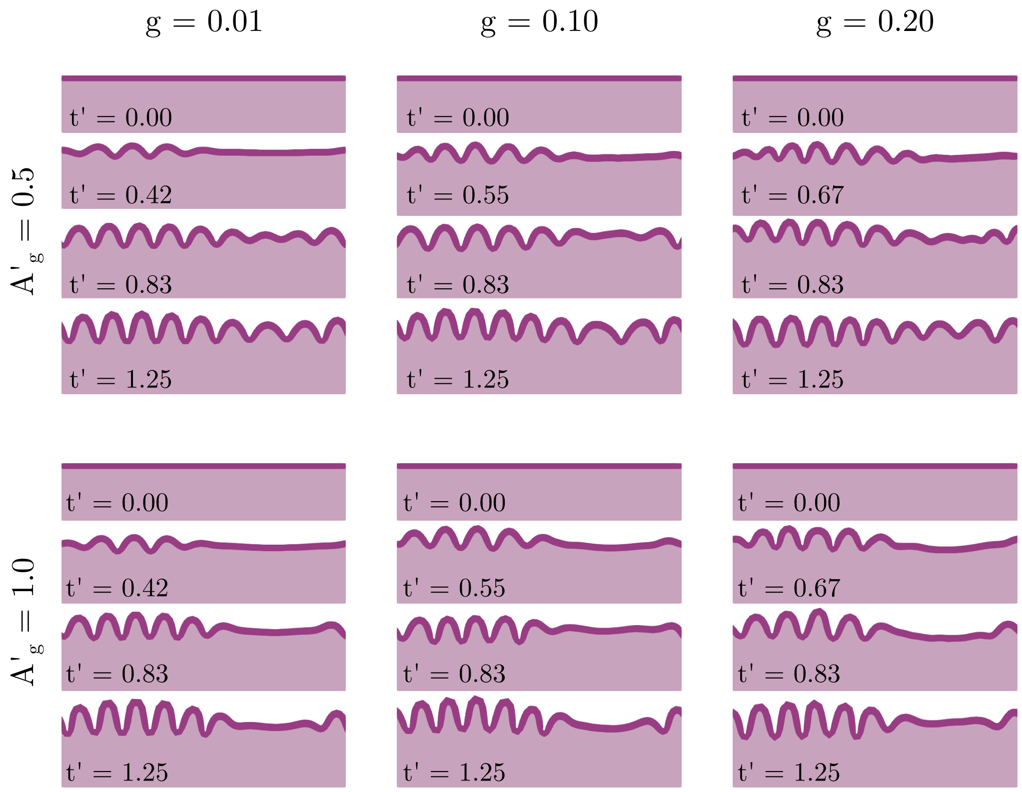

Figure E.4: Dynamics of systems with initial cortical thickness T_0 = 0.2 cm, and growth parameters as shown within the figure.

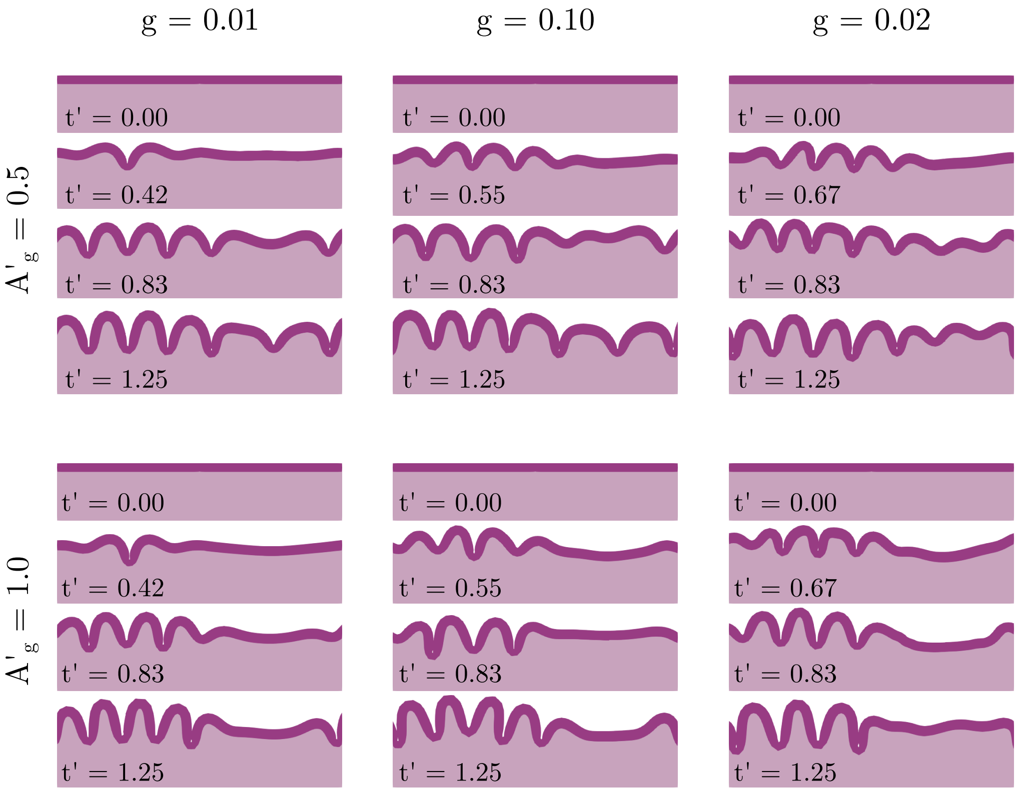

Figure E.5: Dynamics of systems with initial cortical thickness T_0 = 0.3 cm, and growth parameters as shown within the figure.

Appendix F

Other works

NeuroImage 221 (2020) 117140

Contents lists available at ScienceDirect

NeuroImage

journal homepage: www.elsevier.com/locate/neuroimage

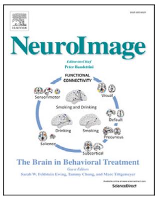

A tutorial and tool for exploring feature similarity gradients with MRI data

Claude J. Bajada[a,b,c,*], Lucas Q. Costa Campos[c,d], Svenja Caspers[c,e,f], Richard Muscat[a], Geoff J.M. Parker[g,h], Matthew A. Lambon Ralph[i], Lauren L. Cloutman[b], Nelson J. Trujillo-Barreto[b,**]

[a] Department of Physiology and Biochemistry, Faculty of Medicine and Surgery, The University of Malta, Malta
[b] Division of Neuroscience & Experimental Psychology, School of Biological Sciences, The University of Manchester, UK
[c] Institute of Neuroscience and Medicine (INM-1), Research Centre Jülich, 52425, Jülich, Germany
[d] Institute of Complex Systems and Institute for Advanced Simulation (ICS-2/IAS-2), Research Centre Jülich, 52425, Jülich, Germany
[e] Institute for Anatomy I, Medical Faculty, Heinrich-Heine-University Duesseldorf, 40221, Duesseldorf, Germany
[f] JARA-BRAIN, Jülich-Aachen Research Alliance, 52425, Jülich, Germany
[g] Centre for Medical Image Computing, Department of Computer Science, and Queen Square MS Centre, Department of Neuroinflammation, UCL Institute of Neurology, University College London, UK
[h] Bioxydyn Limited, Manchester, UK
[i] MRC Cognition and Brain Sciences Unit, University of Cambridge, Cambridge, UK

ARTICLE INFO

Keywords:
Gradients
Spectral clustering
Connectivity-based parcellation
Laplacian eigenmaps
Network analysis
VB Index

ABSTRACT

There has been an increasing interest in examining organisational principles of the cerebral cortex (and subcortical regions) using different MRI features such as structural or functional connectivity. Despite the widespread interest, introductory tutorials on the underlying technique targeted for the novice neuroimager are sparse in the literature.

Articles that investigate various “neural gradients” (for example based on region studied “cortical gradients,” “cerebellar gradients,” “hippocampal gradients” etc … or feature of interest “functional gradients,” “cytoarchitectural gradients,” “myeloarchitectural gradients” etc …) have increased in popularity. Thus, we believe that it is opportune to discuss what is generally meant by “gradient analysis”. We introduce basics concepts in graph theory, such as graphs themselves, the degree matrix, and the adjacency matrix. We discuss how one can think about gradients of feature similarity (the similarity between timeseries in fMRI, or streamline in tractography) using graph theory and we extend this to explore such gradients across the whole MRI scale; from the voxel level to the whole brain level. We proceed to introduce a measure for quantifying the level of similarity in regions of interest. We propose the term “the Vogt-Bailey index” for such quantification to pay homage to our history as a brain mapping community.

We run through the techniques on sample datasets including a brain MRI as an example of the application of the techniques on real data and we provide several appendices that expand upon details. To maximise intuition, the appendices contain a didactic example describing how one could use these techniques to solve a particularly pernicious problem that one may encounter at a wedding. Accompanying the article is a tool, available in both MATLAB and Python, that enables readers to perform the analysis described in this article on their own data.

We refer readers to the graphical abstract as an overview of the analysis pipeline presented in this work.

1. Introduction

Every discrete point in the brain (modelled as a voxel or vertex in the context of MR imaging) has several co-existing features such as the cytological architecture, the functional signature, the receptor density etc … Parcellation is one method of describing neural features and their similarities. The technique groups area of the brain that have similar features together. One of the most recognisable names in modern neuroscience is that of Korbinian Brodmann and his cytoarchitectonic parcellations of the cortex from the early 20th century. Despite his

---

* Corresponding author. Department of Physiology and Biochemistry, Faculty of Medicine and Surgery, The University of Malta, Msida, Malta

** Corresponding author. Division of Neuroscience and Experimental Psychology, School of Biological Sciences, Faculty of Biology, Medicine and Health, University of Manchester, Academic Health Science Centre, Brunswick Street, Manchester, M13 9PL, UK

E-mail address: claude.bajada@um.edu.mt (C.J. Bajada).

https://doi.org/10.1016/j.neuroimage.2020.117140
Received 14 January 2020; Received in revised form 9 June 2020; Accepted 2 July 2020

modern fame, Brodmann was not the most ardent proponent of parcellation. That honour arguably goes to Oskar and Cecile Vogt, who were the true parents of modern parcellation, and Brodmann's mentors.

Brodmann's regions attempted to define areas of local cytoarchitectural homogeneity in the cortex. Unfortunately, the convenience of using such areas in neuroimaging studies comes at a high price. First, Brodmann areas were defined histologically and do not necessarily correspond to gross anatomical landmarks that are visible on MRI (Zilles and Amunts, 2010). Second, Brodmann's maps certainly are not the final word on what constitutes a cytoarchitectural brain parcel. His contemporaries (von Economo and Koskinas, 1925) as well as current researchers (Amunts et al., 2005; Bludau et al., 2014; Caspers et al., 2013, 2006; Rottschy et al., 2007; Scheperjans et al., 2008) are still investigating and refining cytoarchitectonic parcellation. Third, cytoarchitecture is not the only feature with which one can parcellate the cortex. Myeloarchitecture, for instance, has been used since the times of Brodmann (Geyer and Turner, 2013; Nieuwenhuys et al., 2015; Vogt and Vogt, 1911) and recently a vast array of neuroimaging features has been used (Glasser et al., 2016). Fourth, the boundaries (or borders) between areas characterised by any particular feature may sometimes be sharp while other times they can be blurred (Bailey and von Bonin, 1951; Brodmann, 1909; Glasser et al., 2016). Finally, different "distinct" areas may also share some relationship with other areas and thus show a non-random pattern across the whole cortex; for example functional areas involved in resting state networks (Damoiseaux et al., 2006).

In the 1950s, Percival Bailey and Gerhardt von Bonin proposed another, competing conceptualisation of cortical organisation. Vogt and Bailey can be, *prima facie,* thought of as expounding opposing points of views. While the Vogts, championed cortical parcellation, Bailey and von Bonin (1951) argue that the isocortex (or neocortex – the six layered cortex) is much more similar throughout its extent than it is different. They go so far as to state that:

> "The drawing of sharp areal boundaries, on the basis of many structural peculiarities of varying distinctiveness and significance, is the fundamental defect of most maps and has been carried to absurd lengths by the Vogt school." (p. 189)
>
> They elaborate by stating:
>
> "Anybody can see, to give an example, the difference between Brodmann's areas 17 and 18. But the differences between his 18 and 19 are quite tenuous and very difficult to recognize. To draw a map on which these three areas are given three different markings - such as dots, cross-hatchings, and broken lines - is to create an entirely misleading impression. Useful as such maps are for the description of corticocortical connections, they do not translate accurately cytoarchitectonic data." (p. viii)

An interest in similar issues of parcellations versus gradual transitions between areas has reappeared in the modern neuroscience literature. Indeed, Brodmann himself asserted that some regions demonstrated transitionary zones (Brodmann, 1909). While the feature of interest has moved on from cytoarchitecture to fMRI time series analysis or diffusion MRI tractography (more generally within a context of network analysis, connectomes and connectivity based parcellations), some themes of the early debates have lived on. For example: when, and to what extent, is clustering the cortex into distinct parcels appropriate? And, as has been explored by (Mesulam, 2008, 1998), what are the interareal relationships between cortical territories?

In 2004, a novel approach, based on spectral graph theory, appeared in the literature to investigate changes in cortical connectivity patterns across the brain using diffusion MRI tractography (Johansen-Berg et al., 2004). Similar approaches have become a popular tool for parcellating the cerebral cortex using both diffusion and functional MRI (Cloutman et al., 2012; Craddock et al., 2012; Devlin et al., 2006; Eickhoff et al., 2015; O'Donnell et al., 2013, 2006). Recently, similar techniques have also been used to explore interareal connectivity pattern changes (such as structural connectivity through tractography or functional connectivity) as one traverses the cerebral cortex; so-called feature similarity gradients (Bajada et al., 2017; Cerliani et al., 2012; Haak et al., 2018; Jackson et al., 2017; Margulies et al., 2016). Indeed, Margulies et al. (2016) have shown that, under certain constraints that likely depend on the construction of the similarity matrix, the primary rs-fMRI feature gradient reflects the interareal relationships outlined by Mesulam (2008) and elaborated by Buckner et al. (2013) where this gradient has modality selective and modality general cortices on either end. While this concept may not be fully understood by a novice reader, we hope that by the end of this article (and particularly after reading the supplementary text) the interpretation of such a statement will be obvious.

These techniques are appealing to the neuroimaging community since they have the potential to provide a flexible, unified framework for understanding similarities of neural structure or function across the brain (c.f. Paquola et al., 2020, 2019; Vázquez-Rodríguez et al., 2019 for examples of how flexible these concepts can be used across multiple modalities). In this article we further extend this framework by introducing a way to measure how sharply defined each area is, showing the full spectrum of possibilities between the ideas of the Vogts, and those of Bailey and von Bonin; The Vogt-Bailey index.

We use the historical context to highlight the importance of having a way of thinking about cortical organisation through "feature gradients" – e.g. fMRI, tractography, cytoarchtectonic etc … that bridges the gap between old debates. Specifically, we will apply the tools described here to help settle a discussion started in the middle of the 20th century. We have also made available a pair of tools written in MATLAB and Python implementing the algorithms outlined in this work, thus making it possible for the interested reader to calculate the VB index using their own data (https://doi.org/10.5281/zenodo.3609459, https://github.com/VBIndex/) (Da Costa Campos and Bajada, 2020). It is also possible to install the recommended production version of the software using Python's *de facto* package manager, *pip*, with "*pip install vb_toolbox*". Once this is done, the software *vb_tool* will be available for use. For usage details, we refer to the full documentation of the software's GitHub repository (https://github.com/VBIndex/py_vb_toolbox).

We note that various groups have released their own "gradient analysis" pipelines and toolboxes including the early "gradient pipeline" by Margulies et al. (2016), connectotopic mapping focused on regional modes of connectivity changes and their statistical tests by Haak et al. (2018), LittleBrain focusing on Cerebellar gradient by Guell et al. (2019), and BrainSpace a recent all-purpose gradient toolbox by Vos de Wael et al. (2019). All these workflows and toolboxes have minor differences in certain choices that are described below. Some also include the ability to perform statistical testing on gradient maps. The software presented in this article creates similar, but not necessarily identical, 'gradient maps' as the other software packages available, in addition it is the only package to-date, that allows calculation of the VB index (as described in section 5.1).

In the rest of this article we describe and explore the details of the steps needed to extract feature similarity gradients and the VB Index from data. We discuss methods of measuring similarity between brain regions, why it is useful to think of these resultant similarity measurements as a mathematical graph, and how to further process the graph to obtain the desired gradient maps. In this article we restrict our discussion to a technique based heavily upon Laplacian Eigenmaps (c.f. Belkin and Niyogi, 2003, 2002). In general, the problem of finding meaningful structures and geometric descriptions of such data is usually stated as some sort of nonlinear dimensionality reduction. Although several forms of dimensionality reductions for constructing cortical gradients (or subcortical, cerebellar etc.) have been used in the literature (Coifman and Lafon, 2006; Haak et al., 2018; Johansen-Berg et al., 2004; Margulies et al., 2016), they are similar in spirit to the Laplacian Eigen-mapping reviewed here. We refer the interested reader to the relevant literature and hope that the tutorial presented here will serve as a useful introduction to understand the principles behind those related approaches.

2. What is a graph?

Most algorithms for feature gradient analyses emerge from the mathematical discipline of spectral graph theory. This is an approach to studying properties of graphs by computing the eigenvalues and eigenvectors of matrices that summarise the graph. While it would be lengthy to go into a detailed explanation of eigenvalues and eigenvectors in this text, we hope that their use in the context described will become clearer in later sections.

A graph is a mathematical structure that defines relationships between various objects. For example, the structure in Fig. 1 is a graph that defines the relationship between four objects. Each object is called a node.

The nodes could be thought of as voxels (or surface vertices) in the cortex or as cortical regions of interest.

The lines that link the nodes are called edges. The edges can be binary or have a weight associated with them (creating a weighted graph). Within neuroimaging, the edges are almost always undirected meaning that if node a connects to node b, the opposite is also true.

Some basic concepts are needed in order to proceed. The adjacency matrix is a square matrix (i.e., the same number of rows and columns) where every row and every column represent a single node, and the elements in the matrix represent the relationships between the row node and the column node. For the unweighted graph in Fig. 1, the adjacency matrix is

$$\boldsymbol{A} = \begin{pmatrix} 0\,1\,1\,1 \\ 1\,0\,1\,0 \\ 1\,1\,0\,0 \\ 1\,0\,0\,0 \end{pmatrix}.$$

The rows and columns are ordered from 1 to 4 such that entries of 1s in columns 2, 3 and 4 of row 1 means that node *a* (row 1) is connected to nodes *b, c* and *d* (columns 2, 3 and 4).

The degree matrix is a diagonal matrix where the entries along the diagonal represent the degree of each node, that is, the number of nodes that are connected (adjacent) to that node. For example, node *a* has a degree of 3 because it is adjacent to three nodes (*b, c* and *d*). The degree matrix D can be computed as the row/column wise sum of the adjacency matrix. For the graph in Fig. 1, the degree matrix is

$$\boldsymbol{D} = \begin{pmatrix} 3\,0\,0\,0 \\ 0\,2\,0\,0 \\ 0\,0\,2\,0 \\ 0\,0\,0\,1 \end{pmatrix}.$$

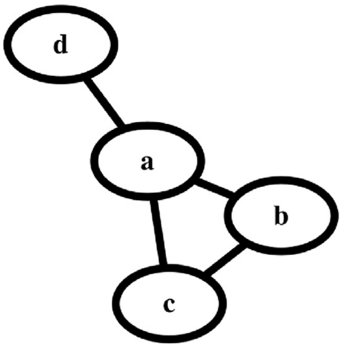

Fig. 1. A representation of a graph with 4 nodes. Every node can be considered to be a voxel or a region of interest. The edges between the nodes represent their relationships; these can either be structural connections or a measure of similarity (affinity) between the nodes.

The Laplacian is defined as the degree matrix minus the adjacency matrix

$$\boldsymbol{L} = \boldsymbol{D} - \boldsymbol{A}.$$

While the exact meaning of the Laplacian may be difficult to intuit for many readers, we hope that the use of it in Section 4 will give the readers some intuition. At this point it is useful to note that in many applications, including in neuroimaging one can define a weighted graph, where each edge connecting the nodes carry different weights. A high weight, for instance, could mean that two nodes are strongly connected, while a low weight would indicate the nodes are not as strongly connected. One can now define a weighted version of the adjacency matrix, which can be used to describe a weighted graph. In the general case, the weighted adjacency matrix can be defined as

$$\boldsymbol{W} = \begin{pmatrix} w_{11} & w_{12} & \cdots & w_{1n} \\ w_{21} & w_{22} & \cdots & w_{2n} \\ \vdots & \vdots & \ddots & \vdots \\ w_{n1} & w_{n2} & \cdots & w_{nn} \end{pmatrix}.$$

We will see later that this matrix can be associated to the concept of a similarity or affinity matrix. In the example above, the weighted adjacency matrix can be written replacing the 1s in the adjacency matrix with the corresponding weights. Weighted versions of the Degree and Laplacian matrices can be defined in the same way as before. Henceforward, unless otherwise specified, we will refer to the Laplacian, degree and adjacency matrix as their generalised weighted versions.

2.1. *Graphs in neuroimaging*

For neuroimaging purposes, a graph can be one of two distinct types. The most conceptually straightforward way of creating a graph of the brain is to consider its structural connections. For example, the nodes in the graph of Fig. 1 can represent brain areas (e.g. cerebellum, brainstem, etc …) and the edges can represent the tracts that connect those brain areas. In other words, these graphs can be obtained through tractography and assuming that each voxel (or region of interest) is a node and that every tract is an edge connecting two nodes. These graphs we refer to as *direct graphs* since the edges are the direct connections between each node. One can think of these as friendship networks where an edge between two individuals is determined on whether they are friends or not.

Another approach to constructing a graph is to compute a measure of similarity between a feature of interest of one region and the same feature of another. For structural data, the whole output of a tractography algorithm (the tractogram of a single voxel) can be considered to be a feature of a voxel and is compared pairwise to obtain a similarity matrix between voxels (Bajada et al., 2017; Cerliani et al., 2012; Devlin et al., 2006; Johansen-Berg et al., 2004). For functional data, one can use the fMRI time series. In this case, the nodes are still voxels, but the edges are weights of how similar one voxel's feature is to another's. If we consider that two people are nodes in a network their edge weight would be determined by how similar two individuals are, based on individual features (e.g. dress sense, job, etc …). We call this a *feature similarity graph*. For simplicity, this is the type of graph that we will be discussing in the rest of this article. It is important to note that much work in the fMRI literature performs the similarity computation not on the features themselves (e.g. the time-series), but on a "functional connectivity" matrix (c.f. Margulies et al., 2016). In terms of the "people network" proposed above, if we assume that the "functional connectivity" gives us information about the "level of friendship" between two individuals, then the similarity matrix of this last approach indicates the similarity between each individual's friendship network.

3. The similarity, affinity or adjacency matrix

The adjacency matrix is a simple mathematical representation of a graph that describes the structure of the connectivity in the graph, that is, whether nodes are connected or not. A more detailed description is provided by using a weighted adjacency matrix. The question is then how to define the weights, which in turn depends on what kind of graph we want to describe.

In neuroimaging the weights can be defined in terms of a *similarity metric* describing to what extent a feature of one voxel, or vertex (e.g. an fMRI time series or a set of streamlines) is similar to every other voxel in the region of interest. This is done across all voxels (or vertices). We will refer to such a weighted adjacency matrix as the *similarity* or *affinity* matrix.

Choosing a similarity metric is extremely important since it will affect any clustering that may be done on the data. By far the most popular similarity measure between two voxels is the Pearson's correlation coefficient, which can be interpreted as a centred and normalised dot product (Cerliani et al., 2012; Craddock et al., 2012; Devlin et al., 2006; Johansen-Berg et al., 2004; Klein et al., 2007; Zhang et al., 2014); see next section for a discussion of the dot product and other similarity measures. In order to understand the utility of correlation as a similarity metric, a short description of its precursors is given below (cf O'Connor, 2012 for an intuitive review). We will then introduce a slight modification that we employ in our adjoining code.

One caveat of the algorithms used for these analyses is that the adjacency matrix must be non-negative. This is not automatically true for most similarity measures, including those introduced in section 4.1. Hence, some technique must be used to ensure that the corresponding similarity matrix only contains non-negative weights (Haak et al., 2018; Johansen-Berg et al., 2004; Von Luxburg, 2007). For example, Johansen-Berg et al. (2004) proposed to add a scalar constant to the similarity matrix to ensure that all values are positive, others have only kept positive values at some threshold (Margulies et al., 2016).

Once a similarity matrix has been created, it can be used to represent the graph that all computations are carried out on. A final consideration regarding the similarity matrix is whether the full set of similarities should be used or if the similarity matrix should be thresholded in some way (Von Luxburg, 2007). For example, all weights below some arbitrary value ε could be set to zero; the remainder of the weights can be retained or binarised (this will be the same as using a simple adjacency matrix). Another approach to limiting the neighbourhood is to restrict the weights to the k-nearest neighbours. Advantages of both these data reduction approaches are that they remove noisy weights and they sparsify the matrix, leading to faster and cheaper computations. For example, in fMRI voxels may have a very low correlation (weight) not because of any intrinsic functional connectivity, but because of noise.

3.1. Similarity measures

The most basic way to measure the similarity of two datasets (thought of as vectors) is the dot product of the two vectors (consider an fMRI time series or a three-dimensional image of a tract density map (or tractogram) that is flattened into one long vector).

Geometrically, the dot product of two vectors is the projection of one vector onto the other. There are many equivalent ways to calculate the dot product. For this paper, the one offers the most insight is

$$dot(\boldsymbol{x},\boldsymbol{y}) = \sqrt{\sum_i x_i^2}\sqrt{\sum_i y_i^2}\cos(\boldsymbol{x},\boldsymbol{y}).$$

In this form, the dot product has two components: the cosine of the angle between the two datasets (treated as vectors) and their magnitudes. This means that magnitude and angular similarity (as measured by the cosine of an angle) are confounded. In order to solve this problem, one can normalise the dot product by dividing by the magnitude of each dataset and that leaves us with the cosine function.

One problem with the cosine similarity is that it is sensitive to relative shifts in the data between samples (such as can occur in fMRI time series due to absolute signal differences that are of no interest). The most common way to create a shift invariant similarity is to mean centre the data and then compute the cosine similarity, which is the sample Pearson's correlation coefficient:

$$corr(\boldsymbol{x},\boldsymbol{y}) = \cos((\boldsymbol{x}-\overline{\boldsymbol{x}}), (\boldsymbol{y}-\overline{\boldsymbol{y}})),$$

where $\overline{\boldsymbol{x}}$ and $\overline{\boldsymbol{y}}$ are constant vectors the size as $\boldsymbol{x}$ and $\boldsymbol{y}$, where each element is the mean of $\boldsymbol{x}$ and $\boldsymbol{y}$, respectively. Being shift invariant is an appealing property of the correlation coefficient and is especially useful to compare variables that have different means. Examples of works in the literature that use the cosine similarity can be found in the following articles (Bajada et al., 2017; Hong et al., 2019; Jackson et al., 2020, 2017; Margulies et al., 2016).

One should remember that the cosine is a sinusoidal function. As a result, a cosine similarity, or a correlation, value of 0.5 does not have the neat interpretation that the angle between the two datasets is 45°. An easy solution to this is to calculate the angle between the two data sets by using the inverse cosine function (the arccosine), normalise by 90° (or $\pi/2$):

$$normAngle = \frac{cos^{-1}(\cos((\boldsymbol{x}-\overline{\boldsymbol{x}}), (\boldsymbol{y}-\overline{\boldsymbol{y}})))}{90}.$$

The above formula will measure a normalised "angular distance" between two datasets bound between 0 and 2. We can thus define the quantity, as follows

$$AngSim = 1 - normAngle.$$

This measure returns a value that has an almost identical interpretation to the correlation coefficient (or cosine similarity) but has the nice property that a value of +0.5 implies that the two datasets are half way between orthogonal and colinear while a value of −0.5 implies that the two datasets are half way between orthogonal and anti-colinear. Examples of works in the literature that use a normalised angle include (Larivière et al., 2020; Vos de Wael et al., 2018).

4. The spectral transformation and the graph laplacian

Once a similarity (also affinity or adjacency) matrix is computed, we have all the information that describes the relationships between individual nodes. Our next step is to embed our data into a low dimensional space (for the moment a one-dimensional line) where the nodes distances from each other and the centre of the space reflect the internodal affinity.

While we refer readers to the supplementary material (Appendix C) for an informal discussion of the problem, the process can be formulated as the solution of an optimisation problem where a suitable cost function $U(\boldsymbol{x})$ is minimised (described by Leskovec et al., 2014)

$$\widehat{\boldsymbol{x}} = \underset{\boldsymbol{x}}{\operatorname{argmin}}\{U(\boldsymbol{x})\}.$$

Shortly, $\widehat{\boldsymbol{x}}$ is the vector that minimises the cost function $U(\boldsymbol{x})$. Such cost function can be written as a weighted sum of squared internode (Euclidean) distances across all connected nodes,

$$U(\boldsymbol{x}) = \sum_{(i,j)\in E} W_{ij}\left(x_i - x_j\right)^2.$$

One can think of the weights W_{ij} as a measure of the relationship between two nodes, for example, cortical vertices. Using graph theory language, one can think of the above situation as defining a weighted graph where the value of each node represents the location of each individual and the weight of the edge connecting two nodes represent their relationship.

The minimisation of the above cost function means that long distances between pairs of vertices with a high relationship value (i.e., high weight) is penalised. As a result, a pair of vertices with a high weight will be placed close to each other, while a pair of vertices with a low weight will be placed far apart. The aim is to find a positioning where the sum of costs associated with all pairs of vertices is at its minimum.

The above problem, however, is not well-posed. First, it has a trivial solution which is to place all vertices at the same location (x is a constant vector), which produces zero cost. While this satisfies the minimisation of our cost function, it is not useful since it tells us nothing about the relationships between vertices. Second, if $\hat{x}$ is a solution then any shifting or re-scaling of $\hat{x}$by a constant value c (i.e., $\hat{y}=\hat{x}+c$ or $\hat{y}= \quad c\hat{x}$, respectively) will also be a solution because the resulting cost function is invariant to shifting or re-scaling. Therefore, in order to circumvent trivial and non-unique solutions some constraints are required. The simplest constraint is that the cost function must be minimised subject to (s.t.) the magnitude of the position vector $\boldsymbol{x}$ being equal to 1. Mathematically this is written as

$$\hat{\boldsymbol{x}}=\underset{x}{\operatorname{argmin}}\{U(\boldsymbol{x})\} \quad s.t. \quad \boldsymbol{x}^T\boldsymbol{x}=1.$$

Note that this constraint does not solve the problem of a constant solution completely since a constant vector, can still produce a zero cost and also satisfy the constraint. We will see later that since this solution is known in advance, one can easily account for it after optimisation. In general, the constrained minimisation problem can be solved using the method of Lagrange multipliers (cf Hagen and Kahng, 1992). While a detailed explanation of Lagrangian multipliers is beyond the scope of this text, the modification makes the computation easier to solve while maintaining its accuracy. The idea of this method is simple: We incorporate the constraints into the cost function itself. Thus, we rewrite the problem as

$$\hat{\boldsymbol{x}}=\underset{x}{\operatorname{argmin}}\left\{U(\boldsymbol{x})+\lambda(1-\boldsymbol{x}^T\boldsymbol{x})\right\}.$$

Now, any putative solution that does not conform to the constraint imposed will be penalised. This penalty is dictated by the weight λ, often called the Lagrange multiplier. We proceed to solve the problem in the following way. First, rewrite the optimisation problem as follows (see Appendix A for details):

$$\hat{\boldsymbol{x}}=\underset{x}{\operatorname{argmin}}\{\tilde{U}(\boldsymbol{x})\}=\underset{x}{\operatorname{argmin}}\left\{\boldsymbol{x}^T\boldsymbol{L}\boldsymbol{x}+\lambda(1-\boldsymbol{x}^T\boldsymbol{x})\right\}.$$

The minimisation can now proceed in the usual way by taking the first derivative of the modified cost function $\tilde{U}(\boldsymbol{x})$ and equating to zero (extremum condition)

$$\partial\frac{\tilde{U}(\boldsymbol{x})}{\partial\boldsymbol{x}}=2\boldsymbol{L}\boldsymbol{x}-2\lambda\boldsymbol{x}=0,$$

and hence

$$\boldsymbol{L}\boldsymbol{x}=\lambda\boldsymbol{x}.$$

The last expression defines a *standard eigenvalue problem* for the Laplacian that can be solved using standard numerical libraries (e.g., the MATLAB function *eig*). The pair $(\lambda,\hat{x})$ is called an eigenpair, with λ called the eigenvalue, and $\hat{x}$ the eigenvector. Eigenvalues and eigenvectors are useful in a broad range of applications, with the interpretation of these pairs depending on the context in which they are used.

In this paper, we will focus on the eigenvectors of the Laplacian, as they contain the information which we will use to create our gradients. However, the eigenvalues also encode important information. Given that the Laplacian matrix is positive semi-definite, the smallest eigenvalue is zero and its associated eigenvector is a constant, thus, we will focus upon the second smallest eigenvalue, which is termed the algebraic connectivity of a graph (Fiedler, 1973).

Fiedler (1973) showed that the magnitude of the algebraic connectivity reflects how well connected the overall graph is, i.e., the larger the algebraic connectivity is, the more difficult it is to cut a graph into independent components. If the algebraic connectivity is zero it means that the graph is not connected; i.e. there are at least two graph partitions. In other words, if a graph has at least two hard clusters (i.e. it is two completely disconnected subgraphs), the algebraic connectivity will be zero. The more connected a graph gets, the higher the algebraic connectivity becomes. This intuition will be revisited in section 5.3.

The fact that the first eigenvalue is zero directly dictates that its associated eigenvector does not carry any useful information regarding the relative position of the nodes. Hence, the optimal solution is encoded in the eigenvector associated with the second smallest eigenvalue. This is called the Fiedler vector after the mathematician who first described this solution in the context of graph partitioning (Fiedler, 1973).

At this stage, it is worth noting that the described solution to the problem is biased in the sense that nodes with high degree will dominate the minimisation since the corresponding row (or column) of the Laplacian matrix is dominant. This means that nodes with a high number of neighbours (i.e., high degree) will tend to be grouped together irrespective of their similarity. This bias can be compensated for by using a modified constraint $x^TDx=1$ so that our optimisation problem is transformed to

$$\hat{\boldsymbol{x}}=\underset{x}{\operatorname{argmin}}\left\{\boldsymbol{x}^T\boldsymbol{L}\boldsymbol{x}+\lambda(1-\boldsymbol{x}^T\boldsymbol{D}\boldsymbol{x})\right\}.$$

The new constraint means that nodes are penalised (i.e., they are assigned a higher cost) according to their degree (Johansen-Berg et al., 2004). By following the same mathematical derivation, as above, the associated eigenvalue problem is then

$$\boldsymbol{L}\boldsymbol{x}=\lambda\boldsymbol{D}\boldsymbol{x}.$$

This is known as the *generalised eigenvalue problem* for matrices $\boldsymbol{L}$ and $\boldsymbol{D}$, which can also be solved numerically using standard toolboxes. Commonly, toolboxes that are able to solve the standard eigenvalue problem can also be used to solve the generalised problem. This is the case, for instance, for MATLAB's and Scipy's *eig* function.

Often, the Laplacian matrix is used in normalised form (i.e., normalised with respect to the nodes degree), so that its diagonal elements are all one. However, it can be demonstrated that normalising the Laplacian is equivalent to changing the constraint of the minimisation problem in some way and therefore one must be clear of how a given normalisation affects the solution. Several versions of the normalised Laplacian have been used in the literature. In Appendix B we describe the symmetric normalised Laplacian and the random walk normalised Laplacian.

5. Reordering, eigenmaps, and the Vogt-Bailey Index

If we think of brain voxels, or cortical surface vertices, as nodes with associated features (such as an fMRI time series, or a tractogram etc …) and the relationships between these features as edges on a graph, we previously described that the second smallest eigenvector describes the location (coordinate) of each node in one dimension, a line, which is dictated by each nodes relationship (affinity) to each-other. Using the location as a heatmap value becomes a way to visualise those relationships on the brain (the so-called macroscale gradients). Further, the components of eigenvectors denote the coordinates of the node in a space containing as many dimensions as there are eigenvectors (it is not restricted to a single dimension). Hence the eigenvector with the second smallest eigenvalue would give coordinates of the nodes on a line, the second and third eigenvectors would give the coordinates on a plane and so on. For this, more complicated visualisations are needed. One may also present the higher dimensional gradients independently, but one must always remember that the second gradient is influenced by the first and the third by the previous two etc.

Further, the algebraic connectivity indicates the sharpness of the best split (or cluster) in the region of interest. If a searchlight VB index analysis is performed on local neighbourhoods (see section 5.3), we can investigate mesoscopic gradients (or transitions between areal borders).

5.1. Spectral reordering

The simplest approach to mapping the embedded location onto the brain is by assigning each voxel or vertex a heatmap value that corresponds to their rank order in the embedding. This approach allows for investigating the general pattern of changes in features across the brain, but, being rank ordered, does not provide any details about the actual feature distance between vertices (c.f. Bajada et al., 2017 for an example; c.f. Johansen-Berg et al., 2004 for the original spectral reordering paper in the literature where it was used for parcellation).

5.2. Eigenmaps

Laplacian eigenmaps (Belkin and Niyogi, 2003, 2002) are closely related to spectral reordering. Use of eigenmaps has been introduced to the neuroscience literature (Cerliani et al., 2012; Haak et al., 2018). In one dimension, the approach uses the coordinate points given by the primary eigenvector of the Laplacian as the intensity of the voxel of interest.

This approach can be particularly advantageous since one can explore the relationships between voxels in more than one dimension. Indeed, coordinates of the similarity or eigen-space can be mapped into a colour palette and the resultant colour map value can be mapped onto the brain space by assigning that value to the corresponding voxel (c.f. Bajada et al., 2019). This means that one can only map as many dimensions as the dimensions of the colour palette (in our case the 3-dimensional RGB colour palette).

Reordering and eigenmaps give us maps of optimal embedding of voxels in a low dimensional space. Effectively, voxels (or ROIs) with a similar value, have a greater affinity to one another. This establishes the large-scale organisational gradients of the cortex. It also gives some indication as to whether there are sharp discontinuities across that gradient but a focus on the eigenvectors alone fails to quantify the extent of discontinuity in cortical intra-areal relationships. The eigenvalues provide a solution.

5.3. The algebraic connectivity and the Vogt-Bailey Index

The algebraic connectivity of a graph is an indicator of how "well connected" that graph is. It is the second smallest eigenvalue of the Laplacian matrix (see section 4).

Once normalised to be bounded between zero and one (by dividing by the mean of all eigenvalues save for the first, which is the maximum value a graph with an affinity matrix one ones would have), the algebraic connectivity can be used as an indicator that a particular neural region has at least one sharp delineation or comprises only graded differences. This allows for a quantification of the historical issue about the degree of interareal transitions present in the cortex. While the Vogts primarily argued for clearly demarcated brain areas, Brodmann, in his 1909 monograph clearly stated that some areal cytoarchitectonic boundaries were graded. In the extreme, Bailey and von Bonin (1951) argued for an effectively graded cortex (with some minor exceptions). We thus propose the term "Vogt-Bailey Index" to describe the normalised algebraic connectivity of the graph Laplacian when used to describe the extent of feature similarity in a neuroscientific context.

Such an approach can be done across the entire cortex to give a single value for the "gradedness" of the whole cortex, across predefined clusters (such as the resting state networks) or to give a value per region of interest that quantifies how similar features in the region are. We note, however, that this value alone tells us little since the value will be affected by smoothing (which exist in MRI signals). It can, however, be used as a relative measure where one can compare regions across the same brain or between different subjects (see section 5.3. for notes on statistical analysis).

Finally, one can use a vertex-wise searchlight to calculate the Vogt-Bailey (VB) Index across the entire cortex. Using this approach, a neighbourhood of adjoining cortical voxels, or vertices (as is assumed in the adjoining code) is calculated and the (normalised) algebraic connectivity of its affinity graph is calculated. The calculated VB index gives a value of how similar a feature (fMRI, tractography, or others) in the centre of the searchlight is to its nearest neighbours. The final result is effectively a cortical edge detection algorithm (see Figs. 2 and 3 for intuitive examples) where boundaries between parcels should emerge

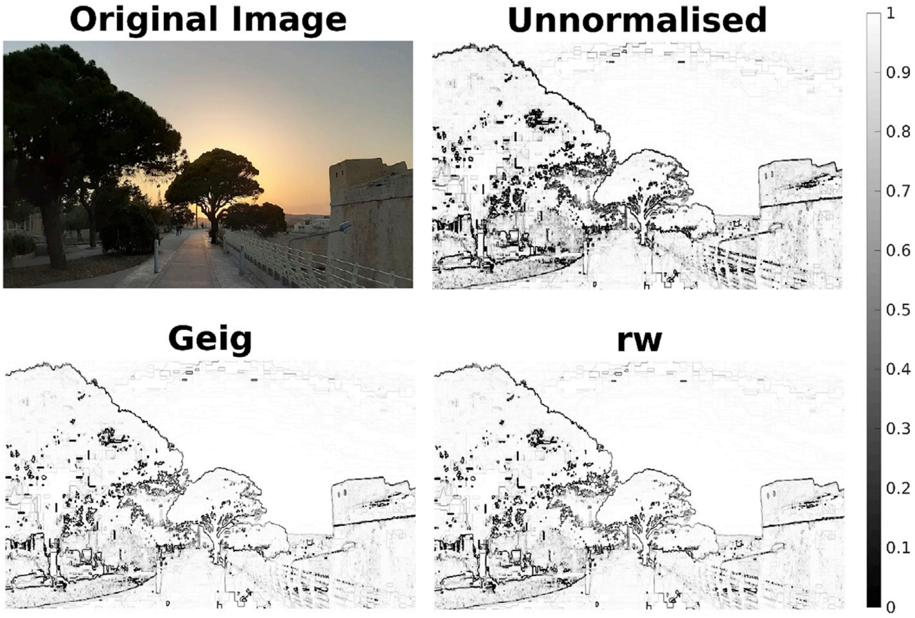

Fig. 2. The VB Index applied to a photograph (top left) using all three normalisations of tha Laplacian matrix. The colormap ranges from black (0) where there are sharp transitions to white (1) where there is homogenous structure in the image.

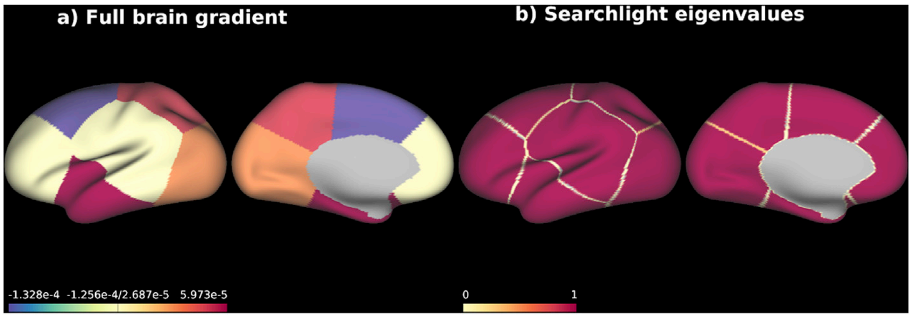

Fig. 3. a) The gradient map on synthetic data showing the expected pattern with values within parcels being extremely similar but different across parcels. b) The VB Index on a cortical surface highlighting the arbitrary parcels. All results show the default generalised eigenvalue problem solution.

naturally and their relative sharpness should be apparent. Of course, smoothing effects and voxel/vertex size will limit the resolution that one can expect. Indeed, such notions in MRI analysis are not new. The idea of a measure of regional homogeneity (ReHo) has been present since the early days of fMRI (Jiang and Zuo, 2016; Zang et al., 2004). Further, the approach has similarities to the observer independent method for microstructural parcellations (Schleicher et al., 1999). Our approach simply fits these ideas of regional homogeneities and boundaries into a flexible and more general framework that does not restrict either the metric for similarity that is used (such as the method for microstructural parcellation) or the feature of interest (such as in both ReHo and the observationally independent approach for microstructural parcellation).

In summary, the VB Index is the proposed term for the normalised algebraic connectivity of the graph Laplacian when used to describe the extent of feature similarity in a neuroscientific context. The adjoining software can produce three “types” of VB Indices: 1) the full brain analysis which also computes a whole brain gradient single VB Index for the whole brain; 2) clustered analysis that computes a gradient and VB Index per region of interest, and 3) the searchlight VB Index which computes a VB Index per vertex based on the neighbourhood data of directly adjacent vertices. The size of the cluster (going from the nearest connected 5 or 6 neighbours to the full brain) is relevant in the interpretation of the VB Index. As Fielder (1973) showed in the original paper, the value of algebraic connectivity provides a measure of how difficult it is to split the graph (higher value indicating more “connectedness”, i.e. more difficult to split). If it is zero, then it indicates that there is at least one complete split in the graph. Hence as the cluster gets larger there is more of a chance that the graph will be easier to split into two, that is what the VB Index measures. In the case of the searchlight, since we are only looking at 5 or 6 connected neighbours, the interpretation is more straightforward: is there an edge near that vertex?

6. Notes on statistical analysis

This article focused on creating a conceptual understanding of the large-scale gradients and the quantification of boundary edges using MRI data.

With respect to the statistical treatment of large-scale feature gradients, a literature is emerging that discusses various statistical approaches to use on gradient maps. The reader is encouraged to explore the articles in this section for current approaches on gradient statistics (Haak et al., 2018; Hong et al., 2019; Langs et al., 2015; Tian and Zalesky, 2018; Xu et al., 2019).

Regarding the statistical analysis of the VB Index maps, future work is needed to disentangle the effects of MR noise and inherent smoothness from real gradations in feature similarity. A research avenue for noise removal includes the generation of null models with similar noise and baseline smoothness as the underlying MRI data (c.f. Gordon et al., 2016; Tian and Zalesky, 2018).

The VB toolbox is a freely available, open source, project under the terms of a GPL licence, we hope that with interest growing in the field of Gradient analysis that the toolbox will grow to also incorporate various statistical approaches for making inferences on both gradient maps and the VB Index.

7. Experiments

7.1. Photography example: searchlight VB index

Before applying the VB Index to the rather abstract notion of function MRI, we have provided a MATLAB script within the respective version of the toolbox that implements the VB Index on a colour photograph (https://github.com/VBIndex/matlab_vb_toolbox/tree/master/vb_index_intuitive_example). Every pixel within the 2D photo can be thought of as a vertex within a brain surface. The functional data is represented by the hue, saturation and their brightness value of the pixel. Performing the VB Index searchlight operation on the photograph, as described in Section 5.3. results in a quantification of boundaries of the image (See Fig. 2). Readers are invited to explore this script with other images made freely available or try it out using their own photographs.

7.2. A neuroimaging example: simulated MRI data example

Following the validation of the technique on colour photographs, the performance of the technique was evaluated on synthetic MRI data where the ground truth is known. To this end a cortical surface from the HCP dataset was arbitrarily split into 6 contiguous parcels. The vertices within the same parcel were assigned identical time-series, which differed across different parcels. The analysis was carried out using version 1.1.0 of the python *vb_tool*. Fig. 3 show the results of applying the proposed method to the simulated data. As expected, the full brain gradient shows a piece-wise constant pattern, reflecting the similarity structures between parcels (unknown) as described above (Fig. 3a). Consistent with this result, the vertex-wise VB Index shows a pattern where the edges between parcels are highlighted (Fig. 3b).

7.3. A neuroimaging example: human connectome project data example

The adjoining toolbox was run on twenty-four (24) individuals (12 F) from the human connectome project database. The calculations were carried out on two separate rs-fMRI runs per participant across both hemispheres. The dataset was pre-processed by the HCP using the minimal processing pipeline (Glasser et al., 2013). The data collection was approved by the Washington University Institutional Review Board (IRB) and further approval for processing the data was obtained by the University of Malta’s University Research Ethics Committee.

The data were processed according to the procedures outlined in the above text using version 1.1.0 of the python *vb_tool*; all calculations used the generalised eigenvalue problem for computations.

First, the whole brain affinity matrix was computed for all 24 subjects

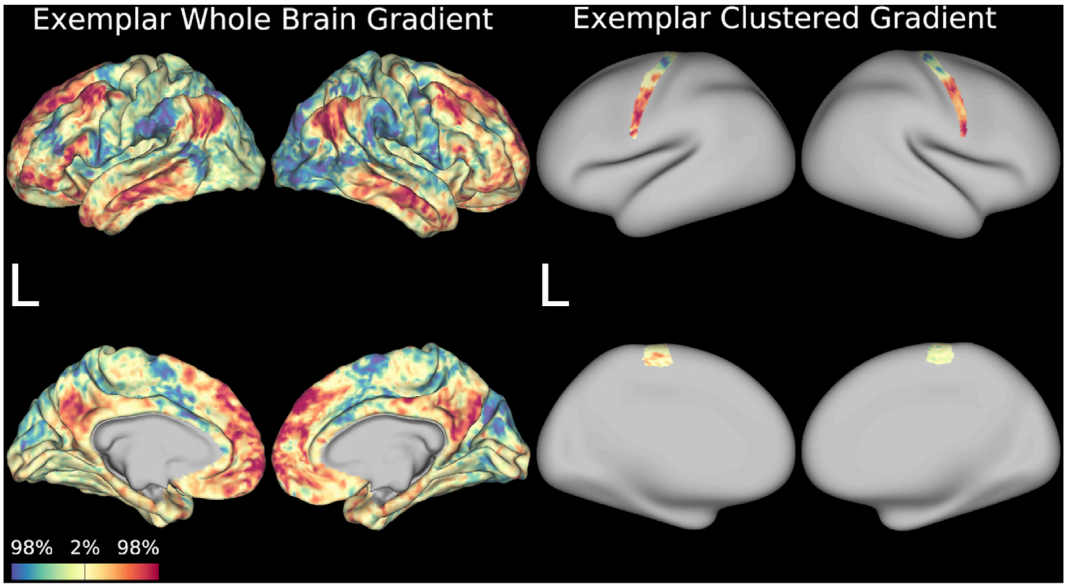

Fig. 4. An exemplar of the principal similarity gradient across the whole cortex based on rs-fMRI as a feature (left). An exemplar of the principal gradient computed on a pre-clustered cortex (using the HCP Multimodal Parcellation, right).

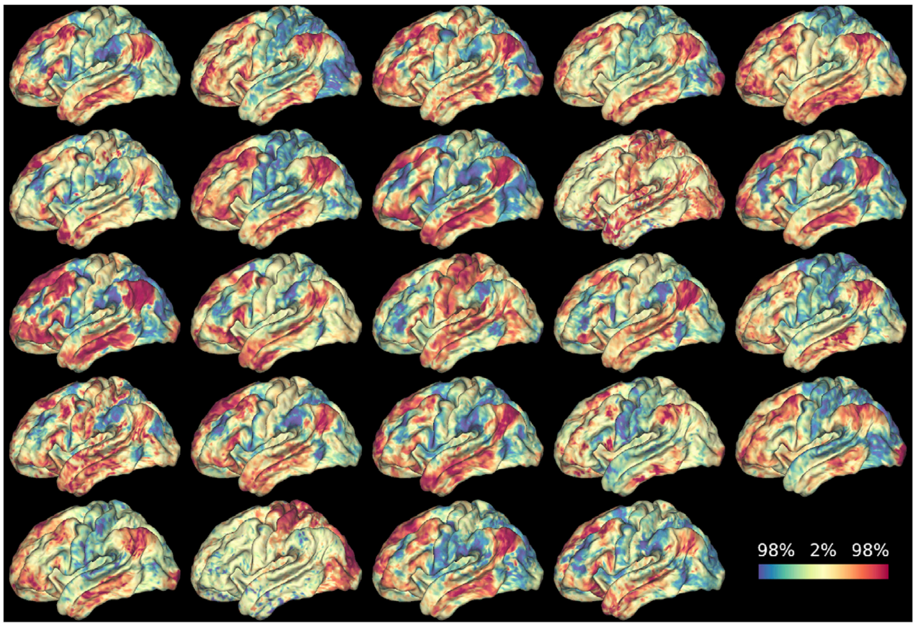

Fig. 5. The principle similarity gradient across 24 individuals on a single run. The image of the same participants on a second fMRI run can be found in the supplementary material.

(per run) and an eigendecomposition of its Laplacian was computed. This resulted in Fig. 4 (left) which shows an exemplar of the primary large scale inter-areal (feature) gradient of the whole cortex in both hemispheres of a single subject. Fig. 5 shows all 24 subjects on the lateral surface of the left hemisphere for a single rs-fMRI run.

We note that the principle gradients differ somewhat from previously published work (c.f. Margulies et al., 2016). This may be due to multiple differences in parameter choices that were made (and discussed briefly in section 2.1). In short, the principle gradient is highly dependent upon the properties of the affinity matrix; the most pertinent difference between our affinity matrix and that of Margulies et al. (2016) was the latter's retention of only the top 10% of functional connections and subsequent re-computation of a cosine similarity while our approach (c.f. Jackson et al., 2020, 2017 for a slightly modified example) accepts all positive correlations that were then transformed to a normalised angular distance. Thresholding plays an important role in the interpretation of the results. A high threshold (such as retaining only the top 10% of connections) will only consider the similarity of “well-connected” vertices giving no weight to moderately and poorly connected ones. Our approach, which only eliminates negative weights, takes these connections into account but would also be more sensitive to “spurious” connections.

Second, the toolbox was used to calculate the primary gradients and their associated VB Index for the data parcellated using the Multimodal HCP parcellation (Glasser et al., 2016). An exemplar of these results can be found in Fig. 3 (right), where the principle gradient is computed in each parcel. Associated with these parcels are the VB Indices per parcel (see Fig. 7 right and a further discussion below).

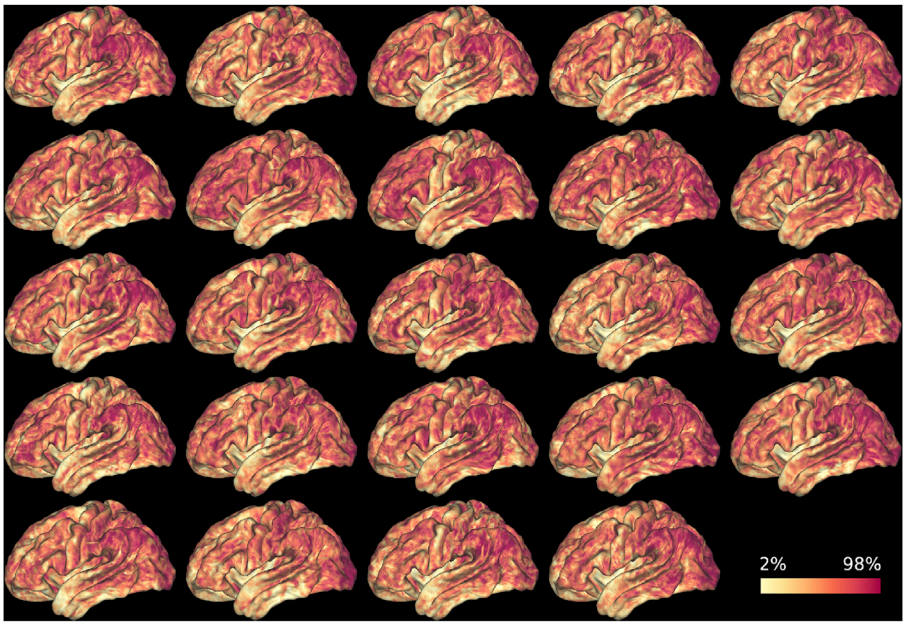

Fig. 6. The VB Index computed across 24 individuals on a single run. The image of the same participants on a second fMRI run can be found in the supplementary material.

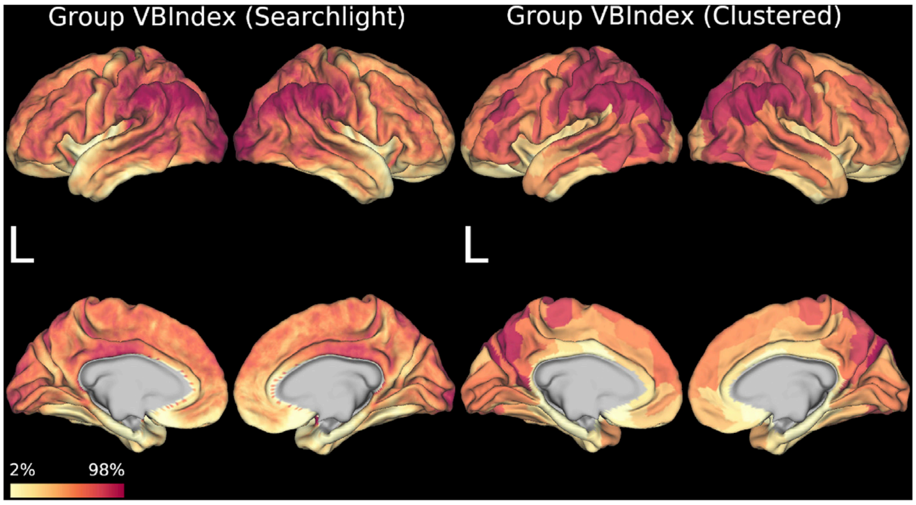

Fig. 7. An average (on a single run) of 24 individual's searchlight, local neighbourhood, whole brain VB-index identifying regions of relatively sharper borders across the cortex.

Finally, the vertex-wise searchlight VB Index was computed on all participants. This approach highlights, in a data-driven fashion, the feature edges and boundaries across the cortex. Fig. 6 shows the searchlight VB Index across all 24 participants while Fig. 7 (left) shows the mean vertex-wise VB Index. One can also see similar patterns between the group vertex-wise VB Index (Fig. 4 left) and the group VB Index computed on clusters (Fig. 7 right).

The full set of results can be found on the HCP BALSA database (https://balsa.wustl.edu/study/show/kND1N).

8. Conclusion

The idea of gradations in neural features has been present since at least the beginning of the twentieth century and has gained traction in the neuroimaging community throughout the early twenty-first. This paper has outlined the general concepts and mathematical intuition behind the spectral transformation and has introduced the related techniques of spectral reordering, Laplacian eigenmaps and clustering. As an accompaniment to this paper, MATLAB and Python tools that performs the different spectral transformations discussed in Section 4 are available. Depending on the size of the data, the technique can take up a considerable amount of RAM and computation time, however, at standard mesh sampling our attached code can run a full brain gradient analysis (using HCP 32K surfaces) on a standard desktop or notebook with 32 GB of RAM.

While the described framework can be used to reason about relationships between neural features, there are plenty of unanswered questions. The first important issue regards the choice of similarity measurement. Although all the metrics discussed above have been used to some extent, a systematic comparison along with guidance regarding which metric to use in different circumstances is needed.

In summary, it is hoped that this article and accompanying tools will be used as a guide to researchers interested in performing anatomical investigations using neural features and their interareal relationships in the brain.

Declaration of competing interest

GJMP is a shareholder and director of Bioxydyn, a company with an interest in imaging services and products.

CRediT authorship contribution statement

Claude J. Bajada: Conceptualization, Data curation, Formal analysis, Investigation, Methodology, Resources, Software, Validation, Visualization, Writing - original draft, Writing - review & editing. **Lucas Q. Costa Campos:** Data curation, Formal analysis, Software, Validation, Writing - review & editing. **Svenja Caspers:** Funding acquisition, Resources, Supervision, Writing - review & editing. **Richard Muscat:** Resources, Supervision, Writing - review & editing. **Geoff J.M. Parker:** Conceptualization, Methodology, Supervision, Writing - review & editing. **Matthew A. Lambon Ralph:** Funding acquisition, Conceptualization, Supervision, Writing - review & editing. **Lauren L. Cloutman:** Funding acquisition, Conceptualization, Supervision, Writing - review & editing. **Nelson J. Trujillo-Barreto:** Formal analysis, Conceptualization, Methodology, Supervision, Writing - original draft, Writing - review & editing.

Acknowledgments

This research was supported by an MRC programme grant to MALR (MR/J004146/1), an EPSRC Research Grant EP/M005909/1 to GJMP, an EPSRC Fellowship (EP/N006771/1) to NJTB and a BBSRC DTP studentship to CJB (BB/J014478/1). SC received support from the Initiative and Networking Fund of the Helmholtz Association as well as from the European Union's Horizon 2020 Research and Innovation Program under grant agreement no. 785907 (Human Brain Project SGA2) and 945539 (Human Brain Project SGA3).

This work is based upon work from COST Action CA18106, supported by COST (European Cooperation in Science and Technology).

The authors would also like to thank Ashely Symons for insightful comments on an early version of this manuscript and Saad Jbabdi for initial discussions regarding the algorithm.

CJB would also like to acknowledge these two invaluable resources that greatly aided in conceptualising parts of this article. The first is a website maintained by Brendan O'Connor (brenocon.com/blog/2012/03) that introduced him to the relationships between dot products, correlations and cosines. The second is the Stanford MOOC by Leskovec, Rajarman and Ullman, "Mining Massive Datasets", which allowed him to understand why an eigendecomposition of a Laplacian matrix does anything sensible.

Data were provided by the Human Connectome Project, WU-Minn Consortium (Principal Investigators: David Van Essen and Kamil Ugurbil; 1U54MH091657) funded by the 16 NIH Institutes and Centers that support the NIH Blueprint for Neuroscience Research; and by the McDonnell Center for Systems Neuroscience at Washington University.

Appendix A. Supplementary data

Supplementary data to this article can be found online at https://doi.org/10.1016/j.neuroimage.2020.117140.

References

Amunts, K., Kedo, O., Kindler, M., Pieperhoff, P., Mohlberg, H., Shah, N.J., Habel, U., Schneider, F., Zilles, K., 2005. Cytoarchitectonic mapping of the human amygdala, hippocampal region and entorhinal cortex: intersubject variability and probability maps. Anat. Embryol. 210, 343–352. https://doi.org/10.1007/s00429-005-0025-5.

Bailey, P., von Bonin, G., 1951. The Isocortex of Man, Illinois Monographs in the Medical Sciences. University of Illinois Press, Urbana.

Bajada, C.J., Jackson, R.L., Haroon, H.A., Azadbakht, H., Parker, G.J.M., Lambon Ralph, M.A., Cloutman, L.L., 2017. A graded tractographic parcellation of the temporal lobe. Neuroimage. https://doi.org/10.1016/j.neuroimage.2017.04.016.

Bajada, C.J., Trujillo-Barreto, N.J., Parker, G.J.M., Cloutman, L.L., Lambon Ralph, M.A., 2019. A structural connectivity convergence zone in the ventral and anterior temporal lobes: data-driven evidence from structural imaging. Cortex 120, 298–307. https://doi.org/10.1016/j.cortex.2019.06.014.

Belkin, M., Niyogi, P., 2002. Laplacian eigenmaps and spectral techniques for embedding and clustering. Adv. Neural Inf. Process. Syst. 14, 585–591. Vols 1 and 2 14.

Belkin, M., Niyogi, P., 2003. Laplacian eigenmaps for dimensionality reduction and data representation. Neural Comput. 15, 1373–1396. https://doi.org/10.1162/089976603321780317.

Bludau, S., Eickhoff, S.B., Mohlberg, H., Caspers, S., Laird, A.R., Fox, P.T., Schleicher, A., Zilles, K., Amunts, K., 2014. Cytoarchitecture, probability maps and functions of the human frontal pole. Neuroimage 93 (Pt 2), 260–275. https://doi.org/10.1016/j.neuroimage.2013.05.052.

Brodmann, K., 1909. In: Brodmann's Localisation in the Cerebral Cortex, (Electronic bk.). Springer, New York, NY]. Springer, c2006.

Buckner, R.L., Krienen, F.M., 2013. The evolution of distributed association networks in the human brain. Trends Cognit. Sci. 17, 648–665. https://doi.org/10.1016/j.tics.2013.09.017.

Caspers, J., Zilles, K., Eickhoff, S.B., Schleicher, A., Mohlberg, H., Amunts, K., 2013. Cytoarchitectonical analysis and probabilistic mapping of two extrastriate areas of the human posterior fusiform gyrus. Brain Struct. Funct. 218, 511–526. https://doi.org/10.1007/s00429-012-0411-8.

Caspers, S., Geyer, S., Schleicher, A., Mohlberg, H., Amunts, K., Zilles, K., 2006. The human inferior parietal cortex: cytoarchitectonic parcellation and interindividual variability. Neuroimage 33, 430–448. https://doi.org/10.1016/j.neuroimage.2006.06.054.

Cerliani, L., Thomas, R.M., Jbabdi, S., Siero, J.C.W., Nanetti, L., Crippa, A., Gazzola, V., D'Arceuil, H., Keysers, C., 2012. Probabilistic tractography recovers a rostrocaudal trajectory of connectivity variability in the human insular cortex. Hum. Brain Mapp. 33, 2005–2034. https://doi.org/10.1002/hbm.21338.

Cloutman, L.L., Binney, R.J., Drakesmith, M., Parker, G.J.M., Lambon Ralph, M.A., 2012. The variation of function across the human insula mirrors its patterns of structural connectivity: evidence from in vivo probabilistic tractography. Neuroimage 59, 3514–3521. https://doi.org/10.1016/j.neuroimage.2011.11.016.

Coifman, R.R., Lafon, S., 2006. Diffusion maps. Appl. Comput. Harmon. Anal. 21, 5–30. https://doi.org/10.1016/j.acha.2006.04.006.

Craddock, R.C., James, G.A., Holtzheimer, P.E., Hu, X.P., Mayberg, H.S., 2012. A whole brain fMRI atlas generated via spatially constrained spectral clustering. Hum. Brain Mapp. 33, 1914–1928. https://doi.org/10.1002/hbm.21333.

Da Costa Campos, L., Bajada, C.J., 2020. VBIndex/py_vb_toolbox 1.0.0. Zenodo. https://doi.org/10.5281/zenodo.3609460.

Damoiseaux, J.S., Rombouts, S.A.R.B., Barkhof, F., Scheltens, P., Stam, C.J., Smith, S.M., Beckmann, C.F., 2006. Consistent resting-state networks across healthy subjects. Proc. Natl. Acad. Sci. U.S.A. 103, 13848–13853. https://doi.org/10.1073/pnas.0601417103.

Devlin, J.T., Sillery, E.L., Hall, D.A., Hobden, P., Behrens, T.E.J., Nunes, R.G., Clare, S., Matthews, P.M., Moore, D.R., Johansen-Berg, H., 2006. Reliable identification of the auditory thalamus using multi-modal structural analyses. Neuroimage 30, 1112–1120. https://doi.org/10.1016/j.neuroimage.2005.11.025.

Eickhoff, S.B., Thirion, B., Varoquaux, G., Bzdok, D., 2015. Connectivity-based parcellation: critique and implications. Hum. Brain Mapp. 36, 4771–4792. https://doi.org/10.1002/hbm.22933.

Geyer, S., Turner, R. (Eds.), 2013. Microstructural Parcellation of the Human Cerebral Cortex: from Brodmann's Post-Mortem Map to in Vivo Mapping with High-Field Magnetic Resonance Imaging, Illustrated. Springer Science & Business Media.

Glasser, M.F., Coalson, T.S., Robinson, E.C., Hacker, C.D., Harwell, J., Yacoub, E., Ugurbil, K., Andersson, J., Beckmann, C.F., Jenkinson, M., Smith, S.M., Van Essen, D.C., 2016. A multi-modal parcellation of human cerebral cortex. Nature 536, 171–178. https://doi.org/10.1038/nature18933.

Glasser, M.F., Sotiropoulos, S.N., Wilson, J.A., Coalson, T.S., Fischl, B., Andersson, J.L., Xu, J., Jbabdi, S., Webster, M., Polimeni, J.R., Van Essen, D.C., Jenkinson, M., WU-Minn HCP Consortium, 2013. The minimal preprocessing pipelines for the Human Connectome Project. Neuroimage 80, 105–124. https://doi.org/10.1016/j.neuroimage.2013.04.127.

Gordon, E.M., Laumann, T.O., Adeyemo, B., Huckins, J.F., Kelley, W.M., Petersen, S.E., 2016. Generation and evaluation of a cortical area parcellation from resting-state correlations. Cerebr. Cortex 26, 288–303. https://doi.org/10.1093/cercor/bhu239.

Guell, X., Goncalves, M., Kaczmarzyk, J.R., Gabrieli, J.D.E., Schmahmann, J.D., Ghosh, S.S., 2019. LittleBrain: a gradient-based tool for the topographical interpretation of cerebellar neuroimaging findings. PloS One 14, e0210028. https://doi.org/10.1371/journal.pone.0210028.

Haak, K.V., Marquand, A.F., Beckmann, C.F., 2018. Connectopic mapping with resting-state fMRI. Neuroimage 170, 83–94.

Hagen, L., Kahng, A.B., 1992. New spectral methods for ratio cut partitioning and clustering. IEEE Trans. Comput. Aided Des. Integrated Circ. Syst. 11, 1074–1085. https://doi.org/10.1109/43.159993.

Hong, S.-J., Vos de Wael, R., Bethlehem, R.A.I., Lariviere, S., Paquola, C., Valk, S.L., Milham, M.P., Di Martino, A., Margulies, D.S., Smallwood, J., Bernhardt, B.C., 2019. Atypical functional connectome hierarchy in autism. Nat. Commun. 10, 1022. https://doi.org/10.1038/s41467-019-08944-1.

Jackson, R.L., Bajada, C.J., Lambon Ralph, M.A., Cloutman, L.L., 2020. The graded change in connectivity across the ventromedial prefrontal cortex reveals distinct subregions. Cerebr. Cortex 30, 165–180. https://doi.org/10.1093/cercor/bhz079.

Jackson, R.L., Bajada, C.J., Rice, G.E., Cloutman, L.L., Lambon Ralph, M.A., 2017. An emergent functional parcellation of the temporal cortex. Neuroimage. https://doi.org/10.1016/j.neuroimage.2017.04.024.

Jiang, L., Zuo, X.-N., 2016. Regional homogeneity: a multimodal, multiscale neuroimaging marker of the human connectome. Neuroscientist 22, 486–505. https://doi.org/10.1177/1073858415595004.

Johansen-Berg, H., Behrens, T.E.J., Robson, M.D., Drobnjak, I., Rushworth, M.F.S., Brady, J.M., Smith, S.M., Higham, D.J., Matthews, P.M., 2004. Changes in connectivity profiles define functionally distinct regions in human medial frontal cortex. Proc. Natl. Acad. Sci. U.S.A. 101, 13335–13340. https://doi.org/10.1073/pnas.0403743101.

Klein, J.C., Behrens, T.E.J., Robson, M.D., Mackay, C.E., Higham, D.J., Johansen-Berg, H., 2007. Connectivity-based parcellation of human cortex using diffusion MRI: establishing reproducibility, validity and observer independence in BA 44/45 and SMA/pre-SMA. Neuroimage 34, 204–211. https://doi.org/10.1016/j.neuroimage.2006.08.022.

Langs, G., Golland, P., Ghosh, S.S., 2015. Predicting activation across individuals with resting-state functional connectivity based multi-atlas label fusion. Med. Imag. Comput. Comput. Assist. Interv. 9350, 313–320. https://doi.org/10.1007/978-3-319-24571-3_38.

Larivière, S., Vos de Wael, R., Hong, S.-J., Paquola, C., Tavakol, S., Lowe, A.J., Schrader, D.V., Bernhardt, B.C., 2020. Multiscale structure-function gradients in the neonatal connectome. Cerebr. Cortex 30, 47–58. https://doi.org/10.1093/cercor/bhz069.

Leskovec, A., Rajaraman, A., Ullman, J.D., 2014. Mining of Massive Datasets. Cambridge University Press, Cambridge. https://doi.org/10.1017/CBO9781139058452.

Margulies, D.S., Ghosh, S.S., Goulas, A., Falkiewicz, M., Huntenburg, J.M., Langs, G., Bezgin, G., Eickhoff, S.B., Castellanos, F.X., Petrides, M., Jefferies, E., Smallwood, J., 2016. Situating the default-mode network along a principal gradient of macroscale cortical organization. Proc. Natl. Acad. Sci. U.S.A. 113, 12574–12579. https://doi.org/10.1073/pnas.1608282113.

Mesulam, M., 2008. Representation, inference, and transcendent encoding in neurocognitive networks of the human brain. Ann. Neurol. 64, 367–378. https://doi.org/10.1002/ana.21534.

Mesulam, M.M., 1998. From sensation to cognition. Brain 121 (Pt 6), 1013–1052. https://doi.org/10.1093/brain/121.6.1013.

Nieuwenhuys, R., Broere, C.A.J., Cerliani, L., 2015. A new myeloarchitectonic map of the human neocortex based on data from the Vogt-Vogt school. Brain Struct. Funct. 220, 2551–2573. https://doi.org/10.1007/s00429-014-0806-9.

O'Connor, B., 2012. Cosine similarity, Pearson correlation, and OLS coefficients [WWW document]. AI and social science. URL. http://brenocon.com/blog/2012/03/cosine-similarity-pearson-correlation-and-ols-coefficients/. accessed 6.1.16.

O'Donnell, L.J., Golby, A.J., Westin, C.-F., 2013. Fiber clustering versus the parcellation-based connectome. Neuroimage 80, 283–289. https://doi.org/10.1016/j.neuroimage.2013.04.066.

O'Donnell, L.J., Kubicki, M., Shenton, M.E., Dreusicke, M.H., Grimson, W.E.L., Westin, C.F., 2006. A method for clustering white matter fiber tracts. AJNR Am. J. Neuroradiol. 27, 1032–1036.

Paquola, C., Seidlitz, J., Benkarim, O., Royer, J., Klimes, P., Bethlehem, R.A.I., Lariviere, S., Vos de Wael, R., Hall, J.A., Frauscher, B., Smallwood, J., Bernhardt, B.C., 2020. The cortical wiring scheme of hierarchical information processing. BioRxiv. https://doi.org/10.1101/2020.01.08.899583.

Paquola, C., Vos De Wael, R., Wagstyl, K., Bethlehem, R.A.I., Hong, S.-J., Seidlitz, J., Bullmore, E.T., Evans, A.C., Misic, B., Margulies, D.S., Smallwood, J., Bernhardt, B.C., 2019. Microstructural and functional gradients are increasingly dissociated in transmodal cortices. PLoS Biol. 17, e3000284 https://doi.org/10.1371/journal.pbio.3000284.

Rottschy, C., Eickhoff, S.B., Schleicher, A., Mohlberg, H., Kujovic, M., Zilles, K., Amunts, K., 2007. Ventral visual cortex in humans: cytoarchitectonic mapping of two extrastriate areas. Hum. Brain Mapp. 28, 1045–1059. https://doi.org/10.1002/hbm.20348.

Scheperjans, F., Hermann, K., Eickhoff, S.B., Amunts, K., Schleicher, A., Zilles, K., 2008. Observer-independent cytoarchitectonic mapping of the human superior parietal cortex. Cerebr. Cortex 18, 846–867. https://doi.org/10.1093/cercor/bhm116.

Schleicher, A., Amunts, K., Geyer, S., Morosan, P., Zilles, K., 1999. Observer-independent method for microstructural parcellation of cerebral cortex: a quantitative approach to cytoarchitectonics. Neuroimage 9, 165–177. https://doi.org/10.1006/nimg.1998.0385.

Tian, Y., Zalesky, A., 2018. Characterizing the functional connectivity diversity of the insula cortex: subregions, diversity curves and behavior. Neuroimage 183, 716–733. https://doi.org/10.1016/j.neuroimage.2018.08.055.

Vázquez-Rodríguez, B., Suárez, L.E., Markello, R.D., Shafiei, G., Paquola, C., Hagmann, P., van den Heuvel, M.P., Bernhardt, B.C., Spreng, R.N., Misic, B., 2019. Gradients of structure-function tethering across neocortex. Proc. Natl. Acad. Sci. U.S.A. 116, 21219–21227. https://doi.org/10.1073/pnas.1903403116.

Vogt, C., Vogt, O., 1911. Nouvelle contribution à l'étude de la myéloarchitecture de l'écorce cérébrale. Presented at the XX. Congres des médecins aliénistes et neurologistes de France (Brüssel).

Von Luxburg, U., 2007. A tutorial on spectral clustering. Stat. Comput. 17, 395–416. https://doi.org/10.1007/s11222-007-9033-z.

von Economo, C., Koskinas, G.N., 1925. Die Cytoarchitektonik der Hirnrinde des erwachsenen Menschen. Atlas mit 112 mikrophotographischen Tafeln inbesonderer Mappe.

Vos de Wael, R., Benkarim, O., Paquola, C., Lariviere, S., Royer, J., Tavakol, S., Xu, T., Hong, S.-J., Valk, S.L., Misic, B., Milham, M.P., Margulies, D.S., Smallwood, J., Bernhardt, B.C., 2019. BrainSpace: a toolbox for the analysis of macroscale gradients in neuroimaging and connectomics datasets. BioRxiv. https://doi.org/10.1101/761460.

Vos de Wael, R., Larivière, S., Caldairou, B., Hong, S.-J., Margulies, D.S., Jefferies, E., Bernasconi, A., Smallwood, J., Bernasconi, N., Bernhardt, B.C., 2018. Anatomical and microstructural determinants of hippocampal subfield functional connectome embedding. Proc. Natl. Acad. Sci. U.S.A. 115, 10154–10159. https://doi.org/10.1073/pnas.1803667115.

Xu, T., Nenning, K.-H., Schwartz, E., Hong, S.-J., Vogelstein, J.T., Fair, D.A., Schroeder, C.E., Margulies, D.S., Smallwood, J., Milham, M.P., Langs, G., 2019. Cross-species functional alignment reveals evolutionary hierarchy within the connectome. BioRxiv. https://doi.org/10.1101/692616.

Zang, Y., Jiang, T., Lu, Y., He, Y., Tian, L., 2004. Regional homogeneity approach to fMRI data analysis. Neuroimage 22, 394–400. https://doi.org/10.1016/j.neuroimage.2003.12.030.

Zhang, Yaqin, Fan, L., Zhang, Yu, Wang, J., Zhu, M., Zhang, Yuanchao, Yu, C., Jiang, T., 2014. Connectivity-based parcellation of the human posteromedial cortex. Cerebr. Cortex 24, 719–727. https://doi.org/10.1093/cercor/bhs353.

Zilles, K., Amunts, K., 2010. Centenary of Brodmann's map–conception and fate. Nat. Rev. Neurosci. 11, 139–145. https://doi.org/10.1038/nrn2776.

Acknowledgments

I would first like to thank my two amazing supervisors, Prof. Dr. Dr. Svenja Caspers and PD Dr. Jens Elgeti, to whom I owe much gratitude for helping and guiding me during this long period, and from whom I have learned much, both in sheer scientitic knowledge as well as the practical aspects of being a scientist. Without their attentive mentorship, navigating between the two fascinating fields of Neuroscience and Biophysics would not have been as fruitful and fascinating as it was. I would also like to thank the other members of my thesis committee, Prof. Dr. Matthias Sperl and Prof. Dr. Thomas Michely, for accepting to read my work.

It is also important to acknowledge the immense positive impact that IHRS BioSoft has imparted on my PhD, by providing both great discussions with colleagues from adjacent fields and a space where I felt safe to try and fail and succeed in developing soft skills.

Most of this work would not have been possible without some of my favorite inhabitants in the whole of Nordrhein-Westfalen, the computer clusters JURECA (FZ Jülich) and CLAIX (RWTH Aachen), as well as their little cousin, imenb033, where I developed, debugged, and analyzed most of my results.

My eternal gratitude goes to all my colleagues, friends, and revisors in INM and IBI, Jan, Camilla, Leona, Leonor, Christiane, Andrea, and Christian, for all their support. I would be remiss to not deeply thank Nora, Johanna, Daniel, and Dominique for helping me so much in the early stages of my life in Germany. In that vein, our secretary in IBI, Meike, deserves the highest praise for being so understanding and hardworking in solving all the issues surrounding my complex inter-institute situation.

Thanks to my good friends, Claude, Maren, and Ksenia, for making my life not only more interesting but also weirder, and to Tobias and Sebastian, for all the sunny beers near rivers. A double special thanks goes to Raphael, as my coauthor and mentor in matters theoretical, and for being the force behind much of the analytical theory that ended up in this work. Enormous thanks go to my flat mates, Ahmet, Flaviano, and Lena, for having the patience to deal with me on a daily basis, which can be no easy task.

Agradeço para todo o sempre ter os amigos que coletei nestes anos todos. Desdos tempo de escola, como Gregório e Polyana, até os tempos de faculdade, com Landau, Raniere, Victor, Flor, Mário, Clarissa, Rebeca e Bictor.

Agradeço também à minha família, tanto nascida como agregada, tanto brasileira quanto alemã ou inglesa, que me deu imenso suporte para que eu pudesse atingir tudo o que atingi.

Finalmente, a Thomas por todo o suporte e paciência tanto nos tempos de desespero quanto nos de hiperatividade, para quem serei eternamente grato.

Erklärung der Selbständigkeit

Hiermit versichere ich an Eides statt, dass ich die vorliegende Dissertation selbstständig und ohne die Benutzung anderer als der angegebenen Hilfsmittel und Literatur angefertigt habe. Alle Stellen, die wörtlich oder sinngemäß aus veröffentlichten und nicht veröffentlichten Werken dem Wortlaut oder dem Sinn nach entnommen wurden, sind als solche kenntlich gemacht. Ich versichere an Eides statt, dass diese Dissertation noch keiner anderen Fakultät oder Universität zur Prüfung vorgelegen hat; dass sie - abgesehen von unten angegebenen Teilpublikationen und eingebundenen Artikeln und Manuskripten - noch nicht veröffentlicht worden ist sowie, dass ich eine Veröffentlichung der Dissertation vor Abschluss der Promotion nicht ohne Genehmigung des Promotionsausschusses vornehmen werde. Die Bestimmungen dieser Ordnung sind mir bekannt. Darüber hinaus erkläre ich hiermit, dass ich die Ordnung zur Sicherung guter wissenschaftlicher Praxis und zum Umgang mit wissenschaftlichem Fehlverhalten der Universität zu Köln gelesen und sie bei der Durchführung der Dissertation zugrundeliegenden Arbeiten und der schriftlich verfassten Dissertation beachtet habe und verpflichte mich hiermit, die dort genannten Vorgaben bei allen wissenschaftlichen Tätigkeiten zu beachten und umzusetzen. Ich versichere, dass die eingereichte elektronische Fassung der eingereichten Druckfassung vollständig entspricht.

Teilpublikation:

- Costa Campos, L. da, Hornung, R., Gompper, G., Elgeti, J., & Caspers, S. (2021). The role of thickness inhomogeneities in hierarchical cortical folding. NeuroImage, 231, 117779. https://doi.org/10.1016/j.neuroimage.2021.117779.
- Bajada, C. J., Costa Campos, L. Q., Caspers, S., Muscat, R., Parker, G. J. M., Lambon Ralph, M. A., Cloutman, L. L., & Trujillo-Barreto, N. J. (2020). A tutorial and tool for exploring feature similarity gradients with MRI data. NeuroImage, 221, 117140. https://doi.org/10.1016/j.neuroimage.2020.117140.
- Herstellung strukturierter Oberflächen. Aktenzeichen als 10 2020 118 555.3.

Datum, Name und Unterschrift

24.05.2021